Alma Mater Studiorum – Università di Bologna

DOTTORATO DI RICERCA IN

CHIMICA

Ciclo XXXIII

Settore Concorsuale: 03/A2

Settore Scientifico Disciplinare: CHIM/02

Computing the structural and vibrational properties of polymorphic organic molecular crystals through van der Waals corrected density functional theory and the electronic properties of organic thin films through microelectrostatic calculations.

Presentata da: Andrea Giunchi

Coordinatore Dottorato

Prof.ssa Domenica Tonelli

Supervisore

Prof. Raffaele Guido Della Valle

Co-Supervisori

Prof.ssa Elisabetta Venuti

Prof. Luca Muccioli

Esame finale anno 2021

Abstract

The present Thesis reports on the various research projects to which I have contributed during my PhD period, working with several research groups, and whose results have been communicated in a number of scientific publications.

The main focus of my research activity was to learn, test, exploit and extend the recently developed vdW-DFT (van der Waals corrected Density Functional Theory) methods for computing the structural, vibrational and electronic properties of ordered molecular crystals from first principles. A secondary, and more recent, research activity has been the analysis with microelectrostatic methods of Molecular Dynamics (MD) simulations of disordered molecular systems.

While only very unreliable methods based on empirical models were practically usable until a few years ago, accurate calculations of the crystal energy are now possible, thanks to very fast modern computers and to the excellent performance of the best vdW-DFT methods. Accurate energies are particularly important for describing organic molecular solids, since they often exhibit several alternative crystal structures (polymorphs), with very different packing arrangements but very small energy differences. Standard DFT methods do not describe the long-range electron correlations which give rise to the vdW interactions. Although weak, these interactions are extremely sensitive to the packing arrangement, and neglecting them used to be a problem. The calculations of reliable crystal structures and vibrational frequencies has been made possible only recently, thanks to development of some good representations of the vdW contribution to the energy (known as "vdW corrections").

As it will be repeatedly seen throughout this Thesis, the first research step is always to compute the properties of the systems of interest and then to compare the computational results with their experimental equivalents. Raman spectroscopy in the low frequency region of the lattice modes is the

main experimental technique with which the computations are confronted because of its sensitivity to polymorphic modifications, together with other measurement methods to complement the gathered information.

The comparison between experimental and calculated results may be used to validate the computational methods or, more fruitfully, to support, guide and verify the analysis of the experiments. The Raman measurements, compared with the computed spectra, were found to be able to clarify ambiguities which otherwise the X-ray measurements were unable to solve. Thanks to the synergy between the two methods it has been possible to identify different polymorphs, to confirm or exclude possible crystal structures, and even to obtain information on the orientational distribution of single crystals and in poly-crystalline assemblies.

Contents

Acronyms vi

1 General introduction **1**

1.1 Research context 1

1.2 Scientific context 2

1.3 Organization of the thesis 6

2 Computational methods **9**

2.1 Introduction 9

2.2 DFT calculations 9

2.3 Choice of k-vector grid and energy cutoff 10

2.4 Distance comparison method 11

2.5 Vibrational frequencies and eigenvectors 11

2.6 Raman intensities 13

2.7 Raman active irreducible representations 13

2.8 One-step calculation of Raman intensities 14

2.9 Temperature dependence of Raman spectra 15

3 Benchmarking van der Waals corrections **17**

3.1 Introduction 17

3.2 Context 18

3.3 Approaches included in the benchmark 19

3.4 Structures chosen for the benchmark 20

3.5 Calculations 22

3.6 Spectra computed with experimental cell volumes 23

3.7 Eigenvector analysis 26

3.8 Cell volume relaxation 28
3.9 Spectra calculated at the relaxed volumes 30
3.10 Conclusions 32

4 Polymorph recognition: Coronene **34**
4.1 Introduction 34
4.2 State of the art 35
4.3 Structural analysis and vdW-DFT calculations 36
4.4 Polymorph discrimination by Raman spectroscopy 40
4.5 Polymorph identification through vdW-DFT spectra 42
4.6 Conclusions 44

5 Polymorph recognition: Indigo **50**
5.1 Introduction 50
5.2 State of the art 51
5.3 Inherent structures 54
5.4 DFT structures and relative stability 55
5.5 Crystallization and X-ray 57
5.6 Raman lattice phonon and DFT comparison 59
5.7 Intramolecular Raman spectra and film identification 62
5.8 Conclusions 65

6 Polymorph recognition: Thioindigo **67**
6.1 Introduction 67
6.2 State of the art 68
6.3 Crystallization and X-ray diffraction 71
6.4 Powder spectra 71
6.5 Crystal spectra 75
6.6 Film 79
6.7 Conclusions 84

7 Polymorph recognition: Tyrian purple **86**
7.1 Introduction 86
7.2 State of the art 87

7.3 Crystallization and X-ray diffraction . . . 90
7.4 Raman Phonon Form I . . . 91
7.5 Raman Phonon Form II . . . 94
7.6 Raman Intramolecular Spectra . . . 96
7.7 Form II stability . . . 97
7.8 Conclusions . . . 99

8 Crystal structure prediction: Phenytoin 101
8.1 Introduction . . . 101
8.2 Context . . . 102
8.3 Form II structure challenge . . . 103
8.4 Grazing Incident X-ray Diffraction results . . . 105
8.5 Crystal Structure Prediction . . . 107
8.5.1 CSP procedure . . . 107
8.5.2 CSP results . . . 111
8.6 Raman Spectroscopy . . . 115
8.6.1 Form I . . . 116
8.6.2 Experimental map of phenytoin films . . . 122
8.6.3 Form II: Pc vs $P2_1/c$ . . . 123
8.7 Conclusions . . . 127

9 Electronic properties of thin films 130
9.1 Introduction . . . 130
9.2 Context . . . 131
9.3 Structure of B2 and B4 films . . . 132
9.4 Electron transfer parameters . . . 138
9.5 Conclusions . . . 145

10 General conclusions 178

Bibliography 181

Acknowlegments 210

Acronyms

API	Active Pharmaceutical Ingredient
B2 or B2PyMT	(4,6-bis(3,5-di(pyridine-2-yl)phenyl)-2-methylpyrimidine
B3LYP	Becke, 3-parameter, Lee-Yang-Parr exchange and correlation functiona
B4 or B4PyMT	(4,6-bis(3,5-di(pyridine-4-yl)phenyl)-2-methylpyrimidine
BAMS	Bar-Assisted Meniscus Shearing
CCD	Charge Coupled Device
CIF	Crystallographic Information File
CSD	Cambridge Structural Database
CSP	Crystal Structure Prediction
D2	pairwise Dispersion corrections of Grimme
D3-BJ	Grimme Dispersion corrections with Becke-Jonson damping
DFPT	Density Functional Perturbation Theory
DFT	Density Functional Theory
ESP	charges derived from the Electro-Static Potential
FDM	Finite Displacement Method
GIXD	Grazing Incidence X-ray Diffraction
MBD or MBD@rsSCS	Many-body Dispersion corrections of Ambrosetti et al.
MD	Molecular Dynamics
NPT	constant Number of particles, Pressure and Temperature
NVT	constant Number of particles, Volume and Temperature
OLED	Organic Light Emitting Diode
PAW	Projector Augmented Wave method
PBE	Perdew-Burke-Ernzerhof exchange and correlation functional
PVT	Physical Vapor Transport
PXRD	Powder X-Ray Diffraction
SCF	Self-Consistent Field
SIP	Surface Induced Polymorph
TS	dispersion corrections of Tkatchenko and Scheffler
XRD	X-ray Diffraction
vdW	van der Waals
vdW-DFT	Density Functional Theory with van der Waals corrections

Chapter 1

General introduction

1.1 Research context

I have spent my Bachelor, Master and PhD research periods working in the Condensed Matter Research Group of the Department of Industrial Chemistry "Toso Montanari" (Bologna University, Bologna, Italy) under the supervision of Raffaele G. Della Valle. It is a mixed experimental-theoretical research group, where experimental and computational techniques are systematically combined. Indeed, these two fields are strongly interconnected: experimental results need calculations in order to be interpreted, while the calculations need the experimental results for the validation or even as a starting point. Having both kinds of methods in the same group is very fruitful since a maximum synergy may be achieved.

During my PhD period, I had the good fortune to win two scholarships which I used to visit and collaborate with two different research groups.

Thanks to an Erasmus+ Mobility for Traineeships, I spent three months in the Solid-State group of the Graz University of Technology (TU Graz, Graz, Austria), under the supervision of Egbert Zojer and Natalia Bedoya-Martínez. This was during my first year as a PhD student and allowed me to learn the main class of methods used for almost all my Thesis projects, namely the Density Functional Theory (DFT) methods for the calculation of various properties of organic molecular crystals.

During my last PhD year and thanks to a Marco Polo scholarship, I spent three months at the Neél Institute CNRS (Grenoble, France) under the supervision of Gabriele D'Avino. Here, I could learn a different class of methods, namely Molecular Dynamics (MD) simulations using empirical classical mechanics potential models. Approaches of this kind may be used also for disordered systems, which are not amenable to vdW-DFT procedures. Combined with microelectrostatic calculations and quantum mechanics *ab initio* methods, MD may be used to estimate the electronic properties of the system.

1.2 Scientific context

The prevalent theme of my PhD thesis projects has been the identification, development and exploitation of accurate methods for computing the structural, vibrational and electronic properties of organic molecular crystals, in order to support, guide and validate the analysis of the experiments, performed by other members of our group, when they concern Raman spectroscopy, otherwise by external collaborators.

The context where the necessity of high accuracy is more evident is Crystal Structure Prediction (CSP) - the calculation from first principles of the structure of a crystal of given chemical composition - which has been a long-standing goal of Chemical-Physics. The difficulty, but also the importance, of achieving this goal are particularly significant for organic molecular crystals, whose crystallographic structures can be very hard to predict because, compared to intra-molecular chemical bonding, inter-molecular interactions are weak, non-directional and long-range. Hundreds of possible structures can exist within a few kcal/mol of the global energy minimum[1] and therefore extreme accuracy is required for a reliable prediction.

The congestion of many different possible crystalline configurations very close in energy is not a theoretical artefact but corresponds to physical reality and, in fact, organic compounds are often found coexisting in more than one crystal structure (polymorphs). While polymorphs are close in energy, other properties may widely differ, causing major problems in qual-

ity control in the manufacturing of polymorphic materials. For example, a polymorphic transformation modifies the detonation sensitivity of explosives (causing industrial accidents), the solubility (changing the effective dose of pharmaceuticals), and the conductibility (affecting the performance of devices based on organic semiconductors).

Until a few years ago, the crystallographic energy was invariably calculated through empirical potential models based on classical mechanics, because there were no alternatives with acceptable computational cost. These models occasionally predicted correct structures,[2,3] proving that the prediction problem is solvable, but were extremely unreliable due to the poor transferability of the models from one chemical to the other and to the inaccuracy of the energies.

The dependence on unreliable potential models has recently been overcome by computing energies and crystallographic structures with the methods of quantum mechanics, thanks to much faster computers and to the development of reliable Density Functional Theory (DFT)[4] software codes for modeling molecular crystals. All codes compute the electronic structure of periodic systems by representing the electronic density in terms of single-electron Kohn-Sham orbitals. Different strategies have been proposed, tipically using either plane wave basis sets[5–8] or linear combinations of atom centered Gaussian functions,[9] and some issues, such as the handling of long-range electron correlations - also known as electron dispersion or van der Waals (vdW) force - are still matter of investigation.[10,11]

Dispersion is an attractive interaction originating from the response of electrons in one region to charge density fluctuations in another. The leading term of this interaction, namely the interaction between fluctuating dipoles and induced dipoles, gives rise to the well known r^{-6} decay of the interaction energy with the interatomic separation r. DFT calculations, although in principle exact, in practice approximate the interactions between the electrons with quite simple exchange-correlation functionals. Standard functionals depend only on local or semi-local quantities such as the electron density and its gradients, and therefore do not describe the long-range electron correlations responsible for the vdW interactions. Although weak, these are extremely

sensitive to differences in packing arrangement and thus are crucial for describing molecular crystals.

Several methods have been proposed for representing the vdW contributions to the energy (known as "vdW corrections")[12–17] and, in a major breakthrough, is has been shown that van der Waals corrected Density Functional Theory (vdW-DFT) methods yield reliable crystal structure predictions.[18,19] More recently, thanks to a computational strategy developed by Natalia Bedoya-Martínez in a work to which I had the privilege of contributing,[20] it has been demonstrated that an accurate calculation of the vibrational spectra of organic molecular crystals is actually feasible. The whole vibrational range, from the highest intramolecular frequencies ($\approx$ 4000 cm^{-1}) down to the lowest modes around 10 cm^{-1}, is well described.

The modes in the low frequency region ($\approx$ 10-150 cm^{-1}) describe lattice vibrations (phonons) and, being therefore dominated by inter-molecular interactions, are extremely sensitive to the details of crystal packing. Experimentally it has indeed been found that lattice phonon spectra in the low energy range of the spectrum are unique for a given structure. Their frequencies thus represent the "fingerprint" of the structure and, in fact, lattice phonon spectroscopy has been consolidated as the experimental technique of choice for detecting the presence of different polymorphs grown in a variety of environments, such as single bulk crystals, nano-crystals, films or at solid interfaces.[21–24]

While the presence of different spectra is enough to show that different polymorphs are present, i.e., to discriminate the polymorphs, for a complete identification one needs to link each experimental spectrum to the appropriate structure. Crystal morphology, color and other macroscopic properties may occasionally be useful. Until now, however, the only foolproof method for polymorph identification was to obtain calibration Raman spectra on a complete set of reference samples, each containing only one polymorph and individually identified by X-ray diffraction (XRD), which is a complicated and time-consuming task.

Thanks to the accuracy of the calculations, this task is now no more necessary. As it will be repeatedly shown in the present Thesis, the differences

between experimental and computed vdW-DFT phonon frequencies (below 5 cm^{-1}) are smaller than the experimental differences between different polymorphs, and even computed and experimental Raman intensities agree very well.[20,25–27] The vdW-DFT phonon spectra computed for each polymorph in fact closely match the corresponding experimental spectra, allowing for a quick and reliable identification of the phase without XRD measurements on the actual samples.

Several systems have been considered in this thesis (ranging from model systems to pigments, semiconductors, pharmaceuticals and co-crystals) and, as expected, the experimental Raman spectra in the "fingerprint" region have been found unique and characteristic of the compound and of its crystal form. The outstanding accuracy of the computed spectra in the same region has allowed us to identify different polymorphs, to confirm or exclude possible crystal structures, to discriminate among different orientations of a crystalline sample, and even to deduce the most probable arrangement on poly-crystalline assemblies.

These are pieces of experimental information which usually can only obtained through X-ray XRD measurements but, in fact, may be efficiently obtained by exploiting the synergy between experimental Raman spectra and highly accurate computed crystal structures and spectra. We have found that this mixed experimental-computational strategy may succeed even in situations where XRD methods fail, such as thin films were there the XRD pattern was very poor or for a structure which was almost, but not exactly, centrosymmetric. Raman spectroscopy could readily check for the presence or absence of inversion symmetry, while XRD could not.

One of the limitations of vdW-DFT methods for periodic systems (i.e. crystals) is that they cannot be used for disordered systems such as the thin molecular films employed in organic electronics. Disordered thin film systems are discussed in one of the last chapters of this thesis. Even in this case the strategy of comparing experimental and computational information, but with a combination of MD, DFT and microelectrostatic theoretical methods, rather than vdW-DFT, has been very fruitful.

1.3 Organization of the thesis

During the thesis period I have collaborated to several scientific projects. These projects have resulted in eight published papers,[25–32] one paper accepted for publication,[33] two submitted,[34,35] and more in preparation. The present thesis describes my contribution to the various publications, except for two[27,32] which are outside the scope of the thesis.[1]

All chapters of the thesis are summarised below. Except for the first and the last, each chapter corresponds to a publication (or two), in an order chosen to clarify the overall logic, rather than chronological.

Chapter 2 describes the general computational methods used through the thesis. Methods specific to individual problems are described in the corresponding Chapter.

Chapter 3 presents a benchmark of several different schemes for implementing the vdW corrections.[26] The various schemes have been tested on a set of sample systems, including different organic molecules and different polymorphs. The vdW-DFT computed structures and vibrational spectra of the crystal have been validated by comparison with their experimental equivalent.

Chapter 4 concerns a study of the temperature-induced phase transition of coronene, which was known but not well characterized. On the experimental side, the observation of abrupt changes in the lattice Raman spectra upon cooling and heating the crystal confirms the transition, showing that it is reversible but with a large hysteresis. The outstanding fidelity of the calculated spectra to the experiments allows for an unambiguously identification of the phases, without recourse to XRD measurements.[25]

Chapter 5 is dedicated to indigo, a commonly used natural dye which has been shown to exhibit a highly promising semiconducting behavior, allowing for the realization of ambipolar devices in thin film form. Two bulk poly-

[1] Paper [27] describes a time-resolved Raman spectroscopy investigation of a photodimerization process in the solid state. My contribution was the reconstruction of the chemical kinetics through the mathematical analysis of the time dependence of the spectra. Paper [32] was a student exercise which originated a publication, and my contribution was negligible.

morphs were known, but it was not known which crystal structure is actually present in the thin films, an information relevant for device applications. XRD results where inconclusive, due to their notorious difficulties with thin films of this system. However, Raman measurements combined with vdW-DFT calculations could readily identify the two polymorphs, showing that they appear concomitantly in most analyzed bulk samples, whereas only one of them grows in the films.[28]

Chapter 6 covers thioindigo, a semiconducting synthetic dye related to indigo, also present in two polymorphs. This compound has been used to develop and test the methods for computing polarized Raman spectra of partially disordered systems. Information on the orientational distribution in sheared thin films could be extracted by comparing computed and experimental spectra.[31]

Chapter 7, similar to the two previous chapters, deals with dibromoindigo, the main component of the Tyrian purple dye, also presenting two polymorphs with semiconductor properties in the film phase. In this case the comparison between experimental and calculated spectra indicated that the thin film structure is related to one of the two bulk polymorphs.[27]

Chapter 8 presents the structure solution for a form of the pharmaceutical compound phenytoin that is only found in thin films.[29,30] The combination of crystal structure prediction (CSP) and grazing incidence X-ray diffraction (GIXD) experiments gave a very reasonable, but not fully confirmed, centrosymmetric candidate structure.[29] Calculated and measured Raman spectra indicated the proposed structure was not correct. In fact, it actually corresponded to a saddle point of the energy landscape of the system, from which a non-centrosymmetric minimum could be reached. This new structure improved the agreement with the GIXD data and gave an excellent match between experimental and calculated Raman spectra.[30] Raman spectroscopy assisted by vdW-DFT calculations effectively complemented GIXD. The reason is that X-ray structures are doubtful for systems which are almost, but not exactly, centrosymmetric. Raman spectroscopy, instead, may readily check for the presence or absence of inversion symmetry.

Chapter 9 describes my first research based on MD simulations rather

that vdW-DFT calculations. It presents a comprehensive computational study of the electron transfer parameters of two molecules (B2PyMPM and B4PyMPM) used as thin films in Organic Light Emitting Diode (OLED).[34] Since the measured parameters for the two molecules are very different, even if their structures are almost identical, significant differences in their supramolecular arrangements appeared likely. To investigate this hypothesis, the vacuum-deposited film structures were modelled by molecular dynamics (MD) and several plausible disordered configurations were generated. Electron transfer parameters were calculated on each configuration with a combination of DFT and microelectrostatic calculations, obtaining a good agreement with the experimental results, an understanding of the effects of the different types of disorder for the two molecules, and a plausible explanation of their differences.

Chapter 10, finally, contains a final summary and general conclusions about the thesis projects.

Chapter 2

Computational methods

2.1 Introduction

This Chapter briefly describes the computational methods repeatedly used through the thesis, approximately in the order in which they are applied for a typical system. Methods specific to individual systems are described in the appropriate Chapters, such as the Crystal Structure Prediction (CSP) procedure described in Chapter 8 or the Molecular Dynamics (MD) and microelectrostatic calculation described in Chapter 9.

2.2 DFT calculations

All structural and vibrational calculations were performed in the framework of Density Functional Theory (DFT)[4] using the Vienna ab initio simulation package (VASP, version 5.4.1).[5–8] The Perdew-Burke-Ernzerhof (PBE) exchange and correlation functional was used in combination with the projector-augmented wave (PAW) approach.[36,37]

Calculations were usually first performed with unit cell parameters constrained at their experimental values (i.e. at the experimental volume V_{exp}), and later at the fully relaxed unit cell (i.e. at the volume V_{calc} calculated for zero external pressure). In both cases atomic coordinates were relaxed to

the energy minimum with a threshold of 10^{-3} eV Å^{-1} for the residual forces, using the GADGET tool.[38]

It should be remarked that the relaxed unit cell structures are minimum potential energy structures appropriate to zero Kelvin and that, furthermore, zero-point energies were not considered. Their inclusion would require phonon calculations for $\boldsymbol{k} \neq 0$ in the quasi-harmonic approximation (i.e., we would need to consider that phonon vibrations change with the cell parameters), which are beyond the scope of this work, and very likely beyond the capacities of present computational resources especially for the larger unit cells. For simple systems like carbon dioxide, ice, acetic acid, and imidazole it has been shown that volume relaxations including zero-point energies could yield volumes 2-3% higher than those predicted from lattice energy relaxations.[39–41] We expect this effect to be much smaller for the comparably heavy molecules studied here, but those observations still suggest that the calculated unit-cell volumes reported in the following represent lower limits to the actual situation at low temperatures. If we were able to include the corresponding thermal expansion in the simulations, an increase of the calculated volumes would occur. Consistent with these considerations, we expect that in most cases the calculations should predict smaller volumes compared to the experimental values.

2.3 Choice of k-vector grid and energy cutoff

VASP represents the Kohn-Sham orbitals in terms of a plane wave basis sets with wavevectors of the form $\boldsymbol{G} + \boldsymbol{k}$, where $\boldsymbol{G}$-vectors lie on reciprocal lattice points and $\boldsymbol{k}$-vectors are distributed on a Monkhorst-Pack grid in the Brillouin zone.[42] In fractional coordinates, this is a 3D grid of points of dimensions $l \times m \times n$ evenly spaced over the unit cell of the reciprocal lattice, while $\boldsymbol{G}$-vectors have integer components.

Although an infinitely dense $\boldsymbol{k}$-vectors grid would give exact integration over the Brillouin zone and an infinitely large $\boldsymbol{G}$-vectors set (i.e., an infinite basis set) would give exact energies, in practice we aim to get as accurate

results at an as low computational cost as possible.

The first step in any calculation is the choice of an appropriate $\boldsymbol{k}$-point grid, which depends on the system under study and is established through a convergence test. The second step, once established the $\boldsymbol{k}$-point grid, is the choice of the energy cutoff E_{cut}. All plane waves with kinetic energy smaller than E_{cut} are included in the basis set, i.e. all wavevectors $|\boldsymbol{G} + \boldsymbol{k}| < G_{\text{cut}}$, with $E_{\text{cut}} = \frac{\hbar^2}{2m_e} G_{\text{cut}}^2$.[1] Much like the $\boldsymbol{k}$-point grid, the appropriate E_{cut} depends on the system under study and is selected through a convergence test.

2.4 Distance comparison method

Differences between experimental and calculated crystallographic structures have been always quantified using the distance comparison method[43,44]. Accordingly, all interatomic distances between a reference molecule and all N neighboring molecules in a spherical coordination shell are listed and sorted. Pairs of structures are then compared by means of the root-mean-square deviation RMSD_N between their lists of distances.

2.5 Vibrational frequencies and eigenvectors

Phonon frequencies can be computed using either the analytic Density Functional Perturbation Theory (DFPT) or the Finite Displacement Method (FDM).[45] We mostly used the latter approach as implemented by the package `Phonopy`[45] because, having at our disposal a computer cluster with many independent processors, it is very convenient to split a demanding calculation into many small parts computed in parallel.

For an unit cell with N atoms, the $3N$ phonon frequencies and eigen-

[1] The energy cutoff actually corresponds to a linear momentum cutoff: $E = \frac{\hbar^2}{2m_e} G^2$ is the kinetic energy $\frac{p^2}{2me_e}$ of an electron with mass m_e and linear momentum $p = \hbar G$.

vectors at $\boldsymbol{k} = 0$ are obtained by diagonalizing the force constant matrix, which is the $3N \times 3N$ matrix of the second derivatives of the energy E with respect to the $3N$ atomic coordinates r_i, $\Phi_{ij} = \partial^2 E / \partial r_i \partial r_j$. Although `VASP` does not actually computes the second derivatives, it evaluates the forces F_i, which are the first derivatives $F_i = \partial E / \partial r_i$. The matrix is thus given by the derivative of the forces, $\Phi_{ij} = \partial F_i / \partial r_j$, which `Phonopy` obtains by numerical differentiation. For this purpose, it displaces a single atomic coordinate r_j by a small amount Δr in the positive and negative directions, runs `VASP` and then manipulates the resulting forces at the displaced configurations, F_i^+ and F_i^-, to obtain $\Phi_{ij} = (F_i^+ - F_i^-)/(2\Delta r)$, for that particular r_j and all coordinates r_i. In this way `Phonopy` requires at most $2 \times 3 \times N$ independent `VASP` calculations at fixed geometries, which may be performed in parallel on a computer cluster.

In most cases the number of `VASP` calculations required by `Phonopy` is actually much smaller, because symmetry is systematically exploited to improve the numerical accuracy and to reduce the computational cost. Whenever possible, force constants Φ_{ij} are completed by applying the symmetry operations. The advantages on the computational cost can be seen even for crystals of quite low symmetry, where a single operation, e.g. an inversion, can halve the total number of displacements.

Depending on the availability DFPT for the chosen vdW-methods in the `VASP` package, some calculations with DFPT were also performed for testing purposes. The calculations based on finite differences were performed using the default value for the atomic displacement distance defined within `Phonopy` (i.e. $\Delta r = 0.01$ Å). Frequencies in perfect agreement with those given by DFPT were obtained.

The precision flag for all `VASP` calculations was set to "`ACCURATE`", as very accurate forces were required. Only phonons at $\boldsymbol{k} = 0$ have to be computed for comparison to optical spectra (infrared or Raman). The resulting phonon properties (eigenfrequencies and eigenvectors) are then used to calculate Raman intensities, as discussed below.

2.6 Raman intensities

Raman intensities can be computed only by finite displacements (FDM) because `VASP` does not provide an appropriate DFPT utility. We have used the method of Porezag and Pederson[46] as implemented in the program `vasp_raman.py`,[47] which employs the `VASP` code as backend. The program reads the eigenvectors obtained from the diagonalization of the force constant matrix and generates displacements along them. In that way, it obtains the derivative of the 3×3 polarizability matrix α_{ij} with respect to each normal mode q, $\alpha_{ij,q} = \partial\alpha_{ij}/\partial q$. The intensity for the mode q with input and output polarizers along the axes i and j is proportional to $\alpha^2_{ij,q}$. Isotropic Raman intensities are given by the proper averages over components, like for gases,[48] as reported in section 6.4 later on.
Raman intensities can differ very significantly if the spectrum is recorded under off-resonant, pre-resonant or resonant conditions. Indigo and 6,6'-dibromoindigo, two of our systems, were measured in pre-resonant and resonant condition respectively, but we neglected this contribution in DFT part. The final agreement obtained between calculations and experiments was always good enough to justify all our argumentations, and this can justify our simplification. However, we are aware that this could be a future improvement.

2.7 Raman active irreducible representations

Since the intensity calculations were very slow, I have optimized the program `vasp_raman.py` by developing a fully general group-theoretical code for determining and exploiting the symmetry of the phonon modes. The code first constructs symmetry coordinates, which are linear combinations of the atomic Cartesian coordinates chosen to behave as the basis vectors of the irreducible representation of the symmetry group. The force constant matrix computed by `Phonopy` in Cartesian coordinates, once transformed into symmetry coordinates becomes block-diagonal, with a block for each irreducible representation of the appropriate symmetry group. Each block

is individually diagonalized, yielding phonon frequencies and eigenvectors, together with their symmetry assignment. Thus, it is possible to neglect the intensity calculation of all those modes which are not active in Raman due to symmetry selection rules. Before this optimization, inactive modes could be discovered only by actually computing their Raman intensity, which turned out to be zero. A procedure highly wasteful of computing time, which is now avoided.

2.8 One-step calculation of Raman intensities

Even after the optimization just described, the calculations of the Raman intensities remained a significant bottleneck in our calculations, especially when we where interested in the whole vibrational spectrum (up to 4000 cm^{-1}), rather than to a selected low frequency region. Further optimization was desirable. The two calculation steps, first frequencies with eigenvectors, second Raman intensities, are really similar. The main difference is the displacement along which the two derivatives are computed: in the first the displacements are along the Cartesian axes while in the second they are along the eigenvectors. Near the end of my PhD activity, therefore, I have merged the two steps by computing in the same job both force and polarizability derivatives along the Cartesian axes and then by performing a change of basis for the polarizabilities. This approach can be convenient if one is interested in a large portion of the spectrum because it avoids repeating twice the common self-consistent field (SCF) calculation.

Furthermore, I could use the `Phonopy` approach of applying the symmetry to save computational time. However, this was very challenging because I had to emulate the same completion algorithm of `Phonopy` but on a more complex tensor: for the frequencies one has to complete forces, which are vectors, while for the Raman intensities I had polarizabilities, which are 3×3 matrices.[2] The procedure that I have developed replaces the program

[2]Instead of $\Phi_{ij} = \partial F_i / \partial r_j$, I need $\alpha_{ij,k} = \partial \alpha_{ij} / \partial r_k$. Under a symmetry operation with rotational part described by a rotation matrix R, force vectors $\boldsymbol{F}$ and polarizability ma-

`vasp_raman.py` and works correctly but has been tested only on a limited set of space groups: triclinic $P1$ and $P\overline{1}$, monoclinic Pc and $P2_1/c$ and orthorhombic $Pnma$.

2.9 Temperature dependence of Raman spectra

The final postprocessing step after the DFT calculation of vibrational frequency ν_q and Raman polarizabilities $\alpha_{ij,q}$ is the inclusion of the frequency and temperature dependence of the Raman intensities. The intensity with input and output polarizers along the axes i and j is proportional to $I^q_{ij} = F(\nu_0, \nu_q, T)\ \alpha^2_{ij,q}$. Here ν_0, ν_q and T are frequency of the exciting radiation, the vibrational frequency of the q-th mode and the temperature at which experiments are performed. For the Stokes component of the Raman spectra (emitted at frequency $\nu_0 - \nu_q$), $F(\nu_0, \nu_q, T) = \frac{(\nu_0-\nu_q)^4}{\nu_q}\ [n(\nu_q, T) + 1]$, where $n(\nu_q, T) + 1 = [1 - \exp(-h\nu_q/k_\mathrm{B}T)]^{-1}$ is the Bose occupation factor.[49]

The factor $F(\nu_0, \nu_q, T)$ is most often ignored in many contexts, for example when comparing experimental and *ab initio* intramolecular vibrational frequencies of isolated molecules. This approximation is justified for intramolecular modes, since their population $n(\nu_q, T) = [\exp(h\nu_q/k_\mathrm{B}T - 1)]^{-1}$ is negligible at room temperature, and mode frequency ν_q and Bose occupation do not significantly change over the spectral range of interest. For the low frequency lattice modes which are the focus of the research, however, the factor $F(\nu_0, \nu_q, T)$ is necessary for reproducing the overall frequency dependence of the Raman intensities.

After including the dependence on exciting frequency and temperature, the simulated spectrum is finally obtained. It is the sum of Lorentzian bands

trices α transform into $R\boldsymbol{F}$ and $R\alpha R^{-1}$, respectively. Furthermore, since a displacement vector $\Delta\boldsymbol{r}$ transforms into $R\Delta\boldsymbol{r}$ (it is covariant), the gradient $\boldsymbol{\nabla_r}$ (i.e. the vector of the three x,y,z derivatives) transforms as $R^{-1}\boldsymbol{\nabla_r}$ (because it is contravariant). Finally, the atom to which the displacement is applied is mapped to a different atom by the symmetry operation.

$L(\nu_0, \nu, \Gamma, I)$ with the computed frequencies and intensities ν_q and I_{ij}^q. Here Γ is the full width at half-maximum (FWHM) of the bands, that we adjust to match the experimental widths, and $L(\nu_0, \nu, \Gamma, I) = I \left[1 + \left(\frac{\nu-\nu_0}{\Gamma}\right)^2\right]^{-1}$.

Chapter 3

Benchmarking van der Waals corrections

3.1 Introduction

In this Chapter we assess the reliability of different van der Waals (vdW) methods to describe lattice vibrations of molecular crystals in the framework of density functional theory (DFT). To accomplish this task, calculated and experimental lattice phonon Raman spectra of a pool of organic molecular crystals are compared. The material described in this Chapter corresponds to the paper entitled "*Towards a reliable description of the lattice vibrations in organic molecular crystals: The impact of van der Waals interactions*", by Bedoya-Martínez, myself, Salzillo, Venuti, Della Valle and Zojer.[26] My contribution to this project was the optimization of the Raman calculation step by developing the group-theoretical code described in Section 2.7 which avoids the intensity calculation for modes not active in Raman due to symmetry selection rules.

We have found that the many-body dispersion (MBD@rsSCS, or MBD for brevity) van der Waals method of Ambrosetti et al.[17] and the pairwise method of Grimme et al.[13] (D3–BJ) outperform the other tested approaches (i.e., the D2 method of Grimme,[12] the TS method of Tkatchenko and Scheffler,[14] and the nonlocal functional vdW-DF-optPBE of Klimeš et al.).[15,16] Interestingly,

when using the experimentally determined unit cell parameters, DFT calculations using the PBE functional without corrections for long-range vdW interactions (no–vdW) provide spectra of similar accuracy as the MBD and D3–BJ simulations.

3.2 Context

From a computational point of view, the ability to correctly predict vibrational properties in organic molecular semiconductors depends on the accuracy of the method to describe forces within (intramolecular) and between (intermolecular) molecules. Density functional theory (DFT) has proven rather accurate for the description of intramolecular interactions at reasonable computational cost. Still a slight overestimation of vibrational energies can arise from the lack of anharmonicities in the calculations, the incomplete incorporation of electron correlation, and the use of finite basis sets.[50] This overestimation, however, has been shown to be systematic and can be corrected by the use of scaling parameters.[50,51]

In contrast, DFT calculations in the low-wavenumber spectral region (< 150 cm^{-1}) are more challenging. Here, intermolecular vibrations dominate, and vdW-interactions are expected to become critically important. Unfortunately, (semi)local DFT functionals do not account for the long-range attractive part of vdW-interactions and appear unsuitable to describe the vibrations of organic molecular crystals in that spectral region.

Multiple approaches to account for the long-range attractive part of vdW-interactions in semi(local) DFT have been proposed in the past years.[52,53] The accuracy and reliability of these methodologies to describe binding and cohesive energies, and to predict crystalline structures, have been extensively addressed. Few works, however, report on the reliability of vdW-corrected DFT methods to describe intermolecular vibrations.[20,54–58] A conclusive test of the most promising approaches, on a pool of sample systems, was the main aim of this research project.

3.3 Approaches included in the benchmark

A van der Waals interaction potential consists of a repulsive (Pauli) and an attractive (London) dispersion part. In DFT only the missing London dispersion needs to be corrected/added, while the repulsive contribution is already included. In the literature, however, vdW is commonly employed as a synonym of London dispersion. Many corrections groups[53] have been proposed. These include the nonlocal density-based or vdW-DF[59,60] (which are modified functional that mostly include a correction to the electronic potential V) and a posteriori interatomic (pairwise or beyond) vdW-correction methods[11–14,17,61–66] (which often apply corrections only to the total energy E).

In our work,[26] we concentrated on a posteriori vdW-correction schemes. Four different vdW-approaches were benchmarked, as listed below.

(i) the pairwise D2 approach of Grimme,[12] that consists in adding pairwise interatomic terms, $C_6 R^{-6} f$, to the total energy. Here the C_6 parameters are tabulated coefficients describing the strength of the interaction, and f is a function to damp the vdW correction upon approaching bonding distances.

(ii) The improved pairwise approach of Grimme et al. in combination with the Becke-Johnson damping function (D3–BJ),[13] which in addition to the $C_6 R^{-6} f_6$ terms adds extra $C_8 R^{-8} f_8$ contributions to the total energy. Here the coefficients and the damping functions are adjusted on the basis of the local geometry (coordination number).

(iii) The pairwise TS approach of Tkatchenko and Scheffler,[14] which has the same functional form as the D2 method. In this case, however, the C_6 parameters and damping function depend on the (Hirshfeld) charge of the atoms, thus taking the local environment into account.

(iv) The MBD approach of Ambrosetti et al.,[17] that goes beyond pairwise interactions and accounts for long-range electrostatic screening. Here, the MBD energy contribution depends on the frequency-dependent polarizability matrix and the long-range interaction tensor. The latter describes the interaction of the screened polarizabilities embedded in the system in a given geometrical arrangement.[66]

Although it was not in the main focus of the present study, a nonlocal functional method of Dion et al.[59] as optimized by Klime et al. for PBE (optPBE)[15,16] was also tested, for the sake of comparison, for the polymorphs of one of the systems considered.

Additionally, we assessed how well the spectra are reproduced by pure semilocal DFT disregarding van der Waals corrections (no–vdW).

3.4 Structures chosen for the benchmark

Among the many different organic molecular crystals reported in the literature, our work focused on organic molecules for which experimental lattice Raman spectra in the low-wavenumber region were available. We have chosen three compounds, two of which exhibit crystalline polymorphism. Since the differences between polymorphs may by subtle, polymorphic compounds provide a particularly stringent test for the calculations. The spectra of all polymorphs were recorded by the Bologna group were I was doing my PhD work.

In total, five systems were considered in the benchmark test: polymorphs α and δ of dibenzotetrathiafulvalene (DB-TTF),[67,68] polymorphs α and γ of 9,10-diphenylanthracene (DPA),[22,69] and the parallel-stacked (PS) form of 2,7-dioctyloxy[1]benzothieno[3,2-b]benzothiophene (OBTBT).[70,71]

Figure 3.1 shows the corresponding unit cells and introduces the nomenclature used throughout the paper. The chosen systems vary in structural details relevant for intermolecular interactions: in the case of DB-TTF, the considered polymorphs have two molecules per unit cell arranged in a herringbone structure, that crystallize either in a monoclinic (α-phase) or triclinic (δ-phase) structure. The main difference between the two polymorphs of DB-TTF is the intermolecular distance along the stacking direction, which is shorter in the α-phase (stacking along c) than in the δ-phase (stacking along a).

While DB-TTF comprises a rigid molecule, DPA features torsional degrees of freedom between the phenyl unit and the anthracene core. In this

case, two polymorphs of the DPA molecule were considered, both crystallizing in a monoclinic structure with four molecules in the unit cell. The α- and γ-phases of DPA differ in the dihedral angle formed by the planes of the anthracene and the phenyl, which for the α-phase is $\sim 68°$ while for the γ-phase it is $\sim 89°$.

Finally, the PS-phase of OBTBT represents a prototypical example of a molecule consisting of a rigid-conjugated backbone with flexible aliphatic side-chains.

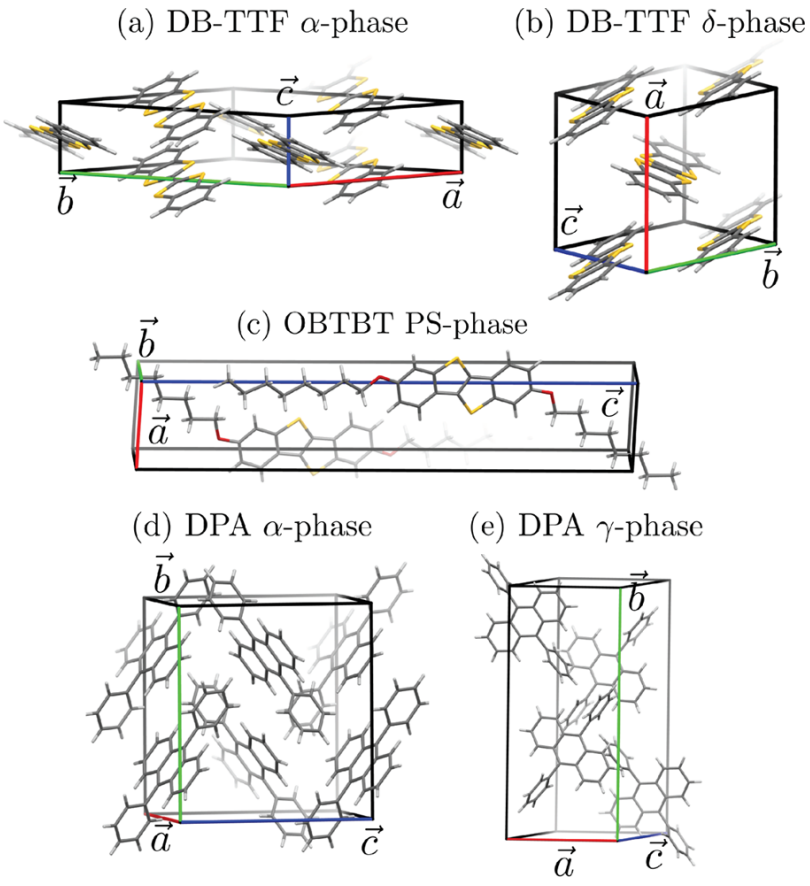

Figure 3.1: Unit cells of the considered crystals. (a) α and (b) δ polymorphs of the DB-TTF molecule. (c) Parallel-stacked (PS) polymorph of the OBTBT molecule. (d) α and (e) γ polymorphs of the DPA molecule. Gray, white, yellow, and red colors denote carbon, hydrogen, sulfur, and oxygen atoms.

3.5 Calculations

Calculations have been performed with the methods described in Chapter 2. The Brillouin zone was sampled with the converged Monkhorst-Pack $\boldsymbol{k}$-point grids listed in Table 3.1. They were chosen to ensure that total energies per atom were converged to at least 0.03 meV. A plane wave cutoff energy of 800 eV was used for all calculations, ensuring a convergence of 0.7 meV/atom compared to a convergence test cutoff of 1200 eV. The total energy during the self-consistency loop of each DFT step was converged to 10^{-8} eV. Atomic relaxations in both cases were performed with a threshold of 10^{-3} eV Å^{-1} for the residual forces using the GADGET tool.[38] Phonon frequencies were calculated using two different cutoff energies (800 and 1200 meV) and two different derivation methods (DFPT and finite difference method, see Chapter 2). With the larger cutoff we obtained a perfect agreement between the two methods, while with the smaller one we obtained an acceptable accuracy of $\ll 0.7$ cm^{-1}.

Table 3.1: Monkhorst-Pack (MP) $\boldsymbol{k}$-grid used to sample the Brillouin zone for each considered system. The same grid has been used for MBD, TS and D2, unless specified otherwise.

Molecule	Polymorph	vdW	$\boldsymbol{k}$-grid
DB-TTF	α	MBD	2×2×6
	α	TS, D2	1×1×3
	δ	MBD, TS, D2	2×2×2
DPA	α	MBD, TS, D2	3×3×2
	γ	MBD, TS, D2	2×1×2
OBTBT	PS	MBD, TS, D2	6×4×1

3.6 Spectra computed with experimental cell volumes

Since the phonon frequencies depend of the cell volume, we first assessed the performance of the various methods at structures in which all the atomic coordinates were relaxed, while the cell parameters were constrained at their experimental values. Later on, we will relax also the cell parameters.

At the experimental cell volumes, all calculations employing the MBD vdW correction (see purple curves in Figure 3.2) can predict lattice vibrations for the pool of considered molecular crystals within an accuracy of $\ll 5$ cm^{-1}, as reported in previous articles.[20] In most instances, the experimentally observed peaks can be clearly identified within the MBD Raman spectra. This allows associating measured vibrational modes with specific (calculated) displacement patterns (i.e., eigenmodes), which is not possible from the experimental data alone. This assignment is crucial for understanding vibrational dependent properties of materials, such as heat or charge transport. The MBD calculated spectra, in addition, provide insight regarding the actual number of Raman active modes contributing to the experimental spectrum.

Below 80 cm^{-1}, the agreement between the MBD simulations and experiments is typically $\ll 4$ cm^{-1}. In some cases, the positions of the high energy MBD Raman active modes (> 80 cm^{-1}) are shifted by 5–7 cm^{-1}.

An excellent performance for describing the Raman spectra of the studied systems, is also observed with the D3–BJ method (cyan curves Figure 3.2). In all cases, the D3–BJ vdW-method reproduces the experimental spectra (deviation $\ll 4$ cm^{-1}) within the same accuracy as the MBD approach. Indeed, in most cases the positions of the D3–BJ calculated peak positions match the MBD values. These results are relevant since the D3–BJ approach is computationally significantly cheaper than the MBD method (faster by a factor from 1.5 to 7.2). Moreover, the D3–BJ approach can serve as an accurate alternative for describing the lattice vibrations of systems for which the MBD method suffers from numerical instabilities.[72]

A much less accurate description of the lattice Raman spectra at cm^{-1}

is provided by the TS method (green curves in Figure 3.2). In this case, the Raman spectra of the considered polymorphs are described with an accuracy of 2 to 22 cm^{-1}. The largest error (22 cm^{-1}) is again observed for the high energy Raman active modes (> 80 cm^{-1}), as for the MBD and D3–BJ calculations. In certain cases, global shifts of the TS spectra toward higher frequencies relative to the experimental data are found. This makes the use of scaling parameters, in analogy to the common practice for the simulation of intramolecular modes,[50,51] at best difficult, if not impossible.

An accuracy of 2 to 15 cm^{-1} for the lattice Raman spectra of the studied polymorphs is obtained when applying the D2 vdW-correction method (red curves in Figure 3.2). The D2 calculated spectra are consistently shifted to lower wavenumbers relative to the other van der Waals correction schemes.

Although the focus of our benchmark is on the performance of a posteriori van der Waals correction schemes, for the sake of comparison, we also tested a nonlocal functional (optPBE) to describe the lattice vibrations of organic molecular crystals. Figure 3.2 (yellow curve) shows the Raman spectra for the polymorphs of DBTTF as predicted by the nonlocal functional proposed by Dion et al. and optimized for PBE (optPBE).[15,16] For none of the polymorphs the optPBE-vdW functional provides a description of the Raman spectra that would be comparable to the MBD or D3–BJ results. In fact, in both cases the agreement with respect to experiments is similar to that obtained in the case of TS, with a tendency to overestimate the positions of the Raman peaks.

An interesting observation is that DFT calculations, which do not include vdW interactions (in the present case using the PBE functional), give Raman spectra as accurate as those obtained with the MBD and D3–BJ approaches, provided that the experimental volume is used. This is clearly shown by the Raman spectra reported as no–vdW in Figure 3.2 (pink curves).

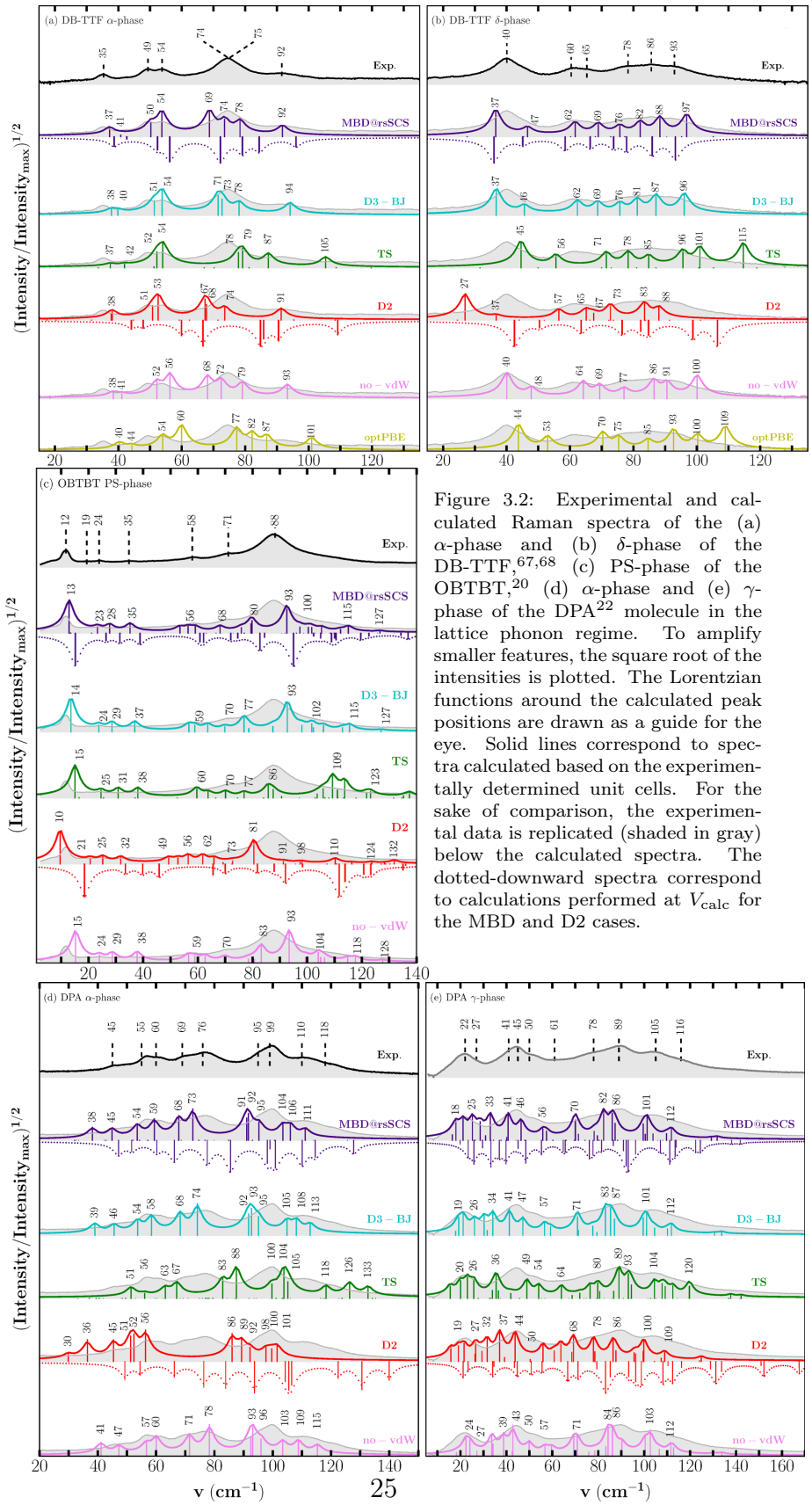

Figure 3.2: Experimental and calculated Raman spectra of the (a) α-phase and (b) δ-phase of the DB-TTF,[67,68] (c) PS-phase of the OBTBT,[20] (d) α-phase and (e) γ-phase of the DPA[22] molecule in the lattice phonon regime. To amplify smaller features, the square root of the intensities is plotted. The Lorentzian functions around the calculated peak positions are drawn as a guide for the eye. Solid lines correspond to spectra calculated based on the experimentally determined unit cells. For the sake of comparison, the experimental data is replicated (shaded in gray) below the calculated spectra. The dotted-downward spectra correspond to calculations performed at V_{calc} for the MBD and D2 cases.

3.7 Eigenvector analysis

The comparison between experimental and calculated spectra provides the ultimate benchmark for the methodologies employed. However, the assignment between measured and calculated peaks can be ambiguous, especially in crowded regions where experimental Raman bands arise from the superposition of several phonon modes.

The dot product between the eigenvectors obtained from the different vdW approaches can be used for a direct and rigorous mathematical assignment. Matching modes, and hence frequencies, correspond to those with the largest dot product between the eigenvectors (equal to unity in the case of perfect correspondence).

Histograms of dot products, using the MBD method as a reference, are shown in Figure 3.3a-e. A key observation is that the MBD, D3–BJ and no–vdW displacement patterns for all considered systems are in very good agreement, with most of the dot products among their eigenvectors lying between 0.9 and 1.0 (see cyan and pink data in Figure 3.3a-e). On the contrary, the agreement of the TS and D2 eigenvectors with those of MBD is poorer, with a much wider spread of dot products and with many values below 0.8 (see green and red data in Figure 3.3a-e) and this suggests that these displacement patterns might be even qualitatively misleading when trying to understand the nature of the vibrations.

A comparison of the frequencies of equivalent vibrations obtained with the different vdW-methods is shown in Figure 3.3f-j. These plots show that equivalent modes essentially keep their relative positions in the spectra. Taking as reference the MBD frequencies, the TS (green circles) and D2 (red squares) methods have the tendency to provide, respectively, higher and lower values. This indicates that compared to MBD calculations the TS method yields a more pronounced increase of intermolecular force constants, while the increase is smaller in the D2 case. D3–BJ method, on the contrary, predicts frequencies in perfect agreement with the MBD data, consistent with the equivalence of their eigenvectors (see cyan triangles in Figure 3.3f-j).

A similar behavior is found when employing pure PBE (no–vdW), in the

absence of any long-range vdW-correction (see pink stars). This means that vdW interactions directly impact on the structures, but not on the vibrations in the lattice-phonon region.

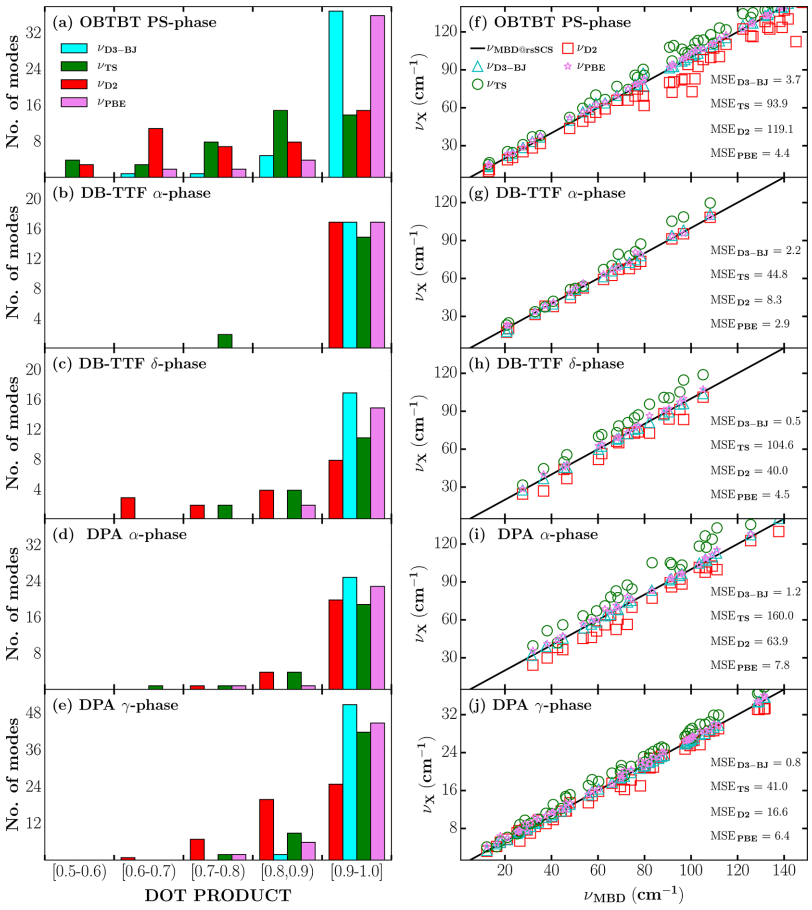

Figure 3.3: (a)-(e) Distribution of dot products between the lattice eigenvectors obtained with MBD and those calculated with D3–BJ, TS, D2, and no–vdW. (f)-(j) TS, D2, D3–BJ, and no–vdW lattice frequencies (ν) as a function of those calculated with MBD. Mean-square-errors are reported inside the graphs.

3.8 Cell volume relaxation

A definite shortcoming of vdW-free DFT calculations is that they necessarily fail in calculating the equilibrium lattice parameters of molecular crystals held together by van der Waals forces. For thus reason, these simulations have to rely on experimentally determined unit cells.

Since a reliable description of the unit-cell parameters is crucial to predict lattice phonon modes of organic molecular crystals in the absence of structural data, we have assessed the accuracy of the various vdW-corrections by computing the relaxed unit cell structures. These are minimum potential energy structures, appropriate to zero Kelvin, and thus are expected to be denser than structures at larger temperatures. Consistent with this consideration, in most cases the calculations predicted smaller volumes compared to the experimental values, as shown in Table 3.2.

To assess also the accuracy of the calculated positions of the individual atoms constituting the molecules, we compared the experimental and calculated relaxed structures, using the distance comparison method. This yielded root-mean-square-deviations (RMSD) between atomic positions ranging from 0.07 to 0.36 Å (see Table 3.2), which are well below 1.0 Å, the threshold normally adopted to determine whether a structure is correctly calculated.[2,3] Comparing the different vdW approaches, the volumes obtained in the MBD and TS simulations are very close to each other (typically within 1–2%) and rather close to the experiments. The D2 approach systematically predicts the most tightly packed systems with unit cell volumes up to 10% below those obtained experimentally. The D3–BJ approach in all cases underestimates the experimental volumes by 1.4–4.7%. In certain cases it predicts values in good agreement with TS and MBD data (PS-OBTBT and α-DPA), while there are systems for which it yields unit cells as tightly packed as those obtained in the D2 calculations (α-DBTTF).

Table 3.2: Comparison between Calculated (V_{calc}) and Experimental (V_{exp}) Volumes for the Considered Systems. Volumes were obtained from lattice energy relaxations. In parentheses relative differences between V_{exp} and V_{calc} are provided in percent. In the case of experimental data the numbers in parentheses are the standard uncertainties in the final digits (when available). The RMSD values were calculated following the distance comparison method described in Section 2.4.

		T (K)	Volume (Å^3)	RMSD (Å)
PS OBTBT triclinic	EXP[70,71]	123	1324.76(13)	
	MBD		1296.12(−2.2)	0.11
	D3–BJ		1299.59(−1.9)	0.08
	TS		1286.34(−2.9)	0.15
	D2		1208.95(−8.7)	0.23
α DB-TTF monoclinic	EXP[67]	300	634.57	
	MBD		625.77(−1.4)	0.11
	D3–BJ		605.25(−4.6)	0.13
	TS		619.78(−2.3)	0.10
	D2		598.52(−5.7)	0.14
δ DB-TTF triclinic	EXP[68]	93.1	628.42(5)	
	MBD		638.90(1.7)	0.10
	D3–BJ		616.78(−1.9)	0.07
	TS		631.07(0.4)	0.07
	D2		607.97(−3.3)	0.10
α DPA monoclinic	EXP[69]	293	1774.45	
	MBD		1705.01(−3.9)	0.11
	D3–BJ		1692.59(−4.6)	0.12
	TS		1697.07(−4.4)	0.11
	D2		1614.94(−9.0)	0.22
γ DPA monoclinic	EXP[22]	300	1818.83(7)	
	MBD		1732.85(−4.7)	0.12
	D3–BJ		1715.21(−5.7)	0.19
	TS		1700.08(−6.5)	0.21
	D2		1635.26(−10.1)	0.36

3.9 Spectra calculated at the relaxed volumes

In order to quantify the impact of the volume relaxation on the vibrational properties, we calculated the lattice Raman spectra at the structures with relaxed cell parameters for the MBD and D2 vdW approaches, which typically provide the smallest and the largest changes in volume relative to the experimental data (see Table 3.2).

For all systems in which the unit-cell volume is smaller in the simulations,

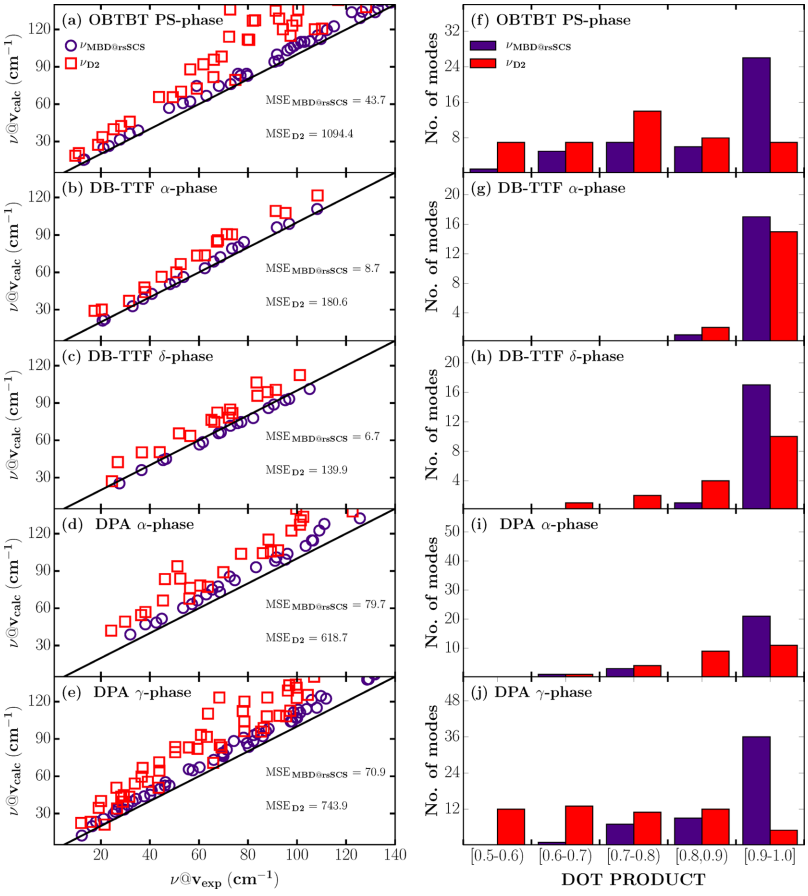

Figure 3.4: (a)-(e) Lattice frequencies calculated at V_{calc} as a function of those obtained at V_{exp} for MBD and D2. The black lines denote the virtual case in which frequencies do not depend on the volume (i.e., V_{exp} against V_{exp}). Mean-square-errors are reported inside the graphs. (f)-(j) Distribution of dot products between the lattice eigenvectors obtained at V_{exp} and V_{calc} when using MBD and D2.

this results in a shift of the peaks to higher wavenumbers, see downward-dotted spectra in Figure 3.2. In the particular case of the δ-phase of DB-TTF, the MBD Raman spectra shifts in the opposite direction, as expected considering the overestimated optimized volume. Nevertheless, even here the agreement between measured and calculated spectra is best when employing the experimental volume (see shaded and downward-dotted purple curves in Figure 3.2). This makes sense considering that both the X-ray diffraction experiments and the Raman spectroscopy were performed at temperatures much higher than zero Kelvin. Overall, the impact of the volume on the MBD lattice vibrations is comparably small, with average changes < 4 cm^{-1}. This is consistent with the rather small change in volume.

In the D2 case, the impact of relaxing the unit-cell is more extreme, with Raman peaks shifting by up to 25 cm^{-1}, in agreement with the large volume changes predicted by this method. In relative numbers, for OBTBT this means that some frequencies change by $\sim 50\%$, while the frequency of the first Raman lattice vibration essentially doubles (see upward-solid and downward-dotted red curves in Figure 3.2c). As in the D2 simulations using the experimental unit cell, the positions of the Raman active modes had been underestimated, the large shift to higher wavenumbers at the relaxed volumes in some instances improves the agreement with experiments. At least, it does not massively deteriorate the situation, albeit now the D2 calculations typically over rather than underestimate the experimentally determined frequencies.

For the D2 case, the entire set of lattice vibrations changes on average ~ 19 cm^{-1}, which is much larger than for the MBD case (< 4 cm^{-1}). As a consequence, the average mean square deviation between the frequencies calculated at V_{calc} and at V_{exp} is by an order of magnitude larger than for the MBD case (~ 337 cm^{-2} vs ~ 41 cm^{-2}), see Figure 3.4a-e.

Besides analyzing the impact of the volume relaxation on the frequencies, it is interesting to assess the change of the eigenvectors. Figure 3.4f-j shows histograms of the dot products between the eigenvectors calculated at V_{calc} and V_{exp}. In all cases the MBD eigenvectors calculated at the two different volumes change much less than those obtained with the D2 method. Most

of the dot products obtained for MBD lie between 0.9 and 1.0, while the D2 method shows a broader distribution with values between 0.5 and 1.0. Not unexpectedly, the broadest distribution of dot products for D2 is obtained for the γ-phase of DPA, for which the D2 method predicts the largest change in volume. Notably, for OBTBT also a very broad spread of the dot products is observed, in this case even for the MBD method. This can be attributed to the comparably complex structure of OBTBT, with a rigid core and flexible aliphatic side-chains, that may be more sensitive to the change in volume.

3.10 Conclusions

We assessed the performance of four different a posterior vdW methods in accounting for long-range vdW interactions in local DFT. The performance was evaluated by comparing calculated and measured lattice Raman spectra in the low-wavenumber region (< 150 cm^{-1}) for several polymorphs of different molecular crystals. The spectra in that range are particularly suited for that purpose, as they are typically dominated by intermolecular vibrations, for which a significant dependence on van der Waals interactions can be expected. Among the tested methodologies, the most reliable and systematic description of the vibrational properties was found for the MBD and D3–BJ approaches. These methods not only provide the best overall agreement with the experimental spectra but comparing the computational results also yield fully consistent frequencies and eigenvectors. From a practical point of view it is interesting to mention that the excellent performance in the D3–BJ scheme is achieved at significantly reduced computational costs. The accuracy of the TS and D2 vdW-correction schemes is typically lower and varies considerably depending on the system and the wavenumber range. The lack of a general trend in these cases also prevents the determination of ad hoc scaling parameters for the frequencies, which are usually employed for high-energy molecular vibrations.

For the sake of comparison, we also tested the nonlocal functional vdW-DF-optPBE for two of the studied polymorphs, where we observed an accu-

racy of the same order as for the TS and D2 approaches (i.e., worse than in the MBD and D3–BJ calculations).

Interestingly, also in PBE simulations disregarding a posteriori van der Waals corrections (no–vdW), an excellent agreement between theory and experiment is obtained for the systems considered here, as long as experimentally determined unit-cell geometries are employed.

As far as the prediction of the structural parameters of the different systems is concerned, all employed a posteriori van der Waals corrections provided a satisfactory agreement. The best fit between simulations (disregarding thermal expansion) and experiments (at finite temperatures) was obtained for the MBD and TS approaches, closely followed by the D3–BJ. Only for the D2 approach, changes of the equilibrium volume amounted to up to 10%. Employing the relaxed rather than the experimental volumes, we typically observed a shift of the spectra to higher wavenumbers for the tested methods (MBD and D2). This effect was particularly pronounced in the D2 case with several frequencies increasing by $> 50\%$. This, however, did not fundamentally improve the performance of the D2 method compared to the experimental Raman spectra.

Overall, our work establishes a frame of reference for the computational study of vibrational properties of organic molecular crystals in the lattice phonon range. This is distinctly relevant, as these vibrations crucially determine, for example, charge- and heat-transport processes. Therefore, we expect that the accurate vibrational properties obtained when employing the MBD and D3–BJ approaches will in the future help to gain unprecedented insights into the relationship between the structures of molecular crystals and a number of their relevant physical properties.

The conclusion that D3–BJ produces excellent results at a lower computational cost was an excellent lesson also for our work (as well as for the larger scientific community), as we initially focused on using MBD. With the computer resources at our disposal, D3–BJ allowed us to speed up our calculations, without the fear of facing systems even more complex than those considered in this thesis.

Chapter 4

Polymorph recognition: Coronene

4.1 Introduction

In this Chapter we show that highly accurate DFT calculations coupled to low-frequency Raman spectroscopy constitutes a valid method for polymorph characterization, alternative/complementary to X-ray. The method is applied here to the temperature induced first order phase transition of coronene (see Figure 4.1), known since a long time, but remained structurally uncharacterized due to crystal breaking during the cooling process. The astonishing fidelity of the Raman calculated spectra to the experiments allows us to unambiguously identify the low temperature phase with the β-coronene polymorph, recently reported as new, and obtained in the presence of a magnetic field. We also suggest that additional measurements are

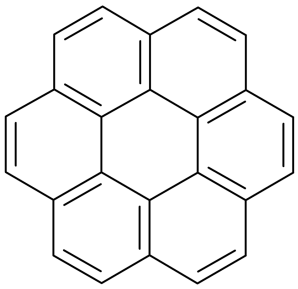

Figure 4.1: Coronene (Hexabenzobenzene) molecular structure, $C_{24}H_{12}$

needed to confirm that the magnetic field can actually drive the growth of a β-polymorph surviving indefinitely at ambient temperature.

The material described in this Chapter corresponds to the paper entitled "*An alternative strategy to polymorph recognition at work: The emblematic case of coronene*", by Salzillo, myself, Masino, Bedoya-Martínez, Della Valle, Brillante, Girlando and Venuti.[25] In this study I have performed all computational work, with the assistance and of Dr. Natalia Bedoya-Martínez, who first designed and programmed the original strategy for computing the vibrational spectra. To this strategy, as mentioned in Section 3, I have contributed the procedure for discarding the modes inactive in Raman due to their symmetry. After all the DFT calculations, I have also taken care of the final post-processing step in which the Raman intensities are adjusted by considering excitation wavelength and temperature dependence of the Bose occupation factor[49] discussed in Section 2.6.

4.2 State of the art

Coronene belongs to the class of polycyclic aromatic hydrocarbons (PAH) and with its derivatives has drawn much attention as a model system, being regarded as the small building block of graphene.[73]

This molecule has been chosen as the perfect first system to test our DFT approach because it is simple and it can be considered as a rigid molecule due to its strong aromaticity. This represents a computational advantage for two reasons: it is easier to reach the crystal energy of minimum energy since there are no multiple molecular conformations to be explored and because the intra-molecular and lattice phonon vibrational modes are not expected to mix and can be studied separately.

Coronene also had an experimental appeal for our group because there are a lot of studies on its polymorphs and on their relative stability. Being the only organic molecular crystal found as a mineral (Carpathite), its phase diagram has been investigated especially at high pressures and temperatures, to determine the conditions in which it is formed and remains stable in nature.[74,75] Phase transitions and polymorph structural data have

been reported as a function of pressure starting from the phase stable at ambient conditions.[74–77] Following the classification developed by Desiraju and Gavezzotti[78] for the packing of aromatic hydrocarbons, this phase is known as γ polymorph.[79]

Less information was available on the ambient pressure, low–temperature behavior: various spectroscopic analyses show a phase transition around 160–140 K„[80–82] but the low–temperature structure remained uncharacterized due to crystal damage at the transition. Powder XRD measurements have probed the partial transformation at ∼150 K of the usual γ polymorph[79] into a β polymorph (following the same classification),[78] thus suggesting that it actually corresponds to the low-temperature phase reported in the past. The final confirmation comes from highly accurate density functional theory calculations coupled to low frequency Raman spectra collected by cooling down a γ-coronene single crystal (top spectrum) from room temperature to 79 K.[25]

There are reports of β-coronene grown above room temperature in the presence of a magnetic field.[79,83] These reports are inconclusive, since the XRD data were collected at 80 K, which is below the transition temperature and because the single crystal XRD data needed to demonstrate that β-coronene can actually also be obtained (and maintained) at high temperature as a result of the application of the magnetic field were not provided.

4.3 Structural analysis and vdW-DFT calculations

As mentioned in the introduction, coronene is known to have two different polymorphs: γ found as a mineral and stable at high temperatures[84] and β, more recently discovered and stable at lower temperatures.[79] The two structures share the same number of molecule per unit cell ($Z = 2$) and the same symmetry $P2_1/n$. The D_{6h} symmetry of the isolated coronene molecule is not preserved in both crystals, but deviations from planarity are minimal in either structure. In fact, they are larger for γ-coronene, with an average distance from the molecular plane of 0.0135 Å (calculated D3–BJ 0.0145 Å),

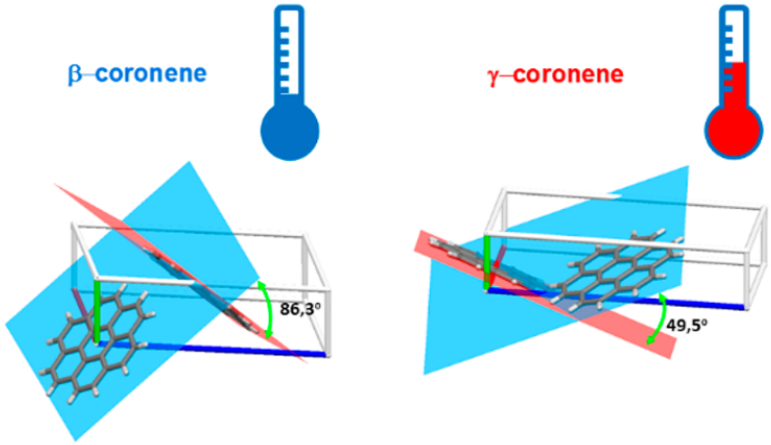

Figure 4.2: Structure of coronene polymorphs: β at low T (left), γ at high T (right).

than for β-coronene, with a value ∼0.007 Å (calculated D3–BJ 0.007 Å).

The differences between the two polymorphs are shown in Figure 4.2 and summarised in Table 4.1. The main difference is in the interplanar angle (the angle between the molecular planes of neighbouring molecules), which defines the structure according to the classification for the packing of aromatic hydrocarbons.[78] It goes from ∼50° for β-coronene up to ∼86° for γ-coronene, with consequences for the cell parameters, where we observe an increase of the stacking axis b at the expense of the other two. At room temperature, γ-coronene presents a larger volume which, as a rule of thumb would indicate weaker interactions and a less stable structure.

The first step of `VASP` DFT calculation is the choice of the Monkhorst-Pack $\boldsymbol{k}$-point grid. This strongly affects the accuracy of crystal properties and, in order to obtain an uniform density of sampling points in all directions, it is necessary to take into account the length of the crystallographic axes of each polymorph.

As described in Chapter 2, we have to spread an $l \times m \times n$ grid evenly over the unit cell of the reciprocal lattice, which has sides a^*, b^*, c^*. The density of the grid is thus controlled by the number of subdivisions along the *longest* of the three reciprocal axes, which corresponds to the *shortest* of the

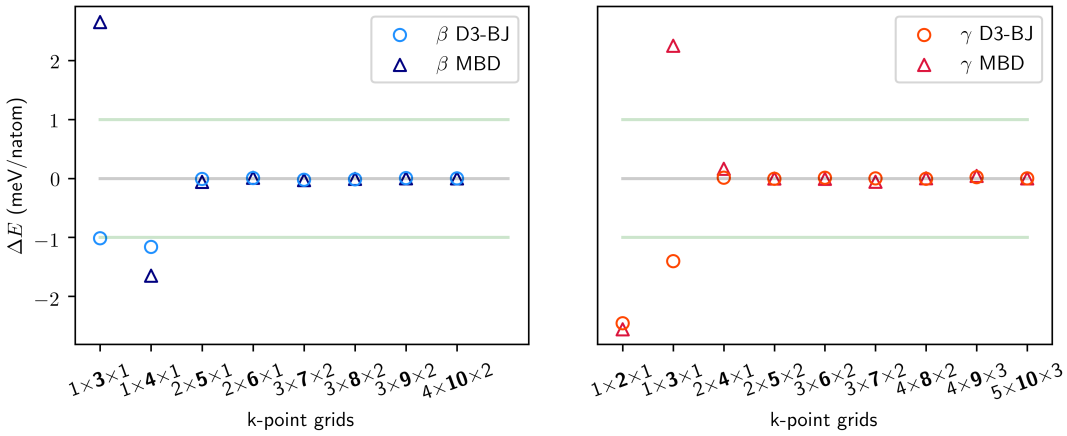

Figure 4.3: Convergence test for $\boldsymbol{k}$-point grids, for β and γ-coronene (left and right panels, respectively). Horizontal axis: $l \times \boldsymbol{m} \times n$ grids with increasing $\boldsymbol{m}$ and best matching l, n. Vertical axis: ΔE with respect to the largest (i.e., denser) grid.

crystallographic axes and which for both polymorphs is b^* (corresponding to b).

The required convergence test is illustrated in Figure 4.3. The effects of the van der Waals (vdW) interactions were included either with the many-body dispersion (MBD)[11] method or the computationally cheaper pair-wise method D3–BJ by Grimme et al.[13] For both polymorphs we have allocated $m = 2, 3, 4, \cdots, 9, 10$ subdivisions to the shortest reciprocal axis b^*, while the number l and n of subdivisions along a^* and c^* was fixed by imposing the same density in all directions: $\frac{a^*}{l} \approx \frac{b^*}{m} \approx \frac{c^*}{n}$ (as best as possible). In this manner, we tested nine grids of increasing density and then we compared their single-point energy with respect to the densest, and thus best converged grid.

The selected $\boldsymbol{k}$-point grids are the less dense (and thus cheaper) grids that return a difference in energy below 0.06 meV per atom and this case are: 2×5×1 and 2×4×1 for D3–BJ β and γ respectively and 2×5×1 for MBD β and γ (see Table 4.2).

The analogous procedure has been followed for the cutoff energy, going

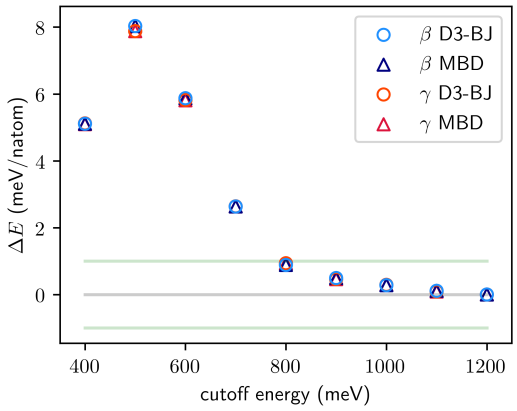

Figure 4.4: Convergence test for the Energy cutoff.

in discrete steps from 400 to 1200 eV and selecting the cutoff that returns an energy difference below 1 meV per atom. As described in Chapter 2, this parameter can be considered as the analogous of the size of the basis set. For our systems, an energy of 800 eV always met the requirement and, therefore, we used this step to check the correct assignment of pseudopotentials. In Figure 4.4 we can observe the typical trend of this curve.

After this preliminary accuracy tuning, we can proceed with atomic relaxation which may, or may not, include fully relaxing also the crystallographic parameters. For a structural comparison we decided to do both using the `GADGET` package[38] and halting when residual forces fell below 1 meV/Å. Fully relaxed structures calculated for γ- and β-coronene with the adopted vdW corrections are compared to the experimental data in Table 4.1, where we also report the computed energies. The agreement between experimental and calculated structures is estimated with the distance comparison method[43,44] described in Section 2.4, which required 18 neighbouring molecules.

At 0 K with D3–BJ, the fully relaxed energy of β is computed to be 0.7 kcal/mol lower than γ's, which is within the accuracy of the method for the energy differences[28] (0.05 kcal/mol). The result thus agrees with the experimental evidence indicating that this is the phase stable at low temperature.

4.4 Polymorph discrimination by Raman spectroscopy

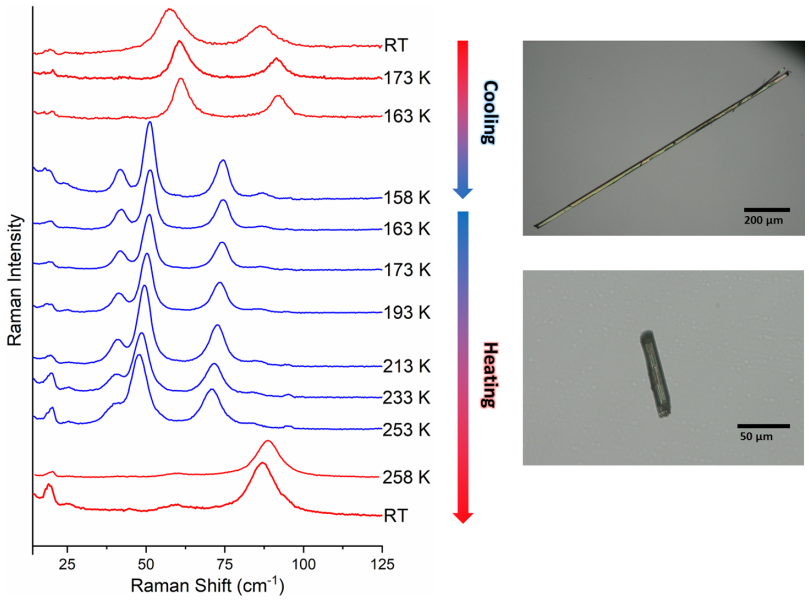

Figure 4.5: Lattice phonon Raman spectra of a coronene crystal recorded during the thermal cycle of a sample across the phase transition occurring above 158 K in this experiment. In red the spectra of the γ polymorph, stable at high temperature; in blue, the spectra of the low-temperature polymorph. On the right-hand side, the images of a coronene crystal subjected to cooling (top) and of one of its fragments selected for the measurements after the transition (bottom).

The aim of the experimental part of this study was to verify if the β polymorph of coronene could be found at low temperatures and if we could follow the transition via lattice phonon spectroscopy. For this purpose, a γ-coronene single crystal was subjected to slow cooling, to minimize the disruptive effects of the observed extended fragmentation, while recording the spectra as a function of the temperature to trace out the transition and to obtain the spectrum of the new phase. The Raman scattering was measured with the energy excitation from a Kr^+ laser tuned at 647.1 nm, spanning the 20-2000 cm^{-1} region but focusing on the analysis of the 10-150 cm^{-1} interval, where lattice phonons are observed.

In Figure 4.5 we report the sequence of the Raman spectra collected by cooling down a γ-coronene single crystal (top spectrum) from room temperature to 79 K. It is possible to observe in the temperature range 298 to 163 K the invariance of the spectra, which correspond to those of the stable γ-coronene form. In a series of experiments performed on different crystals, most of them underwent shattering just below this temperature, but the fragments originating in the process were large enough to allow to be singled out and measured. The spectrum collected at 158 K has changed abruptly, displaying a lattice phonon pattern where none of the spectral features observed in the higher temperature range are left, and which resembles that recorded at much lower resolution reported by Ohno et al.[80] at a single low-temperature value. This marks the occurrence of a (first-order) phase transition, with the transformation to a new polymorph which has involved the entire selected fragment.

On heating the sample, the process is reversible but displays a large hysteresis, as evidenced by the persistence at 253 K of the low-temperature phase bands, which eventually shift to lower wavenumbers as a result of the thermal expansion of the lattice. The spectrum of γ-coronene is fully recovered at 258 K.

The intensity ratios for the peaks of the latter spectrum differ from those of the starting material, likely as a result of either sample movements in the cryostat chamber during the fragmentation, or variable orientations of the crystal domains formed during the thermal cycle. In all the crystals subjected to cooling, the shattering marked the occurrence of the transition, at a temperature T depending on the sample history and dimensions. The highest T recorded on cooling (around 160 K) sets the experimental upper thermodynamic boundary for the existence of the low-temperature phase.

The hysteresis for the backward transition on increasing temperature has also been observed for all samples. However, regardless of the heating rate, the low-temperature phase eventually undergoes the transformation and is never recovered at ambient conditions.

4.5 Polymorph identification through vdW-DFT spectra

The presence of two different spectra is enough to discriminate the two different polymorphs, but for a complete identification we need to link the experimental spectrum to the appropriate structure. One way is to compute the DFT spectra. Vibrational modes, restricted to the Γ point, were therefore computed at the relaxed structures (with unit cell parameters constrained at the experimental values)[79,84] through the force constants obtained with the `Phonopy` package[45] in combination with `VASP`, and used to calculate the Raman spectra with the code `vasp_raman.py`.[47] Raman intensities were finally adjusted by considering excitation wavelength and temperature dependence using the Bose occupation factor.[49] The choice of keeping the experimental cell parameters prevents the shrinkage of the cell volume which would affect the lattice phonon frequencies. In a smaller volume the molecules indeed require more energy to librate and this is reflected in a blue-shift of the phonons.

A comparison between the Raman spectra calculated with vdW corrected methods MBD and D3–BJ in the lattice phonon region used for the polymorph identification is given in Figure 4.6. As already noticed in Chapter 3, frequencies and intensities computed with the two methods closely match, with the advantage for D3–BJ of being computationally much cheaper.

The molecular symmetry lowering in coronene solid state involves a breakdown of the symmetry selection rules which apply in the gas phase, with some forbidden Raman vibrational transitions becoming detectable in the crystal.[85] The molecular inversion centre, however, is maintained and at wavevector $\boldsymbol{k} = 0$ only the 108 vibrational modes of gerade symmetry are Raman active. The other symmetry elements which characterize the $P2_1/c$ space group are the screw axis $(C_2 + T)$ and glide mirror $(C_s + T)$. In the "rigid molecule" approach which separates inter- and intramolecular degrees of freedom, six of these modes have the character of lattice phonons and identify with either in-phase (B_g) or out-phase (A_g) rotations of the two unit cell molecules around their inertia axes.

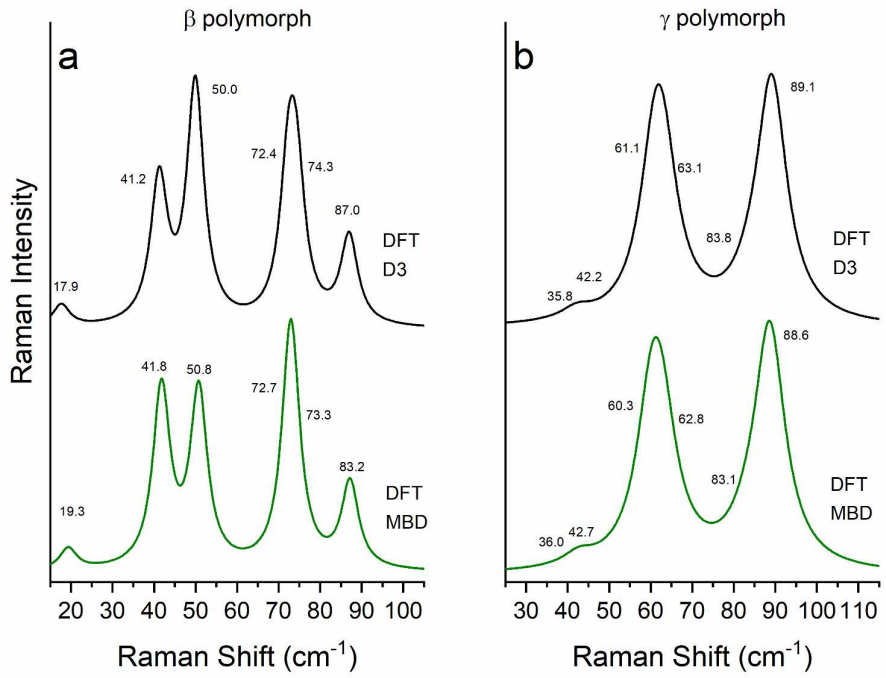

Figure 4.6: Calculated Raman spectra of γ-coronene and β-coronene in the lattice phonon wavenumber range with methods MBD and D3–BJ.

Table 4.3 lists the calculated and experimental Raman shifts of γ-coronene and β-coronene for the six modes of lowest energy, together with the analysis of the calculated eigenvectors, given as their (squared) rotational components around the three inertia axes (denoted as usual as "long" L, "medium" M and "normal" N). For a molecule of D_{6h} symmetry like coronene, or actually for any molecule having a C_n symmetry axis with $n \geq 3$, the inertia moments around the other two axes (L and M in this case) are identical (degenerate). In Table 4.3, for this reason, instead of L and M we report their sum $L+M$. As the squared components all sum up to ∼100% (unity), we can infer that the first six modes do correspond to pure librations of rigid bodies. As expected, coronene behaves as a textbook example of a rigid molecule.

In Figure 4.8, the experimental Raman spectra of coronene crystals at 298 and 158 K below 120 cm^{-1} are compared to the D3–BJ spectra for the γ and β polymorphs, respectively, calculated at the experimentally determined unit

cell parameters,.[79,84] For both polymorphs only six frequencies (the lowest) were obtained in the chosen range, drawn in the figure as Lorentzian bands with FWHM's chosen to conform to the experimental features. Deconvolution has been performed on the experimental bands, checking that the fitted peaks were in agreement with the values returned by the analysis of polarized Raman spectra. In fact, A_g and B_g modes may easily be distinguished in polarized spectra, where they have different selection rules. Polarized are not shown and not further discussed in the present section, to keep it more focused on polymorph recognition. This topic will be extensively discussed in a later section, where experimental and calculated polarized spectra will be compared.

DFT calculation results can explain some spectral characteristics. As it can be seen, the two lattice phonon modes calculated at the lowest wavenumbers for γ-coronene involve solely rotations around the axis N normal to the molecular plane, and display the lowest intensities, in agreement with the experimental findings. The situation for the lowest β-coronene phonon is analogous. For the rotations around the in-plane axes L and M since, as already noticed, the corresponding inertia moments are basically degenerate, the choice of the two axes in the molecular plane is in fact arbitrary. The close spacings calculated between doublets explains why only two broad bands for γ-coronene and four for β-coronene, originating from the convolution of the Raman scattering, can be identified experimentally.

4.6 Conclusions

Even at first sight, the almost perfect match between theoretical and experimental spectra enables us to recognize the low-temperature phase as polymorph β, while the equally good agreement for polymorph γ actually validates the method. The high fidelity of the theoretical spectra to the experiments, not just in reproducing the phonon frequencies but also the relative intensities of the bands, is indeed remarkable.

Thanks to the knowledge of the crystal structures and with the aid of the

calculations, the interpretation of the Raman spectra in the selected energy range is straightforward. We demonstrate that the first calculated (and experimental) six modes of both polymorphs correspond to pure librations of rigid bodies and thus to the lattice phonon vibrations characteristic of each crystal structure.

In summary, the low-temperature phase transition transforming γ-coronene into a new form has been fully investigated by Raman microscopy in the low frequency region, and found to occur around 160 K, in agreement with what has been reported in the past.[80] By means of vdW-DFT corrected calculations of the vibrational properties of coronene crystals, it has been possible to ascertain that such a form corresponds to the β structure recently characterized by XRD measurements.[79] It is necessary to stress that this is an important result, in which the high quality of the calculations exploits the full potential of the spectroscopic technique in the challenging task of identifying solid phases. Until now, lattice phonons calculations have been used to supplement the spectroscopic information about phases whose identity was known. Conversely, here we have been able to make a phase assignment relying only on the precise reproduction, through DFT calculations, of the Raman spectral pattern, thus yielding polymorph recognition independent of X-ray structural determination. In fact, the structure of various possible polymorphs of a substance can be possibly predicted directly in silico.[86]

As for the experimental findings, we may conclude that, once triggered, the transformation goes to completion, as there is no evidence of the coexistence of the two polymorphs, which was instead observed on cooling γ-coronene powder.[79] Puzzlingly, the change of color which should characterize the β polymorph was never detected in our experiments, even though it has been reported to be quite striking and related to the strongly modified optical properties of this material.[79] On the other hand, available electronic absorption measurements of the low temperature phase do not evidence dramatic changes with respect to the ambient temperature one.[82] The β structure is claimed to be obtained between 328 and 298 K via the assistance of a magnetic field, and subsequently to be stabilized at room temperature indefinitely. This raises a question, as the magnetic field might well drive

the kinetics of the polymorph formation, as suggested in Reference [79], thus allowing the preferential growth of a metastable structure, but it certainly cannot change its thermodynamics. While we confirmed the enantiotropic relationship between γ and β polymorphs, our temperature cycling experiments prove that β always reverts back into γ well below room temperature, despite the hysteresis. In these conditions, the lack in the literature of a β structure measured above the detected transition temperature is quite unfortunate and does not provide evidence for reproducibility. Notwithstanding the interest aroused by controlling polymorphism with the additional degree of freedom of the magnetic field, also other factors, such as impurities, may account for the significant property changes observed in some coronene crystals grown at ambient conditions. We believe that further investigations are needed to confirm the effect of magnetic field on the crystal growth process of coronene.

Table 4.1: Lattice parameters of coronene polymorphs. Experiments are compared to calculations performed either with or many-body dispersion (MBD) DFT or with the D3–BJ method. Energies are in eV per mole of unit cells.

Polymorph		T (K)	a (Å)	b (Å)	c (Å)	β (°)	V (Å^3)	Interplanar Angle (°)	$RMSD_{18}$ (Å)	Energy (eV)
	exp[79]	80	10.3855	3.8212	17.2111	96.235	678.984	49.5	–	–
β	MBD	0	10.2808	3.8510	17.1154	95.841	674.104	48.1	0.061	−530.709
	D3–BJ	0	10.3044	3.7997	17.1359	95.943	667.327	48.5	0.062	−531.321
	exp[84]	100	10.0086	4.6651	15.5437	106.576	695.592	86.3	–	–
γ	MBD	0	9.9300	4.7129	15.3609	106.385	689.681	86.2	0.059	−530.670
	D3–BJ	0	9.9393	4.6786	15.3483	106.709	683.591	86.8	0.059	−531.291

Table 4.2: Monkhorst-Pack $\boldsymbol{k}$-point sampling adopted for the Brillouin zone of coronene polymorphs for the different vdW corrections used in this work. For the meaning of densest $\boldsymbol{k}$-grids see text.

Polymorph	vdW correction	$\boldsymbol{k}$-grid	Densest $\boldsymbol{k}$-grid
β-coronene	DFT D3–BJ	2×5×1	4×10×2
	DFT MBD	2×5×1	
γ-coronene	DFT D3–BJ	2×4×1	5×10×3
	DFT MBD	2×5×1	

Table 4.3: Calculated and experimental wavenumbers of the six lowest energy modes of γ and β coronene polymorphs (with symmetry). Calculated squared rotational components around the three inertia axes L, M, N are given as $L + M$ (in plane) and N (normal to plane).

β-coronene					γ-coronene				
Sym	Calc (cm^{-1})	Rotation % $L+M$	N	Exp (cm^{-1})	Sym	Calc (cm^{-1})	Rotation % $L+M$	N	Exp (cm^{-1})
B_g	17.7	2	98	17.8	B_g	35.8	0	100	39.0
A_g	41.2	42	58	41.9	A_g	42.2	2	96	–
A_g	50.0	64	36	51.2	A_g	61.1	96	1	57.5
B_g	72.4	98	0	73.3	B_g	63.2	100	0	60.8
A_g	74.3	92	6	75.2	B_g	83.8	100	0	79.1
B_g	87.0	96	2	86.8	A_g	89.1	98	0	86.3

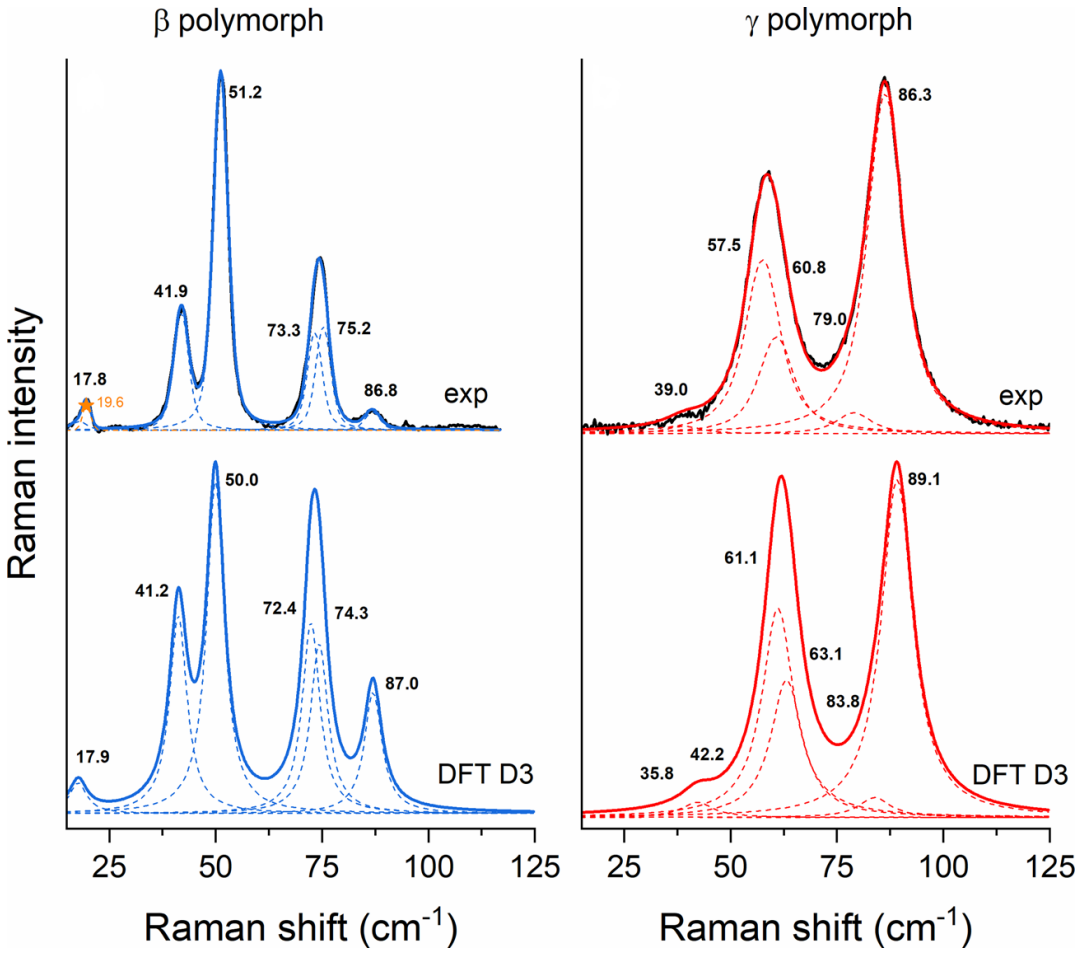

Figure 4.7: Calculated lattice phonon Raman spectra of γ (right) and β (left) polymorphs are compared to the experiments at high and low temperature, respectively. The corresponding Lorentzian band FWHM's are 4.5 and 2.5 cm^{-1}. The scattering at 19.6 cm^{-1}, indicated with a yellow asterisk in the experimental pattern of β, is due to the glass slide in the cryostat.

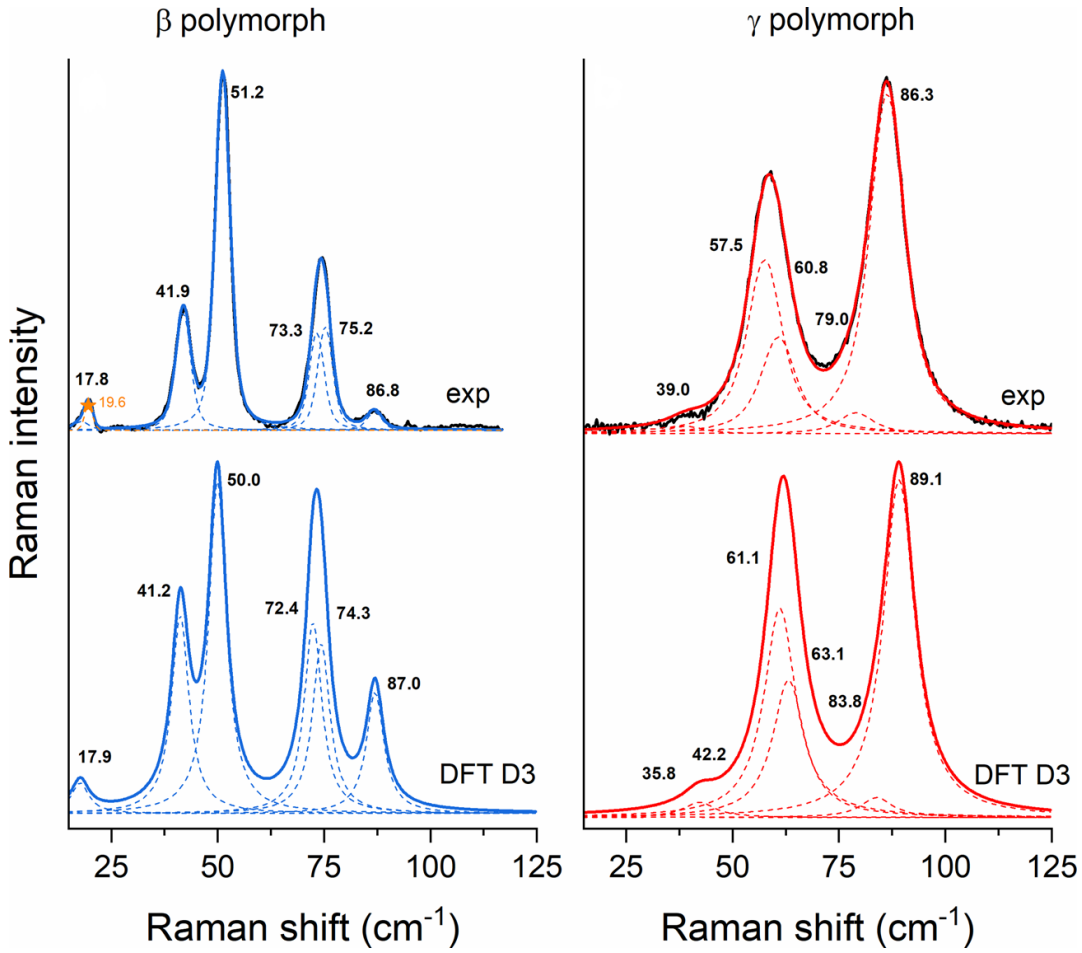

Figure 4.8: Calculated lattice phonon Raman spectra of γ (right) and β (left) polymorphs are compared to the experiments at high and low temperature, respectively. The corresponding Lorentzian band FWHM's are 4.5 and 2.5 cm^{-1}. The scattering at 19.6 cm^{-1}, indicated with a yellow asterisk in the experimental pattern of β, is due to the glass slide in the cryostat.

Chapter 5

Polymorph recognition: Indigo

5.1 Introduction

The present Chapter is concerned with the structural and Raman properties of crystalline Indigo[28] [2,2′-Bis(2,3-dihydro-3-oxoindolyliden)] (see Figure 5.1), a commonly used natural dye which is known in two polymorphic forms, named A and B, displaying similar structures.[87–91] Both are monoclinic $P2_1/n$ with $Z = 2$ molecules per unit cell and similar unit cell parameters. Indigo has been shown to exhibit a highly promising semiconducting behavior, allowing for the realization of ambipolar devices. Nevertheless, it was still unclear which crystal structure is present in the thin films, a piece of information relevant for device applications.

A combination of single-crystal and powder X-ray diffraction (XRD) techniques has been used to characterize bulk and films obtained by drop-casting. The X-ray experiments provide a clear "picture" of the polymorphic compo-

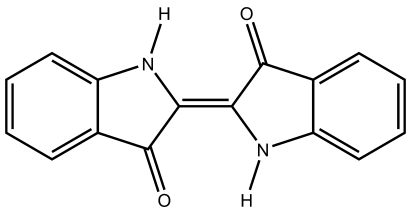

Figure 5.1: Molecular structure of Indigo [2,2′-Bis(2,3-dihydro-3-oxoindolyliden)].

sition in the bulk samples, showing that A and B modifications often coexist and that, at variance with some previous reports,[89] phase B seems to be the predominant one. In the samples obtained by dropcasting, the XRD cannot identify unambiguously which of the two polymorphs is present, a complication that has already been reported and discussed in detail in the literature for the thin films.[92]

DFT calculations with a posteriori van der Waals (vdW-DFT) corrections are used here to assess the relative stability of the A and B polymorphs, and to assist Raman investigations performed on the bulk samples to identify the vibrational fingerprint of each polymorph. This information is thus successfully applied to characterize the drop-cast samples and to reveal that polymorphs coexist at the micron scale in crystallites. The spectral investigation focuses both on the low-energy region (10–150 cm^{-1}), where the lattice phonons are recorded, and on selected intramolecular modes (in the ranges 100–200 and 1550–1600 cm^{-1}), which have been found to be very sensitive to the H bonds. These two energy regimes provide excellent markers for Indigo polymorph discrimination. The knowledge of the phonon spectrum provided by the Raman measurements and DFT calculations[20] also provides information that will be needed in future studies for understanding the role of vibrations for charge transport processes in these systems.[93]

The material described in this Chapter corresponds to the paper entitled "*Structural, spectroscopic and computational assessment of the concomitant polymorphs of the natural semiconductor indigo*", by Salzillo, d'Agostino, Rivalta, myself, Brillante, Della Valle, Bedoya-Martínez, Zojer, Grepioni and Venuti.[28] My contribution to this work was the calculation of DFT Raman spectra of the two polymorphs of indigo. This was essential to achieve polymorph identification even on films, where the XRD pattern was way too poor to allow for structural discrimination.

5.2 State of the art

Five structures are contained in the CSD repository with refcode INDIGO, referring to a number of structural works on this compound.[88–91,95]

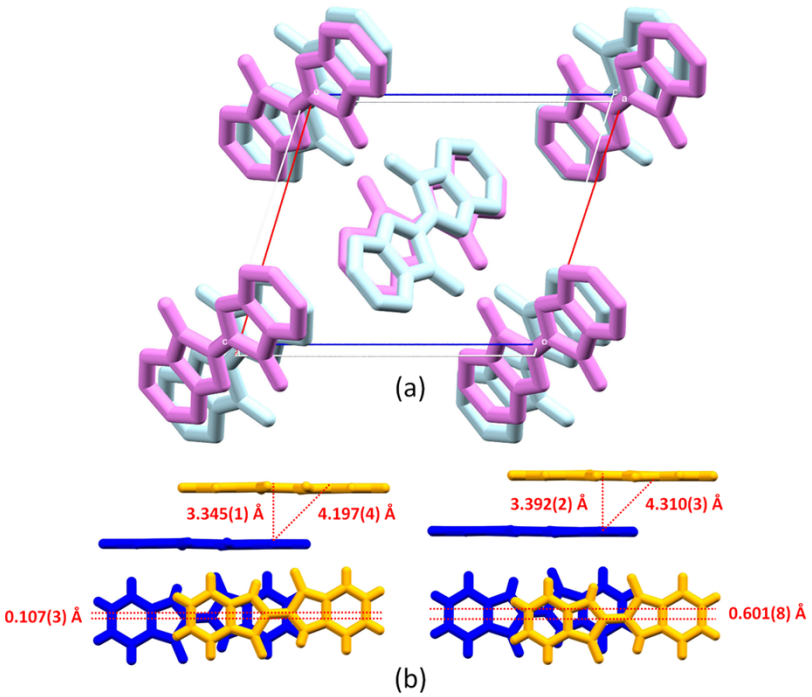

Figure 5.2: (a) Overlay of the packing diagrams showing subtle differences in the unit cell and reciprocal orientation of the molecules for Indigo form A (light blue) and B (pink), determined at 210 K[28] and 213 K,[91] respectively. (b) Particular showing how these differences mirror in slightly different π-stacking interactions for form A (left) and B (right).

References [88, 90, 95] all report the same monoclinic $P2_1/c$ structure, denoted as polymorph A in the CSD files. In Reference [87], the occurrence of a second structure (denoted as polymorph B) is mentioned for the first time: the reported cell parameters are such that, within the experimental errors, only the cell length a and the monoclinic angle β differ from those of polymorph A. More information about form B can be found in References [89] and [91]. In the former paper, with crystallites grown by sublimation, polymorph B was always found to coexist (10%) with polymorph A, whereas in the latter paper, single crystals of B were selectively grown at high temperature and ambient pressure near the decomposition limit of the compound. Structurally very similar to form A, form B is reported as monoclinic $P2_1/c$[89] or $P2_1/n$.[91] Its larger volume (about 3% at room temperature RT) suggests that B might be the structure stable at higher temperature; however, no

Table 5.1: Lattice Parameters and Sublimation Energies $\Delta_{\text{sub}}H(T)$ of Crystalline Indigo. Experiments are compared to calculations, either with the TS[14] or with the MBD DFT[11] method. All the experimental structures have been standardized to the $P2_1/n$ space group.

REFCODE/form	a (Å)	b (Å)	c (Å)	β (°)	Volume (Å^3)	T (K)	$\Delta_{\text{sub}}H(T)$ (kcal/mol)
our work[28]/A	9.2850(9)	5.7941(4)	11.5722(9)	108.710(10)	589.66(8)	295	32[94]
	9.1942(8)	5.7876(6)	11.4878(8)	108.268(9)	580.48(9)	210	
INDIGO[95]/A	9.24	5.77	11.50	108.73	580.65	RT	
INDIGO01[88]/A	9.23	5.74	11.59	108.95	580.82	RT	
INDIGO03[90]/A	9.24	5.77	11.50	108.73	580.50	RT	
INDIGO02[89]/B	9.854	5.887	10.840	107.38	600.12	RT	
INDIGO04[91]/B	9.7990	5.9064	10.7550	106.78	595.96	213	
our work,[28] calc (TS)/A	9.107	5.741	11.489	108.53	569.60	0	45.5
our work,[28] calc (MBD)/A	9.148	5.779	11.465	108.81	573.71	0	37.4
our work,[28] calc (TS)/B	9.633	5.922	10.468	105.94	574.16	0	45.2
our work,[28] calc (MBD)/B	9.732	5.885	10.559	106.90	578.68	0	37.4

phase transition was detected by cooling down to 213 K.[91]

Polymorphs A and B contain two molecules per unit cell ($Z = 2$) related by a 2_1 screw axis and possessing C_i molecular symmetry. Only very small deviations from the C_{2h} planar geometry are found. The latter correspond to the minimum energy configuration determined by the DFT calculation for the isolated molecule. This shows that the influence of crystal packing on the molecular geometry is negligible. Both A and B polymorphs exhibit the same interaction patterns: translationally equivalent molecules are arranged with parallel aromatic rings to form stacks with face-to-face π–π interactions and a network of intra- and inter-hydrogen bonding interactions. Even the packings are nearly identical and the main difference between the polymorphs is in a subtle reciprocal orientation of the molecules, which leads to slightly different stackings (see Figure 5.2). Although small, this difference could affect the electrical properties of Indigo-based thin-film devices, hence the need to know exactly what polymorph we are dealing with.

A summary of the published structures, with cell parameters standardized to the $P2_1/n$ space group, is reported in Table 5.1. This table also contains the values calculated by DFT discussed in more detail in the following section.

5.3 Inherent structures

The inherent structure of a polymorph is the local minimum corresponding to the configuration of mechanical equilibrium[96,97] reached by a steepest descent minimization, which starts from a given configuration of the system on the potential energy surface. In this context, all structures of the same thermodynamic phase lie in the potential basin of the same local minimum and, thus, converge to the same inherent structure. In the case of Indigo, where we are dealing with a collection of very similar structures measured over many years under various conditions and temperatures, the method enables us to identify which of the reported structures actually correspond to different polymorphs. The minimizations could be performed by running DFT optimizations starting from all available experimental structures. When including high-level dispersion corrections, this would yield reliable lattice parameters and energies, but with the risk of wasting computer time by repeatedly reaching the same minimum, whenever supposedly different experimentally determined structures actually correspond to a single polymorph. Luckily, in our experience, it is not necessary to resort to expensive computational methodologies because, although the lattice parameters computed at the minimum obviously depend on the method adopted for the calculations, the identification of the various polymorphs is instead independent of the method itself (provided that it is realistic).[98]

The method relies on the calculation of the crystal structure of minimum energy, which we have determined with an atom-atom potential model for the nonelectrostatic interactions, combined with atomic point charges to treat the electrostatic contributions. Molecular geometries and atomic charges were obtained from an isolated molecule DFT calculation. The lattice energies were minimized starting from all available crystal structures,[87–91] including the data from our work.[28] Unit cell parameters, molecule orientations, and distances within the cell were varied keeping the molecules rigid and interacting through the DREIDING[99] atom-atom potential. The GAMESS[100] program with the B3LYP/6-31G(d) functional and basis set combination was employed for equilibrium molecular geometries and electrostatic poten-

tial atomic charges.

The analysis does confirm that for all the experiments only two distinct minima can be identified, corresponding to form A (our work,[28] and CSD ref codes INDIGO,[95] INDIGO01,[88] and INDIGO03)[90] and form B (INDIGO02[89] and INDIGO04).[91] Notably, the adopted potential model reproduces satisfactorily the experimental sublimation enthalpy[94] [$\Delta_{\text{sub}}H_{\text{exp}}(577K) = 32$ kcal/mol, $\Delta_{\text{sub}}H_{\text{cal}} = 34$ kcal/mol].

An useful way of comparing crystallographic structures is the distance comparison method,[43,44] described in Section 2.4. This analysis further supports the association of all measured structures with two polymorphs, yielding RMSD_{14} values clustered in two sets A and B. All A-A and B-B (same set) RMSD_{14} distances are below 0.08 Å, whereas A-B (different sets) RMSD_{14} distances exceed 0.40 Å.

5.4 DFT structures and relative stability

After this inexpensive screening, DFT calculations were performed only for the two distinct polymorphs A and B, to obtain information about their relative stability.

The lattice parameters computed at the minimum energy structure with TS[14] and MBD[11] vdW-DFT methods [1] by relaxing both the atomic coordinates and the cell axes are reported in Table 5.1. The agreement with the experimental parameters (Table 5.1) is excellent and can be regarded as

[1] Density functional code `VASP` (Vienna ab initio simulation package)[5–8] were used with the Perdew-Burke-Ernzerhof (PBE) exchange correlation functional[101] and projected-augmented wave (PAW) potentials.[36,37] The effects of the vdW interactions have been included with either the pairwise method of Tkatchenko and Scheffler (TS)[14] or the many-body dispersion (MBD) method of Tkatchenko et al.[11] Because of their structural similarity, energy convergence could be achieved with identical settings for the two polymorphs: a plane wave cutoff of 800 eV proved adequate in combination with $3 \times 5 \times 3$ and $4 \times 6 \times 3$ Monkhorst-Pack $\boldsymbol{k}$-point grids for the TS and MBD calculations, respectively. Raising the cutoff energy from 800 to 1200 eV caused energy changes below 1 meV/atom, whereas increasing $\boldsymbol{k}$-point sampling to $6 \times 10 \times 5$ gave energy changes below 0.05 meV/atom. Cell parameters and atomic coordinates were fully relaxed, halting when residual forces fell below 1 meV/Å. For both energy cutoff and $\boldsymbol{k}$-point sampling, energy differences between polymorphs A and B converge faster than absolute energies to within 0.07 meV/atom (i.e., 0.05 kcal/mol of Indigo).

a validation of the method, also considering that calculations did not take thermal expansion into account, while experiments are done above 0 K. Furthermore, the $RMSD_{14}$ distance analysis shows that the computed structures cluster together with the corresponding experimental ones. For the same sets (A-A or B-B), computed versus experimental $RMSD_{14}$ distances are 0.10 and 0.16 Å for the MBD and TS methods, respectively, whereas for different sets (A-B or B-A), the $RMSD_{14}$ distances exceed 0.45 Å.

The relative stability of the two phases as a function of temperature was analyzed by adding the vibrational contribution,[45]

$$F_{\mathrm{vib}}(T) = \tfrac{1}{2}\sum_i \hbar\omega_i + k_B T \sum_i \ln\left[1 - \exp\left(\tfrac{\hbar\omega_i}{k_B T}\right)\right],$$

to the Helmholtz free energy. Here, $\boldsymbol{k}_B$ and T are the Boltzmann constant and the absolute temperature. F_{vib} depends on the vibrational frequencies ω_i and, therefore, on the details of the molecular packing.

Phonon frequencies ω_i were computed with the `Phonopy` software[45] in combination with `VASP`, for an approximately cubic $2 \times 3 \times 2$ supercell with sides of $\sim$ 19 Å. Thanks to the larger computational cell and to the over-converged $\boldsymbol{k}$-point sampling of the primitive cell, the sizable computational cost could be reduced by limiting the $\boldsymbol{k}$-point sampling to the Γ point, which yielded convergence to 0.07 meV/atom. The sum over frequencies ω_i was replaced by the equivalent integral over the phonon density of states $g(\omega)$, determined with 250 symmetry inequivalent wave vectors over a $10 \times 10 \times 10$ mesh in reciprocal space.

Following standard procedures,[102,103] we have computed the sublimation enthalpy $\Delta_{\mathrm{sub}}H_{\mathrm{cal}}(T)$ by subtracting the energy of an isolated molecule from the calculated total energy per molecule in the solid and by adding the $2RT$ Dulong-Petit term. The energy of the isolated molecule was estimated by embedding a single molecule in a cubic cell. The size of the cell was progressively increased from 20 to 35 Å until the energy converged, in order to avoid interaction between periodic images.

The resulting $\Delta_{\mathrm{sub}}H_{\mathrm{cal}}(T)$, reported in Table 5.1, overestimates the exper-

imental values by 13 and 5 kcal/mol for the TS and MBD methods, respectively. These differences are larger but in the same direction as those found in recent benchmark calculations on a set of 23 molecular crystals,[103] with the same PBE functional and vdW corrections but with an explicit treatment of the vibrational contributions instead of the Dulong-Petit term. In that study, on average, experimental $\Delta_{\mathrm{sub}}H_{\mathrm{cal}}(T)$ were overestimated by 3 and 2 kcal/mol for the TS and MBD methods, respectively. These differences are approaching the experimental uncertainties, estimated to be around 1 kcal/mol.[104]

Computed volumes for polymorph A are smaller than for polymorph B, in agreement with the experiments. At 0 K, the A phase is predicted to be slightly more stable than the B phase, by 0.3 and 0.06 kcal/mol for the TS and MBD methods, respectively, in agreement with the rule of thumb that the higher the density, the higher the stability. The energy difference especially in the MBD case is very small, as expected on the basis of the close structural similarities between the two forms, and indeed comparable to the computational accuracy for such differences of 0.05 kcal/mol.

When the temperature-dependent vibrational contribution to the free energy $F_{\mathrm{vib}}(T)$ is included, the stability differences between the two phases decreases with increasing T. In fact, form B becomes more stable beyond 480 ± 70 or 110 ± 70 K with either the TS or the MBD method, where the uncertainty in the temperatures derives from the uncertainty in the energy. These results support the experimental suggestion[89,91] that form B is the stable one at high T.

5.5 Crystallization and X-ray

In the experimental study the following Indigo crystal samples were analyzed by XRD: (i) commercial powder (TCI Chemical); (ii) single crystals grown by physical vapor transport (PVT); (iii) films obtained by drop-casting using a saturated solution in 1,2-dichlorobenzene and acetonitrile.

The single crystals grown by PVT (ii) were analyzed with single-crystal

XRD both at room and at low temperature and unambiguously identified as A. The crystal structure was solved and refined in the monoclinic $P2_1/n$ space group. To confirm the absence of any phase transition upon cooling, additional data sets were acquired at 210 K and the unit cell was also determined at 150 K.

Powder XRD patterns were collected for all the other polycristalline samples. For the commercial product, the peaks appear slightly broadened, but the pattern corresponds to that of polymorph B, with possible traces of A (ca. 7%). After sublimation of (i), a significant enrichment in polymorph A was detected, in agreement with what was observed by Kettner et al.[91] Notably, the amount of polymorph A increases on increasing the deposition temperature of the sublimation (ranging from ≈ 30 to $\approx 50\%$)

The thin films (iii) obtained by drop-casting show very similar diffraction patterns with two peaks (see Figure 5.3). Here, the degree of uncertainty is, however, too high to allow for a safe and unambiguous determination of the type of polymorph from these measurements. A similar problem has been previously encountered by Scherwitzl et al.[92] and by Anokhin et al.[105] in Indigo films grown from vapor on various substrates.

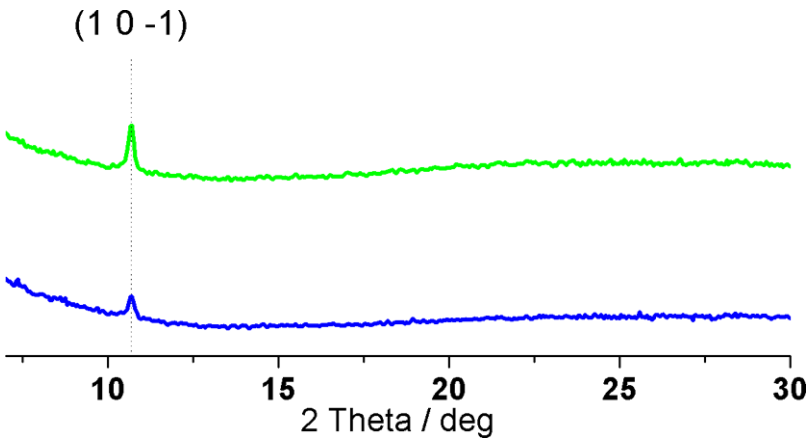

Figure 5.3: XRD pattern of Indigo deposited on Si/SiO_x wafer by dropcasting of 1,2-dichlorobenzene (green line) and acetonitrile (blue line).

5.6 Raman lattice phonon and DFT comparison

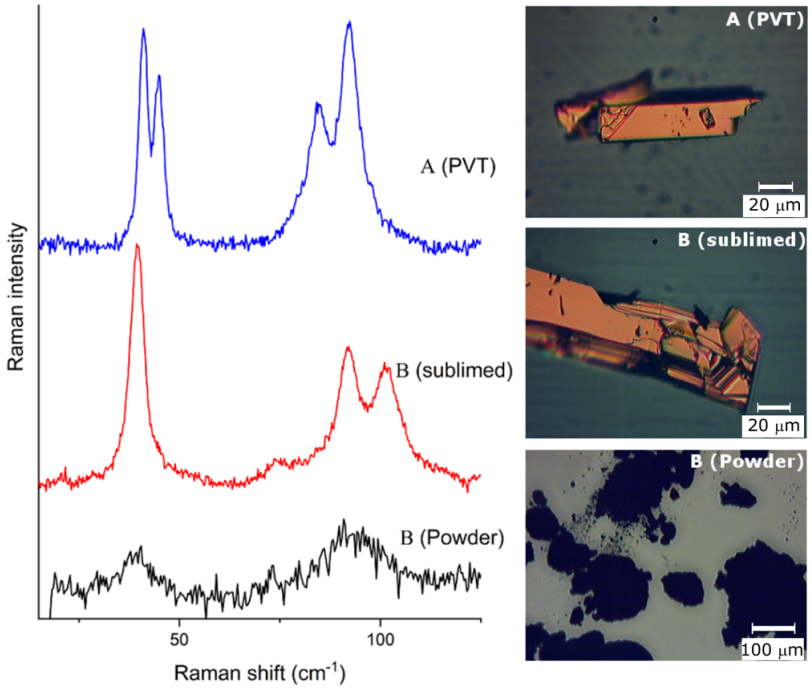

Figure 5.4: Left: lattice phonon Raman spectra, recorded using an excitation wavelength of 752.5 nm, of the various samples of crystalline Indigo, with the two unique patterns that can be identified from the analysis. Right: images of the samples that shows how morphology cannot be used to discriminate between the two polymorphs.

The first crucial step for using Raman spectroscopy to identify polymorphs is to measure and/or calculate the reference spectra for samples in which the actual structure has been identified (i.e., in our case for the bulk crystals).

To obtain the unique lattice phonon Raman pattern of polymorph A, Raman spectra were collected for the Indigo samples grown by PVT (ii) and identified by single-crystal XRD. The lattice phonon Raman spectra, together with that of the commercial powder and sublimated sample (i), are shown in Figure 5.4.

Random sampling of the specimens grown by sublimation (i) confirmed

that two different spectral patterns could be selectively detected on individual crystallites: the first corresponding to polymorph A, assigned on the basis of the analysis performed on the PVT crystals, and a second one, measured for the larger fraction of the crystallites. On the basis of the XRD investigations, this pattern was assigned to polymorph B. It should be noticed that also the spectral patterns of the two crystal forms in the lattice phonon region are quite similar, reflecting the similarities of the lattices.

As expected, the spectrum of the commercial product displays broader bands compared to the single crystals, but judging by spectral positions and shapes we can associate it with polymorph B, in agreement with the powder XRD results.

To confirm the assignment, the experimental Raman spectra of the two polymorphs in the region of the lattice phonons are compared in Figure 5.5 to those calculated by DFT employing the MBD correction.

On the basis of the $P2_1/n$ crystal symmetry (which is the same for both polymorphs A and B of Indigo) and on the assumption that Indigo can be treated as a rigid molecule, six lattice modes of gerade symmetry $3A_g + 3B_g$ are predicted to be Raman active and they correspond to either in-phase (B_g) or out-of-phase (A_g) rotations (librations) of the molecules in the unit cell around their axes of inertia and give rise to three doublets in the Raman spectrum.

Such an analysis is supported by the calculations. The eigenvectors of the six lowest gerade normal modes do correspond to pure librations, with no contribution of intramolecular vibrations. The agreement between simulated and experimental patterns is very good for polymorph A and less so for polymorph B, although close to the accuracy of the theoretical method in the calculation of the vibrational eigenvectors.[20]

As can be seen in Figure 5.5, the experimental feature which most clearly distinguishes polymorph B from polymorph A, i.e. the presence of two almost degenerate lowest energy lattice phonons around 40 cm^{-1}, is very well reproduced by the simulations. However, in the calculated spectra, the differences between the higher energy phonons of the two polymorphs (70–110

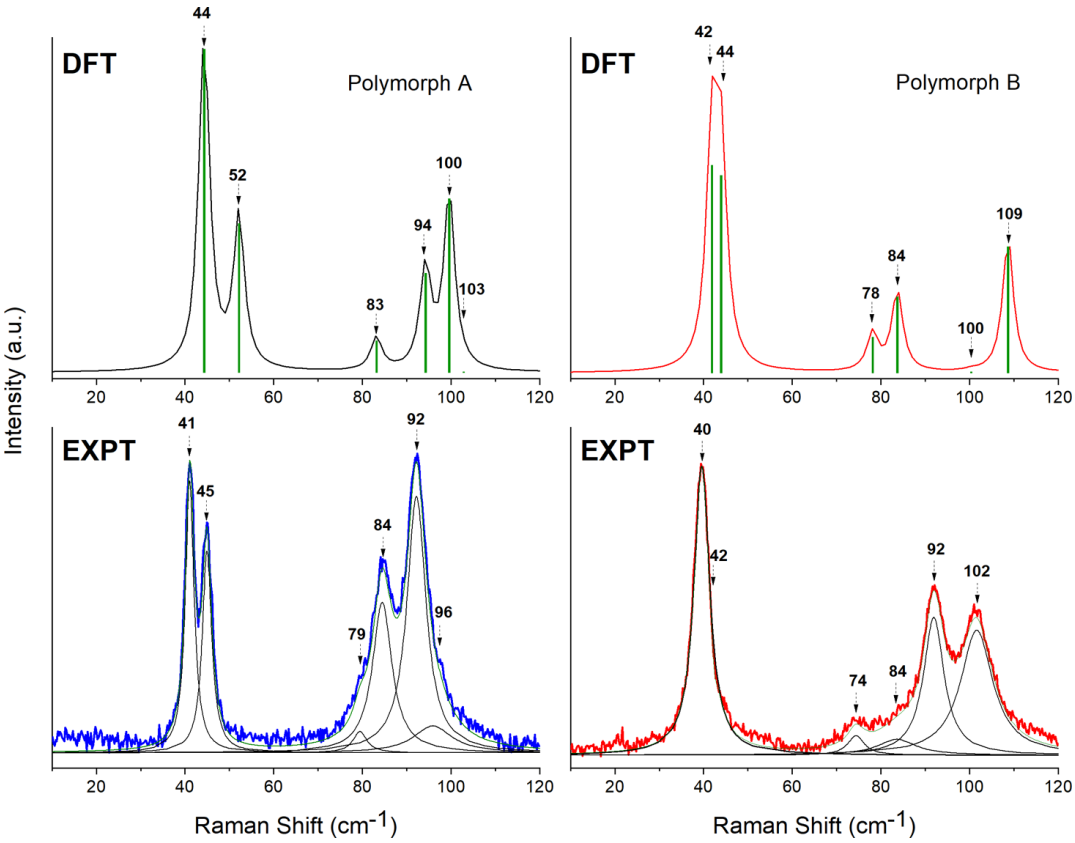

Figure 5.5: Comparison of DFT-MBD and experimental Raman spectra for A and B Indigo polymorphs in the lattice phonon region. The experimental spectra have been deconvoluted as sums of Lorentzian bands. The 42 cm^{-1} peak of the B polymorph can be resolved only in the Raman polarized spectra.

cm^{-1}) are larger than what is observed from the experiments. Residual polarization effects due to sample orientation could explain changes in relative intensities, but further investigation might be needed. Nevertheless, the reproduction of the spectral features, especially for polymorph A, contributes to the validation of the assignment of Raman spectra to specific polymorph structures initially made with the aid of XRD measurements.

5.7 Intramolecular Raman spectra and film identification

Intramolecular vibrational spectra, either IR or Raman, often provide a valid diagnostic tool for the identification of conformational polymorphs. They are, however, usually ineffective for packing polymorphs, which share the same molecular geometry and, thus, the same spectral features for the intramolecular modes. By contrast, Indigo A and B polymorphs can be discerned by some of the strongest bands of their intramolecular Raman spectra. The central panel in Figure 5.6 shows these spectra for the samples of the two polymorphs in the wavenumber region from 100 to 2000 cm^{-1}, whereas at the sides two specific ranges have been zoomed in: (i) 100–200 and (ii) 1450–1650 cm^{-1}.

As expected for packing polymorphs, most bands of forms A and B are overlapping.

The low-wavenumber region shown in the left panel of Figure 5.6 highlights the bands corresponding to the intramolecular mode of the lowest energy. It is split into an $A_g + B_g$ doublet in the crystal with $Z = 2$ molecules/cell, as a result of the factor group splitting[107] between vibrations involving pairs of molecules. In polymorph B, the two peaks lie at 132 and 139 cm^{-1}, whereas in polymorph A, the peaks lie at 136 and 142 cm^{-1}. The Raman calculations on the crystals correctly reproduce the red shift of form B (yielding 135 and 144 cm^{-1}) compared to A (140 and 151 cm^{-1}). The eigenvectors describe this vibration as a large amplitude mode arising from internal rotations, which gives rise to ripples traveling the entire molecular scaffold (top images of Figure 5.6). The nature of this motion suggests it to be a sensitive probe of the strength, and thus the packing, of the intermolecular hydrogen bonds, as these could hinder internal rotations.

The Raman spectra of the two polymorphs also differ in the doublet of the most intense and typical band of Indigo,[108–110] shown in the right panel of Figure 5.6. In polymorph A, the doublet lies at 1578 and 1592 cm^{-1} (calculated 1568 and 1585 cm^{-1}, respectively), and in polymorph B, the doublet lies at 1576 and 1587 cm^{-1} (calculated 1566 and 1580 cm^{-1}, respectively).

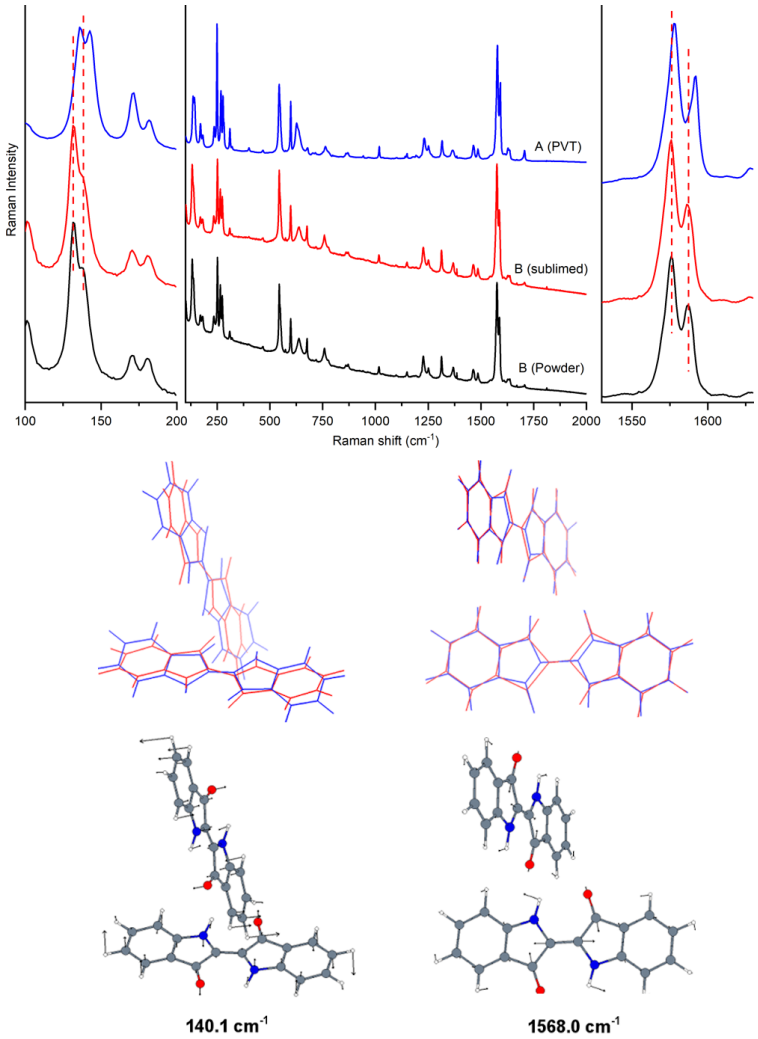

Figure 5.6: Top: Raman spectra, recorded using an excitation wavelength of 752.5 nm, of Indigo polymorphs A (blue) and B (red) and of the commercial powder (black), which was found to be composed mostly of B, in the wavenumber range 100–2000 cm^{-1}. Center: extended spectrum; left and right: zoom into the wavenumber intervals, in which polymorph discrimination can be made on the basis of intramolecular vibrations. Bottom: visualization of the A_g intramolecular mode of the lowest energy (calculated at 140.1 cm^{-1} for the A polymorph) (left) and visualization of the A_g intramolecular mode corresponding to the most intense and typical band of Indigo (calculated at 1568.0 cm^{-1} for the A polymorph) (right). Arrows indicate the direction of the displacements, while blue and red geometries depict the moving of the system.[106]

As can be seen in the eigenvector visualization of Figure 5.6 (bottom images), the corresponding mode is a combination of the central CC and CO stretchings but actually comprises the motion of the entire functional system formed by the two CO acceptor and the two N-H donor groups, called cross-conjugation chromophore.[109,110] The mode is computed around 1596 cm^{-1} for the isolated molecule[108,110] with a large red shift observed[108–110] and calculated in the solid state. Such a variation has been interpreted on the basis of calculations on a dimer[108] as a consequence of the strong intermolecular hydrogen bonds, which affect the vibrational dynamics of the functional groups involved in the interaction.

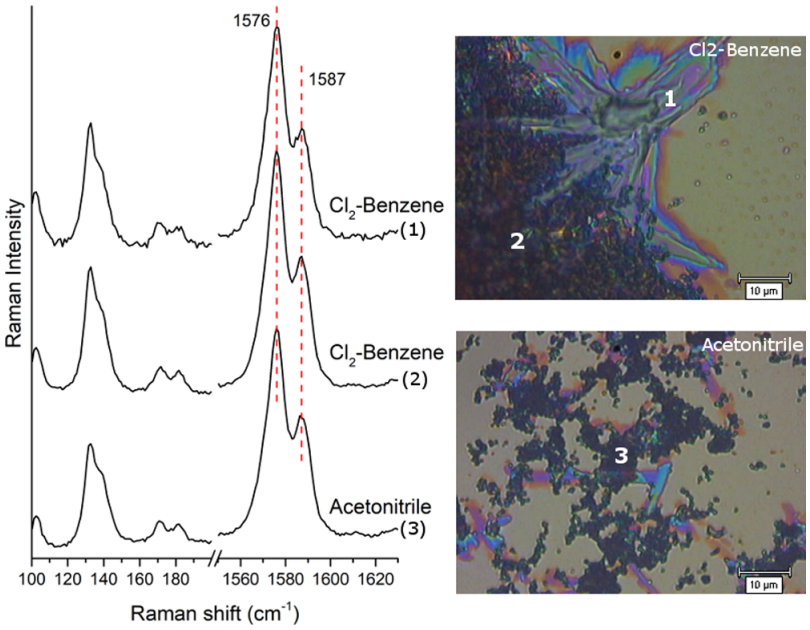

Figure 5.7: Raman spectra of films of Indigo drop-cast from solutions in chlorobenzene and acetonitrile. The wavenumber ranges suitable for polymorph identification are shown. For each spectrum, the number indicates the image area of the sample where the Raman scattering has been collected.

As mentioned above, the X-ray investigation of Indigo films may fail to recognize which crystal modifications are present. The high sensitivity displayed by Raman microscopy for Indigo suggested its application to the screening of the films. Figure 5.6 shows the Raman spectra recorded on films

obtained by drop-casting from 1,2-dichlorobenzene and acetonitrile solutions on Si/SiO_x. Choosing as polymorph markers the intramolecular modes illustrated in the previous section, we investigated phase identity and purity by performing extensive random sampling on the film surfaces. All measurements indicate that B is the only polymorph present. Notably, the films prepared for these measurements are thicker than those reported in previous works. Besides, solution techniques similar to that adopted here do not produce Indigo films of the quality required to test charge transport. However, Raman clearly is very sensitive, as can be judged by the high signal/noise ratio of the spectra presented, and this makes it a good candidate for reliable polymorph identification also in very thin films.

5.8 Conclusions

The characteristics of the concomitant Indigo A and B polymorphs have been revisited by single-crystal and powder XRD and lattice phonon Raman microscopy. Solid-state DFT-TS-vdW and DFT-MBD-vdW calculations have been employed to estimate the relative stability of the two forms, whereas a quick energy minimization based on a model potential has assured us that all the literature structures belong to two and only two forms. Polymorphs A and B are very similar, with close lattice parameters, almost identical packings and closely corresponding interatomic distances. With a threshold of 1 Å, typical in crystal predictions to identify different structures by comparing their lists of interatomic distances, indeed the two forms would be considered identical. Nevertheless, we here show that they are different: experimentally because they exhibit clearly different XRD and Raman spectra and computationally because they converge to distinct minima.

The DFT calculations are in agreement with the empirically proposed energy ranking for the two polymorphs, although they assign the polymorphs to be nearly isoenergetic. At 0 K, the form A is predicted to be more stable than B, by 0.1–0.3 kcal/mol, depending on the method. Such values are very small, but differences around 0.5 kcal/mol are commonly found by

comparable theoretical methods for most nonconformational polymorphs.[111] Moreover, the MBD approach adopted here has been reported to yield an accuracy of ca. 0.2 kcal/mol in the relative energies of a wide range of molecular crystal polymorphs.[112] Our finding that the temperature dependent vibrational contribution to the free energy $F +_{\mathrm{vib}} (T)$ favors polymorph B suggests that this is phase stable at high T. From an experimental point of view, we must notice that in contrast to what has been described in the literature, the commercial powder available to us is almost entirely composed of the B form, which since its first identification has been assumed to be not trivial to isolate and possibly metastable. The same applies to the product of sublimation, where the B form dominates, but which can be enriched in A by changing the deposition conditions.

With the situation of the Indigo polymorphs clarified by the experiments in the bulk phase and the MD simulations for the spectra, and the correlation between structural and dynamic properties established, the characterization of the films has become possible. We have shown that even in cases in which the close similarities of the two structures impair their identification by XRD investigations, the micro-Raman technique is sensitive enough for polymorph discrimination, identifying the B form as the only one present in films obtained by drop-casting.

Chapter 6

Polymorph recognition: Thioindigo

6.1 Introduction

Thioindigo (2-(3-oxo-1-benzothiophen2(3H)-ylidene)-1-benzothiophen-3(2H)-one), (see Figure 6.1) is synthetic indigo derivative where the N−H gruops are replaced by S atoms. This compound was reported to exhibit hole field effect mobility,[113] albeit smaller than indigo Besides, the electrical properties of the silicon/thioindigo heterojunction were studied in view of applications in organic photodiodes and organic photovoltaic devices.[114] In all cases, thin films of the material were fabricated by evaporation techniques, but no information about the polymorph obtained, i.e. the solid phase which determines the final electronic properties, was given[115], even though the compound is

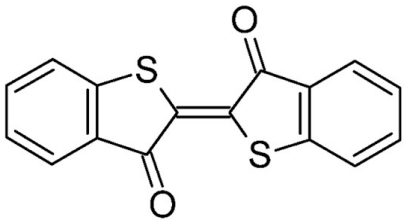

Figure 6.1: Molecular structure of Thioindigo (2-(3-Oxo-1-benzothiophen-2(3H)ylidene)-1-benzothiophen-3(2H)-one).

known to show polymorphism.[116,117]

In the research project where the PhD work was conducted, the occurrence of the two known thioindigo α and β polymorphs under various growth conditions was studied by Raman spectroscopy, discovering that their structural similarity implies they often coexist. However, whereas polymorph β is certainly dominant in the bulk phase, polymorph α grows preferentially on substrates, turning out to be the surface stabilized phase in highly homogeneous and ordered films obtained by the bar-assisted meniscus shearing method (BAMS).[118–120]

DFT calculations support the experimental findings, aiding in the polymorph spectroscopic identification and to the interpretation of the order in the films of polymorph α.[31]

The material described in this Chapter corresponds to the paper entitled "*Crystal alignment of surface stabilized polymorph in thioindigo films*", by d'Agostino, Rivalta, Schrode, Mas-Torrent, Brillante, myself, Pandolfi, Werzer, Demitri, Venuti and Della Valle.[31] My contribution in this work was the calculation of Raman spectra of the two thioindigo polymorphs, and the development of the methods for computing polarized spectra of oriented single crystals and of fully or partially disordered assemblies (powders or sheared films with a preferential orientation, respectively, in this specific application). This required to select and properly average the elements of the polarizability matrix, depending on the geometrical and optical configuration used during the experiment. Information on the orientational distribution could thus be extracted by comparing computed and experiment spectra.

6.2 State of the art

The structures determined for the α and β thioindigo polymorphs are reported in Table 6.1, where the cell parameters are compared to the literature data. The table also contains the structural parameters predicted by the vdW-DFT D3–BJ calculations.

Table 6.1: Crystallographic data for thioindigo polymorphs, as determined in our work[31] and from the literature. Experiments are compared to the results of the vdW-DFT D3–BJ calculations also by means of the $RMSD_{\geq 15}$ of the interatomic distances.

System	Space Group	a (Å)	b (Å)	c (Å)	β (°)	Volume (Å^3)	T (K)	$RMSD_{\geq 15}$ (Å)
SINDIG[116]	$P2_1/c$	7.91(3)	3.97(2)	20.41(3)	93	640.051	RT	
Our work[31] α		7.8130(16)	3.8820(8)	20.503(4)	93.10(3)	620.947	100	0.050
		7.8770(16)	3.9390(8)	20.542(4)	92.67(3)	636.675	RT	0.050
SINDG02[117]	$P2_1/n$	3.981(3)	20.65(2)	7.930(7)	98.84(5)	644.163	RT	
Our work[31] β		3.8644(3)	20.3897(14)	7.8016(5)	98.610(6)	607.791	100	0.043
		3.9342(3)	20.4464(11)	7.8580(6)	98.074(7)	625.834	RT	0.045
Our work,[31] calc α	$P2_1/c$	7.8408	3.8347	20.1538	93.147	605.053	0	
Our work,[31] calc β	$P2_1/n$	3.8481	20.1325	7.8525	97.539	603.089	0	

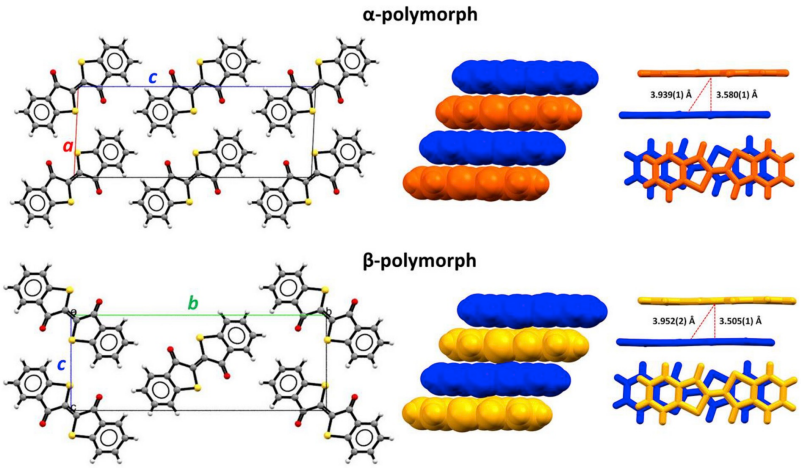

Figure 6.2: Packing of the α- and β-indigo polymorphs; left: projection along the crystallographic axes b and a for polymorphs α and β, respectively; right: representation of the packing along the stacking direction.

The crystal of polymorph α is monoclinic $P2_1/c$, with two molecules per unit cell ($Z = 2$) residing on crystal inversion centres (see Figure 6.1). The molecular geometry is Ci, with very little deviation from a planar C_{2h}. Molecules are stacked along the very short $\boldsymbol{b}$ monoclinic axis. Accordingly, in the projection along $\boldsymbol{b}$, molecules appear lying in parallel rows on the plane $\boldsymbol{ac}$ (see Figure 6.2).

Polymorph β single-crystal structure was solved and refined in the monoclinic $P2_1/n$ space group. Also in this case the monoclinic unit cell contains

two molecules on inversion centres. The molecular geometry is virtually identical in the two polymorphs, but the packing of β is quite different from that of form α, with the molecules stacked along the shortest axis $\boldsymbol{a}$ and appearing in $\boldsymbol{a}$ projection along this axis as shown in Figure 6.2. In both polymorphs $\pi - \pi$ stacking interactions are exerted between the molecules aligned along the short axes of the structure, but while in the α polymorph all the stacks are arranged parallel to each other, in the β neighbouring stacks are rotated with respect to each other. Note that intra-stack distances and relative molecular orientations within the stacks are identical for both structures.

At 100 K and room temperature, the experimentally determined volumes of the two polymorphs differ by about 2%, with form β being the denser, but the trend indicates that the density difference decreases on increasing temperature.

The lattice parameters computed at the minimum energy structure (0 K) by relaxing both the atomic coordinates and cell axes with the vdW-DFT D3–BJ method[1] employed in our work[31] are reported in Table 6.1. Notwithstanding experimental volumes necessarily larger than the calculated ones (which do not include the thermal expansion), the agreement is very good and has been quantitatively checked by computing the RMSD_{15} of the interatomic distances.[43] In agreement with the experimental findings at finite temperature, polymorph β is calculated to be slightly denser than polymorph α at 0 K. The energy difference between the two phases (≈ 0.02 kcal/mol), however, is smaller than the computational accuracy reported for these calculations[112] and, in fact, it is impossible to reliably predict which modification is the more stable.

[1] vdW-DFT D3–BJ simulations on the two thioindigo polymorphs were performed using the code `VASP` (Vienna Ab initio Simulation Package).[5–8,13,36,37,101] For both energy cutoffs (800 eV) and $\boldsymbol{k}$-point sampling ($4 \times 2 \times 1$ for the short, middle and long axis), energy differences between polymorphs α and β converge faster than absolute energies to within 0.04 meV/atom. Atomic coordinates and cell axes were fully relaxed, halting when residual forces fell below 1 meV/Å, using the GADGET package.[38]

6.3 Crystallization and X-ray diffraction

In the experimental part of the work several crystallization techniques have been used to prepare reference samples and films, analyzed by XRD (for single crystals) or GIXD (for films), as listed below.

(i) The commercial and the sublimed crystalline powders are made of polymorph β as checked by X-ray diffraction.

(ii) PVT (Physical Vapor Transport) yielded microcrystals of both α and β polymorph in nearly equal amounts, virtually indistinguishable in morphology but which could be identified by microRaman spectroscopy in the energy range of the lattice phonon modes.

(iii) Crystalline non homogeneous films were obtained by drop casting saturated solutions of various solvents on Si/SiO_x wafers. With most solvents (among which acetonitrile, nitrobenzene and dichloromethane) both α and β polymorph crystals of a few microns were obtained. Deposition from xylene yielded only the α form.

(iv) A final set of thioindigo film samples were fabricated by BAMS on highly n-doped Si wafers or on Teflon bar, if shearing method was used. Heating the substrate (150 °C) and using a controlled speed, an highly textured films of the α polymorph where obtained from pure anisole solution.

6.4 Powder spectra

Lattice phonon microRaman spectroscopy allowed us to discriminate between α and β thioindigo polymorphs, and establish the reference spectra characteristic of each phase. The results obtained, complemented with the Raman measurements in polarized light, contain information about the structural organization of the solid phase.

Vibrational modes and polarizability tensors α has been computed at the experimentally unit cell volumes using `Phonopy` software[45] and vasp_raman.py[47] in combination with `VASP`. Raman intensities were finally adjusted by considering excitation wavelength and temperature dependence.[49] The simulation

of the (unpolarized) spectra of a powder sample involves the calculation of the average over all possible rotations around the three Cartesian axes 1, 2, 3 and thus follows the same rules as gases, yielding

$$I_{\text{powder}} = \frac{45\alpha^2 + 7\beta^2}{45} \tag{6.1}$$

Where α and β are the spherical part and the anisotropy of the polarizability, respectively, computed from the α matrix as:

$$\alpha = \frac{\alpha_{11} + \alpha_{22} + \alpha_{33}}{3} \tag{6.2}$$

$$\beta = \frac{6(\alpha_{12}^2 + \alpha_{13}^2 + \alpha_{23}^2) + (\alpha_{11} - \alpha_{22})^2 + (\alpha_{11} - \alpha_{33})^2 + (\alpha_{22} - \alpha_{33})^2}{2} \tag{6.3}$$

In the left hand side of Figure 6.3, we show the experimental Raman spectra of α-thioindigo crystal below 200 cm^{-1}, together with the vdW-DFT D3–BJ spectrum calculated at the room temperature experimental structure. The spectra were measured on single microcrystals grown from thioindigo solutions in acetonitrile and xylene drop cast on substrates (iii), having the morphologies displayed in the image of the Figure. In the right hand side of Figure 6.3, we report the βthioindigo spectra of the commercial powder (i), as well as those of the samples grown by the PVT (ii) method and from dichloromethane solutions(iii). Again, the experimental profiles are compared to the vdW-DFT D3–BJ spectrum at the experimental structure. Two markedly distinct profiles are found for the two polymorphs, making their recognition easy when analysing still unknown powders and crystals of thioindigo.

For α-thioindigo, only six modes were calculated below 80 cm^{-1}, whereas at the temperature of the experiment, we detect over this range two broad features. The calculations reveal that these are the superimposition of closely located peaks, which are rendered in the computed trace by the convolution

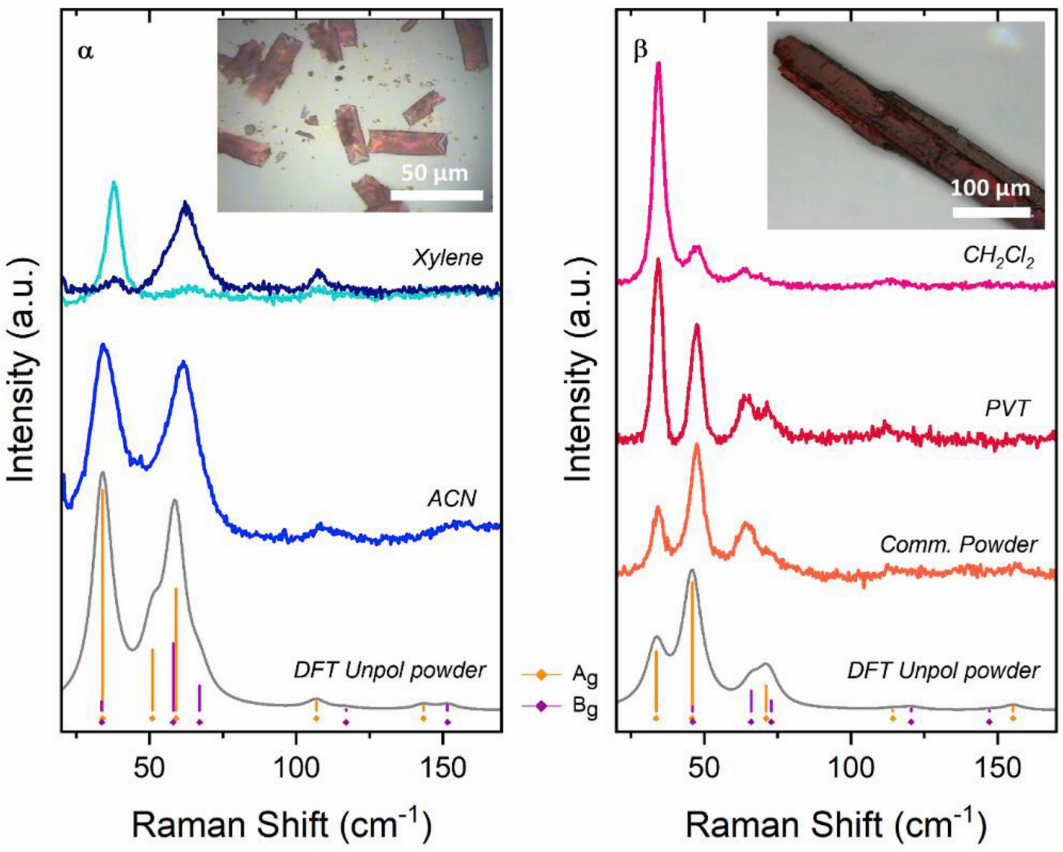

Figure 6.3: Experimental and unpolarized (powder) simulated vdW-DFT D3–BJ Raman spectra and of α (left) and β-thioindigo (right) crystal samples (see images in the inlets; α crystal obtained from xylene and β from CH_2Cl_2) in the range 10–200 cm^{-1}, where lattice phonons are observed. The spectra of α-thioindigo from xylene in are given for two different orientations of the crystal as an instance of crystal anisotropy. Vertical bars of height proportional to the intensity of the mode identify the calculated values, with colour codes yellow and violet for modes of symmetry A_g and B_g, as indicated. The spectral profiles are built by convolution of Lorenzian bands.

of Lorentzian bands with a HWHM (half width at half maximum) of 4 cm^{-1}, to conform to the experimental widths. The β polymorph shows a slightly better resolved profile that, again, can be properly accounted for by the appropriate convolution of the first six calculated modes.

Table 6.2 reports the calculated Raman shifts in the same energy interval, along with the symmetry assignment in the framework of the monoclinic

$P2_1/c$ space group and the component analysis of the calculated eigenvectors. Since both structures belong to centrosymmetric monoclinic crystals with $Z = 2$, we expect six Raman-active lattice phonons, which correspond to the lowest wavenumber peaks. Their symmetry is $3A_g + 3B_g$, and they have the character of pure librations of the unit cell molecules taken as rigid bodies, with virtually no contribution from intra-molecular vibrations. Thus, they unambiguously identify with the vibrational fingerprints of each polymorph. A number of much weaker bands are observed at higher wavenumbers in the range shown in Figure 6.3. They are correctly reproduced in both energy and intensity by the DFT simulations, and correspond to intra-molecular modes, obviously common to both polymorph, as evidenced by comparison of the patterns shown in Figure 6.3.

Table 6.2: Wavenumbers of the six lowest energy vibrational modes of α and β thioindigo polymorphs calculated the at the RT structure, along with their symmetry assignments. The lattice phonon character of each mode is given by the sum of the squared rotational components around the molecular inertia axes. As the sums all yield $\approx 100\%$ (unity), the first six modes closely resemble rigid bodies librations.

α			β		
Sym	Calc (cm^{-1})	Lattice Phonon (%)	Sym	Calc (cm^{-1})	Lattice Phonon (%)
A_g	34.1	100	A_g	33.6	98
B_g	33.7	100	A_g	45.9	100
A_g	51.0	98	B_g	46.1	100
B_g	58.0	98	B_g	66.0	96
A_g	59.0	98	A_g	71.1	98
B_g	67.0	88	B_g	72.8	98

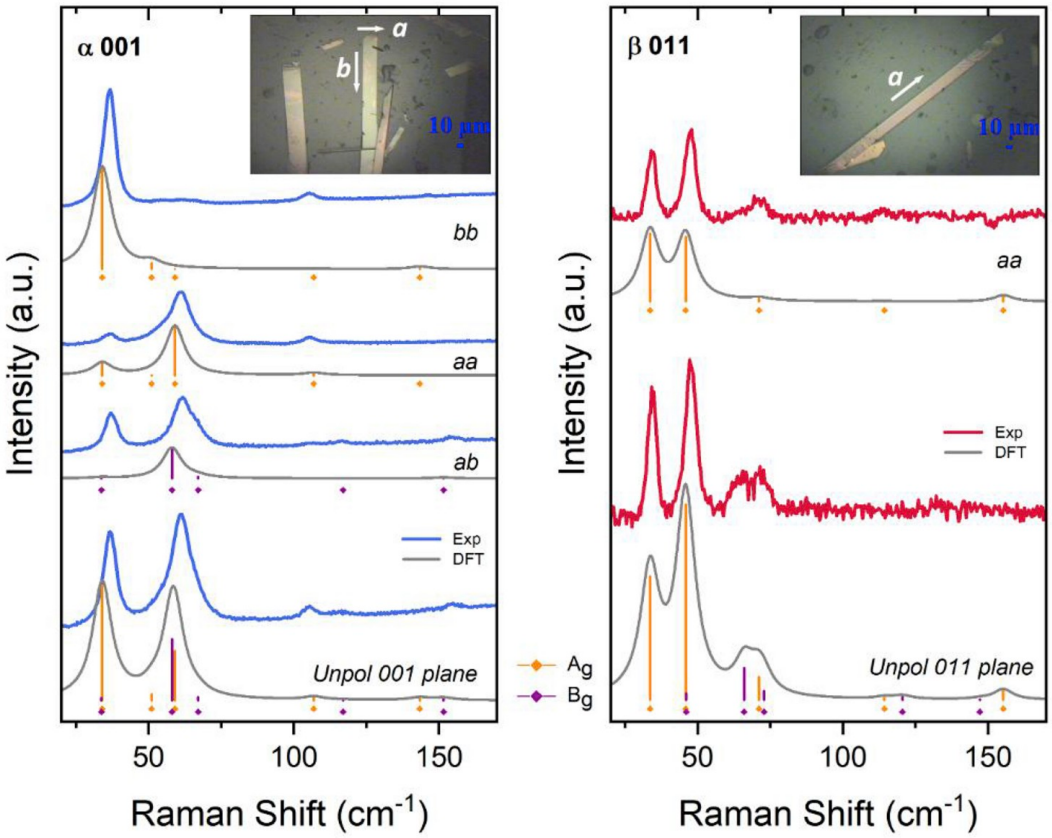

Figure 6.4: Polarized experimental and calculated Raman spectra for α- (left) and β-thioindigo (right) polymorphs. The corresponding crystal images show the crystallographic directions identified on the measured crystals (samples obtained by sublimation). Vertical bars of height proportional to the intensity of the mode identify the calculated values, with colour codes yellow and violet for modes of symmetry A_g and B_g, as indicated.

6.5 Crystal spectra

Depending on the orientation of the crystal with respect to the polarization of the incident and scattered light beams, the Raman intensities[121] for each given crystal vibrational mode q are determined by combinations of the components of the symmetric 3×3 tensor α, which expresses the vibrational modulation of the polarizability, i.e. the polarizability derivatives with respect to normal modes of vibration. To correlate the computed α components of the tensor to the intensities measured in the Raman experiment,

we need to transform the polarizability derivatives from the crystal reference frame ($\boldsymbol{a}$, $\boldsymbol{b}$, $\boldsymbol{c}$) to the laboratory frame. This is done by calculating the new tensor $R\alpha R^{\dagger}$, where R is the rotation matrix from one coordinate system to the other.

The orientation of a single crystal in the Raman experiment is generally specified by the Porto' notation,[122] which results simplified in the backscattering experimental setup, as the exciting and scattered beams always propagate in the Z direction of the laboratory frame. If the crystal is oriented so that at least one of its axes $\boldsymbol{a}$, $\boldsymbol{b}$, $\boldsymbol{c}$ (e.g. $\boldsymbol{a}$) is collinear with one of the laboratory axes X, Y, the only possible configurations in back scattering geometry are represented in the Porto's notation by $Z(aa)Z$ and $Z(aa_{\perp})Z$, where $a_{\perp}$ is the direction normal to $\boldsymbol{a}$. The first letter identifies the propagation direction of the excitation, while the last one refers to the observation direction. They will be dropped as redundant in the notation here adopted. The letters in parentheses specify the polarization directions of the exciting and scattered light, respectively. Besides, and more importantly, they identify the particular element of the Raman tensor responsible for the observed scattering.

The polarized Raman spectra (Figure 6.4) are recorded with input and output polarizers (i.e. polarizer on the excitation and analyser, respectively) aligned on the axes i and j of the laboratory reference frame. Thus vibrational modes have intensities $I_{ij} \propto \alpha_{ij}^2$, controlled by a single ij component of the polarizability tensor α.

By X-ray measurements, the scattering plane of the crystals of the image of figure is found to be the crystallographic face $\boldsymbol{ab}$ or (001), with $\boldsymbol{b}$ being the axis of fastest crystal growth, and $\boldsymbol{a}$ perpendicular to it. This information enables us to interpret the spectra measured with polarized light in backscattering geometry. The labels (aa), (bb) and (ab) of the Figure are used to indicate the polarization vectors of incident (first letter) and scattered (second letter) light in relation to the crystallographic axis of a sample oriented along its extinction directions.[123] The experiments are compared to the vdW-DFT D3–BJ polarized spectra calculated for the given face (001).

$$I_{aa@001} = \alpha_{aa}^2 \tag{6.4}$$

$$I_{ab@001} = \alpha_{ab}^2 \tag{6.5}$$

$$I_{bb@001} = \alpha_{bb}^2 \tag{6.6}$$

For the 001 face of polymorph α, the crystallographic axes $\boldsymbol{a}$ and $\boldsymbol{b}$ lie in the plane XY of the laboratory reference frame, with Z the light propagation direction. $\boldsymbol{b}$ (i.e. the shortest crystallographic axis) coincides with the needle crystal axis. In the measurements the sample is oriented with the needle axis either parallel or perpendicular to the polarization directions of the two polarizer. We then can directly correlate the intensities I_{aa}, I_{ab} and I_{bb} to the computed α_{ij} components of the polarizability tensor α_{aa}, α_{ab}, α_{bb} as following:

Due to the symmetry properties of the polarization matrix, the mode analysis indicates that the spectra (ab) and (ba) recorded in cross polarization must be identical and display only modes of B_g symmetry. On the contrary, spectra labelled (aa) or (bb) must give access to A_g modes only, but the intensities in the two spectral profiles depend on the probed matrix elements, (aa) or (bb), respectively. These considerations allow us, for instance, to solve into an A_g/B_g doublet the broad feature centred at 36 cm^{-1}. Also, we can interpret the shift of the maximum of the other broad feature, centred around 61 cm^{-1}, as depending on the presence of two unsolvable A_g modes in the spectra labelled as (aa) and (bb) and two B_g modes in the (ab) spectra. Such an analysis is strongly assisted by the computed values and can be safely performed given the striking agreement of our theoretical model with the experiment. Notably, in this treatment, more than in the symmetry assignment of each detected mode, the interest lies into linking a specific spectral feature, and its changing intensity in polarized light, to the anisotropy properties of the crystal and to its orientation, a crucial informa-

tion for the study of the films given below.

The unpolarized spectrum is given as a reference in the bottom part of the figure and describes a situation where the light beam impinges normal to the randomly oriented face (001) and no polarization discrimination is applied to the scattered light. The DFT intensities of thezs spectra are simulated by summing over a and $a_\perp$:

$$I_{\mathrm{UNPOL}} = I_{aa} + I_{aa_\perp} + I_{a_\perp a} + I_{a_\perp a_\perp} \tag{6.7}$$

where $I_{a_\perp a} = I_{aa_\perp}$.

In Figure 6.4, on the right, a similar analysis for the polarized Raman spectra of β-thioindigo is given for the single crystal pictured in the inset image. In the needle-like crystals of this form, the excitation beam of the Raman experiment impinges on the face (011), as probed by X-ray diffraction. The needle axis identifies with the crystallographic axis $\boldsymbol{a}$, and when the polarization vectors of incident and scattered light are both parallel to it (aa), only Raman-active modes of A_g symmetry are allowed. In cross polarization, the scattering perpendicular to a does not correspond to any principal component of the polarizability tensor and a mixture of A_g and B_g modes is expected. Therefore, we built the rotation matrix going into the new orthogonal axes given by the miller vector $\boldsymbol{c*}$ (i.e. Z), the $\boldsymbol{a}$ axis (already orthogonal to $\boldsymbol{c*}$) and their cross product (see Figure 6.5).

$$\phi = \frac{b}{\sqrt{c^2 \sin^2 \beta + b^2}} \quad R_a(\phi) = \begin{pmatrix} 1 & 0 & 0 \\ 0 & \cos\phi & -\sin\phi \\ 0 & \sin\phi & \cos\phi \end{pmatrix} \quad \alpha_{\mathrm{LAB}} = R_a \, \alpha_{\mathrm{DFT}} \, R_a^\top$$

By transforming the Raman tensor, we thus find:

$$I_{aa@011} = \alpha_{aa}^2 \tag{6.8}$$

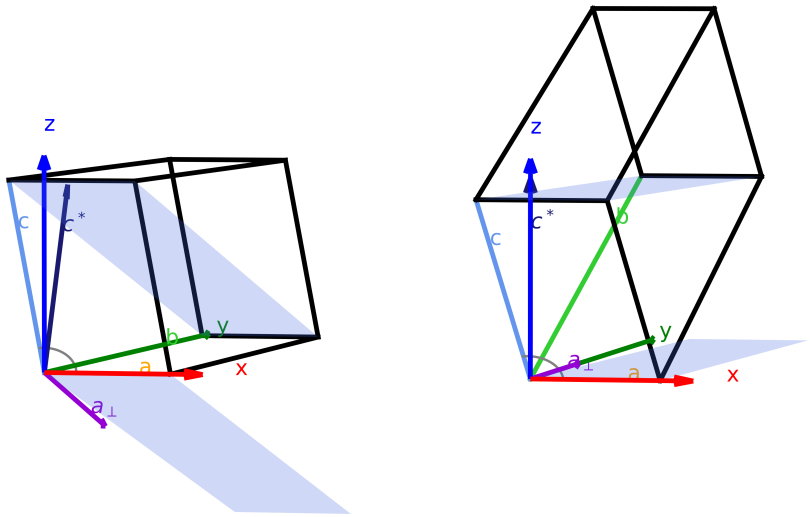

Figure 6.5: Alignment of crystallographic cell with respect to cartertesian frame before (left) and after (right) the rotation. Applying the rotation, the miller plane (011) lies on xy plane, perpendicularly to z that is the experimental measurement direction.

$$I_{aa_\perp@011} = \frac{2(b\ \alpha_{ab} - c\ \sin\beta\ \alpha_{az})^2}{2(b^2 + c^2(1 - \cos 2\beta)} \tag{6.9}$$

$$I_{a_\perp a_\perp@011} = \frac{[2b^2\alpha_{bb} - 4bc\sin\beta\ \alpha_{bz} + c^2(1 - \cos 2\beta)\alpha_{zz}]^2}{2(b^2 + c^2 - c^2\ \cos 2\beta)^2} \tag{6.10}$$

6.6 Film

BAMS growth method is an excellent technique for the film fabrication, as it has been found effective in controlling film morphology and polymorphism by allowing a finer control of the crystallization kinetics and thermodynamics.[118–120,124,125]

Figure 6.6 (top left) gives the scheme of the BAMS method which was applied for the preparation of high quality films. The optical images in polarized light under crossed polarizers suggest the presence of a macroscopic alignment of the domains along the shearing direction. Finally, the XRD pattern of the film reveals the presence of the polymorph α only. The contact plane corresponds to the crystal face ***ab***, with the thioindigo molecules standing at the interface, and the long molecular axis forming an angle of

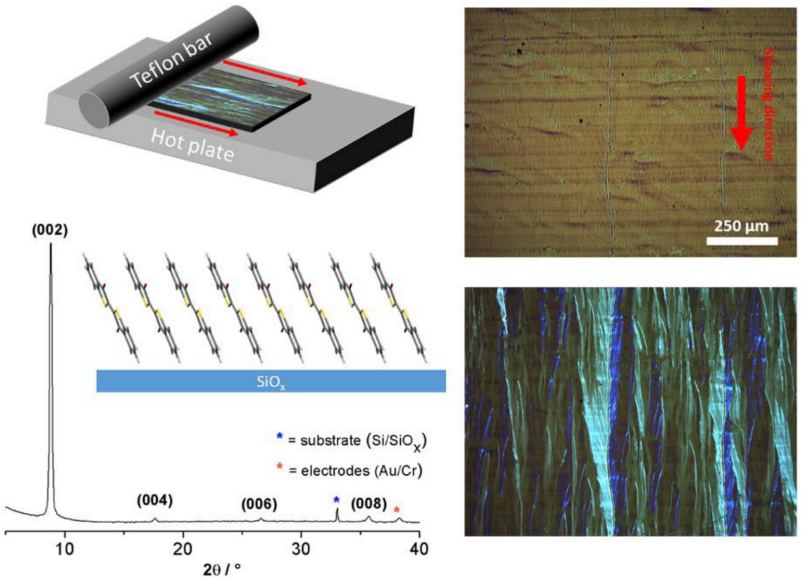

Figure 6.6: Scheme of the BAMS (top left), XRD pattern of the anisole solution sheared film with the representation of the molecule arrangements (bottom left) and optical image of the sample in bright field (top right) and in cross polarization (bottom right).

22° with the normal to the substrate, as shown in the Figure.

To gain access to the other crystallographic directions of the BAMS film, rotating grazing incidence X-ray diffraction measurements were used. The results show that the film clearly displays a preferential in-plane alignment. In particular, the ***a*** axis is found to be parallel to the shearing direction. The optical images in polarized light under crossed polarizers suggest the presence of a macroscopic alignment of the domains along the shearing direction and reveals that adjacent crystals are slightly inclined in their growth direction, which is often observed when using shearing methods on isotropic surface. Using the rotating GIXD this variation is determined to be about 20°. Improvement to the overall growth direction might be obtained by using structured surfaces as demonstrated for similar sample preparations.[126]

In the Raman polarized measurements, shown in Figure 6.7, the film was thus oriented either parallel or perpendicular to the shearing direction, while the polarizations of the exciting and scattered field were set as shown in the Figure.

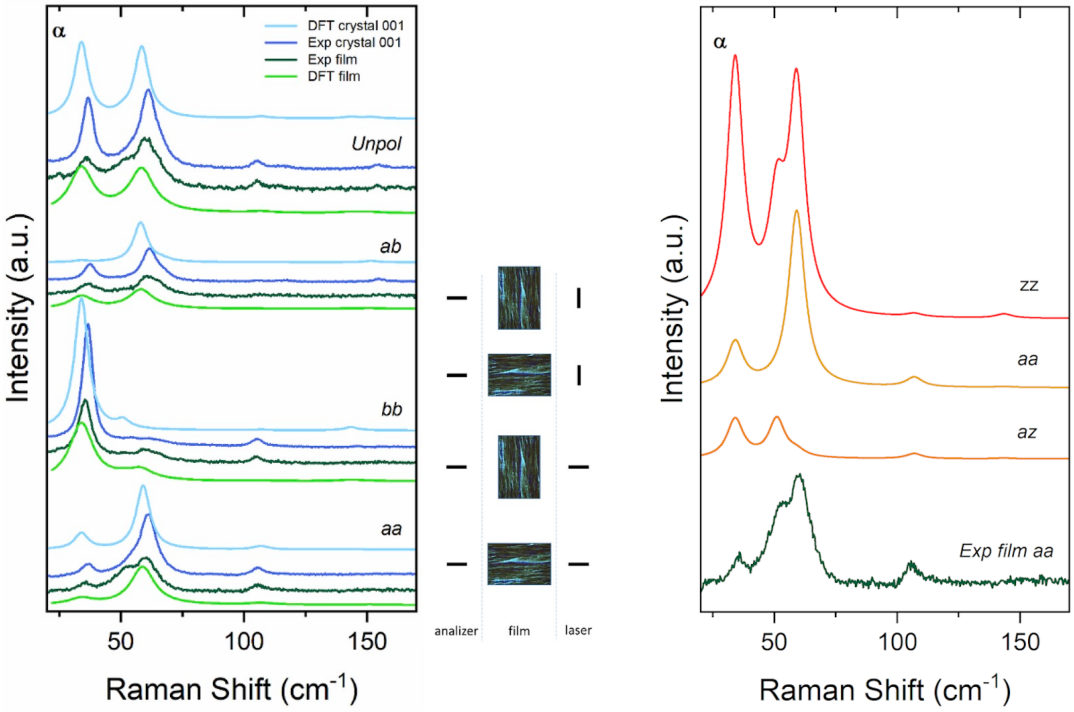

Figure 6.7: Left: Polarized Lattice Phonon Raman Spectra of α-thioindigo film obtained by BAMS from anisole solution. The sample has been aligned with respect to the shearing direction as shown in the right hand side of the Figure, where the black bars give the direction of polarization for the exciting laser light and for scattered light as selected by the analyser. The film spectra are compared to the corresponding ones measured on the (100) face of a single crystal, to the DFT simulations for the same face and to the spectra resulting from the fit where a Gaussian distribution of crystal orientations about the shearing direction is assumed.
Right: Experimental polarized Raman spectra of BAMS α-thiondigo film recorded in the aa configuration (i.e. excitation light and collected scattered light polarization parallel to the shearing direction, found to correspond to the a crystallographic direction) compared to simulated DFT polarized Raman spectra

The outcome of Figure 6.7 is quite remarkable, because all polarized Raman profiles of the film appear as those of the (001) face of the single crystal of the α-polymorph of Figure 6.4, thus indicating a high degree of iso-orientation of the crystal domains, with the $\boldsymbol{a}$ axis aligned with the shearing direction. To confirm this, the experimental profiles in the Figure are compared to the

corresponding DFT calculated polarized spectra. Specifically, the diffraction patterns of the film identify the molecular organization on the substrate, and the polarized Raman spectra also show that this organization is ordered and iso-oriented microscopically, as though the deposited films behaved like a single crystal. Even though the responses of a single crystal perfect lattice and of a film are physically different, what is here observed shows a matching that fully comply with the expectations given by the BAMS deposition of obtaining well oriented films.

Finally, Figure 6.7 also demonstrates how the results of the DFT simulated Raman spectra of oriented crystals can be employed to fit the experimental data to account for the spread of the ***ab*** plane alignment on the shearing direction, already probed by the rotating GIXD measurements. The approach consists in fitting the experiments to a superposition of spectra calculated for single crystals oriented with a Gaussian distribution of angles around the shearing direction. In the films deposited by the BAMS method, the phase α is present with contact plane (001), which coincides with the XY plane of the laboratory reference plane. In a Raman experiment in polarized light, input and output polarizers are set either parallel or perpendicular to the reference laboratory frame axes. Thus, for a crystal randomly oriented in the XY plane, we find the following expression for the intensities:

$$I_{aa}(\theta) = (\alpha_{aa}\cos^2\theta + \alpha_{ab}\sin 2\theta + \alpha_{bb}\sin^2\theta)^2 \tag{6.11}$$

$$I_{bb}(\theta) = (\alpha_{aa}\sin^2\theta - \alpha_{ab}\sin 2\theta + \alpha_{bb}\cos^2\theta)^2 \tag{6.12}$$

$$I_{ab}(\theta) = (-\alpha_{aa}\sin 2\theta + 2\alpha_{ab}\cos 2\theta + \alpha_{bb}\sin 2\theta)^2/4 \tag{6.13}$$

For the value $\theta_0 = 0$, we recover the expression already found for a single crystal exposing the (001) face and aligned along the polarization directions as described above.

The shearing method employed to deposit the film is found to direct the

crystal growth so that the crystallographic direction $\boldsymbol{a}$ is aligned with the shearing direction, with a certain degree of angular spread. To simulate this and determine the spread, we assume a Gaussian distribution of crystal orientations, centered on $\theta_0 = 0$:

$$G(\theta, \sigma) = \frac{e^{-\frac{\theta^2}{2\sigma^2}}}{\sigma\sqrt{2\pi}} \tag{6.14}$$

The resulting intensities can be obtained by integration:

$$\bar{I}(\sigma) = \int_{-\infty}^{\infty} I(\theta) G(\theta, \sigma) d\theta \tag{6.15}$$

The formulas computed for each polarization geometry are:

$$\begin{aligned}\bar{I}_{aa}(\sigma) = [&-4\alpha_{ab}^2 + (\alpha_{aa} - \alpha_{bb})^2 \\ &+ (\alpha_{aa} + \alpha_{bb})(\alpha_{aa} - \alpha_{bb})e^{6\sigma^2} + \\ &(3\alpha_{aa}^2 + 4\alpha_{ab}^2 + 2\alpha_{aa}\alpha_{bb} + 3\alpha_{bb}^2)e^{8\sigma^2}]\frac{1}{8e^{8\sigma^2}}\end{aligned} \tag{6.16}$$

$$\begin{aligned}\bar{I}_{bb}(\sigma) = [&-4\alpha_{ab}^2 + (\alpha_{aa} - \alpha_{bb})^2 \\ &- (\alpha_{aa} + \alpha_{bb})(\alpha_{aa} - \alpha_{bb})e^{6\sigma^2} + \\ &(3\alpha_{aa}^2 + 4\alpha_{ab}^2 + 2\alpha_{aa}\alpha_{bb} + 3\alpha_{bb}^2)e^{8\sigma^2}]\frac{1}{8e^{8\sigma^2}}\end{aligned} \tag{6.17}$$

$$\bar{I}_{ab}(\sigma) = [8\alpha_{ab}^2 \cosh 4\sigma^2 + (\alpha_{aa} - \alpha_{bb})^2 \sinh 4\sigma^2]\frac{1}{4e^{4\sigma^2}} \tag{6.18}$$

It is quite straightforward to verify that the calculation of $\lim_{\sigma\to 0} \bar{I}_{ij}(\sigma)$ already found for a single aligned crystal. All the intensities turn out to be functions of only the standard deviation σ of the distribution. Thus, by fitting the polarized spectra to the corresponding expressions, we can find the

σ width of 21° which better reproduces the experiments, as reported in the main text.

To fully explain the Raman spectral features observed for the BAMS films and in agreement with the information provided by GIXD, we must allow for a certain degree of mosaicity in the sample.

This can be accounted for by considering a small contribution of planes different from (001). For instance, the polarized Raman spectrum labelled (aa) in Figure 6.7 of the main text and in Figure 6.7, contains a band at about 55 cm^{-1} which is reproduced by allowing a tilt of the (001) crystal plane with respect to the surface, thus probing polarization components indicated as z in the Figure. It was found that even a negligible tilt has in fact a relevant effect on the spectrum.

The best fit yields for the distribution a standard deviation $\sigma = 21°$, which is in excellent agreement with the GIXD result. A slight mismatch between experiments and calculations can be accounted for by some mosaicity of the sample, exposing faces different from the (001). To summarize, the films obtained with the BAMS procedure showed the presence of well oriented α-phase only. Examples of surfaces stabilizing selectively a polymorphic modification are now numerous,[23,24,127–131] but less common is combination of selectivity and a high degree of iso-orientation.

6.7 Conclusions

We have dealt with the polymorphism of thioindigo, with the specific purpose of defining the phases present in growths at solid interfaces. This involved the structural and spectroscopic characterization of its bulk phases. For these we have found that, similarly to indigo, it is the polymorph previously thought to be the less stable (i.e. the β form), which is instead present in the commercial product and is obtained in most of the common growth methods, such as sublimation or solvent recrystallization. The α form can be easily detected on surfaces, where it grows together with β without forming

mixed phases. Due to the close energies of the two phases, DFT calculations cannot provide information on their relative stability, but experimental clues in our work and from the literature suggest that the α phase might be metastable at room temperature. The piece of information we gather from the present data is that the α polymorph is however stabilized in growths on a substrate, to the point of becoming the only phase present. The effort of searching for substrate-mediated crystal structures has paved the way to a new approach to address the problem of polymorphism, and the capability of substrates to tune nucleation has been addressed, although the underlying mechanisms are not really understood. The effect of the substrate can be that of a template for molecular deposition[130] or, even more interestingly, the subtle interplay of weak interactions at the interface may eventually lead to fully new molecular arrangements called surface selected polymorphs. Finally, the surface may stabilize a form otherwise metastable in the conditions of growth, and this appears to be the case with thioindigo.

In our study we have applied a deposition method (BAMS), which intrinsically supplies a control of the molecular alignment, on thioindigo dissolved in anisole, obtaining films of the pure α phase, macroscopically oriented along the $\boldsymbol{a}$ axis, which represents the shearing direction of the solution deposited on the hot plate. Polarized Raman and GIXD results confirm the high isoorientation of the film structures, reminiscent of that of a (001) plane of the single crystal. Given the surface selectivity for this phase, it is likely that the charge transport performances reported for devises fabricated with thioindigo must be ascribed to this polymorph.

Chapter 7

Polymorph recognition: Tyrian purple

7.1 Introduction

Recently, structural studies in the thin-film phase of 6,6′-dibromoindigo (Figure 7.1), the main component of the Tyrian purple dye, revealed the presence of surface-induced structures.[132,133] This finding is important, as the system is a good candidate for applications in organic electronics, and knowledge of the film structure is needed to explain the physical properties of the conducting layer. In this subsection, combining the results of low-frequency Raman spectroscopy, X-ray diffraction, and accurate density-functional theory (DFT) calculations of the vibrational properties of the proposed surface induced structures, we suggest that a newly detected 6,6′-dibromoindigo bulk crystal form is structurally closely related to the surface-induced modifica-

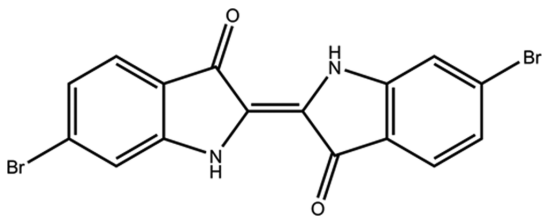

Figure 7.1: Molecular structure of 6,6′-dibromoindigo (6,6′-dibromo1H,1′H-[2,2′]biindolylidene-3,3′-dione).

tions. Thus, 6,6′-dibromoindigo behavior shows similarities and differences at the same time, with respect to other investigated systems.

The material described in this Chapter corresponds to the paper entitled "*In search of surface-induced crystal structures: The case of tyrian purple*", by Pandolfi, Rivalta, Salzillo, myself, D'Agostino, Della Valle, Brillante and Venuti.[27] My contribution in this work was the calculation of Raman spectra of the two thioindigo bulk structures and all the possible modifications found on films. The evident differences observed in the DFT phonon region confirmed how sensitive this technique can be even for small structural deviations.

7.2 State of the art

Two structures are contained in the CSD repository with refcode DIBRING, referring to a two structural works on this compound.[134,135] Both report the same bulk monoclinic polymorph with two molecules per cell ($Z = 2$), and it corresponds to the one named Form I in our work.[27] Crystal data and refinement details can be found in Table 7.1. These structures are very similar to either of the monoclinic indigo polymorphs,[87,95] the molecular arrangement in these systems is driven by the formation of strong intermolecular hydrogen and halogen bonds as well as by $\pi - \pi$ stacking, as shown in Figure 7.2. When molecular geometries of indigo and 6,6′-dibromoindigo are

Table 7.1: Crystal data and refinement details for crystalline 6,6'-Dibromoindigo Form I and Form II.
(*a*) Resel, R. Private Communication

System	Space Group	Z	*a* (Å)	*b* (Å)	*c* (Å)	α (°)	β (°)	γ (°)	Volume (Å^3)
DBRING[134]	$P2_1/a$	2	11.50	4.85	4.85	90	104.0	90	681.89
DBRING01[135]	$P2_1/c$	2	12.609(16)	4.842(2)	11.611(12)	90	104.42(6)	90	686.551
FORM I[27]	$P2_1/c$	2	12.5512(7)	4.8510(3)	11.5644(7)	90	103.935(6)	90	683.39(7)
SIP A[(a)]	$P\bar{1}$	1	3.86	5.83	14.86	81.8	85.8	87.1	??
SIP B[(a)]	$P\bar{1}$	1	3.84	6.00	14.67	86.0	87.0	87.0	??
FORM II[27]	$P\bar{1}$	1	3.783(1)	5.826(2)	15.32(1)	82.01(3)	85.32(4)	86.32(5)	341.80(5)

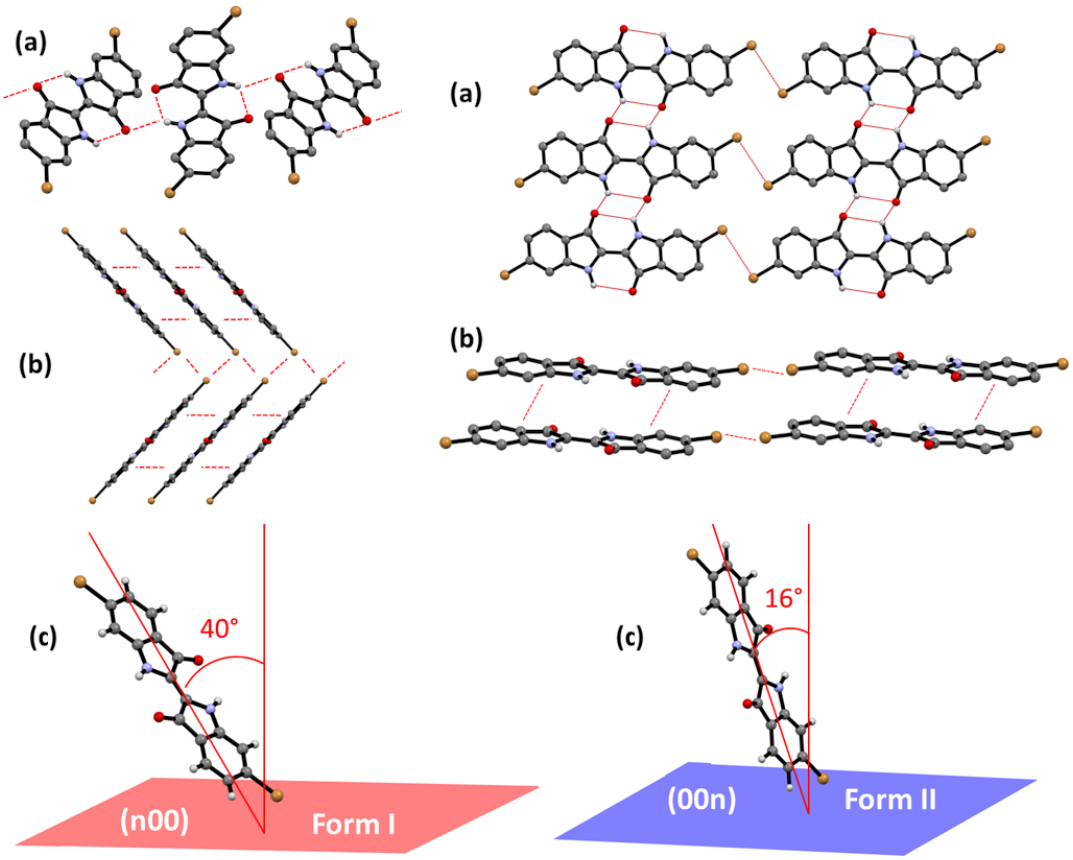

Figure 7.2: Intermolecular interactions detected in crystalline 6,6′dibromoindigo Form I (left) and Form II (right).
(left a) Inter-intramolecular hydrogen bonds $d_{N_{NH}\cdots O_{CO}}$: 2.938(4) and 2.916(4) Å; halogen bonds $d_{Br\cdots Br}$: 3.749(8) Å; $angle_{Br-Br-Br}$: 73.01(1) - 106.99(1)°; (left b) π-stacking: 3.4 Å.
(right a) Inter-intramolecular hydrogen bonds $d_{N_{NH}\cdots O_{CO}}$: 2.475(1) and 3.201(9) Å; halogen bonds $d_{Br\cdots Br}$: 3.749(8) Å; $angle_{Br-Br-Br}$: 86.34(1)°; (right b) π-stacking: 3.797(3) Å.
(c) Orientation of molecules of 6,6′dibromoindigo Form I and Form II with respect to the appropriate Miller planes.

compared, it is evident how bromination does not substantially modify the parent molecule ring system and the interaction pattern.

Various slightly different thin-film phases of 6,6′-dibromoindigo were iden-

Table 7.2: Comparison between experimental and vdW-DFT D3–BJ relaxed structures. $RMSD_N$ ($N = 18$ for Form I, 16 otherwise) and molecular tilt angles are reported. The agreement between these structural parameters indicates that all the vdW-DFT D3–BJ minima are close to the corresponding experimental structure. The $RMSD_{16}$ have been calculated between all vdW-DFT D3–BJ relexed structures for Form II. Due to the symmetry of the matrix, only the upper triangular half is reported. The small RMSD values confirm that all these structures belong to the same cluster.

Structure	$RMSD_N$ (Å)	$angle_{exp}$ (°)	$angle_{DFT}$ (°)
Form I	0.097	39.7	40.2
SIP A	0.164	20.7	24.3
SIP B	0.151	28.5	26.0
Form II	0.263	15.8	15.9

$RMSD_{16}$ (Å)	SIP A	SIP B	Form II
SIP A	0.000	0.136	0.255
SIP B	-	0.000	0.328
Form II	-	-	0.000

tified on a number of substrates, and one of the structures detected on silicon oxide was solved in a combined theoretical and experimental approach,[132,133] which used grazing incidence X-ray diffraction (GIXD) and molecular dynamics (MD) simulations. The two resulting structures were provided by Resel, R. (Private Communication) and are named SIP A and SIP B, respectively. Another very similar structure has been obtained in the bulk phase in our work[27], by refining the polycrystalline powder X-ray data, starting from the SIP structure A. All these structures are characterized by a triclinic cell with $Z = 1$ and symmetry $P\bar{1}$. Crystal data and refinement details can be found in Table 7.1. As shown in Figure 7.2, this new 6,6′-dibromoindigo bulk crystalline phase features a molecular arrangement quite different from that of Form I, even though it still displays strong intermolecular hydrogen and halogen bonds as well as $\pi - \pi$ stacking.

vdW-DFT D3–BJ simulations[1] were performed for the two structures ob-

[1] `VASP` with the PBE exchange correlation functional, PAW pseudopotentials and D3–BJ pairwise correction were performed for all the structures. Energy convergence was

tained in our work[27] and for the two SIPs. vdW-DFT D3–BJ computed versus experimental $RMSD_N$ distances at the minimum energy structures are reported in Table 7.2, ranging from 0.10 Å for Form I to 0.27 for Form II. $RMSD_{16}$ between all DFT minima of Form II (Table 7.2) confirmed that these structures are really close.

7.3 Crystallization and X-ray diffraction

Several crystallization techniques has been used to prepare the reference sample and films and analyzed by X-ray diffraction (for single crystals) or GIXD (for films) in the experimental part of the work.

(i) The commercial powder and the subilmed crystalline powder have a varying polymorph composition.

(ii) PVT (Physical Vapor Transport) yielded single crystal platelets of the known bulk Form I (see Figure 7.3 left).

(iii) Dropcasting technique yielded microcrystals which two different characteristic shapes of plates and needles, respectively blue and pale purple under a polarizer microscope. This observation and X-ray diffraction confirm the occurrence of both polymorphs in these samples (see Figure 7.3 right).

achieved for the various structures as follows: a plane wave cutoff of 800 eV proved to be adequate in combination with 2 × 5 × 2 Monkhorst-Pack ***k***-point sampling for Form I and 6 × 4 × 2 sampling for the SIP modifications. An increase in the cutoff energy from 800 to 1200 eV caused energy variations slightly larger than 1 meV/ atom, while the denser ***k***-point samplings of 4 × 10 × 4 for Form I and 10 × 7 × 3 for the SIPs gave energy changes around 0.1 meV/atom. Less dense ***k***-point samplings actually yield the same accuracy. Atomic coordinates (or atomic coordinates and cell parameters) were fully relaxed, halting when residual forces fell below 1 meV/Å, using the GADGET package. For both energy cutoffs and ***k***-point sampling, energy differences between polymorphs converge faster than absolute energies to within 0.04 meV/atom.

7.4 Raman Phonon Form I

Figure 7.4a shows the Raman spectrum of a single crystal of Form I obtained by the PVT method and measured at an excitation wavelength of 514.5 nm.

The wavenumber range (10–150 cm^{-1}) reported in the figure allows for the detection of both the lattice phonon vibrations, which represent the fingerprint of the crystal structure, and intramolecular low-energy modes. A detailed vibrational assignment of the spectrum of Form I over this range can be made by means of experiments and calculations[2] in polarized light and will be given below. In Figure 7.4a, the spectrum of the single crystal is compared with those of the microcrystalline powders of both the commercial

[2]Vibrational modes, were computed at the experimentally determined unit cell volumes through the force constants obtained with `Phonopy`. Polarizability tensors α for each crystal mode were obtained using the Python program vasp_raman.py.

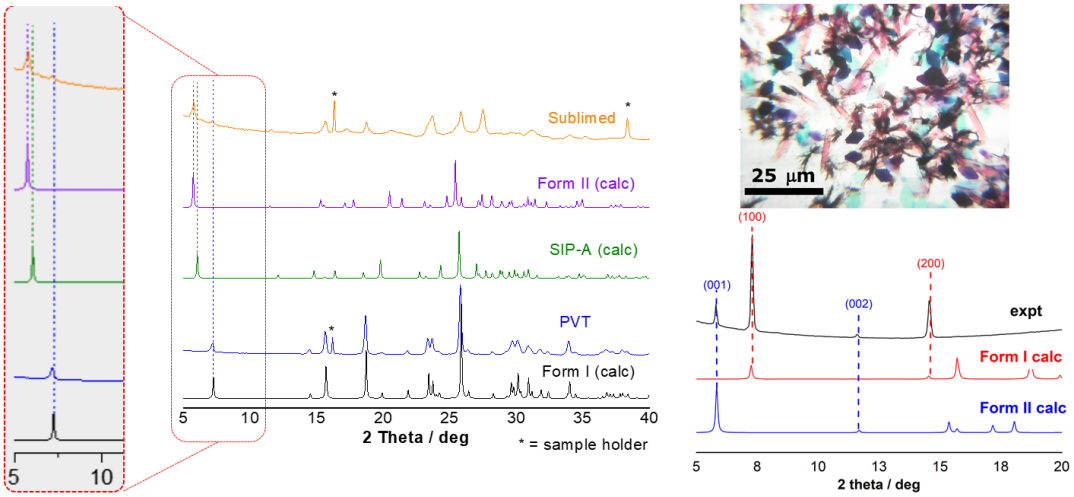

Figure 7.3: Left: Comparison between calculated powder XRD patterns for 6,6'-Dibromoindigo: Form I , SIP-A, and Form II, and the experimental ones recorded on two different samples obtained from physical vapor transport (PVT) and from sublimation.
Top right: picture taken under polarized light of the crystalline materials grown on a glass surface. Bottom right: comparison between the XRD patterns recorded on a polycrystalline sample of 6,6′-dibromoindigo grown on a glass surface and the calculated ones for Form I and Form II.

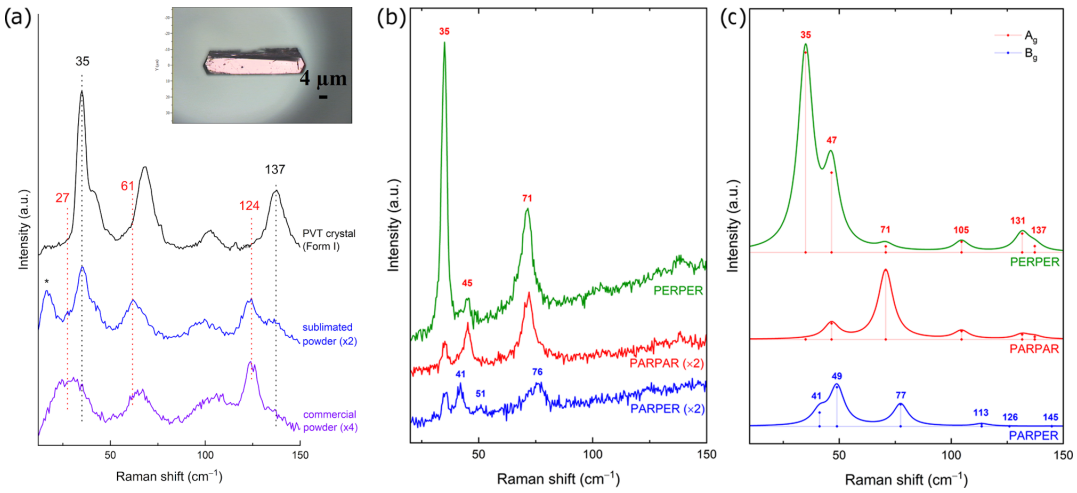

Figure 7.4: (a) Raman spectra of a single crystal of 6,6′-dibromoindigo Form I obtained by the PVT method (inset), of a sublimated and of the commercial powders in the wavenumber range of the lattice phonon modes. $\lambda_{exc} = 514.5$ nm. The peak with an asterisk is an experimental artifact. (b) Raman spectrum in polarized light of a single crystal of 6,6′-dibromoindigo Form I obtained by the PVT method, in the wavenumber range of the lattice phonon modes, with $\lambda_{exc} = 647.1$ nm. (c) vdW-DFT D3–BJ Raman spectra for Form I, simulated in the experimental conditions. For the meaning of labels, see the text.

product and the sample purified by sublimation.

In the powders the appearance of a new vibrational pattern is clearly detectable, even in the presence of some of the strongest bands of Form I. Some features are altogether new, like for instance the signal centered at around 27 cm^{-1} in the commercial product, which certainly originates from the convolution of more bands, or the bands observed at 61 and 124 cm^{-1}, clearly identified in all the powders. Thus, this is an unambiguous proof that both the commercial product and the sublimed material, in addition to the known Form I, contain a second structural modification that will be, in the following, identified as a new form, named from here on as Form II.

To probe spectroscopically the existence of a second crystal modification and in view of the analyses on surface grown crystallites (vide infra), it

was necessary to identify and assign the bands of Form I in the diagnostic low-wavenumber region. This was done with the help of measurements and vdW-DFT D3–BJ vibrational calculations in polarized light, a combination which has proved to be effective for this task.[31]

Figure 7.4b reports the spectra of a thin platelet of 6,6′dibromoindigo, aligned along the extinction direction and perpendicular to it. The excitation laser light was directed normal to the crystal face (100), as determined by XRD, and was linearly polarized in the same plane. Note that one of the crystal extinction directions necessarily coincides with the crystallographic b axis of the monoclinic system.

The $\boldsymbol{k} = 0$ Raman-active modes of a $P2_1/c$ monoclinic system are of either A_g or B_g symmetry. If the electric vectors of the exciting and scattered electromagnetic waves both vibrate parallel or perpendicular to the b axis, only A_g modes are observed (PARPAR and PERPER labels in the figure); when the scattered wave is collected with polarization perpendicular to the excitation, only B_g modes are instead detected (PARPER label in the figure). As confirmed by the calculations and similar to the parent system indigo, the lattice vibrational modes of 6,6′-dibromoindigo can be neatly separated into six lattice phonon modes, corresponding to pure translations and rotations of the rigid molecules, and intramolecular modes (rigid-body approximation). The former modes can be used to identify the lattice of Form I. The latter ones can be mapped onto the vibrations of the isolated molecule, bearing in mind that each molecular Raman-active mode splits into an A_g + B_g doublet in the crystal, arising from the factor group splitting. In turn, 6,6′-dibromoindigo intramolecular vibrations strongly correlate with the indigo's modes, which we have previously analyzed and assigned.[28] Polarized spectra have allowed us to solve the vibrational pattern corresponding to the six lattice phonon bands ($3A_g$ + $3B_g$) that characterize Form I, with the calculations supporting the assignments, as shown in Figure 7.4c and Table 7.3, where experimental and computed values are given. The table also reports the data on Form II, which will be discussed later on.

The only other bands detected and predicted for Form I over this interval are the strong ones at 103 and 137 cm^{-1} (vdW-DFT D3–BJ values at

104.6 and 137.3 cm^{-1}, respectively). Low-wavenumber intramolecular modes of unexpectedly high intensities were also observed in indigo and found to be good markers for polymorph identification, as they are affected by the specific hydrogen bond pattern of the given structure.[28]

Table 7.3: Experimental (Form I and II) and Calculated (Form I, II, and SIPs) Wavenumbers of the Lowest Energy Modes of 6,6′-Dibromoindigo Crystals. The "rotation" percentage is the total calculated squared rotational component $r_x^2 + r_y^2 + r_z^2$ around the three inertia axes x, y, and z, which for purely rotational "g" modes corresponds to the percentage of the lattice phonon character. The difference to 100 is the percentage of the intramolecular character of that mode. The three values reported for the calculations on Form II are obtained for the two different SIPs A and B and for the structure of Form II obtained in this work, in the given order.

Form I sym	Form I exp (cm^{-1})	Form I calc (cm^{-1})	Form I rotation (%)	Form II sym	Form II exp (cm^{-1})	SIPs and Form II calc (cm^{-1})			SIPs and Form II rotation (%)		
A_g	35.0	35.0	100	A_g	21.0	29.2	22.3	30.8	99	100	99
B_g	41.0	41.2	100	A_g	39.0	40.9	27.8	37.3	98	99	98
A_g	45.0	46.6	99	A_g	61.0	71.9	73.0	65.9	61	64	73
B_g	51.0	49.0	99	A_g	98.0	112.2	107.1	100.8	24	21	18
A_g	71.0	70.7	95	A_g	124.0	133.6	130.5	127.2	1	5	0
B_g	76.0	77.4	87	A_g		145.6	144.5	138.4	15	8	9
A_g	103.0	104.6	4								
B_g		113.6	13								
B_g	124	126.0	0								
A_g		131.6	0								
A_g	137.0	137.3	0								
B_g		144.9	0								

7.5 Raman Phonon Form II

Figure 7.5a reports the Raman spectra collected on each of the two morphologies at low wavenumbers (10–150 cm^{-1}). Namely, the blue trace is collected on a plate, which appears blue in the image under the polarizing microscope, and corresponds to that of Form I, despite the morphology being different from the PVT-grown sample. The red trace is collected on a needle oriented along its axis, which is found to coincide with an extinction direction. For this sample, three bands are observed in the range of the lattice

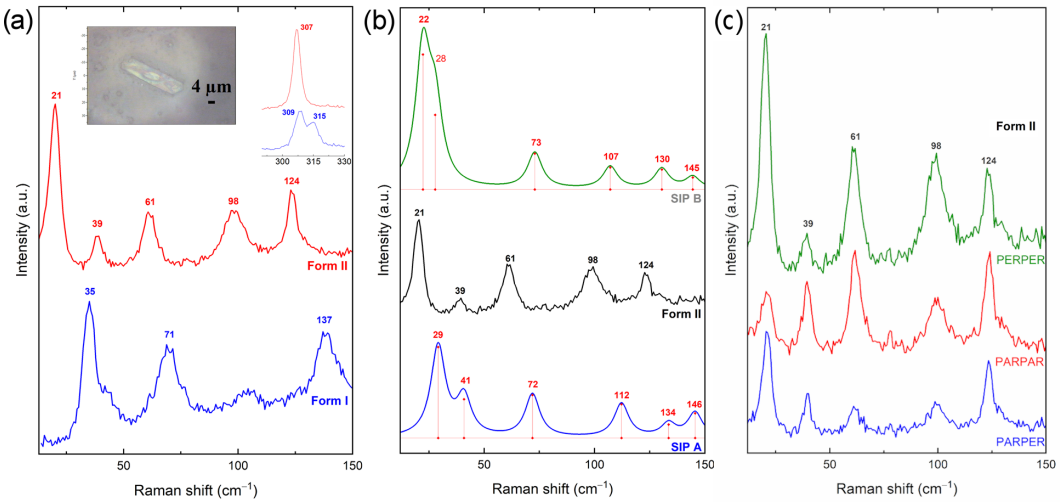

Figure 7.5: Raman spectra, in the wavenumber range of the lattice phonon modes for 6,6′-dibromoindigo crystallites grown after drop-casting: (a) the blue trace corresponds to the spectrum of specimens with a plate morphology and the red trace to the needlelike crystals (inset). (b) The spectrum of the needle is compared to the spectra simulated for the proposed SIP crystal structures, assuming in all cases *ab* as the scattering face. $\lambda_{exc} = 514.5$ nm. (c) Raman spectrum in polarized light of 6,6'-Dibromoindigo Form II in the wavenumber range of the lattice phonon modes.

phonons, at 21, 39, and 61 cm^{-1}, accompanied by two more peaks at 98 and 124 cm^{-1}, which have also been detected in the powder. A comparison with the spectrum of Form I also highlights the absence of the strong band at 137 cm^{-1}, which is a relevant feature of Form I. This yields a lattice phonon and a lowenergy intramolecular mode of the Raman spectrum, which unequivocally identifies the Form II crystal structure, as confirmed by the comparison with the vdW-DFT D3–BJ calculated wavenumbers reported in Table 7.3 for this modification. Notably, the measurements in polarized light given in Figure 7.5 do not reveal any more bands over this range, displaying simply moderate relative intensity changes.

In Figure 7.5b, the experimental Raman spectrum of Form II is compared with the DFT D3–BJ-simulated spectra of two 6,6′dibromoindigo triclinic SIPs, while Table 7.3 gives the values of the corresponding peak wavenum-

bers. It is worth mentioning that the considered SIP structures are very similar to each other and indeed similar to the Form II of our work,[27] as demonstrated by the RMSD_N values given in Table 7.2, which identify them as clearly clustering together.

Given the $P\bar{1}$ crystal symmetry of the triclinic system, the Raman experiment can detect only modes of A_g symmetry, and with one molecule per unit cell, only three of these are expected to have the predominant character of lattice phonons in the rigid-body approximation. The eigenvector analysis given in Table 7.3 for these modes confirms this deduction. The spectra of Figure 7.5b have been simulated for a crystal lying on the (001) face, excited by an electric vector vibrating on the same plane, so as to reproduce the orientation suggested by the experiments for the drop-cast samples.

The general agreement between experimental and simulated vibrational patterns and a direct comparison between the wavenumber values of Table 7.3 hint again at the similarities between Form II and the SIP structures. In weighing such similarities, some factors should be taken into consideration. First, the simulations have been performed on structures that are the best fits to experimental GIXD data, with an expected margin of error larger than what is found when solving a structure from a single-crystal analysis; indeed, small structural variations may lead to large differences in the dynamics of the system, i.e., in its vibrational frequencies. Second, the Form II bulk structure and the SIPs reported in References [132, 133] are not necessarily coincident, as the latter have been detected in thin films. Rather, they could be viewed as a cluster of structures related to a bulk form, possibly through distortion.

7.6 Raman Intramolecular Spectra

At higher energies, the spectra of Forms I and II also differ in an important detail (shown in the inset of Figure 7.3), which allows us to gather information about the symmetry of their respective unit cells. In Form I, the band at 309 cm^{-1} and its shoulder at 315 cm^{-1} can be solved by polarized

measurements (Figure 7.6) into the components of a doublet arising from the factor group splitting, with A_g and B_g symmetries, respectively. Note that the intermolecular coupling of the intramolecular modes is so weak in comparison to their energies that the resulting split is generally observed only for a few low-frequency vibrations, as in this case. Its detection, though, is worth noting here, as it represents the spectroscopic evidence of a centrosymmetric monoclinic lattice with two molecules per cell for Form I. On the contrary, the absence of the split for Form II is in agreement with the presence of just one molecule per unit cell. To dispel any doubt about the chemical identity of the new Form II, its spectrum in the wavenumber range of 200–2000 cm^{-1} has been compared in Figure 7.6 with the spectra of Form I and of the powder. Except for some band splitting/shifting, all of these spectra are virtually identical, in agreement with the assumption that we are dealing with packing polymorphs of the same compound.

Altogether, the findings of both the XRD and Raman investigations confirm that Form II is a centrosymmetric structure with only one molecule per cell, which is compatible with a $P\overline{1}$ crystal symmetry. The key point is that Form II is present in both the samples obtained by drop-casting and the commercial and sublimed powders, in both cases concomitantly with Form I.

7.7 Form II stability

To further probe the relationship between the 6,6′-dibromoindigo phases, a crystallite identified by its needle shape and spectrum as Form II was subjected to slow heating and was observed to transform into Form I at a temperature around 210°C, as clearly demonstrated by the Raman data of Figure 7.7. At around the same temperature, crystallites of Form II appearing pinkish in polarized light underwent quite a sudden change of color, becoming blue as the plates of Form I. The transition seems to be irreversible, as the spectrum (and the color) of Form II cannot be recovered on cooling. This result, indeed, is in very good agreement with what was reported in

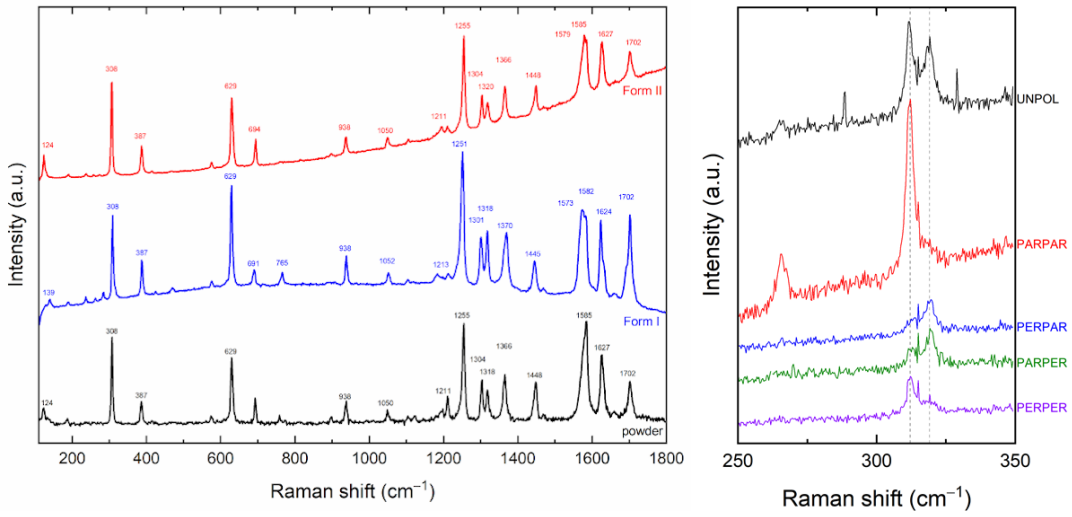

Figure 7.6: Left: spectra in the wavenumber range 100–1800 cm^{-1} of Form I, Form II and of the powder. Right: Polarized measurements of the Davydov's doublet at 309–315 cm^{-1} for the Form I.

Reference [132], where the irreversible temperature-driven phase transition that transforms the surface-mediated structure into the bulk takes place at nearly the same temperature.

Some comments must be made on the different colors that Form I and Form II display in polarized light. Tyrian purple pleochromism,[134] i.e., its color variation with light polarization, was attributed to the dependence of the absorption coefficient on whether the electric field E of the radiation vibrates on the molecular plane parallel or perpendicular to the direction of the central CC bond of the chromophore group. In the first case, the absorption maximum is centered at 640 nm and in the second at 540 nm.[134] In the geometry of our experimental setup, E vibrates on a focal plane parallel to the contact plane of the crystallites on the glass substrate, which is (100) and (001) for Form I and II, respectively. The smaller the angle formed by the long molecular axis with the normal to such a plane, the lower the absorption of the component parallel to the double bond, in the limit that in a "standing-up" molecular arrangement at the interface, only the 540 nm component should be present, imparting a red-violet color to the specimen. The difference in color observed between Form I plates and Form II needles

should therefore be traced back to this effect: in Form I, with an angle of ≈ 40°, polarized light both parallel and perpendicular to the double bond can be absorbed; Form II instead, with an angle of ≈ 16°, approaches the condition of a standing-up geometry, a characteristic shared with the surfaceinduced structures labeled A and B, which display angles of 21 and 29°, respectively.

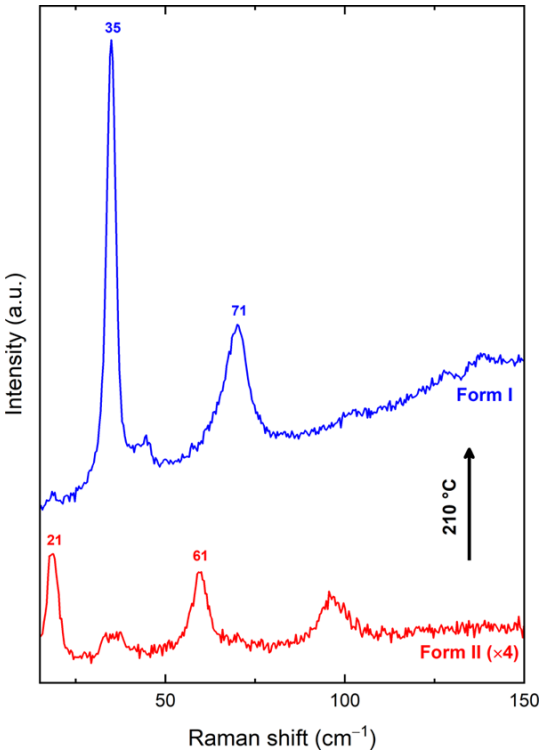

Figure 7.7: Raman spectra of a crystallite of 6,6′-dibromoindigo Form I subjected to heating: the spectrum transforms into that of Form II at T = 210 °C. λexc = 514.5 nm.

7.8 Conclusions

In the previously investigated hydrogen-bonded vat dyes indigo and thioindigo, it was found that in the growth at solid interfaces and film formation the substrate acts as a selector toward one of the known bulk forms of the system.[28,31]

Notwithstanding the strong structural similarities with its parent molecule, 6,6′-dibromoindigo appears to behave in a peculiar way. On one hand, it has been reported to display genuine surface-induced structures. In fact, depending on the nature and the treatment undergone by the surface,[133] slightly different SIPs have been detected. On the other hand, the findings of this work suggest that these structures can be traced back to a bulk structure identified both structurally and spectroscopically through the synergic use of X-ray data, Raman analysis, and DFT spectra simulations.

The result reinforces the conviction that in many instances the structures present in thin films belong to phases already existing as energy minima in the polymorph landscape of the compound, independent of the substrate itself. In turn, it also stresses the importance of crystal structure prediction procedures in assisting the structure solving in these systems.

Chapter 8

Crystal structure prediction: Phenytoin

8.1 Introduction

Phenytoin has been one of the one of the most important systems to which I dedicated myself during the PhD period. The full solution of the thin film structure (form II), which was unknown, required the combined efforts of computational structure generation and prediction (performed by Doris E. Braun[1]), experimental Grazing Incident X-ray Diffraction (GIXD)

[1]Institute of Pharmacy, University of Innsbruck

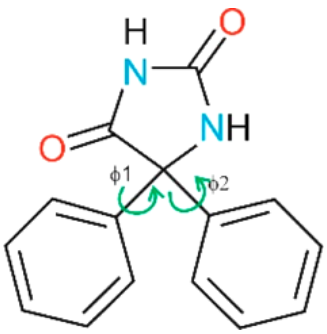

Figure 8.1: Molecular diagram of phenytoin.

measurements (performed by Benedikt Schrode[2] and Oliver Werzer[3]) and experimental and DFT lattice phonon Raman spectroscopy (performed by us in collaboration with Natalia Bedoya-Martínez[2]).[29,30]

Our contribution appears just as small piece added to a complicated puzzle, but it has been crucial for the identification of the correct structure. The results are very satisfactory, and the method might be adapted for other systems, where, due to the limited amount of experimental X-ray data, one must rely on additional approaches to gain access to more detailed information to understand the solid-state behavior.

The material described in this Chapter corresponds to two consecutive papers entitled "*Surface induced phenytoin polymorph. 1. Full structure solution by combining grazing incidence X-ray diffraction and crystal structure prediction*",[29] and "*Surface induced phenytoin polymorph. 2. Structure validation by comparing experimental and Density Functional Theory Raman spectra*",[30] both by myself, Rivalta, Bedoya-Martínez, Schrode, Braun, Werzer, Venuti and Della Valle.

8.2 Context

In general, the selection of a polymorph for drug application is an important decision, as the physiochemical properties vary with the phase.[136] Accordingly, controlling polymorphism is a requirement in drug development to guarantee reproducible performances and is one of the crucial points for regulatory approval.

In addition to conventional bulk (solution) crystal form screening experiments, crystallization becomes more frequently investigated under more restricted environments like pores,[137] matrices,[138] or just at solid surfaces.[139] In each of those cases, the surface contact influences the nucleation. One reason might be the reduced local entropy of the system in the surface vicinity or the substrate-molecule interactions reducing the overall energy due to

[2]Institute of Solid State Physics, NAWI Graz, Graz University of Technology
[3]Institute of Pharmaceutical Science, Department of Pharmaceutical Technology

adhesion or other interactions. Eventually, this leads to a growth process distinct from the bulk case, resulting in a different crystal habit and/or, maybe most importantly, in otherwise inaccessible polymorphs. The latter are often labeled as surface induced[127,128] or surface mediated phases[128] and represent a special cases of heterogeneous crystallization. The extension of the new phases is often also limited in thickness, and they are then referred to as thin film phases. The organic semiconductor pentacene is one of the most prominent and widely studied examples of thin film polymorphism.[140] The occurrence of thin film phases is widespread, but the reason for this is not fully understood yet.

For active pharmaceutical ingredients (APIs) or simple drugs, thin film fabrication technologies have not yet been used extensively, as upscaling into mass production might require processes distinct from already established ones and the structure characterization needed for the market is not trivial in these systems. However, spin coating,[129,141,142] drop casting, inkjet printing, solution shearing,[143] dip coating, and vacuum deposition among others have been employed successfully, either in the search of more appealing physical properties of a new polymorph, or to overcome patent issues. Indeed, the drug dissolution from such layers is often faster compared to bulk systems. This results from larger surface areas being present in the thin films[129] but is also due to higher solubilities of the new forms.[142] These findings are of high importance as the low aqueous solubility of many new drug molecules under development requires improved strategies for successful medication development.

8.3 Form II structure challenge

Phenytoin (5,5-diphenyl-2,4-imidazolidinedione) (see Figure 8.1) is an anticonvulsant drug, also known by the commercial name of Dilantin. Only one crystal form of phenytoin was so far known from the literature (form I). It has an orthorhombic lattice, space group $Pna2_1$ (C^9_{2v}), with four molecules

in the unit cell, all equivalent by symmetry ($Z = 4$, $Z' = 1$).[144,145]

A second phase (form II) had been identified by grazing incidence X-ray diffraction (GIXD) on thin film samples deposited on silica substrates;[142] recognized as a surface induced polymorph (SIP), was not yet fully characterized. GIXD measurements on crystalline phenytoin films detected in all cases diffraction peaks characteristic of form I and, in some cases, additional peaks due to form II. By varying and optimizing the deposition conditions, it was possible to obtain enough peaks for a successful indexing, yielding the lattice parameters of form II, which was found to be monoclinic but a full structure solution was still missing. The strategy to obtain it involved to gather the known information and feed it in a Crystal Structure Prediction procedure.

CSP derives thermodynamically feasible molecular assemblies starting from the chemical structure only (Figure 8.1). The computationally generated structures can thus be used to produce theoretical diffraction patterns to compare to the experiments, finally allowing identification of the solution with the best match.

CSP gave a preliminary $P2_1/c$ (C_{2h}^5) structure with four molecules in the unit cell, all equivalent by symmetry ($Z = 4$, $Z' = 1$).

The proposed $P2_1/c$ structure appeared plausible and reproduced the experimental diffraction pattern. Seeking further validation and full identification of such a structure, we decided to measure and calculate the Raman spectra of both phenytoin crystal forms in the low wavenumber region (up to $\sim$150 cm^{-1}) which probes the lattice vibrations (phonon modes) that are extremely sensitive to the details of crystal packing. Analysis of the spectra, and comparison between experimental and calculated spectra, may thus be used to corroborate and validate any suggested structure. Except for checking the chemical identity of the samples, we did not make use of high wavenumber frequencies characteristic of molecular bonds and functional groups since, being insensitive to the molecular packing, they were not relevant to our analysis.

We therefore used the microRaman technique to map areas of pheny-

toin films where distinct phases appeared, to identify the lattice phonon pattern typical of each of them. Polarized Raman spectroscopy was used to support the assignment of the observed features. The satisfactory match between experiments and calculations for phenytoin form I, both in unpolarized and polarized spectra, demonstrated the reliability of the computational approach. For form II, the same analysis instead led us to revise the preliminary $P2_1/c$ structure, which is centrosymmetric. From a computational point of view, the structure is found to correspond to an energy saddle rather than a minimum, and moreover the calculated spectra display a very poor agreement with the experiments. By perturbing the saddle configuration, a new non-centrosymmetric Pc minimum is reached, with two nonequivalent pairs of molecules in the unit cell ($Z = 4$, $Z' = 2$). Such a minimum, although extremely close to the $P2_1/c$ structure, is characterized by a different set of Raman symmetry selection rules and thus yields very different spectra, which finally do account for the experimental results. Accordingly, the computed GIXD pattern is also very satisfactory and actually represents an improvement to that of the preliminary $P2_1/c$ structure.

8.4 Grazing Incident X-ray Diffraction results

Various reports demonstrated that phenytoin can assemble in two different polymorphs.[129,142] Spin coating, heating from the amorphous phase, or even solvent vapor annealing are shown to produce these phases. While these reports evidenced solely the presence of the bulk form (form I), the formation of solely the surface induced phase is hard to achieve. In the experimental stages of our work,[29] several temperatures and concentrations were tested in order to reduce the amount of form I. Specular scans show that our optimized samples are highly textured for form II, i.e., are characterized by te presence of only one contact plane (or netplane), which is the crystal plane lying on the substrate. Form I (Figure 8.2a top) shows the 002 and 020 bulk netplane, suggesting that this sample has some random powder like character, while form II shows only the 200 peak.

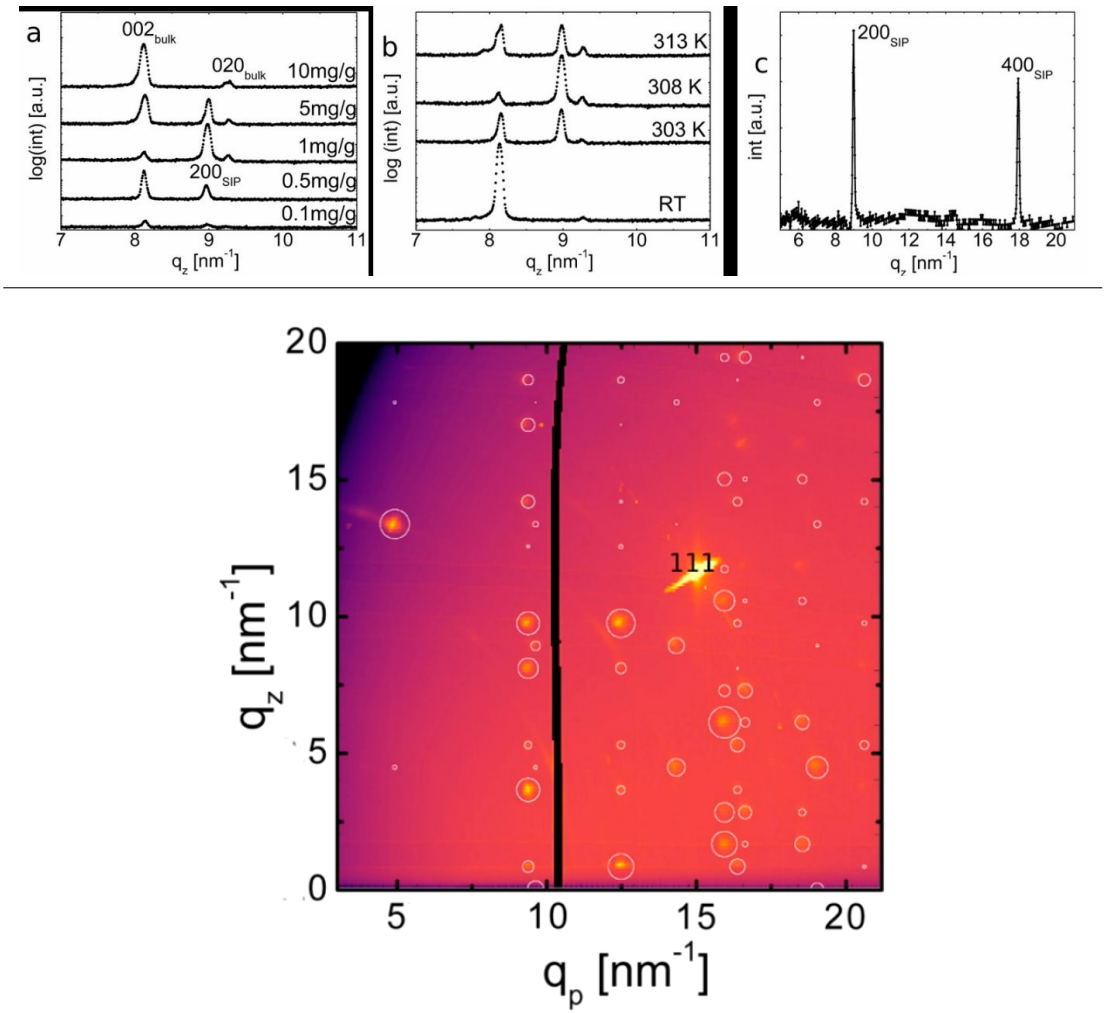

Figure 8.2: Top: Specular X-ray diffraction scans of phenytoin thin films prepared on silicon oxide surfaces. The sample vary by: variation of the concentration at constant 295 K (a), variation of temperature at 10mg/ml (b) and highly optimized sample prepared at 304 K with a solution of 1.2mg/ml (c)
Bottom: Grazing incidence X-ray diffraction pattern of phenytoin form II. Yellow spots are the high intensity Bragg peaks of phenytoin except the labeled peak at qp = 15 and qz = 12 nm^{-1}, which originates from the silicon substrate. The white circles represent calculated structure factors whereby the radius is directly proportional to its values.

The diffraction information for form II was not sufficient to completely solve the structure (due to poor peak quality and to the impossibility of fully rotating the sample). However, it was still possible to obtain a unit cell that explains the observed peak positions using a structure indexing software (DICVol04),[146] (see Table 8.1 together with experimental literature data). Unlike form I, which is orthorhombic, the form II unit cell is monoclinic, with the monoclinic angle of 95.43°. Its unit cell axes a and b are shorter, resulting in a cell volume that is about 5% smaller than the volume of the bulk phase form I. Knowing the unit cell dimensions gives some insight on the new phase, but no molecular or atomic arrangement can be derived.

Table 8.1: Experimental and calculated unit cell dimensions of bulk and SIP phenytoin, from the literature and obtained in our work.[29,30]

Structure	Space Group	T (K)	a (Å)	b (Å)	c (Å)	β (°)	Volume (Å^3)	CSD-refcode structure ID
Form I (bulk)								
exp	$Pna2_1$	RT	6.230(1)	13.581(1)	15.532(2)	90	1314.16	PHYDAN[144]
exp	$Pna2_1$	RT	6.228(1)	13.568(1)	15.520(2)	90	1311.46	PHYDAN01[145]
exp	$Pna2_1$	RT	6.253(4)	15.571(10)	13.632(9)	90	1327.29	PHYDAN02[147]
exp	$Pna2_1$	RT	6.237(4)	15.552(10)	13.614(12)	90	1320.58	PHYDAN03[148]
PBE-TS	$Pna2_1$	0	6.127	15.494	13.442	90	1275.92	780
PBE-D2	$Pna2_1$	0	6.160	15.453	13.226	90	1259.01	780
Form II (SIP)								
exp		395	14.160	12.130	7.260	95.44	1241.37	GIXD
PBE-TS	$P2_1/c$	0	14.102	12.119	7.187	99.25	1212.34	10
PBE-D2	$P2_1/c$	0	13.767	11.927	7.201	98.41	1169.64	10
PBE-TS	Pc	0	14.065	12.132	7.169	95.95	1216.61	10*
PBE-D2	Pc	0	13.796	11.939	7.212	95.41	1182.69	10*

8.5 Crystal Structure Prediction

8.5.1 CSP procedure

Crystal structure prediction was carried out to identify the most stable hypothetical packing arrangements for phenytoin and to support the structure solution of form II. The CSP methodology employed, a multistep process,

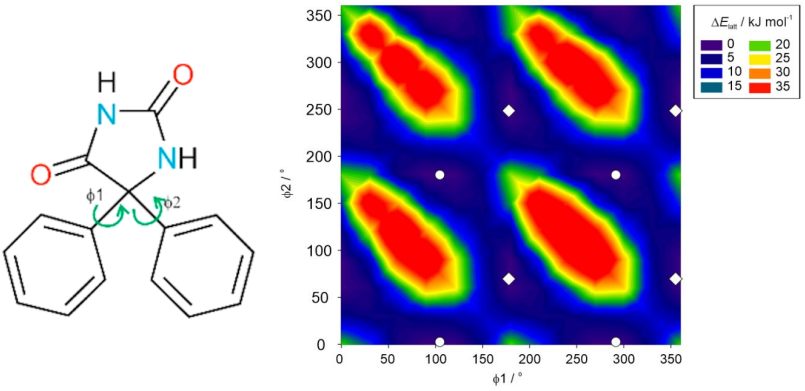

Figure 8.3: Molecular diagram of phenytoin. The intramolecular degrees of freedom (dihedral angles) that were optimized within the crystal energy minimizations are indicated with arrows.

has been implemented successfully into experimental screening and characterization programs.[149,150]

1. **Potential Energy Scans of isolated molecule**: The crystal energy landscape was explored using two different lowest energy conformations of the phenytoin molecule, obtained from Gaussian09[151] isolated molecule calculations, the conformation potential energy surface was mapped. The deformation energy for phenytoin was computed on one 13×13 grid, equivalent to a 30° grid spacing for each dihedral angle in the range 0° to 360° for ϕ_1 and ϕ_2 (Figure 8.3). At each grid point the deformation energy was calculated with the flexible torsions fixed and the rest of the molecule optimized at the B3LYP/6–31G(d,p) level of theory. The potential energy surface scan grid (360° rotation of phenyl rings) results in eight energy minima (non-coplanar phenyl rings), which correspond to two equienergetic minima. In a $Z' = 1$ CSP search only one minimum has to be considered due to the planarity of the phenytoin ring.

2. **Random structure generation**: A total of 300 000 anhydrate structures were randomly generated in 48 space groups ($Z' = 1$, $P1$, $P\bar{1}$, $P2_1$, $P2_1/c$, $P2_12_12$, $P2_12_12_1$, $Pna2_1$, $Pca2_1$, $Pbca$, $Pbcn$, $C2/c$, Cc, $C2$, Pc, Cm, $P2_1/m$, $C2/m$, $P2/c$, $C222_1$, $Pmn2_1$, $Fdd2$, $Pnna$, $Pccn$, $Pbcm$,

$Pnnm$, $Pmmn$, $Pnma$, $P4_1$, $P4_3$, $I\overline{4}$, $P4/n$, $P4_2/n$, $I4/m$, $I4_1/a$, $P4_12_12$, $P4_32_12$, $P3_1$, $P3_2$, $R3$, $P\overline{3}$, $R\overline{3}$, $P3_121$, $P3_221$, $R3c$, $R\overline{3}c$, $P6_1$, $P6_3$, $P6_3/m$) using the program CrystalPredictor2.0.[152–154]

3. **Empirical minimization I and screening**. Each crystal structure was relaxed to a local minimum in the intermolecular lattice energy, calculated with the FIT[155] e^{-6} repulsion-dispersion potential and with atomic charges fitted to the electrostatic potential around the PBE0/6-31G(d,p) charge density using the CHELPG scheme.[156]

4. **Empirical minimization II and screening**. All structures within 35 kJ mol^{-1} of the lowest energy structure (2558 structures) were reminimized using DMACRYS[157] with a more realistic, distributed multipole model[158] for the electrostatic forces, derived using GDMA2[159] to analyze the PBE0/6-31G(d,p) charge density, resulting in 1727 unique structures. Thus, the intermolecular lattice energy includes now the highly directional electrostatic interactions arising from the lone pair and π electrons.

5. **Internal relaxation**. To see the effects of minor changes in the molecular conformation, all structures within 23 kJ mol^{-1} of the rigid body global minimum were further refined by simultaneous relaxation of the "flexible" internal degrees of freedom of the molecules (as defined in Figure 8.3) and the crystal structure. This was done by minimizing the lattice energy (E_{latt}), calculated as the sum of the intermolecular contribution (U_{inter}) and the conformational energy penalty paid for the distortion of the molecular geometry to improve the hydrogen bonding geometries. For each conformation considered in the minimization of E_{latt}, conformational energy penalties (taken as $\Delta E_{\mathrm{intra}}$, with respect to the pyramidal global conformational energy minimum) and isolated molecule charge densities were computed at the PBE0/6-31G(d,p) level. Overall, 278 structures were minimized using the CrystalOptimizer database method.[160]

6. **Periodic DFT and screening**. The most stable structures (91 struc-

tures) were then used as starting points for computationally time-consuming periodic electronic structure calculations. DFT-d calculations were carried out with the CASTEP v6.1 plane wave code[161] using the Perdew-Burke-Ernzerhof (PBE) generalized gradient approximation (GGA) exchange-correlation density functional[101] and ultrasoft pseudopotentials,[162] with the addition of the Tkatchenko and Scheffler (TS)[14] or Grimme 06 (D2)[12] semiempirical dispersion corrections.[4]

7. **Symmetry check**. The crystallographic tool `PLATON`[163] was used in various steps to find the space group symmetry after unconstrained optimizations and to check for convergence to higher symmetries.

8. **Energy**. The pairwise energy contributions to the experimental structures were calculated using CrystalExplorer V17.[164–166] The optimized atomic positions (PBE-TS optimized structures) were used in all subsequent intermolecular interaction energy calculations. The model energies were calculated between all unique nearest neighbor molecular pairs. The model (termed CE-B3LYP) uses B3LYP/6-31G(d,p) molecular wave functions calculated by applying the molecular geometries extracted from the crystal structures. This approach employs electron densities of unperturbed monomers to obtain four separate energy components: electrostatic (E_{E}), polarization (E_{P}), dispersion (E_{D}), and exchange-repulsion (E_{R}). Each energy term is scaled independently to fit a large training set of B3LYP-D2/6-31G(d,p) counterpoise-corrected energies from both organic and inorganic crystals.[165]

Among the many fully converged structures of crystalline phenytoin, possi-

[4]Brillouin zone integrations were performed on a symmetrised Monkhorst–Pack $\boldsymbol{k}$-point grid with the number of $\boldsymbol{k}$-points chosen to provide a maximum spacing of 0.07 $\mathrm{Å}^{-1}$ and a basis set cutoff of 780 eV. The self-consistent field convergence on total energy was set to 1×10^{-5} eV. Energy minimizations were performed using the Broyden-Fletcher-Goldfarb-Shanno optimization scheme within the space group constraints. The optimizations were considered complete when energies were converged to better than 2×10^{-5} eV per atom, atomic displacements to 1×10^{-3} Å, maximum forces to 5×10^{-2} eV $\mathrm{Å}^{-1}$, and maximum stresses to 1×10^{-1} GPa. Energy minimizations with variable unit cells were restarted after the first minimization to reduce the effects of changes in unit cell on the basis set. Phonon calculations performed with CASTEP v.6.1 do not account for dispersion.

ble candidate structures for forms I and II (bulk and SIP, respectively) were identified by matching computed and experimental lattice parameters and then further screened by comparing computed and experimental GIXD patterns.

Since these structures were optimized within space group constraints, it was also necessary to verify that they are local minima of the potential energy surface, i.e., that their energy does not decrease on lowering the symmetry. As a necessary mathematical condition for local stability of the lattice with respect to displacements of the atoms, the potential energy surface must in fact be convex around the stationary point reached by the optimization. Equivalently, the matrix formed by the second derivatives of the potential energy with respect to the atomic displacements must be positive definite; i.e., all the matrix eigenvalues must be positive.[167] A negative eigenvalue means that the system is at a saddle point and that the lattice is unstable with respect to displacements along the corresponding eigenvector. The square root of the eigenvalues represents the vibrational frequencies of the lattice, which are spectroscopically observable. For this reason, calculated vibrational frequencies were used to verify that the candidate structures were stable (imaginary values indicate instability) and to experimentally confirm their correctness. Vibrational frequencies and eigenvectors for form I and II were computed by density functional theory (DFT) methods with the CASTEP v6.1 (without dispersion correction) and `VASP` software (Vienna Ab initio Simulation Package). Whenever an imaginary frequency indicated that the stationary point was a saddle, nearby minima were easily reached by repeating the optimization after perturbing the system along the eigenvector of the mode with imaginary frequency.

8.5.2 CSP results

The PBE-TS and PBE-D2 lattice energy landscapes are shown in Figure 8.4a,b where all the CSP structures are classified by hydrogen bonding motifs and packing modes (shown in Figure 8.4c).

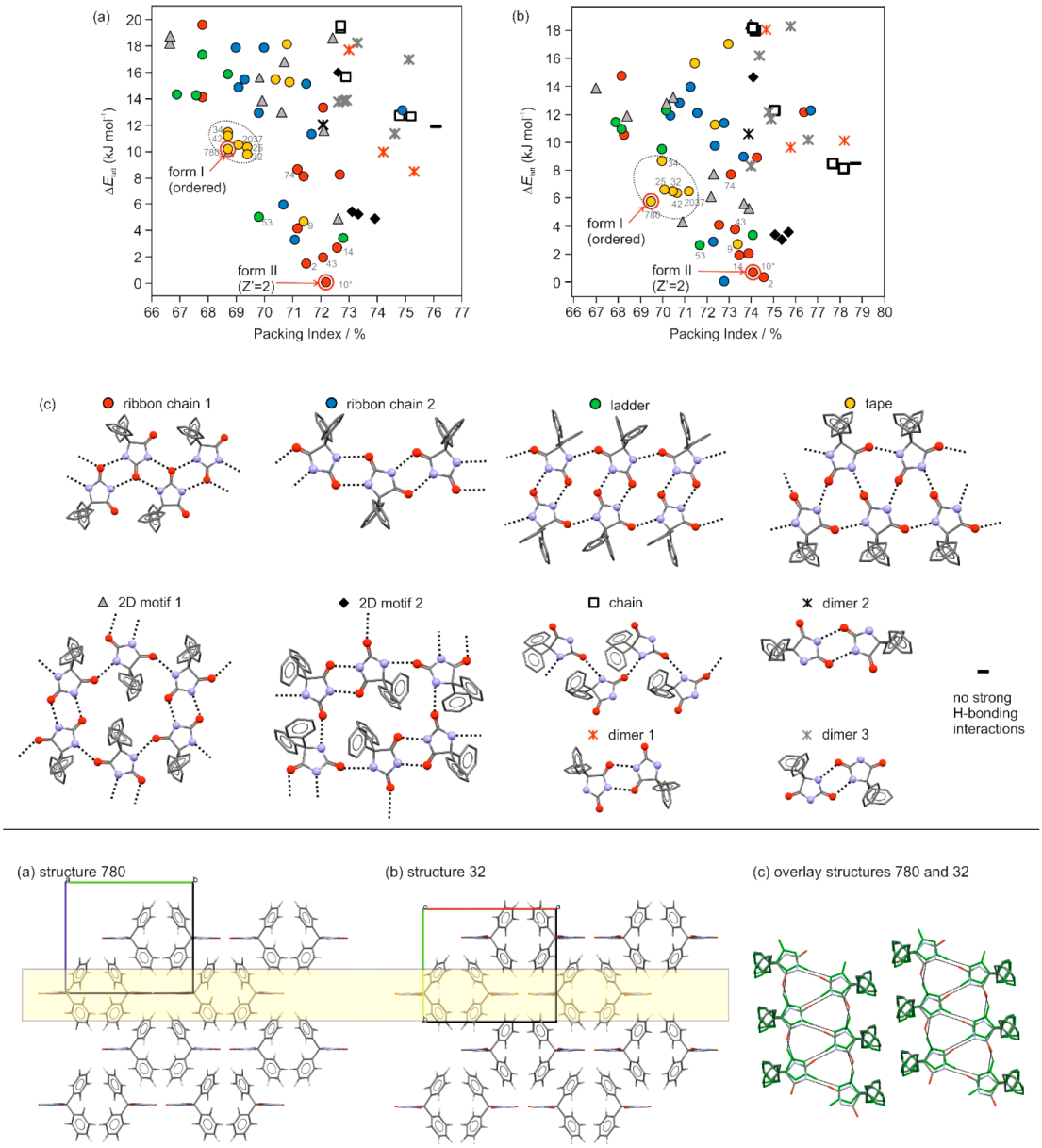

Figure 8.4: Top: (a) PBE-TS and (b) PBE-D2 lattice energy landscapes for phenytoin, classified by H-bonding motif and packing mode (c). Each of the 67 symbols denotes a crystal structure, and each distinct symbol denotes a packing mode. Experimental structures are highlighted with red circles and arrows; structures labeled with structure ID number show packing similarity with the experimental structures. The structures encircled with a dashed ellipsoid show high resemblance in packing and H-bonding motif with form I.

Bottom: Packing diagrams of (a) structure 780 (ordered form I) and (b) structure 32, and a structure overlay of the regions highlighted in yellow in (a) and (b) is given in (c).

The possible candidate structures for forms I and II were identified among the computed structures by matching computed lattice parameters and GIXD patterns against their experimental equivalents. Local stability of the lattice was then checked by computing the vibrational frequencies.

The ordered form I (bulk) was found to correspond to computed structure 780, space group $Pna2_1$, with four molecules per unit cell, all equivalent by symmetry ($Z = 4$, $Z' = 1$). The match between computed and experimental lattice parameters is good; the atomic coordinates are also well described, yielding $RMSD_{15}$ values[43] < 0.12 Å and < 0.18 Å for PBE-TS and PBE-D2 structures, respectively, compared to the experiments. The lattice is found to be stable since all vibrational frequencies are real and, as discussed in the next Section, the experimental Raman spectra are satisfactorily described. All together, these excellent results indicate that the applied computational methods are valid and accurate. The close proximity of other the tape structures ○ in the energy landscape which differ only in the packing may indicate of directional disorder. Indeed, the combination of structures 780 and 32 (Figure 8.4d) reproduces the directional H-bonding disorder described in PHYDAN02[147]. Furthermore, the lower packing indices of the tape motif structures, compared to the other structures, may be indicative of phenyl ring mobility, as seen in the experimental structures.

For form II (SIP), the best match was initially found with computed structure 10, space group $P2_1/c$, with $Z = 4$ and $Z' = 1$. In both the PBE-TS and PBE-D2 lattice energy landscapes, this structure is more stable than form I, and it is characterized by a ribbon chain 1 motif which dominates the lower part of the energy landscape. The agreement between computed and experimental lattice parameters was not perfect (Table 8.1), since the computed β angle (99.25° for PBE-TS, 98.41° for PBE-D2) is larger than the experimental value (95.44°). Despite the slight discrepancy in the β angle, the intensities of the experimental GIXD pattern were also reasonably reproduced with this initial results, showing that the crystal structure predicted is substantially correct. By computing the vibrational frequencies, however, we

found an imaginary frequency (i.e., a negative eigenvalue), indicating that the $P2_1/c$ $Z' = 1$ structure corresponds to a saddle point rather than to a genuine energy minimum. The nearby minimum, therefore, was located by repeating the optimization after perturbing the system along the eigenvector of the mode with an imaginary frequency. Since from the saddle one may go down in two different directions (i.e., one may freely select the + or − sign for the perturbation), two distinct minima can be generated. However, the two optimized structures, which at first sight appeared to display opposite rotations of the phenyls, are actually identical but for a shift of the origin. Thus, the $P2_1/c$ saddle structure may be described as an average of two shifted, but otherwise identical, Pc minima (zero-point and thermal motion average over symmetrically equivalent lower symmetry structures, as seen for racemic naproxene).[168] The relationships among the various structures are illustrated in Figure 8.5.

The optimized structure, labeled 10*, has space group Pc ($Z' = 2$). The latter is slightly more stable than the original $P2_1/c$ saddle point (0.21 kJ mol^{-1} using PBE-D2) and is geometrically extremely close, with an $RMSD_{15}$ value of 0.23 Å (Figure 8.5). Careful examination of the structures revealed that the transformation from the $P2_1/c$ saddle to the Pc minimum involves small rotations of the phenyl groups in opposite directions, yielding two slightly different molecular conformations, not equivalent by symmetry ($Z = 4$, $Z' = 2$).

The lattice parameters computed for the Pc structure 10* closely match the experimental values (Table 8.1). The computed β angle, in particular, is now almost perfect (discrepancy 0.51° for PBE-TS, 0.03° for PBE-D2). The larger discrepancies for the computed $P2_1/c$ structures could be attributed to slight differences in the conformation of the molecules (Figure 8.5), which affect their packing with a more inclined unit cell. Most of the experimental GIXD pattern is reproduced by the Pc structure 10* as shown in Figure 8.2 (structure factors are indicated by the ring size).

Having now two likely structures, i.e., the $P2_1/c$ and Pc, a comparison with the experimental X-ray data show that actually only a small variation in the structure factors is noticeable, and due to the limited data quality

in the GIXD experiment this does not allow us to express a preference for either structure. At last, the experiment on which it was possible to select the correct structure turned out to be Raman spectroscopy.

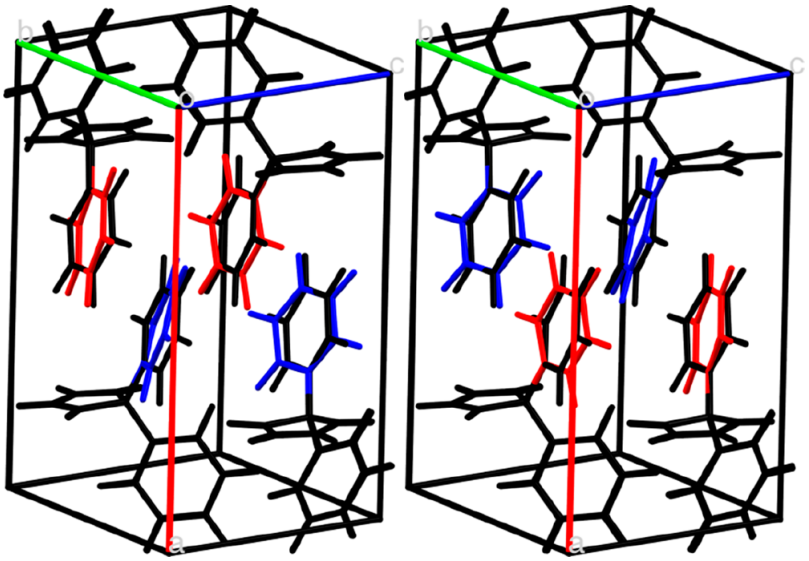

Figure 8.5: Molecular conformation and packing in the computed structures of form II. Overlay of structures $P2_1/c$ (black) and Pc (the two different molecular conformations are coded in color). The Pc structures in the two drawings (left and right) differ in the sign of the perturbation applied to the initial $P2_1/c$ structure, but are actually identical except for a shift of the origin. Their average corresponds to the $P2_1/c$ structure.

8.6 Raman Spectroscopy

As just mentioned, the puzzle was solved by employing Raman spectroscopy combined with DFT calculations[5]. The vibrational spectra are

[5] `VASP` (version 5.4.4) calculations were performed using Perdew-Burke-Ernzerhof (PBE) exchange correlation functional in combination with the projector-augmented wave (PAW) pseudopotentials and D3–BJ vdW corrections. Energy convergence could be achieved for the two polymorphs by using a plane wave energy cutoff of 800 eV, which proved to be adequate. Monkhorst-Pack $\boldsymbol{k}$-point samplings of 2×1×1 and 1×1×2 for forms I and II were used, respectively. Raising the cutoff energy from 800 to 1200 eV caused energy changes below 1 meV per atom, while the differences in energies between the adopted

excellent structural diagnostics since the lattice frequencies are extremely sensitive to the details of the crystal packing and in particular to the change in symmetry.[28]

8.6.1 Form I

The first step was to test the accuracy of our calculation comparing the experimental an DFT spectra of well-kwown form I. Unpolarized Raman spectra in the wavenumber interval 15–200 cm^{-1} of the commercial powder and of a needle-like single crystal are shown in Figure 8.6, along with the computed frequencies and intensities which will be discussed in the following. The two spectra clearly correspond to the same crystal structure, and since the powder certainly belongs to the more common form I, we deduce that the needle belongs to the same form. X-ray indexing of phenytoin needles[147] obtained from EtOH and displaying the same morphology have shown that the needle axis lies in the direction of the crystal axis a. This observation is in agreement with the literature finding for orthorhombic molecular crystals,[169] for which the long side of the crystal, that is, the direction of fastest growth, is usually parallel to the shortest axis (i.e., a).

Starting from the experimental structure,[145] we relaxed it to the equilibrium structure with `VASP` and then computed vibrational frequencies, eigenvectors, and Raman intensities. All frequencies were computed to be positive, proving that the found structure is indeed a stable minimum. Experimental and calculated unpolarized Raman spectra of form I are shown in Figure 8.6. The calculated spectra were obtained at 293 K (i.e., using the experimental lattice parameter corresponding to this temperature), for an exciting laser line at 647.1 nm. They are the sum of Lorentzian bands with the computed frequencies and intensities, and full widths at half-maximum (fwhm) chosen to match the experimental widths and fixed at 5 cm^{-1}. The agreement be-

$\boldsymbol{k}$-point grid and denser ones were below 1 meV per atom. Atomic coordinates were fully relaxed, halting when residual forces fell below 1 meV/Å, using the GADGET package. Lattice parameters were constrained to their experimental values. Vibrational modes and for $\boldsymbol{k} = 0$ were determined with the `Phonopy` program `vasp_raman.py` packages.

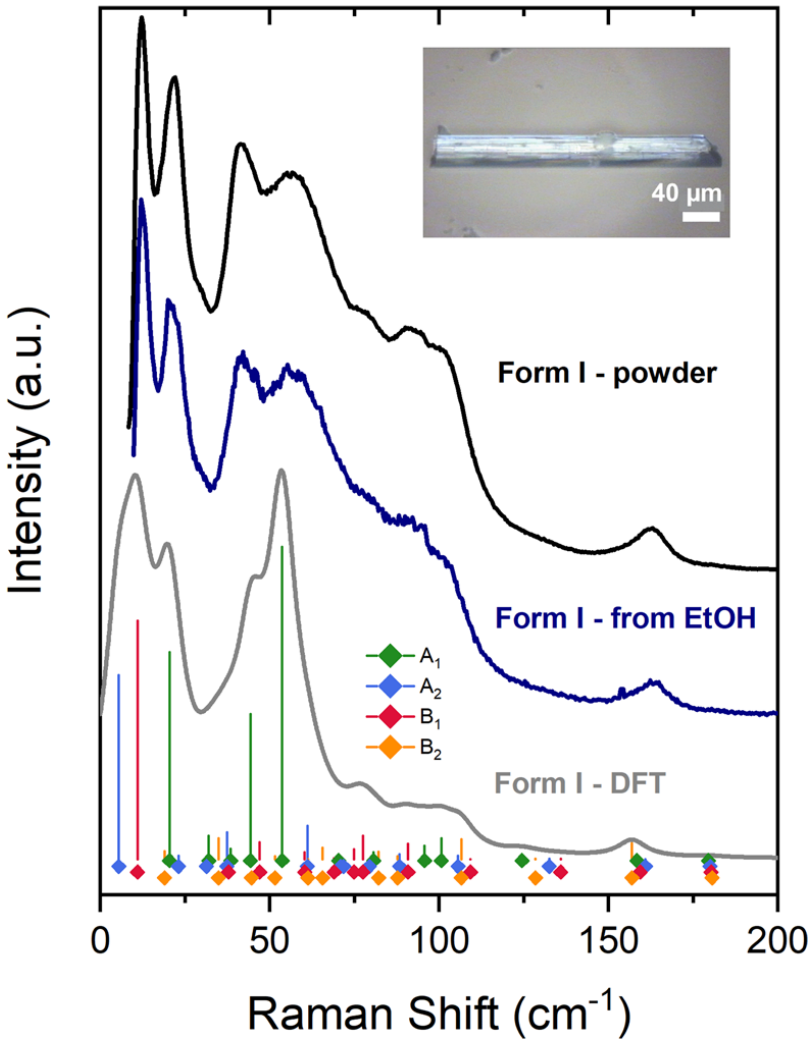

Figure 8.6: Upper traces: Unpolarized Raman spectrum of the commercial powder (form I) and of a single needle-like crystal obtained by deposition from EtOH (sample image shown in the inset) in the wavenumber range 15–200 cm^{-1}. Lower trace: computed unpolarized spectra for form I. Position and height of the vertical bars represent computed frequencies and intensities of the vibrational modes. Mode symmetries are labeled by colors, as indicated in the figure.

tween calculated and experimental spectra is fair, with the exception of the lowest peak around 10 cm^{-1}, for which the calculated intensity exceeds the measured peak height. We consider such a discrepancy as an artifact due to the subtractive monochromator configuration of the experimental setting,

which is designed to cut intensities in the vicinity of the laser exciting line.

Polarized Raman spectra of the same crystal recorded in a backscattering geometry are shown in Figure 8.7. The sample is placed on the stage with the needle axis, which corresponds to one of the extinction directions and identifies with the crystal axis $\boldsymbol{a}$, either parallel or perpendicular to the polarization direction of the analyzer (output polarizer), which, as indicated in the figure, had a fixed orientation, while the polarization direction of the impinging radiation could be rotated. Accordingly, the polarization of exciting and scattered light beams is indicated by the labels $\boldsymbol{a}$ or $\boldsymbol{a}_\perp$, depending on their orientation either parallel or perpendicular to the crystal axis $\boldsymbol{a}$. As expected from theory, spectra recorded in cross-polarization, i.e., $\boldsymbol{a}\boldsymbol{a}_\perp$ or $\boldsymbol{a}_\perp\boldsymbol{a}$ spectra, were found to look identical, and therefore only one of them is shown in Figure 8.7.

Polarized crystal Raman spectra (Figure 8.7 and Table 8.2) with input and output polarizers aligned on the axes i and j have intensities $I_{ij} \propto \alpha_{ij}^2$ controlled by single ij component of the polarizability tensor α. As discussed in Section 8.4, for form I of phenytoin (orthorhombic) we have recorded polarized Raman spectra but we had only partial information about the identity of the crystallographic axes $\boldsymbol{a}$, $\boldsymbol{b}$, $\boldsymbol{c}$ in the needle-like sample. The shortest crystal axis $\boldsymbol{a}$ was certainly along the needle axis, whereas nothing was known about the axes $\boldsymbol{b}$ and $\boldsymbol{c}$ (except that they are perpendicular to $\boldsymbol{a}$ and to each other). In the measurements the two polarizers were chosen to be oriented either parallel or perpendicular to the needle axis $\boldsymbol{a}$ and thus have direction either $\boldsymbol{a}$ or $\boldsymbol{a}_\perp = \boldsymbol{b}\sin\phi + \boldsymbol{c}\cos\phi$, were $\boldsymbol{a}$, $\boldsymbol{b}$, $\boldsymbol{c}$ indicate the direction of the three axes (three orthonormal vectors) and ϕ is the (unknown) angle between $\boldsymbol{a}_\perp$ and $\boldsymbol{b}$.

The correlate the measured intensities (I_{aa}, $I_{aa_\perp}$, $I_{a_\perp a_\perp}$) to the computed α_{ij} components of the polarizability tensor ($\alpha_{aa}, \alpha_{ab} = \alpha_{ab}, \cdots$) we need to transform the polarizability derivatives α from the crystal reference frame ($\boldsymbol{a}$, $\boldsymbol{b}$, $\boldsymbol{c}$) to the laboratory frame ($\boldsymbol{a}$, $\boldsymbol{a}_\perp$, $\boldsymbol{a} \times \boldsymbol{a}_\perp$). We must thus evaluate $\boldsymbol{R}\boldsymbol{\alpha}\boldsymbol{R}^\dagger$ were $\boldsymbol{R}$ is the rotation matrix between the crystal and laboratory

Table 8.2: Calculated wavenumbers of the lowest energy modes of phenytoin form I. Symbols indicate symmetry and correspond to those used in Figures 8.6 and 8.7. For each mode we also report translational, rotational and internal components (%T, %R and %I), unpolarized (Figure 8.6) and polarized (Figure 8.7) Raman intensities for a needle-like sample, infrared and Raman intensities for a powder (given for the sake of completeness). Intensities of inactive modes for the given polarization and symmetry are indicated by hyphens.

Sym	Freq	%T	%R	%I	Needle Raman intensity				Powder	
	(cm^{-1})				I_{unpol}	I_{aa}	$I_{aa_\perp}$	$I_{a_\perp a_\perp}$	I_{IR}	I_{Raman}
A_1	20.4	16	74	10	0.663	0.549	–	0.113	0.001	0.256
	32.0	22	20	58	0.075	0.059	–	0.016	0.002	0.031
	38.5	56	26	18	0.034	0.030	–	0.004	0.024	0.013
	44.3	3	71	26	0.464	0.312	–	0.153	0.017	0.226
	53.7	1	25	74	1.000	0.785	–	0.215	0.013	0.404
	70.4	7	51	42	0.008	0.006	–	0.002	0.121	0.004
	80.7	3	14	83	0.023	0.017	–	0.006	0.032	0.010
	95.7	66	5	29	0.044	0.002	–	0.042	0.002	0.055
	100.6	23	0	77	0.067	0.003	–	0.063	0.006	0.082
	124.5	0	6	94	0.013	0.006	–	0.006	0.002	0.009
	158.4	0	2	98	0.002	0.001	–	0.002	0.132	0.002
	179.5	0	0	100	0.002	0.000	–	0.002	1.000	0.001
B_1	11.0	31	28	41	0.763	–	–	0.763	0.003	1.000
	37.9	3	79	18	0.001	–	–	0.001	0.040	0.001
	47.0	43	44	13	0.054	–	–	0.054	0.004	0.071
	60.3	56	8	36	0.023	–	–	0.023	0.009	0.030
	69.0	24	24	52	0.004	–	–	0.004	0.020	0.005
	74.9	9	3	88	0.032	–	–	0.032	0.012	0.041
	77.5	8	33	59	0.075	–	–	0.075	0.002	0.098
	90.8	22	47	31	0.049	–	–	0.049	0.011	0.064
	109.3	1	25	74	0.001	–	–	0.001	0.001	0.001
	135.9	3	5	92	0.002	–	–	0.002	0.026	0.003
	159.4	0	2	98	0.000	–	–	0.000	0.012	0.000
	180.3	0	0	100	0.000	–	–	0.000	0.000	0.000
A_2	5.4	81	9	10	0.589	–	0.295	–	–	0.386
	23.1	12	71	17	0.012	–	0.006	–	–	0.008
	31.3	86	5	9	0.008	–	0.004	–	–	0.005
	37.4	17	57	26	0.086	–	0.043	–	–	0.056
	61.2	21	11	68	0.108	–	0.054	–	–	0.071
	70.9	4	16	80	0.002	–	0.001	–	–	0.001
	71.8	49	35	16	0.000	–	0.000	–	–	0.000
	79.4	14	1	85	0.001	–	0.000	–	–	0.000
	88.4	10	52	38	0.017	–	0.008	–	–	0.011
	105.6	4	29	67	0.012	–	0.006	–	–	0.008
	132.5	2	5	93	0.001	–	0.001	–	–	0.001
	160.9	0	4	96	0.000	–	0.000	–	–	0.000
	180.0	0	0	100	0.000	–	0.000	–	–	0.000
B_2	19.0	11	30	59	0.026	–	0.013	–	0.000	0.017
	34.9	6	78	16	0.067	–	0.034	–	0.018	0.044
	44.6	1	88	11	0.010	–	0.005	–	0.039	0.007
	51.5	2	26	72	0.011	–	0.005	–	0.006	0.007
	61.3	70	14	16	0.001	–	0.000	–	0.003	0.000
	65.6	1	20	79	0.036	–	0.018	–	0.003	0.024
	82.2	71	9	20	0.024	–	0.012	–	0.019	0.016
	87.8	13	25	62	0.010	–	0.005	–	0.008	0.007
	106.5	21	2	77	0.063	–	0.032	–	0.089	0.042
	128.4	3	7	90	0.002	–	0.001	–	0.009	0.001
	156.9	0	0	100	0.051	–	0.026	–	0.013	0.033
	180.6	0	0	100	0.002	–	0.001	–	0.000	0.001

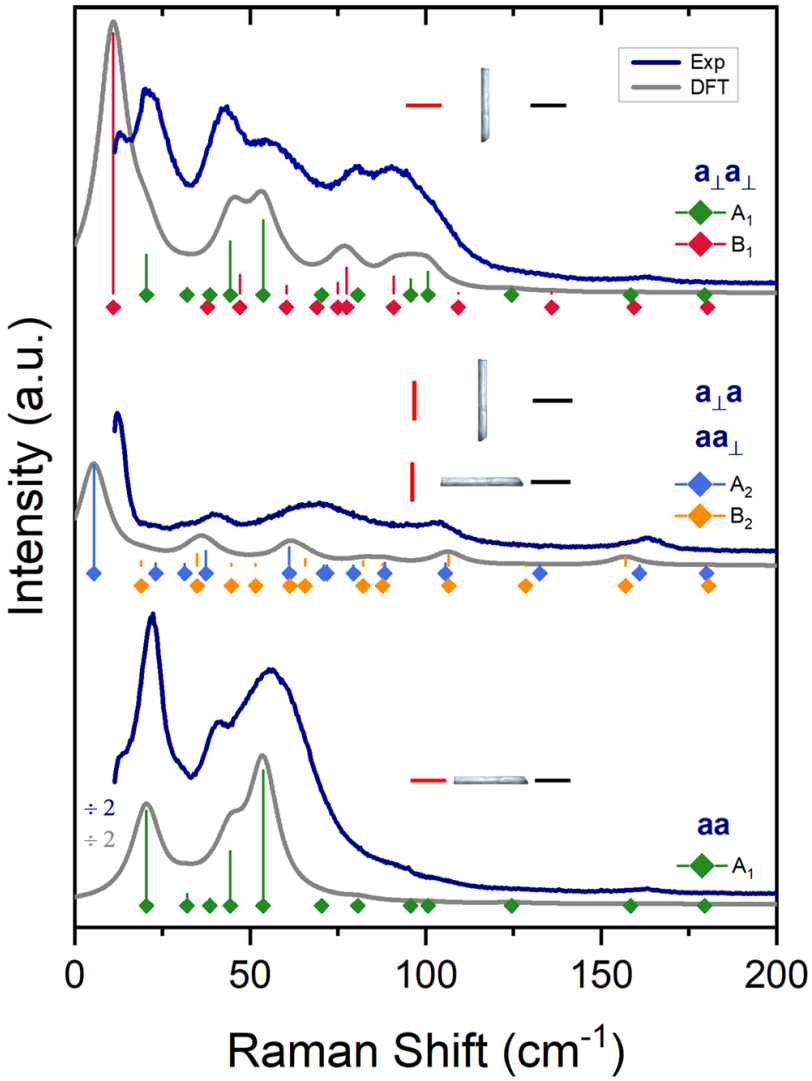

Figure 8.7: Colored traces: Polarized Raman spectra for a single needlelike crystal of form I in the wavenumber range 15–200 cm^{-1}. Horizontal or vertical bars in the insets indicate the direction of the polarization vector of incident and scattered light with respect to the needle axis. The notation a or $a \perp$ indicates a direction parallel or perpendicular to the needle, which grows along the crystal axis a. Gray traces: Calculated spectra evaluated as discussed in the text, for clarity all shown with a downward intensity shift. Position and height of the vertical bars represent computed frequencies and intensities of the vibrational modes. Mode symmetries are labeled by colors, as indicated in the figure.

frames which, for this specific case, is just a simple rotation by an angle ϕ around the $\boldsymbol{a}$ axis. The resulting intensities are

$$I_{aa} = \alpha_{aa}^2 \tag{8.1}$$

$$I_{aa_\perp} = (\alpha_{ab}\sin\phi - \alpha_{ac}\cos\phi)^2 \tag{8.2}$$

$$I_{a_\perp a_\perp} = (\alpha_{bb}\sin^2\phi - 2\alpha_{bc}\sin\phi\cos\phi + \alpha_{cc}\cos^2\phi)^2 \tag{8.3}$$

The Raman spectra depend on the unknown angle ϕ and in theory we could try to deduce ϕ by fitting calculated and experimental spectra. However, this procedure would be very uncertain, and we prefer to average over all possible values of ϕ (from 0 to 2π).

$$I_{aa} = \alpha_{aa}^2 \tag{8.4}$$

$$I_{aa_\perp} = \frac{\alpha_{ab}^2 - \alpha_{ac}^2}{2} \tag{8.5}$$

$$I_{a_\perp a_\perp} = \frac{3\alpha_{bb}^2 + 2\alpha_{bb}\alpha_{cc} + 4\alpha_{bc}^2 + 3\alpha_{cc}^2}{8} \tag{8.6}$$

The unpolarized intensities (Figure 8.6 and Table 8.2) are finally obtained by removing the polarizers, i.e. by summing on

For the purposes of labeling the vibrational symmetry species[48] in the C_{2v}^9 factor group, it is necessary to specify that the C_2 axis lies along $\boldsymbol{b}$ and that we have arbitrarily chosen the σ_v and σ_v' planes to be on bc and ab, respectively (the opposite choice would of course be possible). This information on the symmetry of the crystal is sufficient to interpret and assign the most important spectral features. As mentioned above, polarizations parallel to the needle are aligned to the orthorhombic axis $\boldsymbol{a}$, while those perpendicular to it ($\boldsymbol{a}_\perp$) are along some unknown combination of $\boldsymbol{b}$ and $\boldsymbol{c}$. Therefore, $\boldsymbol{aa}$ spectra probe modes of A_1 symmetry and derive their intensities from the α_{aa}

component of the polarizability tensor. The bands observed in $\boldsymbol{a}_\perp\boldsymbol{a}_\perp$ spectra arise from the α_{bb}, α_{cc}, and α_{bc} polarizability components, and correspond to modes of symmetry A_1 and B_1. Finally, $\boldsymbol{a}\boldsymbol{a}_\perp$ (or $\boldsymbol{a}_\perp\boldsymbol{a}$) spectra involve α_{ab} and α_{ac} polarizability components, thus probing modes of symmetries B_2 and A_2, respectively.

8.6.2 Experimental map of phenytoin films

Films prepared by drop casting adopt very nonuniform morphologies, as shown by the optical image of a typical sample in Figure 8.8. For this sample, we have used the confocal microscope to acquire Raman spectra at all points of the grid superimposed over the image and found different spectral patterns, as illustrated in Figure 8.8, where the spectrum of the commercial powder, which belongs to form I, is also shown. Spectra with lattice peaks precisely matching those of the commercial powder are found at some grid points, where only form I is therefore present. At other grid points, we record spectra where none of the characteristic peaks of form I are visible. It is therefore possible to infer that only the different form II (pure SIP) is present at these areas. At yet other points, we find combinations of the two detected spectra, which clearly correspond to mixtures of the two forms (phase coexistence or mixing). Analogous behavior is found for other samples.

A full map of the relative proportions of the two forms at the various grid points has thus been deduced from the relative intensity of appropriate spectral windows typical of the two forms. We have used the window 53–59 cm^{-1} for form I and 30–36 cm^{-1} for form II, as indicated by the shaded areas in Figure 8.8, resulting the concentration map shown in Figure 8.8 (right panel). As expected, we observe a close correspondence between the Raman map and the optical image (i.e., between spectrum and morphology), with form II corresponding to whitish powder-like portions of the sample, and form I to darker fibrous portions.

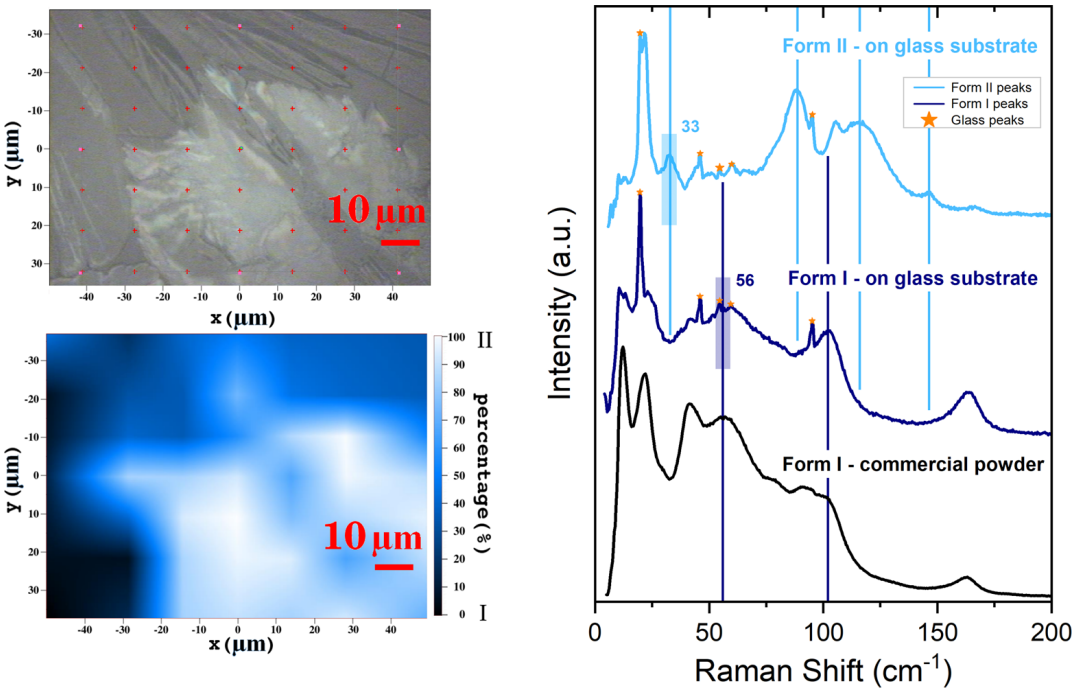

Figure 8.8: Left: Optical image (top) and Raman map (bottom) of a selected film sample. The Raman map refers to the XY grid of points drawn over the optical image, with a color scaling from extremely dark (form I) to extremely light blue (form II).
Right: Low wavenumber Raman spectra of phenytoin commercial powder, and at two different points of a selected film prepared by drop casting. Peaks indicated with stars are due to the glass substrate. Shaded areas indicate spectral windows chosen to quantify the proportion of the two phases.

8.6.3 Form II: Pc vs $P2_1/c$

As already discussed, previous GIXD measurements and CSP calculations gave a $P2_1/c$ (C_{2h}^5) crystal structure that reproduced quite well the experimental diffractogram.[29] By relaxing this structure to the nearest stationary point with `VASP`, and then computing the vibrational modes, however we have now discovered that the experimental spectrum was not properly reproduced, as it can be seen when comparing the experimental and computed unpolarized Raman spectra shown in Figure 8.10. More importantly, we have found an imaginary frequency for an intramolecular mode of B_u symmetry, i.e., with atomic displacements that are antisymmetric with respect to both

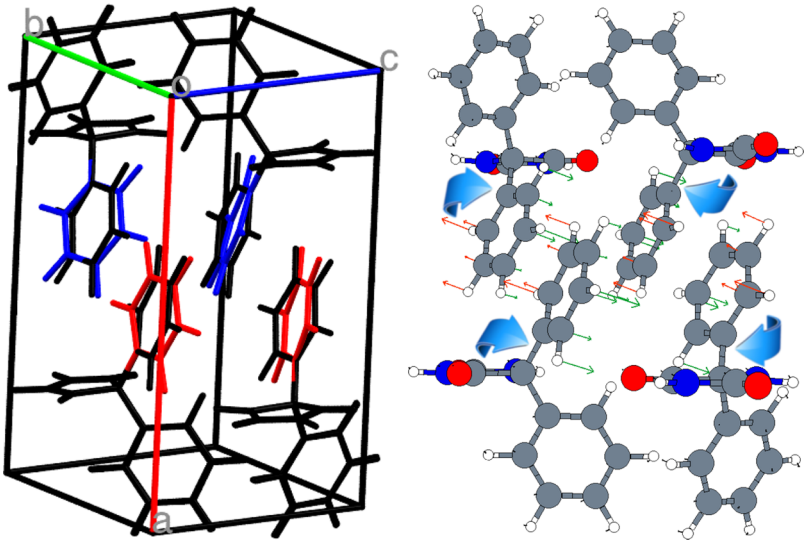

Figure 8.9: Left panel: Overlapped structures of the two DFT-d stationary points of form II. $P2_1/c$ (black) and Pc (colored) structures are respectively an energy saddle and a minimum and differ for the rotation of the phenyl groups. Molecules with the same color are equivalent by symmetry. Right panel: Atomic displacements (eigenvectors) of the B_u mode with imaginary frequency.

the inversion and C_2 operations, indicating that the preliminary $P2_1/c$ packing corresponds to a saddle point rather than to a genuine energy minimum. A graphical representation of this mode is shown in Figure 8.9.

The Pc minimum is only slightly more stable than the original $P2_1/c$ saddle point ($\Delta E = 0.07$ kcal per mole of phenytoin) and is geometrically extremely close to it. So close, in fact, that the standard crystallographic tool `PLATON`[170] used in the CSP search for phenytoin1 to check for higher symmetries, with the default distance tolerance for the identification of atoms equivalent by symmetry (0.25 Å), converts the Pc structure back to the $P2_1/c$ one. This symmetry check therefore had to be disabled for the Pc structure, which could be located only by detecting the lack of local stability of the system diagnosed through the occurrence of the imaginary frequency, accompanied by eigenvector following. The missing of a slightly different structure of lower symmetry could be a problem, which might remain undetected, in CSP searches.

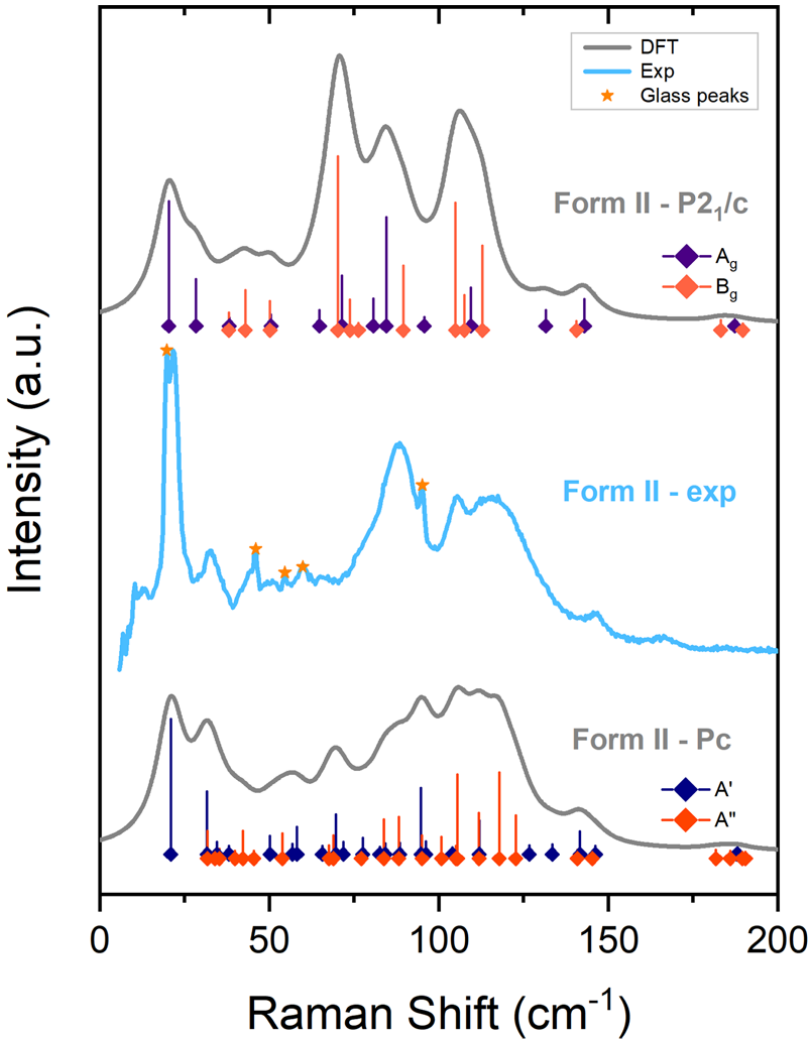

Figure 8.10: Experimental unpolarized Raman spectra for form II of phenytoin (colored trace) and computed powder spectra for the $P2_1/c$ and Pc computed structures (gray traces). Position and height of the vertical bars represent computed frequencies and intensities of the vibrational modes. Mode symmetries are labeled by colors, as indicated in the figure. As discussed in the text, the A_g and B_g modes of $P2_1/c$ are two strict subsets of A' and A'' of Pc, respectively.

Despite their close structural and dynamical similarities, the two structures can be promptly distinguished on the basis of their vibrational properties, because in the Pc packing all the modes become Raman active, as a

Table 8.3: Calculated wavenumbers of the lowest energy modes of phenytoin form II. Symbols indicate symmetry and correspond to those used in Figure 8.10. For each mode we also report translational, rotational and internal components (%T, %R and %I) and infrared and Raman (Figure 8.10) intensities for a powder. Intensities of inactive modes for the given symmetry are indicated by hyphens. The eigenvector of the mode with imaginary frequency (indicated in bold) is represented in Figure 8.9.

Pc							*P*2$_1$/*c*						
Sym	Freq (cm^{-1})	%T	%R	%I	Powder I_{IR}	Powder I_{Raman}	Sym	Freq (cm^{-1})	%T	%R	%I	Powder I_{IR}	Powder I_{Raman}
A'	20.9	82	8	10	0.000	1.000	A_g	20.3	88	0	12	–	0.731
	31.6	16	60	24	0.006	0.456		28.4	8	76	16	–	0.267
	34.5	6	68	26	0.011	0.078		38.2	16	76	8	–	0.038
	38.1	6	84	10	0.029	0.048		50.5	72	8	20	–	0.055
	50.2	66	10	24	0.015	0.124		64.8	0	52	48	–	0.081
	56.8	4	46	50	0.046	0.061		71.5	0	12	88	–	0.287
	58.2	10	64	26	0.651	0.191		80.7	40	0	60	–	0.151
	65.6	2	62	36	0.077	0.048		84.5	12	12	76	–	0.637
	69.7	0	40	60	0.124	0.282		95.7	56	12	32	–	0.039
	71.8	8	30	62	0.030	0.077		109.6	0	40	60	–	0.215
	77.6	34	4	62	0.021	0.106		131.5	0	4	96	–	0.082
	82.6	44	8	48	0.045	0.041		143.0	0	0	100	–	0.148
	84.2	12	6	82	0.013	0.065		187.3	0	0	100	–	0.016
	88.5	4	8	88	0.013	0.070	B_u	**32.6** i	0	16	84	0.090	–
	94.8	20	18	62	0.011	0.481		41.6	0	88	12	0.041	–
	96.2	48	10	42	0.005	0.080		61.1	0	56	44	0.477	–
	104.0	24	20	56	0.123	0.036		69.3	8	68	24	0.077	–
	111.9	2	36	62	0.024	0.238		77.9	16	20	64	0.016	–
	126.7	0	6	94	0.439	0.050		82.9	44	0	56	0.017	–
	133.5	0	6	94	0.098	0.060		88.4	0	12	88	0.021	–
	141.7	0	0	100	0.526	0.157		103.1	28	24	48	0.118	–
	146.2	0	2	98	1.000	0.048		127.1	0	4	96	0.366	–
	187.9	0	0	100	0.002	0.022		144.4	0	0	100	1.000	–
	188.2	0	0	100	0.633	0.000		187.5	0	0	100	0.437	–
A''	31.7	82	2	16	0.000	0.160	B_g	38.0	84	8	8	–	0.067
	34.0	24	68	8	0.002	0.018		42.9	80	12	8	–	0.200
	35.2	60	22	18	0.013	0.024		50.2	44	48	8	–	0.135
	39.9	64	18	18	0.008	0.009		70.2	8	4	88	–	1.000
	42.2	60	30	10	0.001	0.159		73.8	4	88	8	–	0.145
	45.4	34	60	6	0.000	0.009		76.3	32	52	16	–	0.006
	53.9	28	42	30	0.003	0.142		89.5	8	4	88	–	0.348
	67.6	2	30	68	0.037	0.049		104.9	0	8	92	–	0.724
	68.9	6	78	16	0.011	0.126		107.5	8	16	76	–	0.170
	77.1	36	48	16	0.005	0.018		112.9	8	12	80	–	0.466
	83.8	10	14	76	0.018	0.245		140.7	0	0	100	–	0.018
	88.2	6	2	92	0.000	0.265		183.2	16	36	48	–	0.022
	95.1	8	14	78	0.005	0.125		189.6	0	4	96	–	0.003
	100.8	4	12	84	0.001	0.113	A_u	35.0	36	44	20	0.005	–
	105.1	6	10	84	0.032	0.046		37.1	52	24	24	0.012	–
	105.5	4	8	88	0.002	0.582		38.5	60	32	8	0.003	–
	111.9	10	6	84	0.008	0.296		46.2	0	68	32	0.001	–
	117.8	6	6	88	0.068	0.599		67.9	4	36	60	0.027	–
	122.7	0	20	80	0.008	0.277		88.7	12	12	76	0.016	–
	140.9	0	0	100	0.000	0.017		100.5	4	12	84	0.004	–
	145.3	0	2	98	0.008	0.010		109.2	8	0	92	0.092	–
	181.8	18	36	46	0.211	0.019		111.4	4	20	76	0.005	–
	186.0	20	36	44	0.260	0.008		143.6	0	0	100	0.002	–
	189.5	0	0	100	0.000	0.002		184.2	16	36	48	0.350	–
	190.4	2	6	92	0.029	0.002		189.1	0	4	96	0.027	–

result of the symmetry lowering with loss of inversion. For this reason, the calculated Pc spectrum displays more bands and, inversion and C_2 screw axis symmetries of C_{2h}^5 are lost, while the glide plane as shown in Figure 8.10, agrees much better with the experiment.

By analyzing the structures in detail, we find that the transformation leading from the $P2_1/c$ (C_{2h}^5) to the Pc (C_2s) structure involves a slight rotations of the phenyl groups in two opposite directions (see Figure 8.9). As a consequence, the inversion and C_2 screw axis symmetries of C_{2h}^5 are lost, while the glide plane symmetry is preserved. Depending on their parity with respect to the latter symmetry operation, the four irreducible representations of the C_{2h}^5 group merge into the two C_2s representations, with the correlation scheme $A_g + B_u \rightarrow A'$, $A_u + B_g \rightarrow A''$. By examining the calculated intensities in Figure 8.10, in fact, we find that A_g or B_g bands computed for the $P2_1/c$ structure usually have corresponding A' or A'' bands for the Pc structure which, however, display many additional bands, which are those arising from the A_u or B_u Raman inactive $P2_1/c$ modes. The intensities calculated for the Pc and $P2_1/c$ structures of form II are listed in Tables 8.3

8.7 Conclusions

The solution of the crystallographic structure of the surface induced phase (SIP) of phenytoin (thin films known as phase II) has been determinated by combining grazing incidence X-ray diffraction (GIXD) experiments with crystal structure prediction (CSP) calculations.[29]

Peak positions in a diffractogram depend solely on the unit cell parameters, while peak intensities depend on the positions of the atoms within the cell. For form II, the lattice parameters could be determined, whereas the atomic coordinates could not be obtained because of the very limited number of peaks in the thin film diffractogram. This, however, was sufficient to exclude (or possibly confirm) any proposed crystal structure.

Many hypothetical structures was therefore generated and then optimized with CSP calculations using suitable molecule-molecule interaction models.

Nearly 100 of the most stable structures were then used as starting points for DFT calculations with dispersion corrections and several possible candidate structures for forms I (bulk) and II (SIP) were finally identified by matching computed and experimental lattice parameters and GIXD patterns. The best candidate for form I corresponded to the known crystallographic structure of bulk phenytoin, while the best candidate for form II reasonably matched the experimental lattice parameters and GIXD pattern and was therefore considered as a preliminary structure.

In our work,[30] aiming to validate the candidate structure for form II, we have investigated the experimental and calculated Raman spectra of the two crystal forms in the low wavenumber region which probes the lattice vibrations. These, being extremely sensitive to the details of crystal packing, represent the fingerprint of the structure. The comparison between experimental and calculated spectra may thus be used to validate any proposed structure. Vibrational properties are obtained by evaluating and then diagonalizing the dynamical matrix of the system. The computed frequencies can be compared to their experimental equivalents and also can be used to check the stability of the stationary point. Imaginary frequencies in fact indicate that the lattice is at a saddle point, from which one may reach nearby minima by following the modes with imaginary frequencies.

For form I, the experimental structure was correctly reproduced by the best CSP structure, which was confirmed to correspond to a stable minimum and gave computed Raman spectra in excellent agreement with the experiments. These results for the known structure successfully validate the computational method and the calculation was enough accurate to even reproduced polarized spectra of the complex case of needle sample.

For form II, the best CSP structure, although able to reproduce the GIXD measurements, instead gave computed Raman spectra which did not match the experiments and furthermore corresponded to a centrosymmetric saddle point structure with an imaginary frequency. Descent from the saddle reached a non-centrosymmetric minimum, also with the correct GIXD pattern. The saddle and the minimum, although very close, are however char-

acterized by different Raman symmetry selection rules. For the centrosymmetric saddle, the rule of mutual exclusion in fact holds, and no vibrational mode can be both infrared and Raman active, whereas all modes can be Raman active for the non-centrosymmetric minimum. The Raman spectra computed for the minimum, notwithstanding its structural similarity to the saddle point, are therefore very different and actually in excellent agreement with the experimental pattern, thus confirming that the structure is correct.

Convergence to saddle structures of too high symmetry could occur in many CSP searches. Detection of these saddles is often not attempted at DFT for hundreds of structures, although with increasing computer power it could be systematically performed by computing the vibrational spectrum and checking for imaginary frequencies. A related problem, in the opposite direction, was often noticed in the last decades of the 20th century, when it became clear that many of the published X-ray structural studies gave erroneous structures with too low crystallographic symmetry.[171] This problem was eventually solved when software tools like `PLATON`[170] were developed to routinely check the crystallographic coordinates for missing symmetries.[172] By far the most common case is precisely the missing of an inversion center, which is also the most serious case because it leads to incorrect crystal property predictions. Reliable detection of the inversion in borderline situations presents problems even now,[171] since `PLATON` (used by us to discover the space group of the predicted structures) needs to allow for noise in the atomic coordinates. Fortunately, as we have demonstrated in practice, an analysis of the Raman and/or infrared spectra may easily reveal the presence (or absence) of the inversion and thus conclusively validate a structure.

Chapter 9

Electronic properties of thin films

9.1 Introduction

In this Section we study the molecular orientation, the disorder and essential electron transport parameters of two molecules (B2PyMPM and B4PyMPM) used as thin film in Organic Light Emitting Diode (OLED) and characterized by the presence of a hydrogen bond (H-bond) network. To accomplish this task, classical and *ab initio* methods were combined and compared with experimental results. The material described in this Chapter mainly corresponds to the submitted paper entitled "*Bidimensional H-bond network promotes structural order and electron transport in BPyMPs molecular semiconductors: A computational study*", by De Nicola, Correa, myself, Muccioli, D'Avino, Kido and Milano.[34] My contribution to this work was the calculation of the electron affinity (EA) of disordered thin films, under the supervision of Luca Muccioli and Gabriele DAvino. Antonio De Nicola, Giuseppe Milano, Andrea Correa and Junji Kido provided the MD structures and the experimental results.

9.2 Context

Organic Light Emitting Diode (OLED) research field has constantly grown in the last 35 years: Scopus web archive counts roughly 12000 publications from 1994 to 2020, while the number of publications per year is still increasing.

Nowadays OLEDs dominate the display market and show promise for a similar success in lighting applications in the near future, owing to the high brightness and the low power consumption they can offer. New generation OLEDs are produced by vapor-deposition of organic materials which form layers, in which the molecular orientation is a key property to be controlled to improve outcoupling and charge transport efficiency.[173–181]

The vapor deposition process allows producing smooth films, only a few nanometers-thick if needed, by condensing molecules from the gas phase onto a temperature-controlled substrate,[182] but offers much less control over molecular orientation and crystallinity, which are governed by a complex interplay between kinetic and thermodynamic effects, often substrate-dependent.[183,184] A viable strategy to maximize the thermodynamic thrust is to design molecules with specific shapes and functional groups that promote highly directional supramolecular interactions.

In this context, Prof. Yokoyama and co-workers investigated the general relationship between the structural anisotropy of a given molecule and its orientational order and preferred alignment direction in a thin solid film.[185,186] In another series of studies, intermolecular C–H·N hydrogen bonds were exploited for driving the supramolecular assembling, by designing molecules containing multiple pyridine rings properly arranged in order to maximize intermolecular interactions that promote long-range structural order.

This strategy was successful and several molecules were demonstrated to form flat surfaces and regular stacking through self-assembly.[176–178,187] Moreover, the presence of a bidimensional H-bonds network promotes anisotropic optical properties, like the refractive index and extinction coefficient k, and a non-negligible electron mobility.[177]

The present chapter concerns two compounds indicated as B4 (or B4PyMT)

and B2 (or B2PyMTZ), abbreviations of (4,6-bis(3,5-di(pyridine-n-yl)phenyl)-2-methylpyrimidine with $n = 4$ or 2, respectively. Their chemical structures, together with that of the related compound B2PyMTZ are shown in Figure 9.1. The two molecules differ only the position in 4 or 2 of pyridine nitrogens. Time-of-flight measurements by Kido and coauthors[177] revealed a remarkable difference of about two orders of magnitude in the electron mobility between vacuum-deposited films of B4 and B2 (from $\approx 10^{-4}$ cm^2 V^{-1}s^{-1} down to $\approx 10^{-6}$ cm^2 V^{-1}s^{-1}). This surprisingly large difference is unlikely to have an explanation at the molecular level, since the two molecules are almost identical. Rather, it should be attributed to different supramolecular arrangements, indirectly induced by the slight chemical difference.

The understanding of the driving forces regulating molecular orientation and arrangement is mandatory to optimize material properties, such as charge transport, and to design processes and/or compounds to improve device efficiency. In this matter, the molecular dynamics (MD) at atomic resolution constitutes a powerful computational method able to rationalize the microscopic origin of the preferred molecular orientation[188–197] and several successful studies of interfacial properties and molecular arrangement in OLED materials have been reported.[188,189,191,198]

9.3 Structure of B2 and B4 films

Theoretical B2 and B4 film structures were obtained from MD simulations where the coordinates were initialized starting from experimental crystallographic data of B4PyPTZ, which has very similar optical properties and chemical structure (see Figure 9.1). The force field and the preliminary structures were tested on B4PyPTZ, B2 and B4 bulk samples before moving to the simulation of films.

All the atomistic simulations were performed with the GROMACS 5.0 simulation package.[199,200] using a time step of 2 fs, a temperature of 298 K in the NVT ensemble and a pressure of 1 atm in the NPT ensemble.

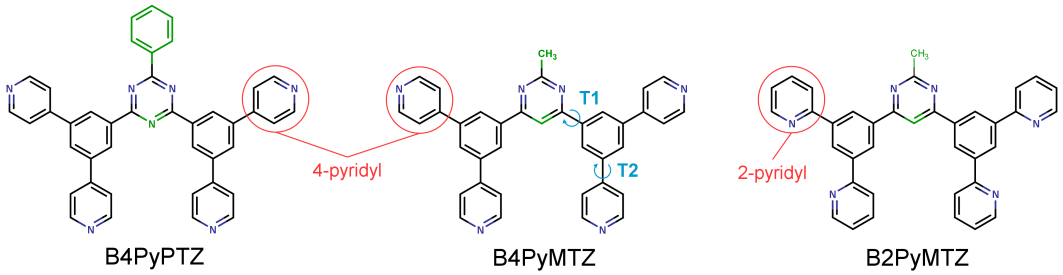

Figure 9.1: Chemical structure of B4PyPTZ, B4 and B2 molecules. The different position of nitrogen atoms in the 4- and 2-pyridyl rings are indicated. In the following sections the T1 and T2 rotations are measured through the dihedral angles φ_{T1} and φ_{T2}.

All the bonds involving hydrogen atoms were constrained using the LINCS algorithm[201] Lennard-Jones interactions were calculated by using a cut-off distance of 1.4 nm, while electrostatic interactions were treated with the Particle Mesh Ewald algorithm with a grid spacing of 0.1 nm.

Atomistic OPLS force field (FF)[202] was adopted, except for soft aryl-aryl torsions which were parameterized against DFT calculations.[203] The torsional energy profiles for φ_{T1} and φ_{T2} dihedrals (see Figure 9.1) were calculated at different fixed aryl-aryl angles (with steps of 10°, as shown in Figure 9.2), at PBE0/6-311G** level,[204–206] using Gaussian09.[207] New Fourier coefficients were obtained by fitting and implemented in our force field.

The crystallographic unit cell[176] of B4PyPTZ, containing 16 molecules, was replicated 2 × 2 × 1 times along a, b, c directions to build a supercell composed of 128 molecules. The crystalline structure of B4PyPTZ is characterized by molecules stacked in columns in which the peculiar position of pyridine nitrogens maximizes the probability to form of intermolecular H-bonds with adjacent columns, forming a bidimensional H-bond network.[176]

The stability of B4PyPTZ sample was checked performing a MD simulation in the NPT ensemble. The equilibrium mass density obtained from the MD simulation (1278 ± 5 kg m^{-3}) slightly underestimates the experimental value[176] of about 3%, however this deviation is similar to those observed for the majority of organic molecules (2 - 4%) modelled by using OPLS force

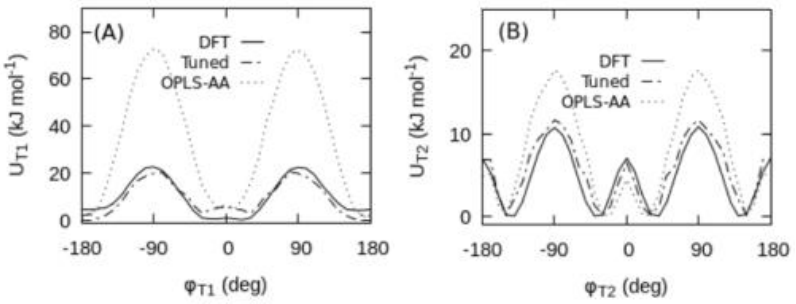

Figure 9.2: Torsional energy profiles for dihedral angles φ_{T1} and φ_{T2}. Solid lines represent the DFT calculations at PBE0/6-311G* level. Dashed lines represent energy profiles obtained with standard OPLS-AA parameters, while dashed dotted lines represent energy profiles obtained from the tuned parameters.

field.[202,208–211] Besides, the lattice constants (a, b, c) of the crystalline structure are reproduced within an error of +1.9%.

The equilibrium structure of the B4PyPTZ supercell was used as initial coordinate set to build B4 and B2 systems. NPT simulations revealed a difference in the equilibrium mass density between the two bulk systems, even if the only difference between the two molecules lies in the position of nitrogen atoms in the pyridine rings (Figure 9.1). Starting from initial configurations, at the same density for both molecules, the bulk of B4 reaches a slightly higher equilibrium density (1197 ± 5 kg m^{-3}) than for B2 (1176 ± 5 kg m^{-3}) revealing a more efficient packing.

To reproduce the experimental conditions of film deposition (obtain by vacuum deposition), several bulk configurations were placed inside an elongated box, with 20 nm of vacuum along the z axis, and MD simulations in NVT ensemble were performed.

Representative snapshots of equilibrium configurations of B2 and B4 systems are reported in Figure 9.3. As it can be seen, B4 molecules show a well-defined columnar structure while B2 molecules are much more disorderly stacked with many of them tilted with the respect to the normal direction (z). A more quantitative indication is gained by computing the X-Ray pow-

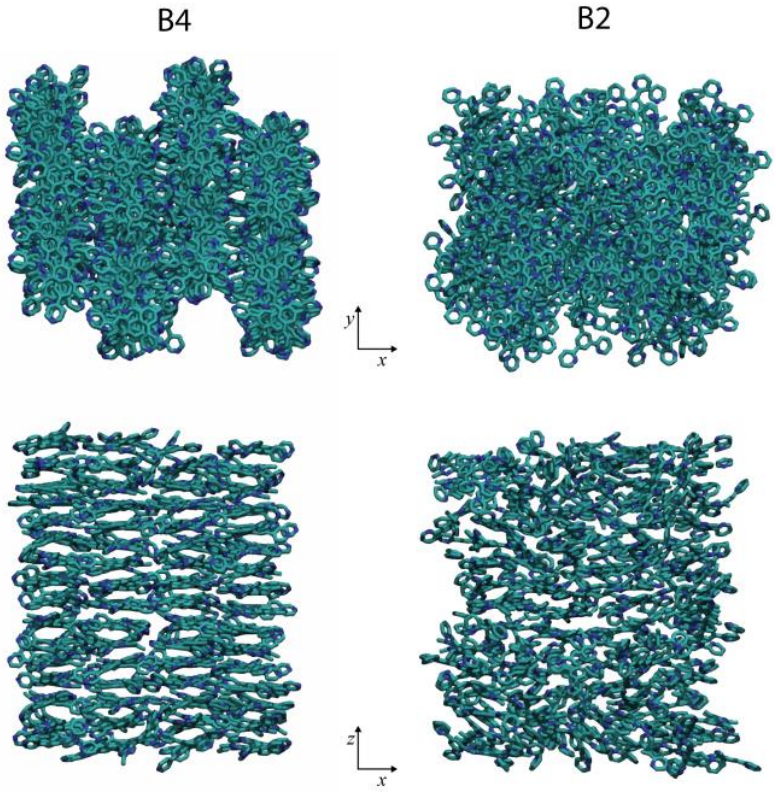

Figure 9.3: Snapshots representative of the equilibrium configuration of B4 and B2 systems. Nitrogen atoms are represented in blue, carbons in cyan and hydrogens in white. The vacuum/bulk interface is perpendicular to z direction.

der pattern and the radial distribution function $g(r)$, and in both cases the B4 profiles are more sharp and well-defined than for B2, denoting a higher positional order (Figure 9.4).

Since structural order and molecular orientation are correlated, a high positional order of B4 structure should correspond to a high orientational order, too. The regularity in molecular orientation can be computed using the orientational order parameter (P_2), which is defined as:

$$\langle P_2 \rangle = \frac{3\langle cos^2\theta \rangle - 1}{2} \tag{9.1}$$

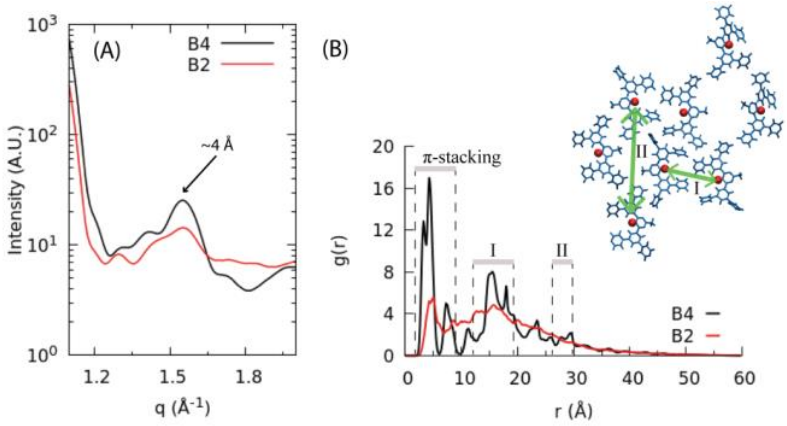

Figure 9.4: (A) Structure factor patterns for B4 (black) and B2 (red) calculated with the ISAACS package.[212] The $q \approx 1.53$ Å^{-1} peak corresponds to molecular π-stacking distance and it is comparable with the experimental spacing of ≈ 4 Å measured on a thin film of B4 material.[177] (B) Radial distribution functions $g(r)$ calculated for the core hydrogens (red dots in the inset figure). In the region of π-stacking ($\approx$ 3–5 Å), fundamental for promoting electron transport, B4 shows peaks about three times more intense than B2. At larger distances, the B4 $g(r)$ shows two main peaks, region I at ≈ 1.5 nm and region II at ≈ 2.8 nm, which represent the characteristic interplanar distances of the nearly hexagonal packing.

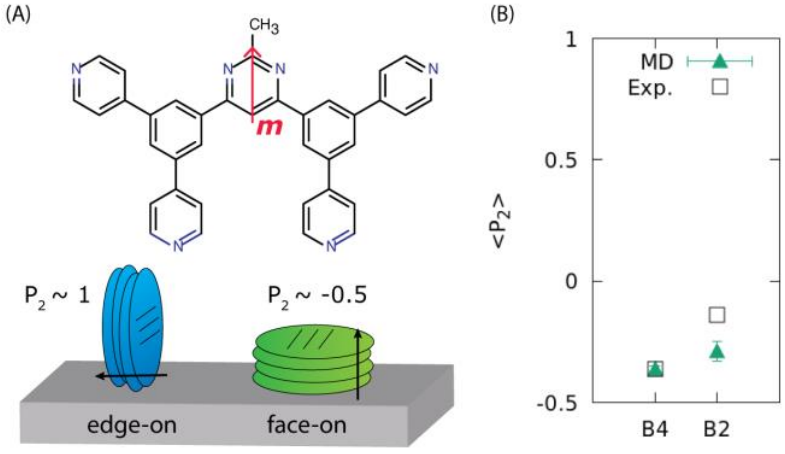

Figure 9.5: (A) scheme showing the definition of the molecular axis m (red arrow) and of face-on, edge-on orientations on a substrate. (B) parameter $\langle P_2 \rangle$ calculated from MD simulations (solid triangles) and from experiments[177] (open squares).

Here θ is the angle between an arbitrarily chosen molecular axis m and a reference direction z. The angle brackets indicate the ensemble average. Following Reference [177], we choose the axis m as the symmetry axis in the pyrimidine plane (as illustrated in Figure 9.5A). With this choice, $P_2 = 1$ when every molecular axis is oriented parallel to the z vector (the normal to the surface), and hence in a perfect edge-on configuration, $P_2 = 0$ for an isotropic distribution of orientations, and $P_2 = -0.5$ for a perfect face-on distribution. In Figure 9.5B, computed and experimental P_2 are compared: while for B2 the orientational order is slightly overestimated with respect to the measured value, the calculated values show the same trend as the experimental data, with B4 being more ordered and exhibiting a more pronounced "face-on" orientation that B2.

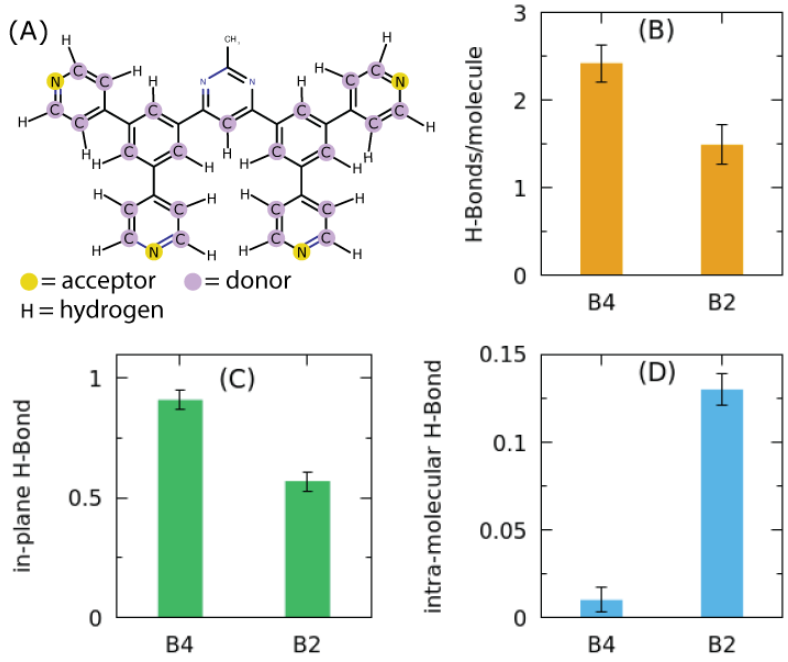

Figure 9.6: (A) Definition of hydrogen bond acceptor and donor sites for B4. (B) Average number of H-bonds/molecule. (C) In-plane H-bond fraction, and (D) intra molecular H-bond fraction.

To detect H-bond features, simulation trajectories were analyzed and hydrogen bond were counted when the distance between acceptor (A) and donor

(D) was shorter or equal than a cutoff distance ($r_C = 0.3$ nm) and the angle $\theta_{(A-H-D)}$ was larger than $\theta_{\text{cutoff}} = 120°$. Furthermore, all the hydrogen bonds were classified as in-plane or out-of-plane, if D-A distance was less than 4 Å (π-stacking distance) or larger, and also as either intramolecular or intermolecular.

In agreement with the experimental evidences,[177,213–217] a higher average number of H-bonds/molecule (≈ 2.5) were found for B4 with respect to B2 (≈ 1.5) (see Figure 9.6B) and, moreover, B4 forms almost exclusively intermolecular H-bonds which promote inter-column connections between pairs of coplanar molecules.

9.4 Electron transfer parameters

As already mentioned, Kido and coauthors[177] measured the electron mobility of B2 and B4 with the time of flight technique, obtaining at room temperature values of the order of 10^{-6} and 10^{-4} cm^2 V^{-1}s^{-1}, respectively. Here, exploiting the atomic resolution of the system morphologies provided by MD simulations, we aim at establishing a link between structural and electronic properties, and analyze the factors that contribute to the large offset between B2 and B4 mobility.

Most organic semiconductors with mobilities below $\approx$1 cm^2/Vs are characterized by thermally activated hopping-like transport. The most popular, semiclassical rate equation for charge hopping is due to Marcus[218], stating a proportionality between the hopping rate k_{ij} between two molecules i and j and the square of the intermolecular electronic coupling J_{ij}, and an Arrhenius-like exponential dependence with activation barrier $(\Delta G_{ij} + \lambda)^2/(4\lambda)$:

$$k_{ij} = \frac{2\pi}{\hbar} \frac{J_{ij}^2}{\sqrt{4\pi\lambda k_B T}} \exp - \frac{(\Delta G_{ij} + \lambda)^2}{4\lambda k_B T} \tag{9.2}$$

Here $\lambda = \lambda_i + \lambda_s$ is the total reorganization energy, quantifying the dynamic

energetic fluctuations and including both the internal (λ_i) and environmental contribution (λ_s); ΔG_{ij} is the difference between the molecular site energies (averaged over dynamic fluctuations) and possiblly including the effect of an applied electric field. For electron transport, the site energies correspond to the electron affinity EA with reversed sign, i.e.

$$\Delta G_{ij} = -EA_j + EA_i \tag{9.3}$$

The site energy of a given molecule includes an intramolecular and an environmental component:[219]

$$EA = EA_{\text{gas}} - \Delta \tag{9.4}$$

The term EA_{gas} corresponds to the electron affinity of the isolated molecule, and we approximated it with the LUMO energy, E_{LUMO}. The environmental component Δ was instead obtained with classical microelectrostatic (ME) calculations using MESCal code,[220] in which molecules interact through forces between atomic permanent charges and induced dipoles, the latter requiring a self-consistent treatment of mutual interactions. The environmental contribution to site energies can be further partitioned into an electrostatic (Δ_E) and an induction (Δ_I) term, $\Delta = \Delta_E + \Delta_I$. In particular, Δ_E corresponds to the energy to charge a molecule in the electrostatic potential of the permanent and induced multipoles of the surrounding molecules in the neutral sample, while Δ_I accounts for the dielectric screening of the added charge by the polarizable medium.[221] The induction term Δ_I affects the absolute values of the energy levels, typically increasing the EA by ≈ 1 eV, but it is essentially isotropic and then contributes only marginally to the spread of the transport levels.[219] This term was therefore disregarded, since our primary interest was the estimation of energetic disorder.

Our simulated samples are in fact characterized by the presence of structural disorder which may strongly affect the energetics of localized charge carriers (see e.g. Reference [222] for a discussion of different effects in play).

Each molecule experiences a different electrostatic environment, and this leads to a broad distribution of charge transport levels. These distributions often feature an approximately Gaussian shape, whose standard deviation σ is taken as a measure of the energetic disorder. The broadening of transport levels was estimated by sampling the EA over all the molecules, and for 11 thin film MD configurations. This allowed us also to compute the static (or positional) and dynamic nature in of the energetic disorder. To such an aim, we consider the average $\overline{x}_m$ and the variance σ_m^2 of the energy of molecule m over different configurations. Static and dynamic disorder are then computed as $\sigma_{\text{static}} = \sqrt{\langle(\overline{x}_m - \langle x\rangle)^2\rangle}$ and $\sigma_{\text{dynamic}} = \sqrt{\langle\overline{x}_m^2\rangle}$, respectively, where angle brackets denote the average over the molecules in the sample. It can be shown that $\sigma_{\text{total}}^2 = \sigma_{\text{static}}^2 + \sigma_{\text{dynamic}}^2$.

For the parameterization of the ME method, molecular polarizability and ESP charges[207] for neutral B2 and B4 molecules and the anions were obtained at the equilibrium geometry by PBE0/ccpVTZ DFT calculations using Gaussian16.[223] The simulated samples were treated as thin films, applying periodic boundary conditions in two dimensions (x, y) and constructing supercells of the original samples. We have verified that a cutoff of 44 nm (about 8 times the average thickness of the samples) ensures a proper convergence of electrostatic interactions, i.e. within 50 meV for absolute energies and 5 meV for energy differences between sites.

Electronic couplings were calculated for every pair of molecules ("dimers", having at least two atoms at distance lower than 7 Å) in a single configuration of the B2 and B4 samples. Calculations were carried out at DFT level B3LYP/6-31G(d), with ORCA code[224] using the dimer projection method.[225] The intermolecular reorganization energies λ_i for B2 and B4 were calculated using the four-point method[226] via PBE0/cc-pVTZ calculations, and amount to 0.3 eV for B2 and 0.32 for B4, respectively. These values are considerably larger than the one of the prototypical n-type organic semiconductor C60 fullerene.[227,228]

We begin the comparison of the charge transport properties of the two

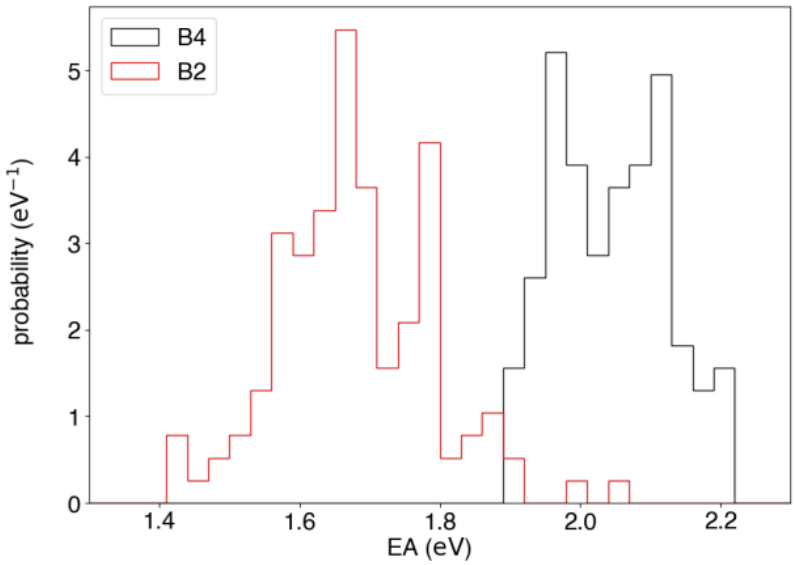

Figure 9.7: Distribution of electron affinities for B4 and B2, averaged on eleven MD configurations. Individual values were obtained as $EA = -E_{\mathrm{LUMO}} - \Delta_E$ by DFT and microelectrostatic calculations.

systems by inspecting the distributions of electron affinities, i.e. the density of states available to charge carriers. The histograms in Figure 9.7 clearly show two main differences: first, B4 has an electron affinity larger than B2, which is a positive characteristic because it improves the air stability of the semiconductor[229] and facilitates a possible doping by electron donating impurities. Moreover, the distribution of electron affinity for B4 is narrower than the one for B2. Again, this goes in favor of superior electron transport in the B4 system, since the standard deviation of the distribution σ quantifies of the energetic disorder, which in turn is one of the main limiting factors for charge mobility.[222]

For a quantitative analysis of the energetic disorder and its nature, we then analyzed the standard deviations of EA, E_{LUMO} and Δ_E, reported in Table 9.1 and Figure 9.8. It is also useful to partition the disorder in a static (or positional) term, that does not change in time and affects the ΔG_{ij} values in Equation (9.2), and a dynamic one which instead has to be included

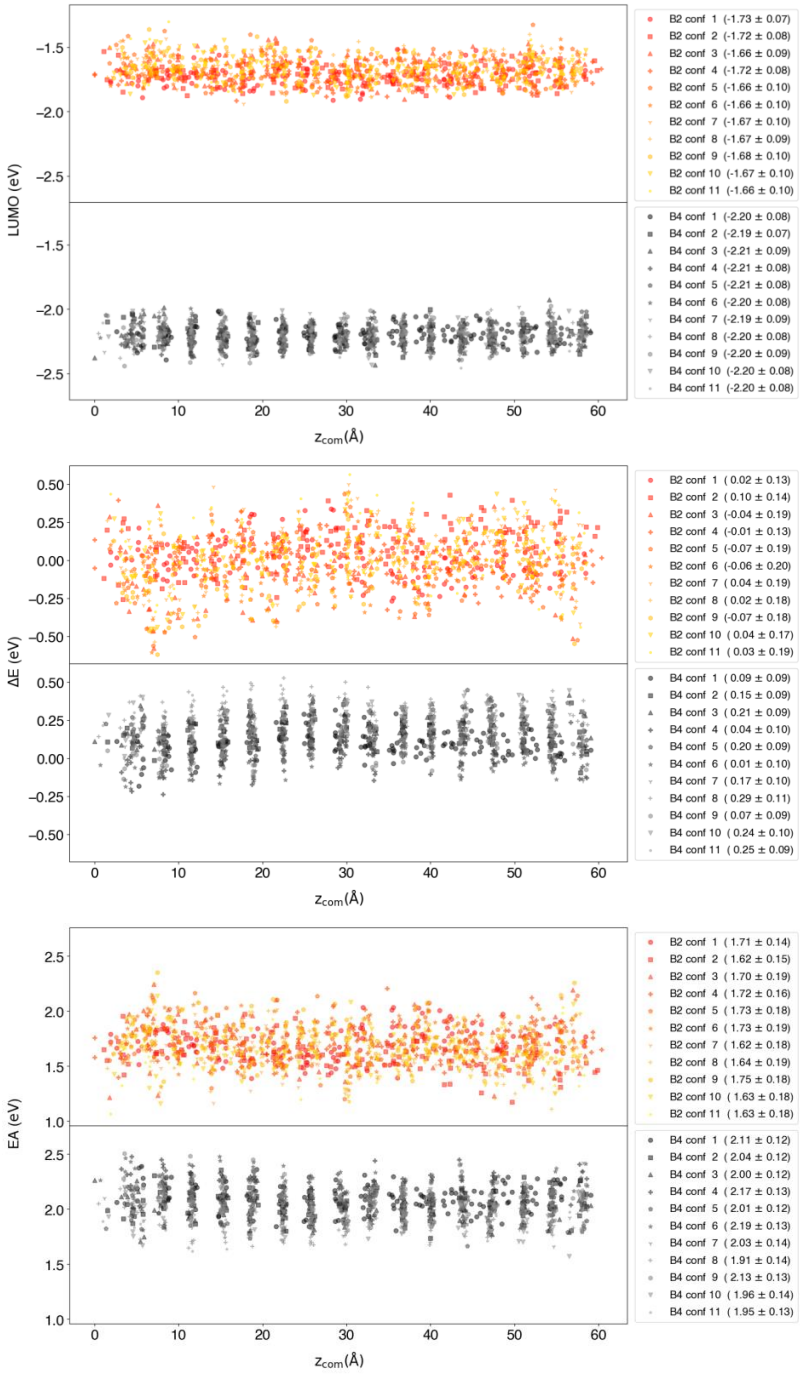

Figure 9.8: Scatter plots of various components of the electronic affinity EA as a function of the coordinate z along the stack axis, calculated on 11 different samples for B2 (color) and B4 (gray). From the top: intramolecular contribution E_{LUMO}, intermolecular contribution Δ_E, total electron affinities $EA = -E_{\mathrm{LUMO}} - \Delta_E$.

Table 9.1: Averages of intramolecular (E_{LUMO}), intermolecular (Δ_E), and total electron affinities ($EA = -E_{\mathrm{LUMO}} - \Delta_E$), and corresponding standard deviations separated in static and dynamic contributions σ_{static} and $\sigma_{\mathrm{dynamic}}$. Average energies are in eV, standard deviations in meV.

B2	average	σ_{total}	σ_{static}	$\sigma_{\mathrm{dynamic}}$
E_{LUMO}	−1.681	97	50	83
Δ_E	0.000	181	124	132
EA	1.681	183	111	145
B4	average	σ_{total}	σ_{static}	$\sigma_{\mathrm{dynamic}}$
E_{LUMO}	−2.201	81	30	75
Δ_E	0.156	129	67	110
EA	2.046	156	81	134

in the reorganization energy λ.[227] Both static and dynamic terms negatively impact charge transfer rates, ultimately reducing the mobility, although each with a distinct physical mechanism.

We note that the calculated static disorder of EA is larger for B2, and qualitatively in line with the experimental values (0.091 and 0.076 eV for B2 and B4, respectively[177]), which were obtained by fitting mobility dependence on electric field and temperature with an empirical but well established equation for amorphous semiconductors.[230] This observation is in line with the higher structural order present in B4 samples. The amount of dynamic disorder is instead rather similar for the two systems, yet again slightly larger for B2. These room-temperature energetic fluctuations correspond to a reorganization energy $\lambda = \frac{\sigma^2_{\mathrm{dynamic}}}{k_B T}$ about 0.12 eV higher for B2. From Table 9.1 it can be further seen that the difference in energetic disorder between the two systems, both for the static and dynamic component, is sourced from the environmental electrostatic contribution Δ_E, while the fluctuations of the LUMO energies are quite similar, albeit again a bit larger for B2.

To explain the higher disorder of the energy levels in B2 and its chiefly dynamic nature, let us consider the four terminal pyridine units: any thermally activated rotation about the pyridine-phenyl bond (T2 torsion in Figure 9.1) marginally affects the electrostatic layout of B4, where the local dipole as-

sociated with the pyridine nitrogen is coaxial with the bond. On the other hand, pyridine rotations can produce a rather large variation of charge distribution for B2, where the dipole is off-axis. This implies that for B2 a given amount of dynamic conformational disorder translates in more important variations of the electrostatic landscape felt by charge carriers. The argument is strengthened by the DFT calculation of the gas phase molecular dipoles along the trajectories, that yields larger values and fluctuations for B2: 2.9 ± 1.3 D versus 0.8 ± 0.3 D for B4.

We now focus our attention on the magnitude and fluctuations of intermolecular electron-transfer couplings J, representing the pre-exponential factor in Equation (9.2), and on their relationship with the structural organization in the simulated samples. Figure 9.9 compares the magnitude and directionality of intermolecular couplings between the two materials, reporting the absolute value of J, computed for molecular pairs in our MD samples, against r_z/r (gray dots), being r the module of the intermolecular distance and r_z its z-axis component. Charge transfer couplings are highly anisotropic in both systems (see also Figure 9.10), attaining appreciable values only when the intermolecular vector is parallel to the stacking direction ($r_z/r > 0.6$). As better appreciated by observing the average values of $|J|$ over r_z/r intervals (red squares), the magnitude of the couplings is significantly larger in B4 than in B2, and this difference determines a superior electronic connectivity with respect to B2. This quantity, shown in Figure 9.9B, corresponds to number of neighbors that, on average, is connected to each molecule by a coupling exceeding a given value of $|J|$. The two systems approach in a very different way the connectivity of 2 characteristic of an ideal 1D semiconductor, with e.g. B4 attaining the value of 1.5 with couplings of $|J| = 41$ meV, and B2 only for 12 meV.

The superior charge transfer properties of B4 as compared to B2 are completely unexpected at the molecular level, given the similar structure and the nearly identical LUMO orbitals (see inset Figure 9.9A) of the two molecules.[177] We infer that the difference between the two materials is due

to the better supramolecular packing of B4 discussed above. To prove this hypothesis with an "alchemical" experiment, impossible to perform with real systems, we have computed the intermolecular couplings for a fictitious B4 phase, obtained from the atomic coordinates of the B2 sample by switching the positions of the N atom and one CH group in the peripheral pyridine rings. Figure 9.9C, compares the couplings of this hypothetical sample, labelled "B4 < B2", with the original B2 ones. This plot reveals a nearly perfect correlation between the two data sets (Pearson coefficient $R = 0.994$), demonstrating that the differences between the charge transport properties of the two materials do not arise from the chemical structure. They have instead to be ascribed to the better molecular organization in B4, in turn resulting from the presence of a two-dimensional H-bond network.

9.5 Conclusions

Combining DFT calculations and MD all-atom simulations we investigated the role of intermolecular hydrogen bonds in the molecular orientation, stacking and electron carrier mobility of thin films composed of pyridine-based molecules B2 and B4.

The only difference between the B4 and B2 chemical structure lies in the position of nitrogen atoms in the four outer pyridine rings, which is surprisingly sufficient for causing a huge difference in the optical and electron transport properties, as experimentally proved. We found that B4 has a higher capability to connect with adjacent molecules, by intermolecular hydrogen bonds, compared with B2 (2.5 vs 1.5 bonds per molecule). The stronger 2D H-bond network formed for B4 is sufficient to stabilize a supramolecular organization in which molecules form ordered layers and columns.

The calculation of essential electron transport parameters, such as reorganization energies, site energies, and electronic couplings revealed that the microscopic origin of the higher electron mobility of B4 with respect to B2 has its roots in lower reorganization energy and electrostatic disorder and, more importantly, in the superior morphology promoted by the hydrogen

bond network.

On a general vein, our findings disclose how intermolecular hydrogen bond interactions promote structural order in molecular thin films, ultimately improving their electron transport properties. The engineering of these weak interactions offers viable opportunities for the rational design of new materials with improved performances in OLED applications.

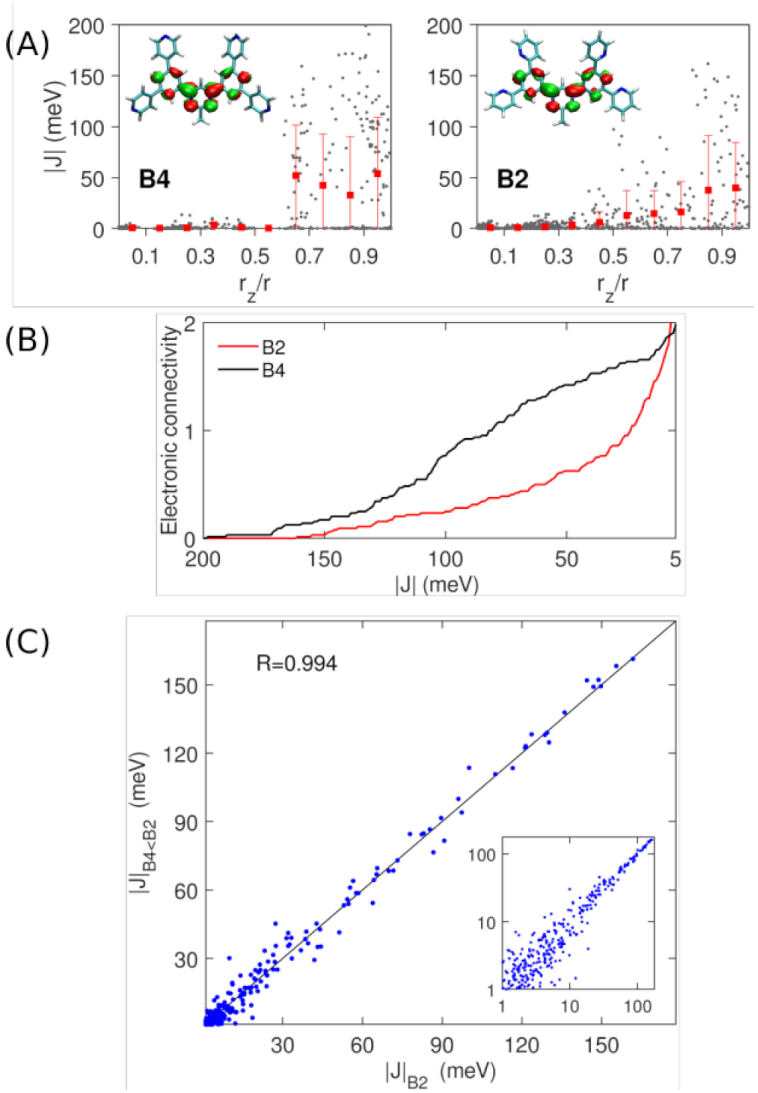

Figure 9.9: (A) Electron-transfer couplings as a function of the normalized projection of the intermolecular vector distance r along the stacking axis z. Gray dots show the couplings computed for molecular pairs extracted from the MD sample, red squared (error bars) show the mean value (standard deviation) over intervals of r_z/r. LUMO orbitals of B4 and B2 are shown as insets. (B) Electronic connectivity, i.e. average number of neighbors per molecule having an electronic coupling larger than the abscissa value. (C) Correlation between the couplings of B2 and those of a fictitious B4 sample obtained modifying the atomistic morphologies of B2 (see text). The quadrant bisector (black line) is shown as a guide for the eye. The same plot in a log-log scale in shown as an inset.

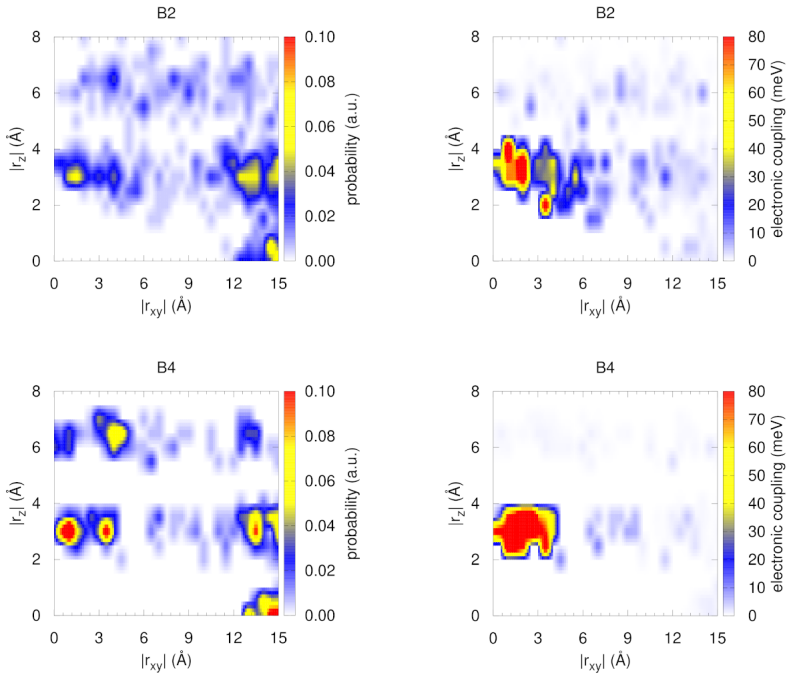

Figure 9.10: Probability of finding a neighbor molecule as a function of the component of the intermolecular vector parallel (r_z) and perpendicular (r_{xy}) to the stacking direction, and (right) corresponding average value of the electronic coupling.

Bibliography

[1] David A. Bardwell et al. "Towards crystal structure prediction of complex organic compounds - a report on the fifth blind test". In: *Acta Crystallographica Section B Structural Science* 67.6 (Nov. 2011), pp. 535–551. DOI: 10.1107/s0108768111042868.

[2] Jos P. M. Lommerse et al. "A test of crystal structure prediction of small organic molecules". In: *Acta Crystallographica Section B Structural Science* 56.4 (Aug. 2000), pp. 697–714. DOI: 10.1107/s0108768100004584.

[3] G. M. Day et al. "A third blind test of crystal structure prediction". In: *Acta Crystallographica Section B Structural Science* 61.5 (Sept. 2005), pp. 511–527. DOI: 10.1107/s0108768105016563.

[4] W. Kohn and L. J. Sham. "Self-Consistent Equations Including Exchange and Correlation Effects". In: *Physical Review* 140.4A (Nov. 1965), A1133–A1138. DOI: 10.1103/physrev.140.a1133.

[5] G. Kresse and J. Hafner. "Ab initiomolecular dynamics for liquid metals". In: *Physical Review B* 47.1 (Jan. 1993), pp. 558–561. DOI: 10.1103/physrevb.47.558.

[6] G. Kresse and J. Hafner. "Ab initiomolecular-dynamics simulation of the liquid-metal-amorphous-semiconductor transition in germanium". In: *Physical Review B* 49.20 (May 1994), pp. 14251–14269. DOI: 10.1103/physrevb.49.14251.

[7] G. Kresse and J. Furthmüller. "Efficiency of ab-initio total energy calculations for metals and semiconductors using a plane-wave basis

set". In: *Computational Materials Science* 6.1 (July 1996), pp. 15–50. DOI: 10.1016/0927-0256(96)00008-0.

[8] G. Kresse and J. Furthmüller. "Efficient iterative schemes forab initiototal-energy calculations using a plane-wave basis set". In: *Physical Review B* 54.16 (Oct. 1996), pp. 11169–11186. DOI: 10.1103/physrevb.54.11169.

[9] Roberto Dovesi et al. "Quantum-mechanical condensed matter simulations with CRYSTAL". In: *Wiley Interdisciplinary Reviews: Computational Molecular Science* 8.4 (Mar. 2018), e1360. DOI: 10.1002/wcms.1360.

[10] Jiří Klimeš and Angelos Michaelides. "Perspective: Advances and challenges in treating van der Waals dispersion forces in density functional theory". In: *The Journal of Chemical Physics* 137.12 (Sept. 2012), p. 120901. DOI: 10.1063/1.4754130.

[11] Alexandre Tkatchenko et al. "Accurate and Efficient Method for Many-Body van der Waals Interactions". In: *Physical Review Letters* 108.23 (June 2012). DOI: 10.1103/physrevlett.108.236402.

[12] Stefan Grimme. "Semiempirical GGA-type density functional constructed with a long-range dispersion correction". In: *Journal of Computational Chemistry* 27.15 (2006), pp. 1787–1799. DOI: 10.1002/jcc.20495.

[13] Stefan Grimme, Stephan Ehrlich, and Lars Goerigk. "Effect of the damping function in dispersion corrected density functional theory". In: *Journal of Computational Chemistry* 32.7 (Mar. 2011), pp. 1456–1465. DOI: 10.1002/jcc.21759.

[14] Alexandre Tkatchenko and Matthias Scheffler. "Accurate Molecular Van Der Waals Interactions from Ground-State Electron Density and Free-Atom Reference Data". In: *Physical Review Letters* 102.7 (Feb. 2009). DOI: 10.1103/physrevlett.102.073005.

[15] Jiří Klimeš, David R Bowler, and Angelos Michaelides. "Chemical accuracy for the van der Waals density functional". In: *Journal of Physics: Condensed Matter* 22.2 (Dec. 2009), p. 022201. DOI: 10.1088/0953-8984/22/2/022201.

[16] Jiří Klimeš, David R. Bowler, and Angelos Michaelides. "Van der Waals density functionals applied to solids". In: *Physical Review B* 83.19 (May 2011). DOI: 10.1103/physrevb.83.195131.

[17] Alberto Ambrosetti et al. "Long-range correlation energy calculated from coupled atomic response functions". In: *The Journal of Chemical Physics* 140.18 (May 2014), 18A508. DOI: 10.1063/1.4865104.

[18] Graeme M. Day et al. "Significant progress in predicting the crystal structures of small organic molecules - a report on the fourth blind test". In: *Acta Crystallographica Section B Structural Science* 65.2 (Mar. 2009), pp. 107–125. DOI: 10.1107/s0108768109004066.

[19] Marcus A. Neumann, Frank J. J. Leusen, and John Kendrick. "A Major Advance in Crystal Structure Prediction". In: *Angewandte Chemie International Edition* 47.13 (Mar. 2008), pp. 2427–2430. DOI: 10.1002/anie.200704247.

[20] Natalia Bedoya-Martínez et al. "DFT-Assisted Polymorph Identification from Lattice Raman Fingerprinting". In: *The Journal of Physical Chemistry Letters* 8.15 (July 2017), pp. 3690–3695. DOI: 10.1021/acs.jpclett.7b01634.

[21] Aldo Brillante et al. "Probing polymorphs of organic semiconductors by lattice phonon Raman microscopy". In: *CrystEngComm* 10.8 (2008), p. 937. DOI: 10.1039/b804317e.

[22] Tommaso Salzillo et al. "Two New Polymorphs of the Organic Semiconductor 9,10-Diphenylanthracene: Raman and X-ray Analysis". In: *The Journal of Physical Chemistry C* 120.3 (Jan. 2016), pp. 1831–1840. DOI: 10.1021/acs.jpcc.5b11115.

[23] Arianna Rivalta et al. "Bulk and Surface-Stabilized Structures of Paracetamol Revisited by Raman Confocal Microscopy". In: *ACS Omega* 3.8 (Aug. 2018), pp. 9564–9571. DOI: 10.1021/acsomega.8b01246.

[24] Benedikt Schrode et al. "Substrate-Induced Phase of a Benzothiophene Derivative Detected by Mid-Infrared and Lattice Phonon Raman Spectroscopy". In: *ChemPhysChem* 19.8 (Mar. 2018), pp. 993–1000. DOI: 10.1002/cphc.201701378.

[25] Tommaso Salzillo et al. "An Alternative Strategy to Polymorph Recognition at Work: The Emblematic Case of Coronene". In: *Crystal Growth & Design* 18.9 (July 2018), pp. 4869–4873. DOI: 10.1021/acs.cgd.8b00934.

[26] Natalia Bedoya-Martínez et al. "Toward a Reliable Description of the Lattice Vibrations in Organic Molecular Crystals: The Impact of van der Waals Interactions". In: *Journal of Chemical Theory and Computation* 14.8 (July 2018), pp. 4380–4390. DOI: 10.1021/acs.jctc.8b00484.

[27] Lorenzo Pandolfi et al. "In Search of Surface-Induced Crystal Structures: The Case of Tyrian Purple". In: *The Journal of Physical Chemistry C* 124.32 (July 2020), pp. 17702–17710. DOI: 10.1021/acs.jpcc.0c05186.

[28] T. Salzillo et al. "Structural, Spectroscopic, and Computational Characterization of the Concomitant Polymorphs of the Natural Semiconductor Indigo". In: *The Journal of Physical Chemistry C* 122.32 (July 2018), pp. 18422–18431. DOI: 10.1021/acs.jpcc.8b03635.

[29] Doris E. Braun et al. "Surface Induced Phenytoin Polymorph. 1. Full Structure Solution by Combining Grazing Incidence X-ray Diffraction and Crystal Structure Prediction". In: *Crystal Growth & Design* 19.11 (Sept. 2019), pp. 6058–6066. DOI: 10.1021/acs.cgd.9b00857.

[30] Andrea Giunchi et al. "Surface Induced Phenytoin Polymorph. 2. Structure Validation by Comparing Experimental and Density Func-

tional Theory Raman Spectra". In: *Crystal Growth & Design* 19.11 (Sept. 2019), pp. 6067–6073. DOI: 10.1021/acs.cgd.9b00863.

[31] A. Rivalta et al. "Crystal alignment of surface stabilized polymorph in thioindigo films". In: *Dyes and Pigments* 172 (Jan. 2020), p. 107847. DOI: 10.1016/j.dyepig.2019.107847.

[32] Flavia Aleotti et al. "Spectral Tuning and Photoisomerization Efficiency in Push-Pull Azobenzenes: Designing Principles". In: *The Journal of Physical Chemistry A* 124.46 (Nov. 2020), pp. 9513–9523. DOI: 10.1021/acs.jpca.0c08672.

[33] L. Pandolfi et al. "The impact of solid-solution composition on kinetics and mechanism of [2+2] photodimerizations of cinnamic acid derivatives." accepted for publication. 2021.

[34] A. De Nicola et al. "Bidimensional H-bond network promotes structural order and electron transport in BPyMPMs molecular semiconductors". currently under review.

[35] A. Rivalta et al. "Growth, Morphology and Molecular Orientation of Controlled Indigo thin films on Silica Surfaces." currently under review. 2020.

[36] P. E. Blöchl. "Projector augmented-wave method". In: *Physical Review B* 50.24 (Dec. 1994), pp. 17953–17979. DOI: 10.1103/physrevb.50.17953.

[37] G. Kresse and D. Joubert. "From ultrasoft pseudopotentials to the projector augmented-wave method". In: *Physical Review B* 59.3 (Jan. 1999), pp. 1758–1775. DOI: 10.1103/physrevb.59.1758.

[38] Tomáš Bučko, Jürgen Hafner, and János G. Ángyán. "Geometry optimization of periodic systems using internal coordinates". In: *The Journal of Chemical Physics* 122.12 (Mar. 2005), p. 124508. DOI: 10.1063/1.1864932.

[39] Gregory J. O. Beran, Joshua D. Hartman, and Yonaton N. Heit. "Predicting Molecular Crystal Properties from First Principles: Finite-Temperature Thermochemistry to NMR Crystallography". In: *Accounts of Chemical Research* 49.11 (Oct. 2016), pp. 2501–2508. DOI: 10.1021/acs.accounts.6b00404.

[40] Yonaton N. Heit and Gregory J. O. Beran. "How important is thermal expansion for predicting molecular crystal structures and thermochemistry at finite temperatures?" In: *Acta Crystallographica Section B Structural Science, Crystal Engineering and Materials* 72.4 (July 2016), pp. 514–529. DOI: 10.1107/s2052520616005382.

[41] Jan Gerit Brandenburg et al. "Thermal Expansion of Carbamazepine: Systematic Crystallographic Measurements Challenge Quantum Chemical Calculations". In: *The Journal of Physical Chemistry Letters* 8.17 (Aug. 2017), pp. 4319–4324. DOI: 10.1021/acs.jpclett.7b01944.

[42] Hendrik J. Monkhorst and James D. Pack. "Special points for Brillouin-zone integrations". In: *Physical Review B* 13.12 (June 1976), pp. 5188–5192. DOI: 10.1103/physrevb.13.5188.

[43] James Alexander Chisholm and Sam Motherwell. "COMPACK: a program for identifying crystal structure similarity using distances". In: *Journal of Applied Crystallography* 38.1 (Jan. 2005), pp. 228–231. DOI: 10.1107/s0021889804027074.

[44] Aurora J. Cruz-Cabeza and Joel Bernstein. "Conformational Polymorphism". In: *Chemical Reviews* 114.4 (Dec. 2013), pp. 2170–2191. DOI: 10.1021/cr400249d.

[45] Atsushi Togo and Isao Tanaka. "First principles phonon calculations in materials science". In: *Scripta Materialia* 108 (Nov. 2015), pp. 1–5. DOI: 10.1016/j.scriptamat.2015.07.021.

[46] Dirk Porezag and Mark R. Pederson. "Infrared intensities and Raman-scattering activities within density-functional theory". In: *Physical Review B* 54.11 (Sept. 1996), pp. 7830–7836. DOI: 10.1103/physrevb.54.7830.

[47] A. Fonari and S. Stauffer. *vasp_raman.py*. https://github.com/raman-sc/VASP/, 2013.

[48] E. Bright Wilson et al. "Molecular Vibrations". In: *American Journal of Physics* 23.8 (Nov. 1955), pp. 550–550. DOI: 10.1119/1.1934101.

[49] Danuta Michalska and Rafał Wysokiński. "The prediction of Raman spectra of platinum(II) anticancer drugs by density functional theory". In: *Chemical Physics Letters* 403.1-3 (Feb. 2005), pp. 211–217. DOI: 10.1016/j.cplett.2004.12.096.

[50] Anthony P. Scott and Leo Radom. "Harmonic Vibrational Frequencies: An Evaluation of Hartree-Fock, Møller-Plesset, Quadratic Configuration Interaction, Density Functional Theory, and Semiempirical Scale Factors". In: *The Journal of Physical Chemistry* 100.41 (Jan. 1996), pp. 16502–16513. DOI: 10.1021/jp960976r.

[51] M. P. Andersson and P. Uvdal. "New Scale Factors for Harmonic Vibrational Frequencies Using the B3LYP Density Functional Method with the Triple-
zeta Basis Set 6-311+G(d,p)". In: *The Journal of Physical Chemistry A* 109.12 (Mar. 2005), pp. 2937–2941. DOI: 10.1021/jp045733a.

[52] Jan Hermann, Robert A. DiStasio, and Alexandre Tkatchenko. "First-Principles Models for van der Waals Interactions in Molecules and Materials: Concepts, Theory, and Applications". In: *Chemical Reviews* 117.6 (Mar. 2017), pp. 4714–4758. DOI: 10.1021/acs.chemrev.6b00446.

[53] Stefan Grimme et al. "Dispersion-Corrected Mean-Field Electronic Structure Methods". In: *Chemical Reviews* 116.9 (Apr. 2016), pp. 5105–5154. DOI: 10.1021/acs.chemrev.5b00533.

[54] Anthony M. Reilly and Alexandre Tkatchenko. "Role of Dispersion Interactions in the Polymorphism and Entropic Stabilization of the Aspirin Crystal". In: *Physical Review Letters* 113.5 (July 2014). DOI: 10.1103/physrevlett.113.055701.

[55] Florian Brown-Altvater, Tonatiuh Rangel, and Jeffrey B. Neaton. "Ab initiophonon dispersion in crystalline naphthalene using van der Waals density functionals". In: *Physical Review B* 93.19 (May 2016). DOI: 10.1103/physrevb.93.195206.

[56] Ido Azuri et al. "THz Spectroscopy of 2,4,6-trinitrotoluene Molecular Solids from First Principles". In: *APS March Meeting Abstracts*. Vol. 2018. APS Meeting Abstracts. Jan. 2018, Y36.002.

[57] M. Bezerra da Silva et al. "Vibrational Properties of Bulk Boric Acid 2A and 3T Polymorphs and Their Two-Dimensional Layers: Measurements and Density Functional Theory Calculations". In: *The Journal of Physical Chemistry A* 122.5 (Jan. 2018), pp. 1312–1325. DOI: 10.1021/acs.jpca.7b10083.

[58] Janine George et al. "Lattice thermal expansion and anisotropic displacements in urea, bromomalonic aldehyde, pentachloropyridine, and naphthalene". In: *The Journal of Chemical Physics* 147.7 (Aug. 2017), p. 074112. DOI: 10.1063/1.4985886.

[59] M. Dion et al. "Van der Waals Density Functional for General Geometries". In: *Physical Review Letters* 92.24 (June 2004). DOI: 10.1103/physrevlett.92.246401.

[60] Kyuho Lee et al. "Higher-accuracy van der Waals density functional". In: *Physical Review B* 82.8 (Aug. 2010). DOI: 10.1103/physrevb.82.081101.

[61] Stefan Grimme et al. "A consistent and accurate ab initio parametrization of density functional dispersion correction (DFT-D) for the 94 elements H-Pu". In: *The Journal of Chemical Physics* 132.15 (Apr. 2010), p. 154104. DOI: 10.1063/1.3382344.

[62] Stephan N. Steinmann and Clemence Corminboeuf. "A generalized-gradient approximation exchange hole model for dispersion coefficients". In: *The Journal of Chemical Physics* 134.4 (Jan. 2011), p. 044117. DOI: 10.1063/1.3545985.

[63] Tomáš Bučko et al. “Improved Density Dependent Correction for the Description of London Dispersion Forces”. In: *Journal of Chemical Theory and Computation* 9.10 (Sept. 2013), pp. 4293–4299. DOI: 10.1021/ct400694h.

[64] Tomáš Bučko et al. “Extending the applicability of the Tkatchenko-Scheffler dispersion correction via iterative Hirshfeld partitioning”. In: *The Journal of Chemical Physics* 141.3 (July 2014), p. 034114. DOI: 10.1063/1.4890003.

[65] Kristian Berland et al. “van der Waals forces in density functional theory: a review of the vdW-DF method”. In: *Reports on Progress in Physics* 78.6 (May 2015), p. 066501. DOI: 10.1088/0034-4885/78/6/066501.

[66] Tomáš Bučko et al. “Many-body dispersion corrections for periodic systems: an efficient reciprocal space implementation”. In: *Journal of Physics: Condensed Matter* 28.4 (Jan. 2016), p. 045201. DOI: 10.1088/0953-8984/28/4/045201.

[67] Aldo Brillante et al. “The four polymorphic modifications of the semiconductor dibenzo-tetrathiafulvalene”. In: *CrystEngComm* 10.12 (2008), p. 1899. DOI: 10.1039/b810993a.

[68] Aldo Brillante et al. “Phase recognition by lattice phonon Raman spectra: The triclinic structure of the organic semiconductor dibenzo-tetrathiafulvalene”. In: *Chemical Physics Letters* 523 (Jan. 2012), pp. 74–77. DOI: 10.1016/j.cplett.2011.12.026.

[69] H.-D. Becker and V. Langer. “Crystal structure of 9,10-diphenylanthracene, (C6H5XC14H8XC6H5)”. In: *Zeitschrift für Kristallographie - Crystalline Materials* 199.1-4 (Jan. 1992). DOI: 10.1524/zkri.1992.199.14.313.

[70] Andrew O. F. Jones et al. “Substrate-Induced Phase of a [1]Benzothieno[3,2-b]benzothiophene Derivative and Phase Evolution by Aging and Solvent Vapor Annealing”. In: *ACS Applied Materials & Interfaces* 7.3 (Jan. 2015), pp. 1868–1873. DOI: 10.1021/am5075908.

[71] Christian Ruzié et al. "Design, synthesis, chemical stability, packing, cyclic voltammetry, ionisation potential, and charge transport of [1]benzothieno[3,2-b][1]benzothiophene derivatives". In: *Journal of Materials Chemistry C* 4.22 (2016), pp. 4863–4879. DOI: 10.1039/c6tc01409g.

[72] Tim Gould et al. "A Fractionally Ionic Approach to Polarizability and van der Waals Many-Body Dispersion Calculations". In: *Journal of Chemical Theory and Computation* 12.12 (Dec. 2016), pp. 5920–5930. DOI: 10.1021/acs.jctc.6b00925.

[73] Ismael Diez-Perez et al. "Gate-controlled electron transport in coronenes as a bottom-up approach towards graphene transistors". In: *Nature Communications* 1.1 (June 2010). DOI: 10.1038/ncomms1029.

[74] E. Jennings, W. Montgomery, and Ph. Lerch. "Stability of Coronene at High Temperature and Pressure". In: *The Journal of Physical Chemistry B* 114.48 (Dec. 2010), pp. 15753–15758. DOI: 10.1021/jp105020f.

[75] A. D. Chanyshev et al. "Compressibility, phase transitions and amorphization of coronene at pressures up to 6 GPa". In: *Journal of Structural Chemistry* 57.7 (Dec. 2016), pp. 1489–1492. DOI: 10.1134/s002247661607026x.

[76] Xiao-Miao Zhao et al. "Phase transformations and vibrational properties of coronene under pressure". In: *The Journal of Chemical Physics* 139.14 (Oct. 2013), p. 144308. DOI: 10.1063/1.4824384.

[77] Takahiro Yamamoto et al. "Exciton—phonon coupling and pressure-induced structural phase changes in coronene crystals". In: *Chemical Physics* 184.1-3 (June 1994), pp. 247–254. DOI: 10.1016/0301-0104(94)00084-0.

[78] G. R. Desiraju and A. Gavezzotti. "Crystal structures of polynuclear aromatic hydrocarbons. Classification, rationalization and prediction from molecular structure". In: *Acta Crystallographica Section B Structural Science* 45.5 (Oct. 1989), pp. 473–482. DOI: 10.1107/s0108768189003794.

[79] Jason Potticary et al. “An unforeseen polymorph of coronene by the application of magnetic fields during crystal growth”. In: *Nature Communications* 7.1 (May 2016). DOI: 10.1038/ncomms11555.

[80] Koichi Ohno, Takashi Kajiwara, and Hiroo Inokuchi. “Vibrational Analysis of Electronic Transition Bands of Coronene”. In: *Bulletin of the Chemical Society of Japan* 45.4 (Apr. 1972), pp. 996–1004. DOI: 10.1246/bcsj.45.996.

[81] Elisabetta Venuti et al. “Phonons and structures of tetracene polymorphs at low temperature and high pressure”. In: *Physical Review B* 70.10 (Sept. 2004). DOI: 10.1103/physrevb.70.104106.

[82] R. Totoki, T. Aoki-Matsumoto, and K. Mizuno. “Density of states of the lowest exciton band and the exciton bandwidth in coronene single crystals”. In: *Journal of Luminescence* 112.1-4 (Apr. 2005), pp. 308–311. DOI: 10.1016/j.jlumin.2004.09.096.

[83] Jason Potticary et al. “Low temperature magneto-morphological characterisation of coronene and the resolution of previously observed unexplained phenomena”. In: *Scientific Reports* 6.1 (Dec. 2016). DOI: 10.1038/srep38696.

[84] Olga Kataeva et al. “Crystal Growth, Dynamic and Charge Transfer Properties of New Coronene Charge Transfer Complexes”. In: *Crystal Growth & Design* 16.1 (Nov. 2015), pp. 331–338. DOI: 10.1021/acs.cgd.5b01301.

[85] Petar D. Todorov, Leonardus W. Jenneskens, and Joop H. van Lenthe. “Assignment of phantom bands in the solid-state infrared and Raman spectra of coronene: The importance of a minute out-of-plane distortion”. In: *The Journal of Chemical Physics* 132.3 (Jan. 2010), p. 034504. DOI: 10.1063/1.3282331.

[86] Graeme M. Day and Carl Henrik Görbitz. “Introduction to the special issue on crystal structure prediction”. In: *Acta Crystallographica Section B Structural Science, Crystal Engineering and Materials* 72.4 (Aug. 2016), pp. 435–436. DOI: 10.1107/s2052520616012348.

[87] H. von Eller-Pandraud. “Sur Le Polymorphisme de l’indigo”. In: *Bull Soc Chim Fr* (1955), p. 316.

[88] EA Gribova, GS Zhdanov, and GA Golder. “X-Ray Determination of the Structure of Indigo and Thorindigo”. In: *Kristallografiya* 1 (1956), pp. 53–60.

[89] P Süsse et al. “A new crystalline phase of indigo”. In: (1980).

[90] Peter Süsse, Manfred Steins, and Vladimir Kupcik. “Indigo: Crystal structure refinement based on synchrotron data”. In: *Zeitschrift für Kristallographie* 184.3-4 (Jan. 1988), pp. 269–273. DOI: 10.1524/zkri.1988.184.3-4.269.

[91] Florian Kettner et al. “Selective crystallization of indigo B by a modified sublimation method and its redetermined structure”. In: *Acta Crystallographica Section E Structure Reports Online* 67.11 (Oct. 2011), o2867–o2867. DOI: 10.1107/s1600536811040220.

[92] Boris Scherwitzl, Roland Resel, and Adolf Winkler. “Film growth, adsorption and desorption kinetics of indigo on SiO2”. In: *The Journal of Chemical Physics* 140.18 (May 2014), p. 184705. DOI: 10.1063/1.4875096.

[93] Alessandro Troisi. “Charge transport in high mobility molecular semiconductors: classical models and new theories”. In: *Chemical Society Reviews* 40.5 (2011), p. 2347. DOI: 10.1039/c0cs00198h.

[94] K Nishida et al. “Vapour Pressures and Heats of Sublimation of Some Vat Dyes”. In: *Journal of the Society of Dyers and Colourists* 102.1 (Oct. 2008), pp. 18–20. DOI: 10.1111/j.1478-4408.1986.tb01039.x.

[95] H. von Eller. “Structure de colorants indigoïdes. III-Structure cristalline de l’indigo”. In: *Bull Soc Chim Fr* (1955), p. 1433.

[96] Raffaele Guido Della Valle et al. “Inherent structures of crystalline pentacene”. In: *The Journal of Chemical Physics* 118.2 (Jan. 2003), pp. 807–815. DOI: 10.1063/1.1527896.

[97] Frank H. Stillinger and Thomas A. Weber. "Hidden structure in liquids". In: *Physical Review A* 25.2 (Feb. 1982), pp. 978–989. DOI: 10.1103/physreva.25.978.

[98] Elisabetta Venuti et al. "Probing Pentacene Polymorphs by Lattice Dynamics Calculations". In: *Journal of the American Chemical Society* 124.10 (Mar. 2002), pp. 2128–2129. DOI: 10.1021/ja0166949.

[99] Stephen L. Mayo, Barry D. Olafson, and William A. Goddard. "DREIDING: a generic force field for molecular simulations". In: *The Journal of Physical Chemistry* 94.26 (Dec. 1990), pp. 8897–8909. DOI: 10.1021/j100389a010.

[100] Michael W. Schmidt et al. "General atomic and molecular electronic structure system". In: *Journal of Computational Chemistry* 14.11 (Nov. 1993), pp. 1347–1363. DOI: 10.1002/jcc.540141112.

[101] John P. Perdew, Kieron Burke, and Matthias Ernzerhof. "Generalized Gradient Approximation Made Simple". In: *Physical Review Letters* 77.18 (Oct. 1996), pp. 3865–3868. DOI: 10.1103/physrevlett.77.3865.

[102] Angelo Gavezzotti. *Molecular aggregation: Structure analysis and molecular simulation of crystals and liquids*. Oxford University Press, 2007. ISBN: 9780198570806.

[103] Anthony M. Reilly and Alexandre Tkatchenko. "Understanding the role of vibrations, exact exchange, and many-body van der Waals interactions in the cohesive properties of molecular crystals". In: *The Journal of Chemical Physics* 139.2 (July 2013), p. 024705. DOI: 10.1063/1.4812819.

[104] J. Chickos. "Enthalpies of Sublimation after a Century of Measurement: A View as Seen through the Eyes of a Collector". In: 2003. DOI: 10.11311/jscta1974.30.116.

[105] Denis V. Anokhin et al. "Towards understanding the behavior of indigo thin films in organic field-effect transistors: a template effect of the aliphatic hydrocarbon dielectric on the crystal structure and electrical performance of the semiconductor". In: *Chemical Communications* 50.57 (2014), p. 7639. DOI: 10.1039/c4cc02431a.

[106] William Humphrey, Andrew Dalke, and Klaus Schulten. "VMD: Visual molecular dynamics". In: *Journal of Molecular Graphics* 14.1 (Feb. 1996), pp. 33–38. DOI: 10.1016/0263-7855(96)00018-5.

[107] Aleksandr Sergeevich Davydov. *Theory of Molecular Excitons*. Springer US, 1971. DOI: 10.1007/978-1-4899-5169-4.

[108] Anna Amat et al. "Theoretical and experimental investigation on the spectroscopic properties of indigo dye". In: *Journal of Molecular Structure* 993.1-3 (May 2011), pp. 43–51. DOI: 10.1016/j.molstruc.2010.11.046.

[109] Ellen Tatsch and Bernhard Schrader. "Near-infrared fourier transform Raman spectroscopy of indigoids". In: *Journal of Raman Spectroscopy* 26.6 (June 1995), pp. 467–473. DOI: 10.1002/jrs.1250260611.

[110] W. Lüttke, H. Hermann, and M. Klessinger. "Theoretically and Experimentally Determined Properties of the Fundamental Indigo Chromophore". In: *Angewandte Chemie International Edition in English* 5.6 (June 1966), pp. 598–599. DOI: 10.1002/anie.196605982.

[111] Aurora J. Cruz-Cabeza, Susan M. Reutzel-Edens, and Joel Bernstein. "Facts and fictions about polymorphism". In: *Chemical Society Reviews* 44.23 (2015), pp. 8619–8635. DOI: 10.1039/c5cs00227c.

[112] Noa Marom et al. "Many-Body Dispersion Interactions in Molecular Crystal Polymorphism". In: *Angewandte Chemie International Edition* 52.26 (May 2013), pp. 6629–6632. DOI: 10.1002/anie.201301938.

[113] Mihai Irimia-Vladu et al. “Indigo - A Natural Pigment for High Performance Ambipolar Organic Field Effect Transistors and Circuits”. In: *Advanced Materials* 24.3 (Nov. 2011), pp. 375–380. DOI: 10.1002/adma.201102619.

[114] N. M. Khusayfan, E. F. M. El-Zaidia, and M. M. El-Nahass. “Fabrication and Electrical Characteristics of Thioindigo/Silicon Heterojunction”. In: *Silicon* 10.6 (Apr. 2018), pp. 2519–2526. DOI: 10.1007/s12633-018-9786-3.

[115] Raphael Pfattner et al. “Tuning Crystal Ordering, Electronic Structure, and Morphology in Organic Semiconductors: Tetrathiafulvalenes as a Model Case”. In: *Advanced Functional Materials* 26.14 (Oct. 2015), pp. 2256–2275. DOI: 10.1002/adfm.201502446.

[116] H. von Helle. “Structure de colorants indigoïdes. IV-Structure cristalline du thioindigo”. In: *Bull Soc Chim Fr* (1955), p. 1438.

[117] W. Haase-Wessel, M. Ohmasa, and P. Süsse. “Thioindigo: Crystal structural data for modification II”. In: *Naturwissenschaften* 64.8 (Aug. 1977), pp. 435–435. DOI: 10.1007/bf00508700.

[118] Freddy G. del Pozo et al. “Single Crystal-Like Performance in Solution-Coated Thin-Film Organic Field-Effect Transistors”. In: *Advanced Functional Materials* 26.14 (Sept. 2015), pp. 2379–2386. DOI: 10.1002/adfm.201502274.

[119] S. Georgakopoulos, F. G. del Pozo, and M. Mas-Torrent. “Flexible organic transistors based on a solution-sheared PVDF insulator”. In: *Journal of Materials Chemistry C* 3.47 (2015), pp. 12199–12202. DOI: 10.1039/c5tc02488a.

[120] Inés Temiño et al. “A Rapid, Low-Cost, and Scalable Technique for Printing State-of-the-Art Organic Field-Effect Transistors”. In: *Advanced Materials Technologies* 1.5 (June 2016), p. 1600090. DOI: 10.1002/admt.201600090.

[121] P. L. Polavarapu. "Ab initio vibrational Raman and Raman optical activity spectra". In: *The Journal of Physical Chemistry* 94.21 (Oct. 1990), pp. 8106–8112. DOI: 10.1021/j100384a024.

[122] T. C. Damen, S. P. S. Porto, and B. Tell. "Raman Effect in Zinc Oxide". In: *Physical Review* 142.2 (Feb. 1966), pp. 570–574. DOI: 10.1103/physrev.142.570.

[123] "Raman Microscopy". In: *Field Guide to Nonlinear Optics*. Society of Photo-Optical Instrumentation Engineers. DOI: 10.1117/3.1002081.ch62.

[124] Sergi Galindo et al. "Control of Polymorphism and Morphology in Solution Sheared Organic Field-Effect Transistors". In: *Advanced Functional Materials* 27.25 (Apr. 2017), p. 1700526. DOI: 10.1002/adfm.201700526.

[125] Sergi Riera-Galindo, Adrián Tamayo, and Marta Mas-Torrent. "Role of Polymorphism and Thin-Film Morphology in Organic Semiconductors Processed by Solution Shearing". In: *ACS Omega* 3.2 (Feb. 2018), pp. 2329–2339. DOI: 10.1021/acsomega.8b00043.

[126] Ying Diao et al. "Morphology control strategies for solution-processed organic semiconductor thin films". In: *Energy Environ. Sci.* 7.7 (2014), pp. 2145–2159. DOI: 10.1039/c4ee00688g.

[127] Fiora Artusio and Roberto Pisano. "Surface-induced crystallization of pharmaceuticals and biopharmaceuticals: A review". In: *International Journal of Pharmaceutics* 547.1-2 (Aug. 2018), pp. 190–208. DOI: 10.1016/j.ijpharm.2018.05.069.

[128] Andrew O. F. Jones et al. "Substrate-Induced and Thin-Film Phases: Polymorphism of Organic Materials on Surfaces". In: *Advanced Functional Materials* 26.14 (Jan. 2016), pp. 2233–2255. DOI: 10.1002/adfm.201503169.

[129] Christian Röthel et al. "Alteration of texture and polymorph of phenytoin within thin films and its impact on dissolution". In: *CrystEngComm* 18.4 (2016), pp. 588–595. DOI: 10.1039/c5ce01889g.

[130] Ingo Salzmann et al. "Epitaxial Growth of *pi*-Stacked Perfluoropentacene on Graphene-Coated Quartz". In: *ACS Nano* 6.12 (Nov. 2012), pp. 10874–10883. DOI: 10.1021/nn3042607.

[131] Paul Beyer et al. "Lattice Matching as the Determining Factor for Molecular Tilt and Multilayer Growth Mode of the Nanographene Hexa-peri-hexabenzocoronene". In: *ACS Applied Materials & Interfaces* 6.23 (Nov. 2014), pp. 21484–21493. DOI: 10.1021/am506465b.

[132] Magdalena Truger et al. "Surface-Induced Phase of Tyrian Purple (6,6′-Dibromoindigo): Thin Film Formation and Stability". In: *Crystal Growth & Design* 16.7 (June 2016), pp. 3647–3655. DOI: 10.1021/acs.cgd.6b00104.

[133] Magdalena Truger et al. "Crystallization of Tyrian purple (6,6′-dibromoindigo) thin films: The impact of substrate surface modifications". In: *Journal of Crystal Growth* 447 (Aug. 2016), pp. 73–79. DOI: 10.1016/j.jcrysgro.2016.05.001.

[134] P. Süsse and C. Krampe. "6,6?-Dibromo-indigo, a main component of tyrian Purple". In: *Naturwissenschaften* 66.2 (Feb. 1979), pp. 110–110. DOI: 10.1007/bf00373504.

[135] Sine Larsen et al. "The Crystal and Molecular Structures of Tyrian Purple (6,6'-Dibromoindigotin) and 2,2'-Dimethoxyindigotin." In: *Acta Chemica Scandinavica* 34a (1980), pp. 171–176. DOI: 10.3891/acta.chem.scand.34a-0171.

[136] Sudha R. Vippagunta, Harry G. Brittain, and David J.W. Grant. "Crystalline solids". In: *Advanced Drug Delivery Reviews* 48.1 (May 2001), pp. 3–26. DOI: 10.1016/s0169-409x(01)00097-7.

[137] Ying Diao et al. "Surface Design for Controlled Crystallization: The Role of Surface Chemistry and Nanoscale Pores in Heterogeneous Nucleation". In: *Langmuir* 27.9 (May 2011), pp. 5324–5334. DOI: 10.1021/la104351k.

[138] Thomas Kellner et al. "Crystallographic Textures and Morphologies of Solution Cast Ibuprofen Composite Films at Solid Surfaces". In: *Molecular Pharmaceutics* 11.11 (Oct. 2014), pp. 4084–4091. DOI: 10.1021/mp500264e.

[139] Nima Yazdanpanah et al. "Continuous Heterogeneous Crystallization on Excipient Surfaces". In: *Crystal Growth & Design* 17.6 (May 2017), pp. 3321–3330. DOI: 10.1021/acs.cgd.7b00297.

[140] Stefan Pachmajer et al. "Self-Limited Growth in Pentacene Thin Films". In: *ACS Applied Materials & Interfaces* 9.13 (Mar. 2017), pp. 11977–11984. DOI: 10.1021/acsami.6b15907.

[141] Oliver Werzer et al. "Particular Film Formation of Phenytoin at Silica Surfaces". In: *Molecular Pharmaceutics* 11.2 (Jan. 2014), pp. 610–616. DOI: 10.1021/mp4006479.

[142] Daniela Reischl et al. "Surface-Induced Polymorphism as a Tool for Enhanced Dissolution: The Example of Phenytoin". In: *Crystal Growth & Design* 15.9 (Aug. 2015), pp. 4687–4693. DOI: 10.1021/acs.cgd.5b01002.

[143] Stephanie M. Guthrie, Detlef-M. Smilgies, and Gaurav Giri. "Controlling Polymorphism in Pharmaceutical Compounds Using Solution Shearing". In: *Crystal Growth & Design* 18.2 (Jan. 2018), pp. 602–606. DOI: 10.1021/acs.cgd.7b01686.

[144] A. Camerman and N. Camerman. "The stereochemical basis of anticonvulsant drug action. I. The crystal and molecular structure of diphenylhydantoin, a noncentrosymmetric structure solved by centric symbolic addition". In: *Acta Crystallographica Section B Structural Crystallography and Crystal Chemistry* 27.11 (Nov. 1971), pp. 2205–2211. DOI: 10.1107/s0567740871005570.

[145] T. K. Chattopadhyay, R. A. Palmer, and J. N. Lisgarten. "X-ray structural and potential energy studies on zentropil (5,5-diphenyl-2,4-imidazolidine dione)". In: *Journal of Crystallographic and Spec-*

troscopic Research 23.2 (Feb. 1993), pp. 149–152. DOI: 10.1007/bf01195449.

[146] Ali Boultif and Daniel Louër. "Powder pattern indexing with the dichotomy method". In: *Journal of Applied Crystallography* 37.5 (Sept. 2004), pp. 724–731. DOI: 10.1107/s0021889804014876.

[147] Kei Moriyama, Naoko Furuno, and Naoki Yamakawa. "Crystal face identification by Raman microscopy for assessment of crystal habit of a drug". In: *International Journal of Pharmaceutics* 480.1-2 (Mar. 2015), pp. 101–106. DOI: 10.1016/j.ijpharm.2015.01.031.

[148] Chinnasamy Kalaiarasi et al. "Crystal structure and theoretical charge density studies of dilantin molecule". In: *Journal of Molecular Structure* 1170 (Oct. 2018), pp. 105–118. DOI: 10.1016/j.molstruc.2018.05.030.

[149] Doris E. Braun et al. "Computational and Experimental Characterization of Five Crystal Forms of Thymine: Packing Polymorphism, Polytypism/Disorder, and Stoichiometric 0.8-Hydrate". In: *Crystal Growth & Design* 16.6 (May 2016), pp. 3480–3496. DOI: 10.1021/acs.cgd.6b00459.

[150] Doris E. Braun, Maria Orlova, and Ulrich J. Griesser. "Creatine: Polymorphs Predicted and Found". In: *Crystal Growth & Design* 14.10 (Sept. 2014), pp. 4895–4900. DOI: 10.1021/cg501159c.

[151] MJEA Frisch et al. *Gaussian 09, revision D. 01*. 2009.

[152] Panagiotis G. Karamertzanis and Constantinos C. Pantelides. "Ab initio crystal structure prediction?I. Rigid molecules". In: *Journal of Computational Chemistry* 26.3 (2004), pp. 304–324. DOI: 10.1002/jcc.20165.

[153] P. G. Karamertzanis† and C. C. Pantelides. "Ab initiocrystal structure prediction. II. Flexible molecules". In: *Molecular Physics* 105.2-3 (Jan. 2007), pp. 273–291. DOI: 10.1080/00268970601143317.

[154] Matthew Habgood et al. “Efficient Handling of Molecular Flexibility in Ab Initio Generation of Crystal Structures”. In: *Journal of Chemical Theory and Computation* 11.4 (Mar. 2015), pp. 1957–1969. DOI: 10.1021/ct500621v.

[155] David S. Coombes et al. “Role of Electrostatic Interactions in Determining the Crystal Structures of Polar Organic Molecules. A Distributed Multipole Study”. In: *The Journal of Physical Chemistry* 100.18 (Jan. 1996), pp. 7352–7360. DOI: 10.1021/jp960333b.

[156] Curt M. Breneman and Kenneth B. Wiberg. “Determining atom-centered monopoles from molecular electrostatic potentials. The need for high sampling density in formamide conformational analysis”. In: *Journal of Computational Chemistry* 11.3 (Apr. 1990), pp. 361–373. DOI: 10.1002/jcc.540110311.

[157] Sarah L. Price et al. “Modelling organic crystal structures using distributed multipole and polarizability-based model intermolecular potentials”. In: *Physical Chemistry Chemical Physics* 12.30 (2010), p. 8478. DOI: 10.1039/c004164e.

[158] Anthony J Stone. “Distributed multipole analysis: Stability for large basis sets”. In: *Journal of Chemical Theory and Computation* 1.6 (2005), pp. 1128–1132. DOI: 10.1021/ct050190+.

[159] AJ Stone. “GDMA: A program for performing distributed multipole analysis of wave functions calculated using the Gaussian program system”. In: *University of Cambridge Cambridge, United Kingdom* (2010).

[160] A. V. Kazantsev et al. “Efficient Handling of Molecular Flexibility in Lattice Energy Minimization of Organic Crystals”. In: *Journal of Chemical Theory and Computation* 7.6 (May 2011), pp. 1998–2016. DOI: 10.1021/ct100597e.

[161] Stewart J. Clark et al. “First principles methods using CASTEP”. In: *Zeitschrift für Kristallographie - Crystalline Materials* 220.5/6 (Jan. 2005). DOI: 10.1524/zkri.220.5.567.65075.

[162] David Vanderbilt. "Soft self-consistent pseudopotentials in a generalized eigenvalue formalism". In: *Physical Review B* 41.11 (Apr. 1990), pp. 7892–7895. DOI: 10.1103/physrevb.41.7892.

[163] Anthony L. Spek. "Structure validation in chemical crystallography". In: *Acta Crystallographica Section D Biological Crystallography* 65.2 (Jan. 2009), pp. 148–155. DOI: 10.1107/s090744490804362x.

[164] Michael J. Turner et al. "Energy frameworks: insights into interaction anisotropy and the mechanical properties of molecular crystals". In: *Chemical Communications* 51.18 (2015), pp. 3735–3738. DOI: 10.1039/c4cc09074h.

[165] Michael J. Turner et al. "Accurate and Efficient Model Energies for Exploring Intermolecular Interactions in Molecular Crystals". In: *The Journal of Physical Chemistry Letters* 5.24 (Nov. 2014), pp. 4249–4255. DOI: 10.1021/jz502271c.

[166] Campbell F. Mackenzie et al. "CrystalExplorermodel energies and energy frameworks: extension to metal coordination compounds, organic salts, solvates and open-shell systems". In: *IUCrJ* 4.5 (July 2017), pp. 575–587. DOI: 10.1107/s205225251700848x.

[167] Max Born and Kun Huang. *Dynamical Theory of Crystal Lattices (Oxford Classic Texts in the Physical Sciences)*. Oxford University Press, USA, 1998. ISBN: 9780198503699.

[168] Doris E. Braun et al. "Racemic Naproxen: A Multidisciplinary Structural and Thermodynamic Comparison with the Enantiopure Form". In: *Crystal Growth & Design* 11.12 (Dec. 2011), pp. 5659–5669. DOI: 10.1021/cg201203u.

[169] E. Menard et al. "Nanoscale Surface Morphology and Rectifying Behavior of a Bulk Single-Crystal Organic Semiconductor". In: *Advanced Materials* 18.12 (June 2006), pp. 1552–1556. DOI: 10.1002/adma.200502569.

[170] A. L. Spek. "Single-crystal structure validation with the programPLATON". In: *Journal of Applied Crystallography* 36.1 (Jan. 2003), pp. 7–13. DOI: 10.1107/s0021889802022112.

[171] Richard E. Marsh et al. "Some 60 new space-group corrections". In: *Acta Crystallographica Section B Structural Science* 58.1 (Jan. 2001), pp. 62–77. DOI: 10.1107/s0108768101017128.

[172] Y. Le Page. "MISSYM1.1 - a flexible new release". In: *Journal of Applied Crystallography* 21.6 (Dec. 1988), pp. 983–984. DOI: 10.1107/s0021889888007022.

[173] Tommaso Marcato and Chih-Jen Shih. "Molecular Orientation Effects in Organic Light-Emitting Diodes". In: *Helvetica Chimica Acta* 102.5 (May 2019), e1900048. DOI: 10.1002/hlca.201900048.

[174] Belinda J Boehm, Huong T L Nguyen, and David M Huang. "The interplay of interfaces, supramolecular assembly, and electronics in organic semiconductors". In: *Journal of Physics: Condensed Matter* 31.42 (July 2019), p. 423001. DOI: 10.1088/1361-648x/ab2ac2.

[175] Satoru Ohisa et al. "Molecular Interdiffusion between Stacked Layers by Solution and Thermal Annealing Processes in Organic Light Emitting Devices". In: *ACS Applied Materials & Interfaces* 7.37 (Sept. 2015), pp. 20779–20785. DOI: 10.1021/acsami.5b05818.

[176] Yuichiro Watanabe et al. "Simultaneous Manipulation of Intramolecular and Intermolecular Hydrogen Bonds in n-Type Organic Semiconductor Layers: Realization of Horizontal Orientation in OLEDs". In: *Advanced Optical Materials* 3.6 (Jan. 2015), pp. 769–773. DOI: 10.1002/adom.201400532.

[177] Daisuke Yokoyama et al. "Molecular Stacking Induced by Intermolecular C-H···N Hydrogen Bonds Leading to High Carrier Mobility in Vacuum-Deposited Organic Films". In: *Advanced Functional Materials* 21.8 (Mar. 2011), pp. 1375–1382. DOI: 10.1002/adfm.201001919.

[178] Yuichiro Watanabe et al. "Control of Molecular Orientation in Organic Semiconductor Films using Weak Hydrogen Bonds". In: *Advanced Materials* 31.18 (Mar. 2019), p. 1808300. DOI: 10.1002/adma.201808300.

[179] Steffen Duhm et al. "Orientation-dependent ionization energies and interface dipoles in ordered molecular assemblies". In: *Nature Materials* 7.4 (Feb. 2008), pp. 326–332. DOI: 10.1038/nmat2119.

[180] Jörg Frischeisen et al. "Increased light outcoupling efficiency in dye-doped small molecule organic light-emitting diodes with horizontally oriented emitters". In: *Organic Electronics* 12.5 (May 2011), pp. 809–817. DOI: 10.1016/j.orgel.2011.02.005.

[181] Philipp Liehm et al. "Comparing the emissive dipole orientation of two similar phosphorescent green emitter molecules in highly efficient organic light-emitting diodes". In: *Applied Physics Letters* 101.25 (Dec. 2012), p. 253304. DOI: 10.1063/1.4773188.

[182] M. D. Ediger, Juan de Pablo, and Lian Yu. "Anisotropic Vapor-Deposited Glasses: Hybrid Organic Solids". In: *Accounts of Chemical Research* 52.2 (Jan. 2019), pp. 407–414. DOI: 10.1021/acs.accounts.8b00513.

[183] M. D. Ediger. "Perspective: Highly stable vapor-deposited glasses". In: *The Journal of Chemical Physics* 147.21 (Dec. 2017), p. 210901. DOI: 10.1063/1.5006265.

[184] Otello Maria Roscioni et al. "Pentacene Crystal Growth on Silica and Layer-Dependent Step-Edge Barrier from Atomistic Simulations". In: *The Journal of Physical Chemistry Letters* 9.23 (Nov. 2018), pp. 6900–6906. DOI: 10.1021/acs.jpclett.8b03063.

[185] Daisuke Yokoyama et al. "Horizontal molecular orientation in vacuum-deposited organic amorphous films of hole and electron transport materials". In: *Applied Physics Letters* 93.17 (Oct. 2008), p. 173302. DOI: 10.1063/1.2996258.

[186] D YOKOYAMA et al. "Horizontal orientation of linear-shaped organic molecules having bulky substituents in neat and doped vacuum-deposited amorphous films". In: *Organic Electronics* 10.1 (Feb. 2009), pp. 127–137. DOI: 10.1016/j.orgel.2008.10.010.

[187] Hisahiro Sasabe et al. "Influence of Substituted Pyridine Rings on Physical Properties and Electron Mobilities of 2-Methylpyrimidine Skeleton-Based Electron Transporters". In: *Advanced Functional Materials* 21.2 (Oct. 2010), pp. 336–342. DOI: 10.1002/adfm.201001252.

[188] Dongsun Yoo et al. "A molecular dynamics study on the interface morphology of vapor-deposited amorphous organic thin films". In: *Physical Chemistry Chemical Physics* 21.3 (2019), pp. 1484–1490. DOI: 10.1039/c8cp05294h.

[189] Yong Youn et al. "All-atom simulation of molecular orientation in vapor-deposited organic light-emitting diodes". In: *Journal of Materials Chemistry C* 6.5 (2018), pp. 1015–1022. DOI: 10.1039/c7tc05278b.

[190] Y. Olivier et al. "Computational Design of Thermally Activated Delayed Fluorescence Materials: The Challenges Ahead". In: *The Journal of Physical Chemistry Letters* 9.20 (Sept. 2018), pp. 6149–6163. DOI: 10.1021/acs.jpclett.8b02327.

[191] Taiping Hu et al. "Origin of High Efficiencies for Thermally Activated Delayed Fluorescence Organic Light-Emitting Diodes: Atomistic Insight into Molecular Orientation and Torsional Disorder". In: *The Journal of Physical Chemistry C* 122.48 (Nov. 2018), pp. 27191–27197. DOI: 10.1021/acs.jpcc.8b08169.

[192] Luca Muccioli, Gabriele D'Avino, and Claudio Zannoni. "Simulation of Vapor-Phase Deposition and Growth of a Pentacene Thin Film on C60(001)". In: *Advanced Materials* 23.39 (Sept. 2011), pp. 4532–4536. DOI: 10.1002/adma.201101652.

[193] Diane M. Walters et al. "Influence of Molecular Shape on the Thermal Stability and Molecular Orientation of Vapor-Deposited Organic

Semiconductors". In: *The Journal of Physical Chemistry Letters* 8.14 (July 2017), pp. 3380–3386. DOI: 10.1021/acs.jpclett.7b01097.

[194] Lucas W. Antony et al. "Influence of Vapor Deposition on Structural and Charge Transport Properties of Ethylbenzene Films". In: *ACS Central Science* 3.5 (Apr. 2017), pp. 415–424. DOI: 10.1021/acscentsci.7b00041.

[195] Thomas Lee et al. "The Molecular Origin of Anisotropic Emission in an Organic Light-Emitting Diode". In: *Nano Letters* 17.10 (Sept. 2017), pp. 6464–6468. DOI: 10.1021/acs.nanolett.7b03528.

[196] Claire Tonnelé et al. "Elucidating the Spatial Arrangement of Emitter Molecules in Organic Light-Emitting Diode Films". In: *Angewandte Chemie* 129.29 (Feb. 2017), pp. 8522–8526. DOI: 10.1002/ange.201610727.

[197] Guangchao Han, Xingxing Shen, and Yuanping Yi. "Deposition Growth and Morphologies of C60on DTDCTB Surfaces: An Atomistic Insight into the Integrated Impact of Surface Stability, Landscape, and Molecular Orientation". In: *Advanced Materials Interfaces* 2.17 (Sept. 2015), p. 1500329. DOI: 10.1002/admi.201500329.

[198] Makoto Yoneya et al. "Self-assembly of donor-acceptor semiconducting polymers in solution thin films: a molecular dynamics simulation study". In: *Journal of Materials Chemistry C* 5.37 (2017), pp. 9602–9610. DOI: 10.1039/c7tc01014a.

[199] H.J.C. Berendsen, D. van der Spoel, and R. van Drunen. "GROMACS: A message-passing parallel molecular dynamics implementation". In: *Computer Physics Communications* 91.1-3 (Sept. 1995), pp. 43–56. DOI: 10.1016/0010-4655(95)00042-e.

[200] Berk Hess et al. "GROMACS 4: Algorithms for Highly Efficient, Load-Balanced, and Scalable Molecular Simulation". In: *Journal of Chemical Theory and Computation* 4.3 (Feb. 2008), pp. 435–447. DOI: 10.1021/ct700301q.

[201] Berk Hess et al. “LINCS: A linear constraint solver for molecular simulations”. In: *Journal of Computational Chemistry* 18.12 (Sept. 1997), pp. 1463–1472. DOI: 10.1002/(sici)1096-987x(199709)18:12<1463::aid-jcc4>3.0.co;2-h.

[202] Markus K. Dahlgren et al. “Characterization of Biaryl Torsional Energetics and its Treatment in OPLS All-Atom Force Fields”. In: *Journal of Chemical Information and Modeling* 53.5 (May 2013), pp. 1191–1199. DOI: 10.1021/ci4001597.

[203] Luca Muccioli et al. “Supramolecular Organization of Functional Organic Materials in the Bulk and at Organic/Organic Interfaces: A Modeling and Computer Simulation Approach”. In: *Topics in Current Chemistry*. Springer Berlin Heidelberg, 2013, pp. 39–101. DOI: 10.1007/128_2013_470.

[204] G. A. Petersson et al. “A complete basis set model chemistry. I. The total energies of closed-shell atoms and hydrides of the first-row elements”. In: *The Journal of Chemical Physics* 89.4 (Aug. 1988), pp. 2193–2218. DOI: 10.1063/1.455064.

[205] Matthias Ernzerhof and John P. Perdew. “Generalized gradient approximation to the angle- and system-averaged exchange hole”. In: *The Journal of Chemical Physics* 109.9 (Sept. 1998), pp. 3313–3320. DOI: 10.1063/1.476928.

[206] G. A. Petersson and Mohammad A. Al-Laham. “A complete basis set model chemistry. II. Open-shell systems and the total energies of the first-row atoms”. In: *The Journal of Chemical Physics* 94.9 (May 1991), pp. 6081–6090. DOI: 10.1063/1.460447.

[207] M. J. Frisch et al. *Gaussian 09 Revision D.01*. Gaussian Inc. Wallingford CT.

[208] Bin Chen, Marcus G. Martin, and J. Ilja Siepmann. “Thermodynamic Properties of the Williams, OPLS-AA, and MMFF94 All-Atom Force Fields for Normal Alkanes”. In: *The Journal of Physical Chemistry B* 102.14 (Apr. 1998), pp. 2578–2586. DOI: 10.1021/jp9801065.

[209] Nora A. McDonald and William L. Jorgensen. "Development of an All-Atom Force Field for Heterocycles. Properties of Liquid Pyrrole, Furan, Diazoles, and Oxazoles". In: *The Journal of Physical Chemistry B* 102.41 (Oct. 1998), pp. 8049–8059. DOI: 10.1021/jp981200o.

[210] Carlos E. S. Bernardes and Abhinav Joseph. "Evaluation of the OPLS-AA Force Field for the Study of Structural and Energetic Aspects of Molecular Organic Crystals". In: *The Journal of Physical Chemistry A* 119.12 (Mar. 2015), pp. 3023–3034. DOI: 10.1021/jp512349r.

[211] M. Moral et al. "Cost-Effective Force Field Tailored for Solid-Phase Simulations of OLED Materials". In: *Journal of Chemical Theory and Computation* 11.7 (June 2015), pp. 3383–3392. DOI: 10.1021/acs.jctc.5b00164.

[212] Sébastien Le Roux and Valeri Petkov. "ISAACS- interactive structure analysis of amorphous and crystalline systems". In: *Journal of Applied Crystallography* 43.1 (Jan. 2010), pp. 181–185. DOI: 10.1107/s0021889809051929.

[213] Ulrich Ziener et al. "Supramolecular Assemblies of a Bis(terpyridine) Ligand and of its [2×2] Grid-type ZnII and CoII Complexes on Highly Ordered Pyrolytic Graphite". In: *Chemistry - A European Journal* 8.4 (Feb. 2002), pp. 951–957. DOI: 10.1002/1521-3765(20020215)8:4<951::aid-chem951>3.0.co;2-9.

[214] Christoph Meier et al. "Weak Hydrogen Bonds as a Structural Motif for Two-Dimensional Assemblies of Oligopyridines on Highly Oriented Pyrolytic Graphite: An STM Investigation". In: *The Journal of Physical Chemistry B* 109.44 (Nov. 2005), pp. 21015–21027. DOI: 10.1021/jp054271d.

[215] Ulrich Ziener. "Self-Assembled Nanostructures of Oligopyridine Molecules". In: *The Journal of Physical Chemistry B* 112.47 (Nov. 2008), pp. 14698–14717. DOI: 10.1021/jp805846d.

[216] Christoph Meier, Katharina Landfester, and Ulrich Ziener. "Adsorbate-Substrate-Mediated Growth of Oligopyridine Monolayers at the Solid/Liquid Interface". In: *The Journal of Physical Chemistry C* 113.4 (Jan. 2009), pp. 1507–1514. DOI: 10.1021/jp808431t.

[217] Christoph Meier et al. "Concentration and Coverage Dependent Adlayer Structures: From Two-Dimensional Networks to Rotation in a Bearing". In: *The Journal of Physical Chemistry C* 114.2 (Nov. 2009), pp. 1268–1277. DOI: 10.1021/jp910029z.

[218] David M. Adams et al. "Charge Transfer on the Nanoscale: Current Status". In: *The Journal of Physical Chemistry B* 107.28 (July 2003), pp. 6668–6697. DOI: 10.1021/jp0268462.

[219] Gabriele D'Avino et al. "Electrostatic phenomena in organic semiconductors: fundamentals and implications for photovoltaics". In: *Journal of Physics: Condensed Matter* 28.43 (Sept. 2016), p. 433002. DOI: 10.1088/0953-8984/28/43/433002.

[220] Gabriele D'Avino et al. "Electronic Polarization in Organic Crystals: A Comparative Study of Induced Dipoles and Intramolecular Charge Redistribution Schemes". In: *Journal of Chemical Theory and Computation* 10.11 (Oct. 2014), pp. 4959–4971. DOI: 10.1021/ct500618w.

[221] Gabriele D'Avino et al. "Electrostatic Interactions Shape Molecular Organization and Electronic Structure of Organic Semiconductor Blends". In: *Chemistry of Materials* 32.3 (Jan. 2020), pp. 1261–1271. DOI: 10.1021/acs.chemmater.9b04763.

[222] Sai Manoj Gali et al. "Energetic fluctuations in amorphous semiconducting polymers: Impact on charge-carrier mobility". In: *The Journal of Chemical Physics* 147.13 (Oct. 2017), p. 134904. DOI: 10.1063/1.4996969.

[223] M. J. Frisch et al. *Gaussian 16 Revision C.01*. Gaussian Inc. Wallingford CT. 2016.

[224] Frank Neese. "The ORCA program system". In: *WIREs Computational Molecular Science* 2.1 (June 2011), pp. 73–78. DOI: 10.1002/wcms.81.

[225] K. Senthilkumar et al. "Charge transport in columnar stacked triphenylenes: Effects of conformational fluctuations on charge transfer integrals and site energies". In: *The Journal of Chemical Physics* 119.18 (Nov. 2003), pp. 9809–9817. DOI: 10.1063/1.1615476.

[226] Omar López-Estrada et al. "Reassessment of the Four-Point Approach to the Electron-Transfer Marcus-Hush Theory". In: *ACS Omega* 3.2 (Feb. 2018), pp. 2130–2140. DOI: 10.1021/acsomega.7b01425.

[227] Naga Rajesh Tummala et al. "Static and Dynamic Energetic Disorders in the C60, PC61BM, C70, and PC71BM Fullerenes". In: *The Journal of Physical Chemistry Letters* 6.18 (Sept. 2015), pp. 3657–3662. DOI: 10.1021/acs.jpclett.5b01709.

[228] Carina Faber et al. "Electron-phonon coupling in the C60fullerene within the many-bodyGWapproach". In: *Physical Review B* 84.15 (Oct. 2011). DOI: 10.1103/physrevb.84.155104.

[229] Zhengyang Bin et al. "Efficient n-Dopants and Their Roles in Organic Electronics". In: *Advanced Optical Materials* 6.18 (July 2018), p. 1800536. DOI: 10.1002/adom.201800536.

[230] H. Bässler. "Charge Transport in Disordered Organic Photoconductors a Monte Carlo Simulation Study". In: *physica status solidi (b)* 175.1 (Jan. 1993), pp. 15–56. DOI: 10.1002/pssb.2221750102.

Chapter 10

General conclusions

The study of the phenomenon of polymorphism in organic molecular systems is a very topical subject which, together with selection and control, is part of an emerging design strategy for obtaining materials with specified characteristics, as it allows modulating their functional properties. XRD and electron microscopy methods still are the techniques of choice for the identification of the crystal structure of a compound, also for growths on surfaces and in confined environments. However, each technique has limitations, instrumental or intrinsic to the sample, and for this reason it is always advisable to combine different methods.

Lattice Raman spectroscopy is a perfect candidate for solid-state investigations, since the vibrational spectra in the low-wavenumber region drastically depends on structure. For some structural parameters, such as symmetry, it is more sensitive than XRD, and therefore complementary to it. Accurate vdW-DFT calculations have been found to be fundamental to complete Raman spectroscopy and XRD, for a detailed analysis of the spectra and for structure identification.

The present thesis shows the evolution of the projects and of the relative methods faced during my PhD period, which have been determined by the main research topic of the research group, Raman spectroscopy, but also by the collaborations undertaken.

Several systems, often chosen because they were of interest for the group,

were in fact used as model systems, because each of them was characterized by polymorphism in a non-trivial way and could profit by the application of a multi-methodological approach. Raman spectroscopy was adopted as the experimental technique of choice, along with other measurement methods. For each system, basically similar strategies have guided the investigation.

Starting from the collaboration/scholarship with Natalia Bedoya-Martínez, we learned the vdW-DFT methods for describing molecular crystals and, in particular, to calculate minimum energy structures, frequencies and Raman intensities. The study focused on testing various vdW corrections in order to best reproduce the experimental spectra.

We then applied the learned method to study the Coronene case. The simplicity and rigidity of this molecule made it an excellent model system and the accuracy of the calculations allowed us to identify the polymorphs and to follow its temperature induced phase transition via Raman spectroscopy in the lattice region of the spectra.

We then moved on to indigoids, a class of compounds whose application in organic electronics led us to the study of the polymorphism in thin films. After a preliminary study of the bulk forms, the film samples were fabricated and analyzed by our group and collaborators. Thanks to the calculations, we were able to identify polymorphs via Raman spectroscopy, even when the structures were so similar that XRD failed to distinguish them (Indigo). We were able to simulate the polarized spectra of ordered crystals of Thioindigo and to use this information to describe the spectra of partially ordered films. Finally we were able to identify the surface induced polymorph obtained for Tyrian purple and to see how small modifications can lead to different vibrational spectra.

Thanks to another collaboration, we were able to study the case of phenytoin, a pharmaceutical compound whose film polymorph was not yet known. Given the impossibility of solving the structure with the GIXD technique alone, our collaborators fed this incomplete data into a computational crystal structure prediction tool which gave a plausible structure. However, only after the validation offered by the Raman calculations and experiments, we did find the correct structure. The final result was really interesting, as it

was the simple application of the Raman selection rules that has enabled us to choose between two slightly different structures, which differed only by the presence (or the absence) of the inversion centre.

Finally, we started studying the electronic properties of organic molecular films. Thanks to the empirical methods of microelectrostatics taught by Gabriele D'Avino, we were able to analyze thin films of B2 and B4 which had been simulated by our collaborators, and to observe how the disorder in the films affected the electronic parameters of the two systems.

Beside the interest for the various systems and for the computational procedures, we will like to stress the effectiveness of combining several different experimental and theoretical methods. Currently, we are using the same strategies for studying solid-state photoreactions, co-crystals and solid solutions.

Bibliography

[1] David A. Bardwell et al. "Towards crystal structure prediction of complex organic compounds - a report on the fifth blind test". In: *Acta Crystallographica Section B Structural Science* 67.6 (Nov. 2011), pp. 535–551. DOI: 10.1107/s0108768111042868.

[2] Jos P. M. Lommerse et al. "A test of crystal structure prediction of small organic molecules". In: *Acta Crystallographica Section B Structural Science* 56.4 (Aug. 2000), pp. 697–714. DOI: 10.1107/s0108768100004584.

[3] G. M. Day et al. "A third blind test of crystal structure prediction". In: *Acta Crystallographica Section B Structural Science* 61.5 (Sept. 2005), pp. 511–527. DOI: 10.1107/s0108768105016563.

[4] W. Kohn and L. J. Sham. "Self-Consistent Equations Including Exchange and Correlation Effects". In: *Physical Review* 140.4A (Nov. 1965), A1133–A1138. DOI: 10.1103/physrev.140.a1133.

[5] G. Kresse and J. Hafner. "Ab initiomolecular dynamics for liquid metals". In: *Physical Review B* 47.1 (Jan. 1993), pp. 558–561. DOI: 10.1103/physrevb.47.558.

[6] G. Kresse and J. Hafner. "Ab initiomolecular-dynamics simulation of the liquid-metal-amorphous-semiconductor transition in germanium". In: *Physical Review B* 49.20 (May 1994), pp. 14251–14269. DOI: 10.1103/physrevb.49.14251.

[7] G. Kresse and J. Furthmüller. "Efficiency of ab-initio total energy calculations for metals and semiconductors using a plane-wave basis

set". In: *Computational Materials Science* 6.1 (July 1996), pp. 15–50. DOI: 10.1016/0927-0256(96)00008-0.

[8] G. Kresse and J. Furthmüller. "Efficient iterative schemes forab initiototal-energy calculations using a plane-wave basis set". In: *Physical Review B* 54.16 (Oct. 1996), pp. 11169–11186. DOI: 10.1103/physrevb.54.11169.

[9] Roberto Dovesi et al. "Quantum-mechanical condensed matter simulations with CRYSTAL". In: *Wiley Interdisciplinary Reviews: Computational Molecular Science* 8.4 (Mar. 2018), e1360. DOI: 10.1002/wcms.1360.

[10] Jiří Klimeš and Angelos Michaelides. "Perspective: Advances and challenges in treating van der Waals dispersion forces in density functional theory". In: *The Journal of Chemical Physics* 137.12 (Sept. 2012), p. 120901. DOI: 10.1063/1.4754130.

[11] Alexandre Tkatchenko et al. "Accurate and Efficient Method for Many-Body van der Waals Interactions". In: *Physical Review Letters* 108.23 (June 2012). DOI: 10.1103/physrevlett.108.236402.

[12] Stefan Grimme. "Semiempirical GGA-type density functional constructed with a long-range dispersion correction". In: *Journal of Computational Chemistry* 27.15 (2006), pp. 1787–1799. DOI: 10.1002/jcc.20495.

[13] Stefan Grimme, Stephan Ehrlich, and Lars Goerigk. "Effect of the damping function in dispersion corrected density functional theory". In: *Journal of Computational Chemistry* 32.7 (Mar. 2011), pp. 1456–1465. DOI: 10.1002/jcc.21759.

[14] Alexandre Tkatchenko and Matthias Scheffler. "Accurate Molecular Van Der Waals Interactions from Ground-State Electron Density and Free-Atom Reference Data". In: *Physical Review Letters* 102.7 (Feb. 2009). DOI: 10.1103/physrevlett.102.073005.

[15] Jiří Klimeš, David R Bowler, and Angelos Michaelides. "Chemical accuracy for the van der Waals density functional". In: *Journal of Physics: Condensed Matter* 22.2 (Dec. 2009), p. 022201. DOI: 10.1088/0953-8984/22/2/022201.

[16] Jiří Klimeš, David R. Bowler, and Angelos Michaelides. "Van der Waals density functionals applied to solids". In: *Physical Review B* 83.19 (May 2011). DOI: 10.1103/physrevb.83.195131.

[17] Alberto Ambrosetti et al. "Long-range correlation energy calculated from coupled atomic response functions". In: *The Journal of Chemical Physics* 140.18 (May 2014), 18A508. DOI: 10.1063/1.4865104.

[18] Graeme M. Day et al. "Significant progress in predicting the crystal structures of small organic molecules - a report on the fourth blind test". In: *Acta Crystallographica Section B Structural Science* 65.2 (Mar. 2009), pp. 107–125. DOI: 10.1107/s0108768109004066.

[19] Marcus A. Neumann, Frank J. J. Leusen, and John Kendrick. "A Major Advance in Crystal Structure Prediction". In: *Angewandte Chemie International Edition* 47.13 (Mar. 2008), pp. 2427–2430. DOI: 10.1002/anie.200704247.

[20] Natalia Bedoya-Martínez et al. "DFT-Assisted Polymorph Identification from Lattice Raman Fingerprinting". In: *The Journal of Physical Chemistry Letters* 8.15 (July 2017), pp. 3690–3695. DOI: 10.1021/acs.jpclett.7b01634.

[21] Aldo Brillante et al. "Probing polymorphs of organic semiconductors by lattice phonon Raman microscopy". In: *CrystEngComm* 10.8 (2008), p. 937. DOI: 10.1039/b804317e.

[22] Tommaso Salzillo et al. "Two New Polymorphs of the Organic Semiconductor 9,10-Diphenylanthracene: Raman and X-ray Analysis". In: *The Journal of Physical Chemistry C* 120.3 (Jan. 2016), pp. 1831–1840. DOI: 10.1021/acs.jpcc.5b11115.

[23] Arianna Rivalta et al. "Bulk and Surface-Stabilized Structures of Paracetamol Revisited by Raman Confocal Microscopy". In: *ACS Omega* 3.8 (Aug. 2018), pp. 9564–9571. DOI: 10.1021/acsomega.8b01246.

[24] Benedikt Schrode et al. "Substrate-Induced Phase of a Benzothiophene Derivative Detected by Mid-Infrared and Lattice Phonon Raman Spectroscopy". In: *ChemPhysChem* 19.8 (Mar. 2018), pp. 993–1000. DOI: 10.1002/cphc.201701378.

[25] Tommaso Salzillo et al. "An Alternative Strategy to Polymorph Recognition at Work: The Emblematic Case of Coronene". In: *Crystal Growth & Design* 18.9 (July 2018), pp. 4869–4873. DOI: 10.1021/acs.cgd.8b00934.

[26] Natalia Bedoya-Martínez et al. "Toward a Reliable Description of the Lattice Vibrations in Organic Molecular Crystals: The Impact of van der Waals Interactions". In: *Journal of Chemical Theory and Computation* 14.8 (July 2018), pp. 4380–4390. DOI: 10.1021/acs.jctc.8b00484.

[27] Lorenzo Pandolfi et al. "In Search of Surface-Induced Crystal Structures: The Case of Tyrian Purple". In: *The Journal of Physical Chemistry C* 124.32 (July 2020), pp. 17702–17710. DOI: 10.1021/acs.jpcc.0c05186.

[28] T. Salzillo et al. "Structural, Spectroscopic, and Computational Characterization of the Concomitant Polymorphs of the Natural Semiconductor Indigo". In: *The Journal of Physical Chemistry C* 122.32 (July 2018), pp. 18422–18431. DOI: 10.1021/acs.jpcc.8b03635.

[29] Doris E. Braun et al. "Surface Induced Phenytoin Polymorph. 1. Full Structure Solution by Combining Grazing Incidence X-ray Diffraction and Crystal Structure Prediction". In: *Crystal Growth & Design* 19.11 (Sept. 2019), pp. 6058–6066. DOI: 10.1021/acs.cgd.9b00857.

[30] Andrea Giunchi et al. "Surface Induced Phenytoin Polymorph. 2. Structure Validation by Comparing Experimental and Density Func-

tional Theory Raman Spectra". In: *Crystal Growth & Design* 19.11 (Sept. 2019), pp. 6067–6073. DOI: 10.1021/acs.cgd.9b00863.

[31] A. Rivalta et al. "Crystal alignment of surface stabilized polymorph in thioindigo films". In: *Dyes and Pigments* 172 (Jan. 2020), p. 107847. DOI: 10.1016/j.dyepig.2019.107847.

[32] Flavia Aleotti et al. "Spectral Tuning and Photoisomerization Efficiency in Push-Pull Azobenzenes: Designing Principles". In: *The Journal of Physical Chemistry A* 124.46 (Nov. 2020), pp. 9513–9523. DOI: 10.1021/acs.jpca.0c08672.

[33] L. Pandolfi et al. "The impact of solid-solution composition on kinetics and mechanism of [2+2] photodimerizations of cinnamic acid derivatives." accepted for publication. 2021.

[34] A. De Nicola et al. "Bidimensional H-bond network promotes structural order and electron transport in BPyMPMs molecular semiconductors". currently under review.

[35] A. Rivalta et al. "Growth, Morphology and Molecular Orientation of Controlled Indigo thin films on Silica Surfaces." currently under review. 2020.

[36] P. E. Blöchl. "Projector augmented-wave method". In: *Physical Review B* 50.24 (Dec. 1994), pp. 17953–17979. DOI: 10.1103/physrevb.50.17953.

[37] G. Kresse and D. Joubert. "From ultrasoft pseudopotentials to the projector augmented-wave method". In: *Physical Review B* 59.3 (Jan. 1999), pp. 1758–1775. DOI: 10.1103/physrevb.59.1758.

[38] Tomáš Bučko, Jürgen Hafner, and János G. Ángyán. "Geometry optimization of periodic systems using internal coordinates". In: *The Journal of Chemical Physics* 122.12 (Mar. 2005), p. 124508. DOI: 10.1063/1.1864932.

[39] Gregory J. O. Beran, Joshua D. Hartman, and Yonaton N. Heit. "Predicting Molecular Crystal Properties from First Principles: Finite-Temperature Thermochemistry to NMR Crystallography". In: *Accounts of Chemical Research* 49.11 (Oct. 2016), pp. 2501–2508. DOI: 10.1021/acs.accounts.6b00404.

[40] Yonaton N. Heit and Gregory J. O. Beran. "How important is thermal expansion for predicting molecular crystal structures and thermochemistry at finite temperatures?" In: *Acta Crystallographica Section B Structural Science, Crystal Engineering and Materials* 72.4 (July 2016), pp. 514–529. DOI: 10.1107/s2052520616005382.

[41] Jan Gerit Brandenburg et al. "Thermal Expansion of Carbamazepine: Systematic Crystallographic Measurements Challenge Quantum Chemical Calculations". In: *The Journal of Physical Chemistry Letters* 8.17 (Aug. 2017), pp. 4319–4324. DOI: 10.1021/acs.jpclett.7b01944.

[42] Hendrik J. Monkhorst and James D. Pack. "Special points for Brillouin-zone integrations". In: *Physical Review B* 13.12 (June 1976), pp. 5188–5192. DOI: 10.1103/physrevb.13.5188.

[43] James Alexander Chisholm and Sam Motherwell. "COMPACK: a program for identifying crystal structure similarity using distances". In: *Journal of Applied Crystallography* 38.1 (Jan. 2005), pp. 228–231. DOI: 10.1107/s0021889804027074.

[44] Aurora J. Cruz-Cabeza and Joel Bernstein. "Conformational Polymorphism". In: *Chemical Reviews* 114.4 (Dec. 2013), pp. 2170–2191. DOI: 10.1021/cr400249d.

[45] Atsushi Togo and Isao Tanaka. "First principles phonon calculations in materials science". In: *Scripta Materialia* 108 (Nov. 2015), pp. 1–5. DOI: 10.1016/j.scriptamat.2015.07.021.

[46] Dirk Porezag and Mark R. Pederson. "Infrared intensities and Raman-scattering activities within density-functional theory". In: *Physical Review B* 54.11 (Sept. 1996), pp. 7830–7836. DOI: 10.1103/physrevb.54.7830.

[47] A. Fonari and S. Stauffer. *vasp_raman.py*. https://github.com/raman-sc/VASP/, 2013.

[48] E. Bright Wilson et al. "Molecular Vibrations". In: *American Journal of Physics* 23.8 (Nov. 1955), pp. 550–550. DOI: 10.1119/1.1934101.

[49] Danuta Michalska and Rafał Wysokiński. "The prediction of Raman spectra of platinum(II) anticancer drugs by density functional theory". In: *Chemical Physics Letters* 403.1-3 (Feb. 2005), pp. 211–217. DOI: 10.1016/j.cplett.2004.12.096.

[50] Anthony P. Scott and Leo Radom. "Harmonic Vibrational Frequencies: An Evaluation of Hartree-Fock, Møller-Plesset, Quadratic Configuration Interaction, Density Functional Theory, and Semiempirical Scale Factors". In: *The Journal of Physical Chemistry* 100.41 (Jan. 1996), pp. 16502–16513. DOI: 10.1021/jp960976r.

[51] M. P. Andersson and P. Uvdal. "New Scale Factors for Harmonic Vibrational Frequencies Using the B3LYP Density Functional Method with the Triple-
zeta Basis Set 6-311+G(d,p)". In: *The Journal of Physical Chemistry A* 109.12 (Mar. 2005), pp. 2937–2941. DOI: 10.1021/jp045733a.

[52] Jan Hermann, Robert A. DiStasio, and Alexandre Tkatchenko. "First-Principles Models for van der Waals Interactions in Molecules and Materials: Concepts, Theory, and Applications". In: *Chemical Reviews* 117.6 (Mar. 2017), pp. 4714–4758. DOI: 10.1021/acs.chemrev.6b00446.

[53] Stefan Grimme et al. "Dispersion-Corrected Mean-Field Electronic Structure Methods". In: *Chemical Reviews* 116.9 (Apr. 2016), pp. 5105–5154. DOI: 10.1021/acs.chemrev.5b00533.

[54] Anthony M. Reilly and Alexandre Tkatchenko. "Role of Dispersion Interactions in the Polymorphism and Entropic Stabilization of the Aspirin Crystal". In: *Physical Review Letters* 113.5 (July 2014). DOI: 10.1103/physrevlett.113.055701.

[55] Florian Brown-Altvater, Tonatiuh Rangel, and Jeffrey B. Neaton. "Ab initiophonon dispersion in crystalline naphthalene using van der Waals density functionals". In: *Physical Review B* 93.19 (May 2016). DOI: 10.1103/physrevb.93.195206.

[56] Ido Azuri et al. "THz Spectroscopy of 2,4,6-trinitrotoluene Molecular Solids from First Principles". In: *APS March Meeting Abstracts*. Vol. 2018. APS Meeting Abstracts. Jan. 2018, Y36.002.

[57] M. Bezerra da Silva et al. "Vibrational Properties of Bulk Boric Acid 2A and 3T Polymorphs and Their Two-Dimensional Layers: Measurements and Density Functional Theory Calculations". In: *The Journal of Physical Chemistry A* 122.5 (Jan. 2018), pp. 1312–1325. DOI: 10.1021/acs.jpca.7b10083.

[58] Janine George et al. "Lattice thermal expansion and anisotropic displacements in urea, bromomalonic aldehyde, pentachloropyridine, and naphthalene". In: *The Journal of Chemical Physics* 147.7 (Aug. 2017), p. 074112. DOI: 10.1063/1.4985886.

[59] M. Dion et al. "Van der Waals Density Functional for General Geometries". In: *Physical Review Letters* 92.24 (June 2004). DOI: 10.1103/physrevlett.92.246401.

[60] Kyuho Lee et al. "Higher-accuracy van der Waals density functional". In: *Physical Review B* 82.8 (Aug. 2010). DOI: 10.1103/physrevb.82.081101.

[61] Stefan Grimme et al. "A consistent and accurate ab initio parametrization of density functional dispersion correction (DFT-D) for the 94 elements H-Pu". In: *The Journal of Chemical Physics* 132.15 (Apr. 2010), p. 154104. DOI: 10.1063/1.3382344.

[62] Stephan N. Steinmann and Clemence Corminboeuf. "A generalized-gradient approximation exchange hole model for dispersion coefficients". In: *The Journal of Chemical Physics* 134.4 (Jan. 2011), p. 044117. DOI: 10.1063/1.3545985.

[63] Tomáš Bučko et al. “Improved Density Dependent Correction for the Description of London Dispersion Forces”. In: *Journal of Chemical Theory and Computation* 9.10 (Sept. 2013), pp. 4293–4299. DOI: 10.1021/ct400694h.

[64] Tomáš Bučko et al. “Extending the applicability of the Tkatchenko-Scheffler dispersion correction via iterative Hirshfeld partitioning”. In: *The Journal of Chemical Physics* 141.3 (July 2014), p. 034114. DOI: 10.1063/1.4890003.

[65] Kristian Berland et al. “van der Waals forces in density functional theory: a review of the vdW-DF method”. In: *Reports on Progress in Physics* 78.6 (May 2015), p. 066501. DOI: 10.1088/0034-4885/78/6/066501.

[66] Tomáš Bučko et al. “Many-body dispersion corrections for periodic systems: an efficient reciprocal space implementation”. In: *Journal of Physics: Condensed Matter* 28.4 (Jan. 2016), p. 045201. DOI: 10.1088/0953-8984/28/4/045201.

[67] Aldo Brillante et al. “The four polymorphic modifications of the semiconductor dibenzo-tetrathiafulvalene”. In: *CrystEngComm* 10.12 (2008), p. 1899. DOI: 10.1039/b810993a.

[68] Aldo Brillante et al. “Phase recognition by lattice phonon Raman spectra: The triclinic structure of the organic semiconductor dibenzo-tetrathiafulvalene”. In: *Chemical Physics Letters* 523 (Jan. 2012), pp. 74–77. DOI: 10.1016/j.cplett.2011.12.026.

[69] H.-D. Becker and V. Langer. “Crystal structure of 9,10-diphenylanthracene, (C6H5XC14H8XC6H5)”. In: *Zeitschrift für Kristallographie - Crystalline Materials* 199.1-4 (Jan. 1992). DOI: 10.1524/zkri.1992.199.14.313.

[70] Andrew O. F. Jones et al. “Substrate-Induced Phase of a [1]Benzothieno[3,2-b]benzothiophene Derivative and Phase Evolution by Aging and Solvent Vapor Annealing”. In: *ACS Applied Materials & Interfaces* 7.3 (Jan. 2015), pp. 1868–1873. DOI: 10.1021/am5075908.

[71] Christian Ruzié et al. "Design, synthesis, chemical stability, packing, cyclic voltammetry, ionisation potential, and charge transport of [1]benzothieno[3,2-b][1]benzothiophene derivatives". In: *Journal of Materials Chemistry C* 4.22 (2016), pp. 4863–4879. DOI: 10.1039/c6tc01409g.

[72] Tim Gould et al. "A Fractionally Ionic Approach to Polarizability and van der Waals Many-Body Dispersion Calculations". In: *Journal of Chemical Theory and Computation* 12.12 (Dec. 2016), pp. 5920–5930. DOI: 10.1021/acs.jctc.6b00925.

[73] Ismael Diez-Perez et al. "Gate-controlled electron transport in coronenes as a bottom-up approach towards graphene transistors". In: *Nature Communications* 1.1 (June 2010). DOI: 10.1038/ncomms1029.

[74] E. Jennings, W. Montgomery, and Ph. Lerch. "Stability of Coronene at High Temperature and Pressure". In: *The Journal of Physical Chemistry B* 114.48 (Dec. 2010), pp. 15753–15758. DOI: 10.1021/jp105020f.

[75] A. D. Chanyshev et al. "Compressibility, phase transitions and amorphization of coronene at pressures up to 6 GPa". In: *Journal of Structural Chemistry* 57.7 (Dec. 2016), pp. 1489–1492. DOI: 10.1134/s002247661607026x.

[76] Xiao-Miao Zhao et al. "Phase transformations and vibrational properties of coronene under pressure". In: *The Journal of Chemical Physics* 139.14 (Oct. 2013), p. 144308. DOI: 10.1063/1.4824384.

[77] Takahiro Yamamoto et al. "Exciton—phonon coupling and pressure-induced structural phase changes in coronene crystals". In: *Chemical Physics* 184.1-3 (June 1994), pp. 247–254. DOI: 10.1016/0301-0104(94)00084-0.

[78] G. R. Desiraju and A. Gavezzotti. "Crystal structures of polynuclear aromatic hydrocarbons. Classification, rationalization and prediction from molecular structure". In: *Acta Crystallographica Section B Structural Science* 45.5 (Oct. 1989), pp. 473–482. DOI: 10.1107/s0108768189003794.

[79] Jason Potticary et al. “An unforeseen polymorph of coronene by the application of magnetic fields during crystal growth”. In: *Nature Communications* 7.1 (May 2016). DOI: 10.1038/ncomms11555.

[80] Koichi Ohno, Takashi Kajiwara, and Hiroo Inokuchi. “Vibrational Analysis of Electronic Transition Bands of Coronene”. In: *Bulletin of the Chemical Society of Japan* 45.4 (Apr. 1972), pp. 996–1004. DOI: 10.1246/bcsj.45.996.

[81] Elisabetta Venuti et al. “Phonons and structures of tetracene polymorphs at low temperature and high pressure”. In: *Physical Review B* 70.10 (Sept. 2004). DOI: 10.1103/physrevb.70.104106.

[82] R. Totoki, T. Aoki-Matsumoto, and K. Mizuno. “Density of states of the lowest exciton band and the exciton bandwidth in coronene single crystals”. In: *Journal of Luminescence* 112.1-4 (Apr. 2005), pp. 308–311. DOI: 10.1016/j.jlumin.2004.09.096.

[83] Jason Potticary et al. “Low temperature magneto-morphological characterisation of coronene and the resolution of previously observed unexplained phenomena”. In: *Scientific Reports* 6.1 (Dec. 2016). DOI: 10.1038/srep38696.

[84] Olga Kataeva et al. “Crystal Growth, Dynamic and Charge Transfer Properties of New Coronene Charge Transfer Complexes”. In: *Crystal Growth & Design* 16.1 (Nov. 2015), pp. 331–338. DOI: 10.1021/acs.cgd.5b01301.

[85] Petar D. Todorov, Leonardus W. Jenneskens, and Joop H. van Lenthe. “Assignment of phantom bands in the solid-state infrared and Raman spectra of coronene: The importance of a minute out-of-plane distortion”. In: *The Journal of Chemical Physics* 132.3 (Jan. 2010), p. 034504. DOI: 10.1063/1.3282331.

[86] Graeme M. Day and Carl Henrik Görbitz. “Introduction to the special issue on crystal structure prediction”. In: *Acta Crystallographica Section B Structural Science, Crystal Engineering and Materials* 72.4 (Aug. 2016), pp. 435–436. DOI: 10.1107/s2052520616012348.

[87] H. von Eller-Pandraud. “Sur Le Polymorphisme de l’indigo”. In: *Bull Soc Chim Fr* (1955), p. 316.

[88] EA Gribova, GS Zhdanov, and GA Golder. “X-Ray Determination of the Structure of Indigo and Thorindigo”. In: *Kristallografiya* 1 (1956), pp. 53–60.

[89] P Süsse et al. “A new crystalline phase of indigo”. In: (1980).

[90] Peter Süsse, Manfred Steins, and Vladimir Kupcik. “Indigo: Crystal structure refinement based on synchrotron data”. In: *Zeitschrift für Kristallographie* 184.3-4 (Jan. 1988), pp. 269–273. DOI: 10.1524/zkri.1988.184.3-4.269.

[91] Florian Kettner et al. “Selective crystallization of indigo B by a modified sublimation method and its redetermined structure”. In: *Acta Crystallographica Section E Structure Reports Online* 67.11 (Oct. 2011), o2867–o2867. DOI: 10.1107/s1600536811040220.

[92] Boris Scherwitzl, Roland Resel, and Adolf Winkler. “Film growth, adsorption and desorption kinetics of indigo on SiO2”. In: *The Journal of Chemical Physics* 140.18 (May 2014), p. 184705. DOI: 10.1063/1.4875096.

[93] Alessandro Troisi. “Charge transport in high mobility molecular semiconductors: classical models and new theories”. In: *Chemical Society Reviews* 40.5 (2011), p. 2347. DOI: 10.1039/c0cs00198h.

[94] K Nishida et al. “Vapour Pressures and Heats of Sublimation of Some Vat Dyes”. In: *Journal of the Society of Dyers and Colourists* 102.1 (Oct. 2008), pp. 18–20. DOI: 10.1111/j.1478-4408.1986.tb01039.x.

[95] H. von Eller. “Structure de colorants indigoïdes. III-Structure cristalline de l’indigo”. In: *Bull Soc Chim Fr* (1955), p. 1433.

[96] Raffaele Guido Della Valle et al. “Inherent structures of crystalline pentacene”. In: *The Journal of Chemical Physics* 118.2 (Jan. 2003), pp. 807–815. DOI: 10.1063/1.1527896.

[97] Frank H. Stillinger and Thomas A. Weber. "Hidden structure in liquids". In: *Physical Review A* 25.2 (Feb. 1982), pp. 978–989. DOI: 10.1103/physreva.25.978.

[98] Elisabetta Venuti et al. "Probing Pentacene Polymorphs by Lattice Dynamics Calculations". In: *Journal of the American Chemical Society* 124.10 (Mar. 2002), pp. 2128–2129. DOI: 10.1021/ja0166949.

[99] Stephen L. Mayo, Barry D. Olafson, and William A. Goddard. "DREIDING: a generic force field for molecular simulations". In: *The Journal of Physical Chemistry* 94.26 (Dec. 1990), pp. 8897–8909. DOI: 10.1021/j100389a010.

[100] Michael W. Schmidt et al. "General atomic and molecular electronic structure system". In: *Journal of Computational Chemistry* 14.11 (Nov. 1993), pp. 1347–1363. DOI: 10.1002/jcc.540141112.

[101] John P. Perdew, Kieron Burke, and Matthias Ernzerhof. "Generalized Gradient Approximation Made Simple". In: *Physical Review Letters* 77.18 (Oct. 1996), pp. 3865–3868. DOI: 10.1103/physrevlett.77.3865.

[102] Angelo Gavezzotti. *Molecular aggregation: Structure analysis and molecular simulation of crystals and liquids*. Oxford University Press, 2007. ISBN: 9780198570806.

[103] Anthony M. Reilly and Alexandre Tkatchenko. "Understanding the role of vibrations, exact exchange, and many-body van der Waals interactions in the cohesive properties of molecular crystals". In: *The Journal of Chemical Physics* 139.2 (July 2013), p. 024705. DOI: 10.1063/1.4812819.

[104] J. Chickos. "Enthalpies of Sublimation after a Century of Measurement: A View as Seen through the Eyes of a Collector". In: 2003. DOI: 10.11311/jscta1974.30.116.

[105] Denis V. Anokhin et al. "Towards understanding the behavior of indigo thin films in organic field-effect transistors: a template effect of the aliphatic hydrocarbon dielectric on the crystal structure and electrical performance of the semiconductor". In: *Chemical Communications* 50.57 (2014), p. 7639. DOI: 10.1039/c4cc02431a.

[106] William Humphrey, Andrew Dalke, and Klaus Schulten. "VMD: Visual molecular dynamics". In: *Journal of Molecular Graphics* 14.1 (Feb. 1996), pp. 33–38. DOI: 10.1016/0263-7855(96)00018-5.

[107] Aleksandr Sergeevich Davydov. *Theory of Molecular Excitons*. Springer US, 1971. DOI: 10.1007/978-1-4899-5169-4.

[108] Anna Amat et al. "Theoretical and experimental investigation on the spectroscopic properties of indigo dye". In: *Journal of Molecular Structure* 993.1-3 (May 2011), pp. 43–51. DOI: 10.1016/j.molstruc.2010.11.046.

[109] Ellen Tatsch and Bernhard Schrader. "Near-infrared fourier transform Raman spectroscopy of indigoids". In: *Journal of Raman Spectroscopy* 26.6 (June 1995), pp. 467–473. DOI: 10.1002/jrs.1250260611.

[110] W. Lüttke, H. Hermann, and M. Klessinger. "Theoretically and Experimentally Determined Properties of the Fundamental Indigo Chromophore". In: *Angewandte Chemie International Edition in English* 5.6 (June 1966), pp. 598–599. DOI: 10.1002/anie.196605982.

[111] Aurora J. Cruz-Cabeza, Susan M. Reutzel-Edens, and Joel Bernstein. "Facts and fictions about polymorphism". In: *Chemical Society Reviews* 44.23 (2015), pp. 8619–8635. DOI: 10.1039/c5cs00227c.

[112] Noa Marom et al. "Many-Body Dispersion Interactions in Molecular Crystal Polymorphism". In: *Angewandte Chemie International Edition* 52.26 (May 2013), pp. 6629–6632. DOI: 10.1002/anie.201301938.

[113] Mihai Irimia-Vladu et al. “Indigo - A Natural Pigment for High Performance Ambipolar Organic Field Effect Transistors and Circuits”. In: *Advanced Materials* 24.3 (Nov. 2011), pp. 375–380. DOI: 10.1002/adma.201102619.

[114] N. M. Khusayfan, E. F. M. El-Zaidia, and M. M. El-Nahass. “Fabrication and Electrical Characteristics of Thioindigo/Silicon Heterojunction”. In: *Silicon* 10.6 (Apr. 2018), pp. 2519–2526. DOI: 10.1007/s12633-018-9786-3.

[115] Raphael Pfattner et al. “Tuning Crystal Ordering, Electronic Structure, and Morphology in Organic Semiconductors: Tetrathiafulvalenes as a Model Case”. In: *Advanced Functional Materials* 26.14 (Oct. 2015), pp. 2256–2275. DOI: 10.1002/adfm.201502446.

[116] H. von Helle. “Structure de colorants indigoïdes. IV-Structure cristalline du thioindigo”. In: *Bull Soc Chim Fr* (1955), p. 1438.

[117] W. Haase-Wessel, M. Ohmasa, and P. Süsse. “Thioindigo: Crystal structural data for modification II”. In: *Naturwissenschaften* 64.8 (Aug. 1977), pp. 435–435. DOI: 10.1007/bf00508700.

[118] Freddy G. del Pozo et al. “Single Crystal-Like Performance in Solution-Coated Thin-Film Organic Field-Effect Transistors”. In: *Advanced Functional Materials* 26.14 (Sept. 2015), pp. 2379–2386. DOI: 10.1002/adfm.201502274.

[119] S. Georgakopoulos, F. G. del Pozo, and M. Mas-Torrent. “Flexible organic transistors based on a solution-sheared PVDF insulator”. In: *Journal of Materials Chemistry C* 3.47 (2015), pp. 12199–12202. DOI: 10.1039/c5tc02488a.

[120] Inés Temiño et al. “A Rapid, Low-Cost, and Scalable Technique for Printing State-of-the-Art Organic Field-Effect Transistors”. In: *Advanced Materials Technologies* 1.5 (June 2016), p. 1600090. DOI: 10.1002/admt.201600090.

[121] P. L. Polavarapu. "Ab initio vibrational Raman and Raman optical activity spectra". In: *The Journal of Physical Chemistry* 94.21 (Oct. 1990), pp. 8106–8112. DOI: 10.1021/j100384a024.

[122] T. C. Damen, S. P. S. Porto, and B. Tell. "Raman Effect in Zinc Oxide". In: *Physical Review* 142.2 (Feb. 1966), pp. 570–574. DOI: 10.1103/physrev.142.570.

[123] "Raman Microscopy". In: *Field Guide to Nonlinear Optics*. Society of Photo-Optical Instrumentation Engineers. DOI: 10.1117/3.1002081.ch62.

[124] Sergi Galindo et al. "Control of Polymorphism and Morphology in Solution Sheared Organic Field-Effect Transistors". In: *Advanced Functional Materials* 27.25 (Apr. 2017), p. 1700526. DOI: 10.1002/adfm.201700526.

[125] Sergi Riera-Galindo, Adrián Tamayo, and Marta Mas-Torrent. "Role of Polymorphism and Thin-Film Morphology in Organic Semiconductors Processed by Solution Shearing". In: *ACS Omega* 3.2 (Feb. 2018), pp. 2329–2339. DOI: 10.1021/acsomega.8b00043.

[126] Ying Diao et al. "Morphology control strategies for solution-processed organic semiconductor thin films". In: *Energy Environ. Sci.* 7.7 (2014), pp. 2145–2159. DOI: 10.1039/c4ee00688g.

[127] Fiora Artusio and Roberto Pisano. "Surface-induced crystallization of pharmaceuticals and biopharmaceuticals: A review". In: *International Journal of Pharmaceutics* 547.1-2 (Aug. 2018), pp. 190–208. DOI: 10.1016/j.ijpharm.2018.05.069.

[128] Andrew O. F. Jones et al. "Substrate-Induced and Thin-Film Phases: Polymorphism of Organic Materials on Surfaces". In: *Advanced Functional Materials* 26.14 (Jan. 2016), pp. 2233–2255. DOI: 10.1002/adfm.201503169.

[129] Christian Röthel et al. "Alteration of texture and polymorph of phenytoin within thin films and its impact on dissolution". In: *CrystEngComm* 18.4 (2016), pp. 588–595. DOI: 10.1039/c5ce01889g.

[130] Ingo Salzmann et al. "Epitaxial Growth of *pi*-Stacked Perfluoropentacene on Graphene-Coated Quartz". In: *ACS Nano* 6.12 (Nov. 2012), pp. 10874–10883. DOI: 10.1021/nn3042607.

[131] Paul Beyer et al. "Lattice Matching as the Determining Factor for Molecular Tilt and Multilayer Growth Mode of the Nanographene Hexa-peri-hexabenzocoronene". In: *ACS Applied Materials & Interfaces* 6.23 (Nov. 2014), pp. 21484–21493. DOI: 10.1021/am506465b.

[132] Magdalena Truger et al. "Surface-Induced Phase of Tyrian Purple (6,6′-Dibromoindigo): Thin Film Formation and Stability". In: *Crystal Growth & Design* 16.7 (June 2016), pp. 3647–3655. DOI: 10.1021/acs.cgd.6b00104.

[133] Magdalena Truger et al. "Crystallization of Tyrian purple (6,6′-dibromoindigo) thin films: The impact of substrate surface modifications". In: *Journal of Crystal Growth* 447 (Aug. 2016), pp. 73–79. DOI: 10.1016/j.jcrysgro.2016.05.001.

[134] P. Süsse and C. Krampe. "6,6?-Dibromo-indigo, a main component of tyrian Purple". In: *Naturwissenschaften* 66.2 (Feb. 1979), pp. 110–110. DOI: 10.1007/bf00373504.

[135] Sine Larsen et al. "The Crystal and Molecular Structures of Tyrian Purple (6,6'-Dibromoindigotin) and 2,2'-Dimethoxyindigotin." In: *Acta Chemica Scandinavica* 34a (1980), pp. 171–176. DOI: 10.3891/acta.chem.scand.34a-0171.

[136] Sudha R. Vippagunta, Harry G. Brittain, and David J.W. Grant. "Crystalline solids". In: *Advanced Drug Delivery Reviews* 48.1 (May 2001), pp. 3–26. DOI: 10.1016/s0169-409x(01)00097-7.

[137] Ying Diao et al. "Surface Design for Controlled Crystallization: The Role of Surface Chemistry and Nanoscale Pores in Heterogeneous Nucleation". In: *Langmuir* 27.9 (May 2011), pp. 5324–5334. DOI: 10.1021/la104351k.

[138] Thomas Kellner et al. "Crystallographic Textures and Morphologies of Solution Cast Ibuprofen Composite Films at Solid Surfaces". In: *Molecular Pharmaceutics* 11.11 (Oct. 2014), pp. 4084–4091. DOI: 10.1021/mp500264e.

[139] Nima Yazdanpanah et al. "Continuous Heterogeneous Crystallization on Excipient Surfaces". In: *Crystal Growth & Design* 17.6 (May 2017), pp. 3321–3330. DOI: 10.1021/acs.cgd.7b00297.

[140] Stefan Pachmajer et al. "Self-Limited Growth in Pentacene Thin Films". In: *ACS Applied Materials & Interfaces* 9.13 (Mar. 2017), pp. 11977–11984. DOI: 10.1021/acsami.6b15907.

[141] Oliver Werzer et al. "Particular Film Formation of Phenytoin at Silica Surfaces". In: *Molecular Pharmaceutics* 11.2 (Jan. 2014), pp. 610–616. DOI: 10.1021/mp4006479.

[142] Daniela Reischl et al. "Surface-Induced Polymorphism as a Tool for Enhanced Dissolution: The Example of Phenytoin". In: *Crystal Growth & Design* 15.9 (Aug. 2015), pp. 4687–4693. DOI: 10.1021/acs.cgd.5b01002.

[143] Stephanie M. Guthrie, Detlef-M. Smilgies, and Gaurav Giri. "Controlling Polymorphism in Pharmaceutical Compounds Using Solution Shearing". In: *Crystal Growth & Design* 18.2 (Jan. 2018), pp. 602–606. DOI: 10.1021/acs.cgd.7b01686.

[144] A. Camerman and N. Camerman. "The stereochemical basis of anticonvulsant drug action. I. The crystal and molecular structure of diphenylhydantoin, a noncentrosymmetric structure solved by centric symbolic addition". In: *Acta Crystallographica Section B Structural Crystallography and Crystal Chemistry* 27.11 (Nov. 1971), pp. 2205–2211. DOI: 10.1107/s0567740871005570.

[145] T. K. Chattopadhyay, R. A. Palmer, and J. N. Lisgarten. "X-ray structural and potential energy studies on zentropil (5,5-diphenyl-2,4-imidazolidine dione)". In: *Journal of Crystallographic and Spec-*

troscopic Research 23.2 (Feb. 1993), pp. 149–152. DOI: 10.1007/bf01195449.

[146] Ali Boultif and Daniel Louër. "Powder pattern indexing with the dichotomy method". In: *Journal of Applied Crystallography* 37.5 (Sept. 2004), pp. 724–731. DOI: 10.1107/s0021889804014876.

[147] Kei Moriyama, Naoko Furuno, and Naoki Yamakawa. "Crystal face identification by Raman microscopy for assessment of crystal habit of a drug". In: *International Journal of Pharmaceutics* 480.1-2 (Mar. 2015), pp. 101–106. DOI: 10.1016/j.ijpharm.2015.01.031.

[148] Chinnasamy Kalaiarasi et al. "Crystal structure and theoretical charge density studies of dilantin molecule". In: *Journal of Molecular Structure* 1170 (Oct. 2018), pp. 105–118. DOI: 10.1016/j.molstruc.2018.05.030.

[149] Doris E. Braun et al. "Computational and Experimental Characterization of Five Crystal Forms of Thymine: Packing Polymorphism, Polytypism/Disorder, and Stoichiometric 0.8-Hydrate". In: *Crystal Growth & Design* 16.6 (May 2016), pp. 3480–3496. DOI: 10.1021/acs.cgd.6b00459.

[150] Doris E. Braun, Maria Orlova, and Ulrich J. Griesser. "Creatine: Polymorphs Predicted and Found". In: *Crystal Growth & Design* 14.10 (Sept. 2014), pp. 4895–4900. DOI: 10.1021/cg501159c.

[151] MJEA Frisch et al. *Gaussian 09, revision D. 01*. 2009.

[152] Panagiotis G. Karamertzanis and Constantinos C. Pantelides. "Ab initio crystal structure prediction?I. Rigid molecules". In: *Journal of Computational Chemistry* 26.3 (2004), pp. 304–324. DOI: 10.1002/jcc.20165.

[153] P. G. Karamertzanis† and C. C. Pantelides. "Ab initiocrystal structure prediction. II. Flexible molecules". In: *Molecular Physics* 105.2-3 (Jan. 2007), pp. 273–291. DOI: 10.1080/00268970601143317.

[154] Matthew Habgood et al. “Efficient Handling of Molecular Flexibility in Ab Initio Generation of Crystal Structures”. In: *Journal of Chemical Theory and Computation* 11.4 (Mar. 2015), pp. 1957–1969. DOI: 10.1021/ct500621v.

[155] David S. Coombes et al. “Role of Electrostatic Interactions in Determining the Crystal Structures of Polar Organic Molecules. A Distributed Multipole Study”. In: *The Journal of Physical Chemistry* 100.18 (Jan. 1996), pp. 7352–7360. DOI: 10.1021/jp960333b.

[156] Curt M. Breneman and Kenneth B. Wiberg. “Determining atom-centered monopoles from molecular electrostatic potentials. The need for high sampling density in formamide conformational analysis”. In: *Journal of Computational Chemistry* 11.3 (Apr. 1990), pp. 361–373. DOI: 10.1002/jcc.540110311.

[157] Sarah L. Price et al. “Modelling organic crystal structures using distributed multipole and polarizability-based model intermolecular potentials”. In: *Physical Chemistry Chemical Physics* 12.30 (2010), p. 8478. DOI: 10.1039/c004164e.

[158] Anthony J Stone. “Distributed multipole analysis: Stability for large basis sets”. In: *Journal of Chemical Theory and Computation* 1.6 (2005), pp. 1128–1132. DOI: 10.1021/ct050190+.

[159] AJ Stone. “GDMA: A program for performing distributed multipole analysis of wave functions calculated using the Gaussian program system”. In: *University of Cambridge Cambridge, United Kingdom* (2010).

[160] A. V. Kazantsev et al. “Efficient Handling of Molecular Flexibility in Lattice Energy Minimization of Organic Crystals”. In: *Journal of Chemical Theory and Computation* 7.6 (May 2011), pp. 1998–2016. DOI: 10.1021/ct100597e.

[161] Stewart J. Clark et al. “First principles methods using CASTEP”. In: *Zeitschrift für Kristallographie - Crystalline Materials* 220.5/6 (Jan. 2005). DOI: 10.1524/zkri.220.5.567.65075.

[162] David Vanderbilt. "Soft self-consistent pseudopotentials in a generalized eigenvalue formalism". In: *Physical Review B* 41.11 (Apr. 1990), pp. 7892–7895. DOI: 10.1103/physrevb.41.7892.

[163] Anthony L. Spek. "Structure validation in chemical crystallography". In: *Acta Crystallographica Section D Biological Crystallography* 65.2 (Jan. 2009), pp. 148–155. DOI: 10.1107/s090744490804362x.

[164] Michael J. Turner et al. "Energy frameworks: insights into interaction anisotropy and the mechanical properties of molecular crystals". In: *Chemical Communications* 51.18 (2015), pp. 3735–3738. DOI: 10.1039/c4cc09074h.

[165] Michael J. Turner et al. "Accurate and Efficient Model Energies for Exploring Intermolecular Interactions in Molecular Crystals". In: *The Journal of Physical Chemistry Letters* 5.24 (Nov. 2014), pp. 4249–4255. DOI: 10.1021/jz502271c.

[166] Campbell F. Mackenzie et al. "CrystalExplorermodel energies and energy frameworks: extension to metal coordination compounds, organic salts, solvates and open-shell systems". In: *IUCrJ* 4.5 (July 2017), pp. 575–587. DOI: 10.1107/s205225251700848x.

[167] Max Born and Kun Huang. *Dynamical Theory of Crystal Lattices (Oxford Classic Texts in the Physical Sciences)*. Oxford University Press, USA, 1998. ISBN: 9780198503699.

[168] Doris E. Braun et al. "Racemic Naproxen: A Multidisciplinary Structural and Thermodynamic Comparison with the Enantiopure Form". In: *Crystal Growth & Design* 11.12 (Dec. 2011), pp. 5659–5669. DOI: 10.1021/cg201203u.

[169] E. Menard et al. "Nanoscale Surface Morphology and Rectifying Behavior of a Bulk Single-Crystal Organic Semiconductor". In: *Advanced Materials* 18.12 (June 2006), pp. 1552–1556. DOI: 10.1002/adma.200502569.

[170] A. L. Spek. "Single-crystal structure validation with the programPLATON". In: *Journal of Applied Crystallography* 36.1 (Jan. 2003), pp. 7–13. DOI: 10.1107/s0021889802022112.

[171] Richard E. Marsh et al. "Some 60 new space-group corrections". In: *Acta Crystallographica Section B Structural Science* 58.1 (Jan. 2001), pp. 62–77. DOI: 10.1107/s0108768101017128.

[172] Y. Le Page. "MISSYM1.1 - a flexible new release". In: *Journal of Applied Crystallography* 21.6 (Dec. 1988), pp. 983–984. DOI: 10.1107/s0021889888007022.

[173] Tommaso Marcato and Chih-Jen Shih. "Molecular Orientation Effects in Organic Light-Emitting Diodes". In: *Helvetica Chimica Acta* 102.5 (May 2019), e1900048. DOI: 10.1002/hlca.201900048.

[174] Belinda J Boehm, Huong T L Nguyen, and David M Huang. "The interplay of interfaces, supramolecular assembly, and electronics in organic semiconductors". In: *Journal of Physics: Condensed Matter* 31.42 (July 2019), p. 423001. DOI: 10.1088/1361-648x/ab2ac2.

[175] Satoru Ohisa et al. "Molecular Interdiffusion between Stacked Layers by Solution and Thermal Annealing Processes in Organic Light Emitting Devices". In: *ACS Applied Materials & Interfaces* 7.37 (Sept. 2015), pp. 20779–20785. DOI: 10.1021/acsami.5b05818.

[176] Yuichiro Watanabe et al. "Simultaneous Manipulation of Intramolecular and Intermolecular Hydrogen Bonds in n-Type Organic Semiconductor Layers: Realization of Horizontal Orientation in OLEDs". In: *Advanced Optical Materials* 3.6 (Jan. 2015), pp. 769–773. DOI: 10.1002/adom.201400532.

[177] Daisuke Yokoyama et al. "Molecular Stacking Induced by Intermolecular C-H···N Hydrogen Bonds Leading to High Carrier Mobility in Vacuum-Deposited Organic Films". In: *Advanced Functional Materials* 21.8 (Mar. 2011), pp. 1375–1382. DOI: 10.1002/adfm.201001919.

[178] Yuichiro Watanabe et al. "Control of Molecular Orientation in Organic Semiconductor Films using Weak Hydrogen Bonds". In: *Advanced Materials* 31.18 (Mar. 2019), p. 1808300. DOI: 10.1002/adma.201808300.

[179] Steffen Duhm et al. "Orientation-dependent ionization energies and interface dipoles in ordered molecular assemblies". In: *Nature Materials* 7.4 (Feb. 2008), pp. 326–332. DOI: 10.1038/nmat2119.

[180] Jörg Frischeisen et al. "Increased light outcoupling efficiency in dye-doped small molecule organic light-emitting diodes with horizontally oriented emitters". In: *Organic Electronics* 12.5 (May 2011), pp. 809–817. DOI: 10.1016/j.orgel.2011.02.005.

[181] Philipp Liehm et al. "Comparing the emissive dipole orientation of two similar phosphorescent green emitter molecules in highly efficient organic light-emitting diodes". In: *Applied Physics Letters* 101.25 (Dec. 2012), p. 253304. DOI: 10.1063/1.4773188.

[182] M. D. Ediger, Juan de Pablo, and Lian Yu. "Anisotropic Vapor-Deposited Glasses: Hybrid Organic Solids". In: *Accounts of Chemical Research* 52.2 (Jan. 2019), pp. 407–414. DOI: 10.1021/acs.accounts.8b00513.

[183] M. D. Ediger. "Perspective: Highly stable vapor-deposited glasses". In: *The Journal of Chemical Physics* 147.21 (Dec. 2017), p. 210901. DOI: 10.1063/1.5006265.

[184] Otello Maria Roscioni et al. "Pentacene Crystal Growth on Silica and Layer-Dependent Step-Edge Barrier from Atomistic Simulations". In: *The Journal of Physical Chemistry Letters* 9.23 (Nov. 2018), pp. 6900–6906. DOI: 10.1021/acs.jpclett.8b03063.

[185] Daisuke Yokoyama et al. "Horizontal molecular orientation in vacuum-deposited organic amorphous films of hole and electron transport materials". In: *Applied Physics Letters* 93.17 (Oct. 2008), p. 173302. DOI: 10.1063/1.2996258.

[186] D YOKOYAMA et al. "Horizontal orientation of linear-shaped organic molecules having bulky substituents in neat and doped vacuum-deposited amorphous films". In: *Organic Electronics* 10.1 (Feb. 2009), pp. 127–137. DOI: 10.1016/j.orgel.2008.10.010.

[187] Hisahiro Sasabe et al. "Influence of Substituted Pyridine Rings on Physical Properties and Electron Mobilities of 2-Methylpyrimidine Skeleton-Based Electron Transporters". In: *Advanced Functional Materials* 21.2 (Oct. 2010), pp. 336–342. DOI: 10.1002/adfm.201001252.

[188] Dongsun Yoo et al. "A molecular dynamics study on the interface morphology of vapor-deposited amorphous organic thin films". In: *Physical Chemistry Chemical Physics* 21.3 (2019), pp. 1484–1490. DOI: 10.1039/c8cp05294h.

[189] Yong Youn et al. "All-atom simulation of molecular orientation in vapor-deposited organic light-emitting diodes". In: *Journal of Materials Chemistry C* 6.5 (2018), pp. 1015–1022. DOI: 10.1039/c7tc05278b.

[190] Y. Olivier et al. "Computational Design of Thermally Activated Delayed Fluorescence Materials: The Challenges Ahead". In: *The Journal of Physical Chemistry Letters* 9.20 (Sept. 2018), pp. 6149–6163. DOI: 10.1021/acs.jpclett.8b02327.

[191] Taiping Hu et al. "Origin of High Efficiencies for Thermally Activated Delayed Fluorescence Organic Light-Emitting Diodes: Atomistic Insight into Molecular Orientation and Torsional Disorder". In: *The Journal of Physical Chemistry C* 122.48 (Nov. 2018), pp. 27191–27197. DOI: 10.1021/acs.jpcc.8b08169.

[192] Luca Muccioli, Gabriele D'Avino, and Claudio Zannoni. "Simulation of Vapor-Phase Deposition and Growth of a Pentacene Thin Film on C60(001)". In: *Advanced Materials* 23.39 (Sept. 2011), pp. 4532–4536. DOI: 10.1002/adma.201101652.

[193] Diane M. Walters et al. "Influence of Molecular Shape on the Thermal Stability and Molecular Orientation of Vapor-Deposited Organic

Semiconductors". In: *The Journal of Physical Chemistry Letters* 8.14 (July 2017), pp. 3380–3386. DOI: 10.1021/acs.jpclett.7b01097.

[194] Lucas W. Antony et al. "Influence of Vapor Deposition on Structural and Charge Transport Properties of Ethylbenzene Films". In: *ACS Central Science* 3.5 (Apr. 2017), pp. 415–424. DOI: 10.1021/acscentsci.7b00041.

[195] Thomas Lee et al. "The Molecular Origin of Anisotropic Emission in an Organic Light-Emitting Diode". In: *Nano Letters* 17.10 (Sept. 2017), pp. 6464–6468. DOI: 10.1021/acs.nanolett.7b03528.

[196] Claire Tonnelé et al. "Elucidating the Spatial Arrangement of Emitter Molecules in Organic Light-Emitting Diode Films". In: *Angewandte Chemie* 129.29 (Feb. 2017), pp. 8522–8526. DOI: 10.1002/ange.201610727.

[197] Guangchao Han, Xingxing Shen, and Yuanping Yi. "Deposition Growth and Morphologies of C60on DTDCTB Surfaces: An Atomistic Insight into the Integrated Impact of Surface Stability, Landscape, and Molecular Orientation". In: *Advanced Materials Interfaces* 2.17 (Sept. 2015), p. 1500329. DOI: 10.1002/admi.201500329.

[198] Makoto Yoneya et al. "Self-assembly of donor-acceptor semiconducting polymers in solution thin films: a molecular dynamics simulation study". In: *Journal of Materials Chemistry C* 5.37 (2017), pp. 9602–9610. DOI: 10.1039/c7tc01014a.

[199] H.J.C. Berendsen, D. van der Spoel, and R. van Drunen. "GROMACS: A message-passing parallel molecular dynamics implementation". In: *Computer Physics Communications* 91.1-3 (Sept. 1995), pp. 43–56. DOI: 10.1016/0010-4655(95)00042-e.

[200] Berk Hess et al. "GROMACS 4: Algorithms for Highly Efficient, Load-Balanced, and Scalable Molecular Simulation". In: *Journal of Chemical Theory and Computation* 4.3 (Feb. 2008), pp. 435–447. DOI: 10.1021/ct700301q.

[201] Berk Hess et al. “LINCS: A linear constraint solver for molecular simulations”. In: *Journal of Computational Chemistry* 18.12 (Sept. 1997), pp. 1463–1472. DOI: 10.1002/(sici)1096-987x(199709)18:12<1463::aid-jcc4>3.0.co;2-h.

[202] Markus K. Dahlgren et al. “Characterization of Biaryl Torsional Energetics and its Treatment in OPLS All-Atom Force Fields”. In: *Journal of Chemical Information and Modeling* 53.5 (May 2013), pp. 1191–1199. DOI: 10.1021/ci4001597.

[203] Luca Muccioli et al. “Supramolecular Organization of Functional Organic Materials in the Bulk and at Organic/Organic Interfaces: A Modeling and Computer Simulation Approach”. In: *Topics in Current Chemistry*. Springer Berlin Heidelberg, 2013, pp. 39–101. DOI: 10.1007/128_2013_470.

[204] G. A. Petersson et al. “A complete basis set model chemistry. I. The total energies of closed-shell atoms and hydrides of the first-row elements”. In: *The Journal of Chemical Physics* 89.4 (Aug. 1988), pp. 2193–2218. DOI: 10.1063/1.455064.

[205] Matthias Ernzerhof and John P. Perdew. “Generalized gradient approximation to the angle- and system-averaged exchange hole”. In: *The Journal of Chemical Physics* 109.9 (Sept. 1998), pp. 3313–3320. DOI: 10.1063/1.476928.

[206] G. A. Petersson and Mohammad A. Al-Laham. “A complete basis set model chemistry. II. Open-shell systems and the total energies of the first-row atoms”. In: *The Journal of Chemical Physics* 94.9 (May 1991), pp. 6081–6090. DOI: 10.1063/1.460447.

[207] M. J. Frisch et al. *Gaussian 09 Revision D.01*. Gaussian Inc. Wallingford CT.

[208] Bin Chen, Marcus G. Martin, and J. Ilja Siepmann. “Thermodynamic Properties of the Williams, OPLS-AA, and MMFF94 All-Atom Force Fields for Normal Alkanes”. In: *The Journal of Physical Chemistry B* 102.14 (Apr. 1998), pp. 2578–2586. DOI: 10.1021/jp9801065.

[209] Nora A. McDonald and William L. Jorgensen. "Development of an All-Atom Force Field for Heterocycles. Properties of Liquid Pyrrole, Furan, Diazoles, and Oxazoles". In: *The Journal of Physical Chemistry B* 102.41 (Oct. 1998), pp. 8049–8059. DOI: 10.1021/jp981200o.

[210] Carlos E. S. Bernardes and Abhinav Joseph. "Evaluation of the OPLS-AA Force Field for the Study of Structural and Energetic Aspects of Molecular Organic Crystals". In: *The Journal of Physical Chemistry A* 119.12 (Mar. 2015), pp. 3023–3034. DOI: 10.1021/jp512349r.

[211] M. Moral et al. "Cost-Effective Force Field Tailored for Solid-Phase Simulations of OLED Materials". In: *Journal of Chemical Theory and Computation* 11.7 (June 2015), pp. 3383–3392. DOI: 10.1021/acs.jctc.5b00164.

[212] Sébastien Le Roux and Valeri Petkov. "ISAACS- interactive structure analysis of amorphous and crystalline systems". In: *Journal of Applied Crystallography* 43.1 (Jan. 2010), pp. 181–185. DOI: 10.1107/s0021889809051929.

[213] Ulrich Ziener et al. "Supramolecular Assemblies of a Bis(terpyridine) Ligand and of its [2×2] Grid-type ZnII and CoII Complexes on Highly Ordered Pyrolytic Graphite". In: *Chemistry - A European Journal* 8.4 (Feb. 2002), pp. 951–957. DOI: 10.1002/1521-3765(20020215)8:4<951::aid-chem951>3.0.co;2-9.

[214] Christoph Meier et al. "Weak Hydrogen Bonds as a Structural Motif for Two-Dimensional Assemblies of Oligopyridines on Highly Oriented Pyrolytic Graphite: An STM Investigation". In: *The Journal of Physical Chemistry B* 109.44 (Nov. 2005), pp. 21015–21027. DOI: 10.1021/jp054271d.

[215] Ulrich Ziener. "Self-Assembled Nanostructures of Oligopyridine Molecules". In: *The Journal of Physical Chemistry B* 112.47 (Nov. 2008), pp. 14698–14717. DOI: 10.1021/jp805846d.

[216] Christoph Meier, Katharina Landfester, and Ulrich Ziener. "Adsorbate-Substrate-Mediated Growth of Oligopyridine Monolayers at the Solid/Liquid Interface". In: *The Journal of Physical Chemistry C* 113.4 (Jan. 2009), pp. 1507–1514. DOI: 10.1021/jp808431t.

[217] Christoph Meier et al. "Concentration and Coverage Dependent Adlayer Structures: From Two-Dimensional Networks to Rotation in a Bearing". In: *The Journal of Physical Chemistry C* 114.2 (Nov. 2009), pp. 1268–1277. DOI: 10.1021/jp910029z.

[218] David M. Adams et al. "Charge Transfer on the Nanoscale: Current Status". In: *The Journal of Physical Chemistry B* 107.28 (July 2003), pp. 6668–6697. DOI: 10.1021/jp0268462.

[219] Gabriele D'Avino et al. "Electrostatic phenomena in organic semiconductors: fundamentals and implications for photovoltaics". In: *Journal of Physics: Condensed Matter* 28.43 (Sept. 2016), p. 433002. DOI: 10.1088/0953-8984/28/43/433002.

[220] Gabriele D'Avino et al. "Electronic Polarization in Organic Crystals: A Comparative Study of Induced Dipoles and Intramolecular Charge Redistribution Schemes". In: *Journal of Chemical Theory and Computation* 10.11 (Oct. 2014), pp. 4959–4971. DOI: 10.1021/ct500618w.

[221] Gabriele D'Avino et al. "Electrostatic Interactions Shape Molecular Organization and Electronic Structure of Organic Semiconductor Blends". In: *Chemistry of Materials* 32.3 (Jan. 2020), pp. 1261–1271. DOI: 10.1021/acs.chemmater.9b04763.

[222] Sai Manoj Gali et al. "Energetic fluctuations in amorphous semiconducting polymers: Impact on charge-carrier mobility". In: *The Journal of Chemical Physics* 147.13 (Oct. 2017), p. 134904. DOI: 10.1063/1.4996969.

[223] M. J. Frisch et al. *Gaussian 16 Revision C.01*. Gaussian Inc. Wallingford CT. 2016.

[224] Frank Neese. "The ORCA program system". In: *WIREs Computational Molecular Science* 2.1 (June 2011), pp. 73–78. DOI: 10.1002/wcms.81.

[225] K. Senthilkumar et al. "Charge transport in columnar stacked triphenylenes: Effects of conformational fluctuations on charge transfer integrals and site energies". In: *The Journal of Chemical Physics* 119.18 (Nov. 2003), pp. 9809–9817. DOI: 10.1063/1.1615476.

[226] Omar López-Estrada et al. "Reassessment of the Four-Point Approach to the Electron-Transfer Marcus-Hush Theory". In: *ACS Omega* 3.2 (Feb. 2018), pp. 2130–2140. DOI: 10.1021/acsomega.7b01425.

[227] Naga Rajesh Tummala et al. "Static and Dynamic Energetic Disorders in the C60, PC61BM, C70, and PC71BM Fullerenes". In: *The Journal of Physical Chemistry Letters* 6.18 (Sept. 2015), pp. 3657–3662. DOI: 10.1021/acs.jpclett.5b01709.

[228] Carina Faber et al. "Electron-phonon coupling in the C60fullerene within the many-bodyGWapproach". In: *Physical Review B* 84.15 (Oct. 2011). DOI: 10.1103/physrevb.84.155104.

[229] Zhengyang Bin et al. "Efficient n-Dopants and Their Roles in Organic Electronics". In: *Advanced Optical Materials* 6.18 (July 2018), p. 1800536. DOI: 10.1002/adom.201800536.

[230] H. Bässler. "Charge Transport in Disordered Organic Photoconductors a Monte Carlo Simulation Study". In: *physica status solidi (b)* 175.1 (Jan. 1993), pp. 15–56. DOI: 10.1002/pssb.2221750102.

Acknowlegments

The authors declare no competing financial interest. We thank CINECA Supercomputing Center for providing computer time through the ISCRA scheme. A. Giunchi acknowledges funding by the exchange program Erasmus+ Mobilita per tirocinio 2017/ 2018 and Marco Polo 2019.